VOLUME 75 JUNE 10, 1971 NUMBER 12

JPCHAx

THE JOURNAL OF PHYSICAL CHEMISTRY

PUBLISHED BIWEEKLY BY THE AMERICAN CHEMICAL SOCIETY

RADIATION CHEMISTRY

ADVANCES IN CHEMISTRY SERIES NOS. 81 AND 82

Seventy-seven papers and 34 abstracts from the International Conference on Radiation Chemistry at Argonne National Laboratories, chaired by Edwin J. Hart. Includes review and research papers from 12 countries besides U.S., Canada, and England, including 8 from U.S.S.R. and two other East European countries.

Volume I groups papers on radiation in aqueous media, radiation of biological systems, dosimetry, and one plenary lecture.

Volume II has papers on radiation of gases, of solids, and of organic liquids, plus three plenary lectures.

No. 81 Radiation Chemistry—I — 616 pages with index
No. 82 Radiation Chemistry—II — 558 pages with index
Each $16.00
Cloth (1968) Ordered together $30.00

Set of L.C. cards free with library orders.

Other books in the ADVANCES IN CHEMISTRY SERIES in physical and colloid chemistry include:

No. 68 Mössbauer Effect and its Application in Chemistry. Ten papers that will familiarize chemists with Mössbauer spectroscopy as an analytical tool, for studying chemical bonding, crystal structure, electron density, magnetism, and other properties. 178 pages
Cloth (1967) $8.00

No. 67 Equilibrium Concepts in Natural Water Systems. Sixteen papers represent the collaboration of aquatic chemists, analytical chemists, geologists, oceanographers, limnologists, and sanitary engineers, working with simplified models to produce fruitful generalizations and valuable insights into the factors that control the chemistry of natural systems. 344 pages
Cloth (1967) $11.00

No. 64 Regenerative EMF Cells. Seventeen papers survey current progress and research on regenerative systems for converting and storing electrical energy. Principal emphasis is on thermally regenerative systems, but chemical and photochemical systems are considered. 309 pages
Cloth (1967) $11.00

No. 63 Ordered Fluids and Liquid Crystals. Twenty-two studies on characterization, properties, and occurance of these phenomena in many substances such as tristearin, p-azoxyanisole, mono-and di-hydric alcohols, phospholipids and polypeptides. 332 pages
Cloth (1967) $11.50

No. 58 Ion-Molecule Reactions in the Gas Phase. Eighteen papers survey spectrometric and other methods for producing and studying ion-molecule reactions, such as pulsed sources for studing thermal ions, reactions in flames and electrical discharges. 336 pages
Cloth (1966) $10.50

No. 54 Advanced Propellant Chemistry. Primarily directed to the search for new oxidizers; 26 papers survey oxygen-containing oxidizers, fuels and binders, fluorine systems including oxygen difluoride and difluoramines and liquid systems. 290 pages
Cloth (1966) $10.50

No. 47 Fuel Cell Systems. Developments in theory, performance, construction, and new systems for the energy converter that is proving itself in military and space uses. 360 pages
Cloth (1965) $10.50

No. 43 Contact Angle, Wettability, and Adhesion. Twenty-six papers on theoretical and practical approaches to wettability and adhesion; with summary of the surface chemical studies of W. A. Zisman, the 1963 Kendall Award winner. 389 pages
Cloth (1964) $10.50

No. 40 Mass Spectral Correlations. By Fred W. McLafferty. Over 4000 spectral listed by mass/charge ratios of fragment ions with the most probable original structures for each. 117 pages
Paper (1963) $6.00

No. 33 Solid Surfaces and the Gas-Solid Interface. Thirty-seven papers from the Kendall Award Symposium honoring Stephen Brunauer. Theory and techniques for studying surface phenomena.
Cloth (1961) $12.00

No. 31 Critical Solution Temperatures. By Alfred W. Francis. CST answers the question, "Do two liquids mix?" and is widely used for screening solvents. Over 6000 systems are included, 70% with a hydrocarbon as one component; nearly 1100 non-hydrocarbon solvents are listed. 246 pages
Cloth (1961) $8.00

No. 29 Physical Properties of Chemical Compounds—III. By Robert R. Dreisbach. Supplements earlier volumes with properties of 434 aliphatic compounds and 22 miscellaneous compounds and elements. Index to volumes I, II, and III. 489 pages
Cloth (1961) $10.00

No. 25 Physical Functions of Hydrocolloids. Papers on natural gums, gelatin pectins and related polysaccharides, and theoretical and functional aspects of hydrocolloids, emulsions, foams, and dispersions. Strong food industry emphasis. 103 pages
Paper (1960) $5.00

No. 22 Physical Properties of Chemical Compounds—II. By Robert R. Dreisbach. Properties of 476 alkanes, haloalkanes, alkenes, haloalkenes, diolefins, and alkynes. 491 pages
Cloth (1959) $10.00

No. 18 Thermodynamic Properties of the Elements. By D. R. Stull and G. C. Sinke. Tabulated values of heat capacity, heat content, entropy, and free energy function of solid, liquid, and gas states of first 92 elements in range of 298° to 3000°K. Some auxiliary data frequently included.
Cloth (1956) $8.00

No. 15 Physical Properties of Chemical Compounds. By Robert R. Dreisbach. Tables of parameters for calculating physical properties of 511 organic cyclic compounds. 536 pages
Cloth (1955) $10.00

All books postpaid in U.S. and Canada; plus 30 cents in PUAS and elsewhere.

Order from: SPECIAL ISSUES SALES,
AMERICAN CHEMICAL SOCIETY
1155 SIXTEENTH ST., N.W.
WASHINGTON, D.C. 20036

THE JOURNAL OF

PHYSICAL CHEMISTRY

 Published biweekly by the American Chemical Society at 20th and Northampton Sts., Easton, Pa. 18042. Second-class postage paid at Easton, Pa.

All manuscripts should be sent to *The Journal of Physical Chemistry,* Department of Chemistry, University of Minnesota, Minneapolis, Minn. 55455.

Additions and Corrections are published once yearly in the final issue. See Volume 74, Number 26 for the proper form.

Extensive or unusual alterations in an article after it has been set in type are made at the author's expense, and it is understood that by requesting such alterations the author agrees to defray the cost thereof.

The American Chemical Society and the Editor of *The Journal of Physical Chemistry* assume no responsibility for the statements and opinions advanced by contributors.

Correspondence regarding accepted copy, proofs, and reprints should be directed to Editorial Production Office, American Chemical Society, 20th and Northampton Sts., Easton, Pa. 18042. Manager: CHARLES R. BERTSCH. Assistant Editor: EDWARD A. BORGER. Editorial Assistant: EVELYN J. UHLER.

Advertising Office: Century Communications Corporation, 142 East Avenue, Norwalk, Conn. 06851.

Business and Subscription Information

Remittances and orders for subscriptions and for single copies, notices of changes of address and new professional connections, and claims for missing numbers should be sent to the Subscription Service Department, American Chemical Society, 1155 Sixteenth St., N.W., Washington, D. C. 20036. Allow 4 weeks for changes of address. Please include an old address label with the notification.

Claims for missing numbers will not be allowed (1) if received more than sixty days from date of issue, (2) if loss was due to failure of notice of change of address to be received before the date specified in the preceding paragraph, or (3) if the reason for the claim is "missing from files."

Subscription rates (1971): members of the American Chemical Society, $20.00 for 1 year; to nonmembers, $40.00 for 1 year. Those interested in becoming members should write to the Admissions Department, American Chemical Society, 1155 Sixteenth St., N.W., Washington, D. C. 20036. Postage to Canada and countries in the Pan-American Union, $4.00; all other countries, $5.00. Single copies for current year: $2.00. Rates for back issues from Volume 56 to date are available from the Special Issues Sales Department, 1155 Sixteenth St., N.W., Washington, D. C. 20036.

This publication and the other ACS periodical publications are now available on microfilm. For information write to: MICROFILM, Special Issues Sales Department, 1155 Sixteenth St., N.W., Washington, D. C. 20036.

Notice to Authors printed on pages 5A and 6A

Platinum Group Metals and Compounds

ADVANCES IN CHEMISTRY SERIES
NO. 98

Eleven papers from a symposium by the Division of Inorganic Chemistry of the American Chemical Society chaired by U. V. Rao.

What new complexes of the platinum group metals have been synthesized? Here is a collection of papers presenting data on chalcogenides, oxides, nitrido and hydrido complexes, as well as the catalytic properties of these metals and their alloys. Information is included on

- synthesis
- structure
- magnetic susceptibility
- double bond migration

The platinum group metals are considered from the viewpoints of both industry and research. Their magnetic and thermodynamic properties are explored, as well as recent chemistry of σ- and π-bonded complexes. Crystal structure is discussed by several authors, with data presented in the form of

- x-ray scattering data
- absorption spectra
- crystal spectra
- infrared spectra
- Mossbauer spectra
- vibrational spectra

165 pages with index. Cloth bound (1971) $9.00
Postpaid in U.S. and Canada; plus 35 cents elsewhere.
Set of L. C. cards with library orders upon request.

Other books in the ADVANCES IN CHEMISTRY SERIES of interest to inorganic chemists include:

No. 89 Isotope Effects in Chemical Processes
278 pages Cloth bound (1969) $13.00

No. 82 Radiation Chemistry — II
558 pages Cloth bound (1968) $16.00

No. 81 Radiation Chemistry — I
616 pages Cloth bound (1968) $16.00

No. 81 and No. 82 ordered together $30.00

No. 78 Literature of Chemical Technology
732 pages Cloth bound (1968) $17.50

No. 73 Trace Inorganics in Water
396 pages Cloth bound (1968) $12.50

No. 72 Mass Spectrometry in Inorganic Chemistry
329 pages Cloth bound (1968) $12.00

Order from:
Special Issues Sales
American Chemical Society
1155 16th St., N. W.
Washington, D. C. 20036

THE JOURNAL OF

PHYSICAL CHEMISTRY

Volume 75, Number 12 June 10, 1971

AUTHOR INDEX

NOTICE TO AUTHORS

I. General Considerations

The Journal of Physical Chemistry is devoted to reporting both experimental and theoretical research dealing with fundamental aspects of physical chemistry. Space limitations necessitate giving preference to research articles dealing with previously unanswered basic questions in physical chemistry. Acceptable topics are those of general interest to physical chemists, especially work involving new concepts, techniques, and interpretations. Research that may lead to reexaminations of generally accepted views is, of course, welcome.

The Journal of Physical Chemistry publishes three types of manuscripts: *Articles*, *Notes*, and *Communications to the Editor*.

Authors reporting data should include, if possible, an interpretation of the data and its relevance to the theories of the properties of matter. However, the discussion should be concise and to the point and excessive speculation is to be discouraged. Papers reporting redeterminations of existing data will be acceptable only if there is reasonable justification for repetition: for example, if the more recent or more accurate data lead to new questions or to a reexamination of well known theories. Manuscripts that are essentially applications of chemical data or reviews of the literature are, in general, not suitable for publication in *The Journal of Physical Chemistry*. Detailed comparisons of methods of data analysis will be considered only if the paper also contains original data, or if such comparison leads to a genesis of new ideas.

Authors should include an introductory statement outlining the scientific rationale for the research. The statement should clearly specify the questions for which answers are sought and the connection of the present work with previous work in the field. All manuscripts are subject to critical review. It is to be understood that the final decision relating to a manuscript's suitability rests solely with the editorial staff.

Symposium papers are sometimes published as a group, but only after special arrangement with the editor.

Authors' attention is called to the "Handbook for Authors," available from the Special Issues Sales Department, American Chemical Society, 1155 Sixteenth St., N.W., Washington, D. C. 20036, in which pertinent material is to be found.

II. Types of Manuscripts

A. Articles should cover their subjects with thoroughness, clarity, and completeness. However, authors should also strive to make their *Articles* as concise as possible, avoiding unnecessary historical background. Abstracts to *Articles* should be brief—300 words is a maximum—and should serve to summarize the significant data and conclusions. The abstract should convey the essence of the *Article* to the reader.

B. Notes. Papers submitted in the category of *Notes* should report work that represents a complete and self-contained study of limited scope. *Notes* are a luxury in the present scientific literature; authors should not use a *Note* to report work that is part of a continuing study. *Notes* are not to be used for reporting preliminary results; reports of such work should be postponed until the work is completed or should be submitted as *Communications* if the results are of immediate or unusual interest to physical chemists. The same criteria of suitability for publication apply to *Notes* as to *Articles* (see General Considerations). The length of a *Note*, including tables, figures, and text, must not exceed 1.5 journal pages (1500 words or the equivalent). A *Note* should not be accompanied by an abstract.

C. Communications to the Editor are of two types, *Letters* and *Comments*. Both types are restricted to three-quarters of a page (750 words or the equivalent) including tables, figures, and text, and both types of *Communications* are subject to critical review, but special efforts will be made to expedite publication.

Letters should report preliminary results whose immediate availability to the scientific community is deemed important, and whose topic is timely enough to justify the double publication that usually results from the publication of a *Letter*.

Comments include significant remarks on the work of others. The editorial staff will generally permit the authors of the work being discussed to reply.

III. Introduction

All manuscripts submitted should contain brief introductory remarks describing the purpose of the work and giving sufficient background material to allow the reader to appreciate the state-of-knowledge at the time when the work was done. The introductory remarks in an *Article* should constitute the first section of the paper and should be labeled accordingly. In *Notes* and *Communications*, the introductory material should not be in such a separate section. To judge the appropriateness of the manuscript for *The Journal of Physical Chemistry*, the editorial staff will place considerable weight on the author's intentions as stated in the Introduction.

IV. Functions of Reviewers

The editorial staff requests the scientific advice of reviewers who are active in the area of research covered by the manuscript. The reviewers act only in an advisory capacity and the final decision concerning a manuscript is the responsibility of the editorial staff. The reviewers are asked to comment not only on the scientific content, but also on the manuscript's suitability for *The Journal of Physical Chemistry*. With respect to *Communications*, the reviewers are asked to comment specifically on the urgency of publication. All reviews are anonymous and the reviewing process is most effective

if reviewers do not reveal their identities to the authors. An exception arises in connection with a manuscript submitted for publication in the form of a comment on the work of another author. Under such circumstances the first author will, in general, be allowed to review the communication and to write a rebuttal, if he so chooses. The rebuttal and the original communication may be published together in the same issue of the journal. Revised manuscripts are generally sent back to the original reviewers, who are asked to comment on the revisions. If only minor revisions are involved, the editorial staff examines the revised manuscript in light of the recommendations of the reviewers and without seeking further opinions. For the convenience of reviewers, authors are advised to indicate clearly, either in the manuscript or in a covering letter, the specific revisions that have been made.

V. Submission of Manuscripts

All manuscripts must be submitted at least in duplicate and preferably in triplicate to expedite handling. Manuscripts must be typewritten, double-spaced copy, on $8^1/_2 \times 11$ in. paper. Legal sized paper is not acceptable. Authors should be certain that copies of the manuscript are clearly reproduced and readable. **Authors submitting figures must include the original drawings or photographs thereof, plus two xerographic copies for review purposes. These reproductions of the figures should be on $8^1/_2 \times 11$ in. paper.** Graphs must be in black ink on white or blue paper. Lettering at the sides of graphs may be penciled in and will be typeset. Figures and tables should be held to a minimum consistent with adequate presentation of information. All original data which the author deems pertinent must be submitted along with the manuscript. For example, a paper reporting a crystal structure should include structure factor tables for use by the reviewers.

Footnotes and references to the literature should be numbered consecutively within the paper; the number should also be placed in parentheses in the left margin opposite the line in which the reference first appears. A complete list of references should appear at the end of the paper. Initials of the authors referred to in the citations should be included in the complete reference at the back of the paper. Nomenclature should conform to that used in *Chemical Abstracts* and mathematical characters should be underlined for italics, Greek letters should be annotated, and subscripts and superscripts clearly marked.

Papers should not depend for their usefulness on unpublished material, and excessive reference to material in press is discouraged. References not readily available (*e.g.*, private technical reports, preprints, or articles in press) that are necessary for a complete review of the paper must be included with the manuscript for use by the reviewers.

VI. Revised Manuscripts

A manuscript sent back to an author for revision should be returned to the editor within 6 months; otherwise it will be considered withdrawn and treated as a new manuscript when and if it is returned. Revised manuscripts returned to the editor must be submitted in duplicate and all changes should be made by typewriter. **Unless the changes are very minor, all pages affected by revision must be retyped.** If revisions are so extensive that a new typescript of the manuscript is necessary, it is requested that a copy of the original manuscript be submitted along with the revised one.

VII. Supplementary Material

By arrangement with the National Auxiliary Publications Service (NAPS) of the American Society for Information Science (ASIS), supplementary material, such as extensive tables, graphs, spectra, and calculations, can be distributed in the form of microfiche copies or photoprints readable without optical aids. This material should accompany the manuscript for review by the editors and reviewers. Upon acceptance, it will be sent by the editor to NAPS where it is assigned a document number. A deposit fee of $12.50 (for 60 manuscript pages or less) is required and should be included with the material sent to the editor. The check must be made payable to CCMIC–NAPS. Further details may be obtained from NAPS, c/o CCM Information Corp., 909 3rd Ave., New York, N. Y. 10022.

VIII. Proofs and Reprints

Galley proofs, original manuscript, cut copy, and reprint order form are sent by the printer directly to the author who submitted the manuscript. The attention of the authors is directed to the instructions which accompany the proof, especially the requirement that all corrections, revisions, and additions be entered on the proof and not on the manuscript. Proofs should be checked against the manuscript (in particular all tables, equations, and formulas, since this is not done by the editor) and returned as soon as possible. No paper is released for printing until the author's proof has been received. Alterations in an article after it has been set in type are made at the author's expense, and it is understood that by entering such alterations on proofs the author agrees to defray the cost thereof. The filled-out reprint form must be returned with the proof, and if a price quotation is required by the author's organization a request for it should accompany the proof. Since reprinting is generally done from the journal press forms, all orders must be filed before press time. None can be accepted later, unless a previous request has been made to hold the type. Reprint shipments are made a month or more after publication, and bills are issued by the printer subsequent to shipment. Neither the editors nor the Washington office keeps any supply of reprints. Therefore, only the authors can be expected to meet requests for single copies of papers.

A page charge is assessed to cover in part the cost of publication. Although payment is expected, it is not a condition for publication. Articles are accepted or rejected only on the basis of merit, and the editor's decision to publish the paper is made before the charge is assessed. The charge per journal page is $50.

THE JOURNAL OF
PHYSICAL CHEMISTRY

VOLUME 75, NUMBER 12 JUNE 10, 1971

Mass Spectral Study of the Decomposition of Chlorine Fluoride behind Shock Waves[1]

by J. A. McIntyre* and R. W. Diesen

Chemical Physics Research Laboratory, The Dow Chemical Company, Midland, Michigan 48640
(Received November 4, 1970)

Publication costs assisted by The Dow Chemical Company

The thermal decomposition of chlorine fluoride has been studied over the temperature range 2000–2950°K using the technique of mass spectral sampling behind reflected shock waves. The reaction has been found to be complex, and evidence is offered to support the suggested mechanism which consists of the reactions

$$ClF + M \xrightarrow{k_1} Cl + F + M \quad (a)$$

$$Cl + ClF \underset{k_{-2}}{\overset{k_2}{\rightleftharpoons}} Cl_2 + F \quad (b)$$

$$Cl_2 + M \xrightarrow{k_3} 2Cl + M \quad (c)$$

From experimental data, k_{-2} is estimated to be greater than 1×10^{12} cc/mol sec.

Introduction

It is surprising to note that, of the very few known[2-5] investigations of the thermal decomposition of the chlorine fluorides (ClF, ClF_3, ClF_5), the simplest system, ClF, for which an unambiguous interpretation of experimental results is most likely, was most recently undertaken.[5] Even in this system the kinetics may be complex, since many reactions are possible at high temperatures in a dissociating system containing two or more atomic species. The reactions listed below are those that seem most likely to be important under the conditions of this investigation.[6]

$$ClF + M \longrightarrow Cl + F + M \quad (1)$$

$$Cl + ClF \rightleftharpoons Cl_2 + F \quad (2)$$

$$Cl_2 + M \longrightarrow 2Cl + M \quad (3)$$

$$F + ClF \rightleftharpoons Cl + F_2 \quad (4)$$

$$F_2 + M \longrightarrow 2F + M \quad (5)$$

In eq 1–5, M is a collision partner.

Some of the above reactions have been suggested[7] as being important steps in the mechanism of the reaction between Cl_2 and F_2 to yield ClF. That study, performed in a static reactor at temperatures between

(1) This work was sponsored by the U. S. Office of Naval Research under Contract No. Nonr 3814(00).

(2) J. A. Blauer, H. G. McMath, and F. C. Jaye, *J. Phys. Chem.*, **73**, 2683 (1969).

(3) A. E. Axworthy and J. M. Sullivan, *ibid.*, **74**, 949 (1970).

(4) J. A. Blauer, H. G. McMath, F. C. Jaye, and V. S. Engleman, *ibid.*, **74**, 1183 (1970).

(5) J. A. Blauer, V. S. Engleman, and W. C. Solomon, private communication.

(6) For Cl_2 and F_2-free ClF, reactions 3 and 5 can only be important if reactions 2 and 4 are.

(7) E. A. Fletcher and B. E. Dahneke, *J. Amer. Chem. Soc.*, **91**, 1603 (1969).

130 and 170°, disagreed with theoretical predictions which had been made[8,9] (and which also disagreed) concerning that reaction.

With this background,[5] a study of the thermal decomposition of chlorine fluoride by means of the technique of mass spectral sampling behind reflected shock waves was undertaken. For dilute solutions of ClF in neon in the temperature range 2000–2950°K, we have found the reaction to be complex and report here a mechanism which adequately accounts for the known experimental results.

Experimental Section

The apparatus and the methods used to obtain kinetic information have been described previously.[10–12] Samples were prepared from Ozark–Mahoning ClF, purified[13] just before use by trap-to-trap distillation at various temperatures between −80 and −145°, Matheson research grade Cl_2 (also distilled), General Chemical F_2 (99%), Dow argon (99.99%), and Matheson research grade neon. Airco helium and Dow argon were used as driver gases without purification.

For all samples neon was used as the primary diluent, with argon added at 0.25% as an internal pressure standard.[10] Mixtures for decomposition experiments contained nominally[14] 0.5% reactant. Mixtures for the $Cl_2 + F_2$ reaction studies contained 0.5% of each, and were ClF-free.

Results and Discussion

By analogy with the halogens, one may be inclined to treat the experimental results for the disappearance of ClF in terms of the pseudo-first-order reaction (1) above, where M is the inert gas diluent. Using this analysis we have obtained apparent rate constants over the temperature range 2000–2950°K. An Arrhenius plot of these apparent rate constants[15] is shown in Figure 1.

From a least-squares treatment of the data the apparent rate constant, k_a, is described by the equation

$$k_a = 10^{12.9\pm0.4} \exp\left(\frac{-41{,}500 \pm 4000}{RT}\right) \text{ cc/mol sec} \quad (6)$$

Our experimental activation energy is in reasonable agreement with that normally observed for Cl_2 dissociation in shock tubes.[8,16–19] Since the dissociation energies of Cl_2 and ClF only differ by approximately 2% (1.2 kcal/mol), this agreement would not be unexpected, particularly since the activation energies for halogen dissociation generally have been found (see, for instance, ref 20 for discussion) to be lower than the bond dissociation energy. However, additional information, discussed below, indicates that the reaction is more complex than this.

For the ClF system, the mass spectral technique gives one the advantage of being able to monitor independently and *simultaneously* the disappearance of ClF and Cl_2. Thus, when the data for the disappearance of Cl_2 in mixtures containing small amounts of ClF are interpreted

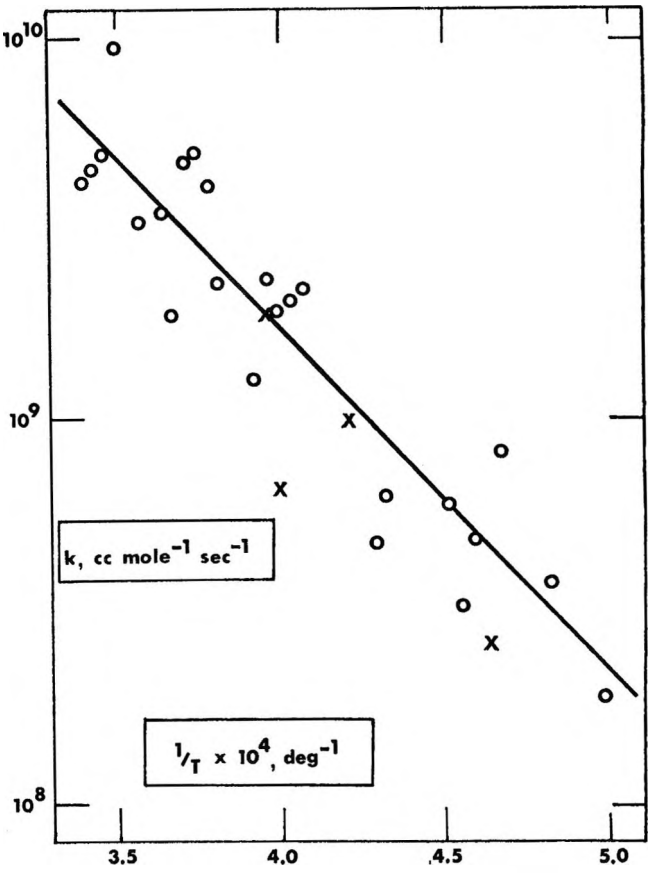

Figure 1. Arrhenius plot of apparent rate constants: O, first-order rate constants for the disappearance of ClF in nominally pure ClF samples, based on 48 experimental values; ×, first-order rate constants for the disappearance of Cl_2 in Cl_2 + ClF mixtures.

(8) S. W. Benson and G. W. Haugen, *J. Amer. Chem. Soc.*, 87, 4036 (1965).

(9) R. M. Noyes, *ibid.*, 88, 4311, 4318 (1966).

(10) R. W. Diesen and W. J. Felmlee, *J. Chem. Phys.*, 39, 2115 (1963).

(11) R. W. Diesen, *ibid.*, 39, 2121 (1963).

(12) R. W. Diesen, *ibid.*, 44, 3662 (1966).

(13) Considerable care and effort were spent in attempts to obtain 100% ClF; mass spectral analysis always showed 1–2% residual Cl_2. We remain skeptical of claims of 100% purity due to the extreme reactivity of ClF. We have found that the rate of disappearance of ClF increases rapidly in the presence of small amounts of oxygen. The mass spectral sampling technique allows us to exclude this possibility for the results we report here.

(14) The purity of ClF has been discussed.[13] Our own attempts at preparing ClF gave a product high in Cl_2, which was used for the Cl_2 in ClF experiments.

(15) For reactions which will become obvious we do not tabulate these rate constants. The reflected shock pressures were in the range 300–550 Torr.

(16) H. Hiraoka and R. Hardwick, *J. Chem. Phys.*, 36, 1715 (1962).

(17) T. A. Jacobs and R. R. Giedt, *ibid.*, 37, 747 (1963).

(18) M. van Thiel, D. J. Seery, and D. J. Britton, *J. Phys. Chem.*, 69, 834 (1965).

(19) R. A. Carabetta and H. B. Palmer, *J. Chem. Phys.*, 46, 1333 (1967); 47, 2202 (1967).

(20) See, for example, H. O. Pritchard, *Transfer Stor. Energy Mol.*, 2, 368 (1969); G. Burns and R. J. Brown, *J. Chem. Phys.*, 53, 3318 (1970).

in terms of reaction 3, the apparent rate constants are found to be very similar to those resulting from an equivalent treatment of the data for nominally pure ClF (see Figure 1). Further, the apparent rate for the disappearance of Cl_2 in nominally pure ClF (where Cl_2 is about 3–5% of the ClF concentration) is found to be very small, and in some cases Cl_2 increases slightly. Moreover, in the *same shock*, the apparent rate constants for Cl_2 disappearance became comparable. Thus, the results imply coupling between the ClF and Cl_2 and suggest the importance[21] of reaction 2.

In this case, reaction 3 also must be considered. This leads then to the suggested mechanism, which involves the reactions (rewritten here for convenience)

$$ClF + M \xrightarrow{k_1} Cl - F + M \quad (1)$$

$$Cl + ClF \underset{k_{-2}}{\overset{k_2}{\rightleftharpoons}} Cl_2 + F \quad (2)$$

$$Cl_2 + M \xrightarrow{k_3} 2Cl + M \quad (3)$$

From these equations one obtains

$$\frac{-d[ClF]}{dt} = k_1[M][ClF] + k_2[Cl][ClF] - k_{-2}[F][Cl_2] \quad (7)$$

$$\frac{-d[Cl_2]}{dt} = k_3[M][Cl_2] - k_2[Cl][ClF] + k_{-2}[F][Cl_2] \quad (8)$$

or, from addition of (7) and (8)

$$\frac{-d[ClF]}{dt} + \frac{-d[Cl_2]}{dt} = k_1[M][ClF] + k_3[M][Cl_2] \quad (9)$$

which can be rearranged to

$$\frac{-d \ln [ClF]}{dt} = k_1[M] + \left[k_3[M] - \frac{-d \ln [Cl_2]}{dt}\right] \frac{[Cl_2]}{[ClF]} \quad (10)$$

Note that eq 10 involves no approximations or assumptions other than that reactions 1, 2, and 3 describe the mechanism. To have any validity the proposed mechanism must account for the observations that (a) the disappearance of ClF can be described by pseudo-first-order kinetics; (b) at lower temperatures in high [ClF]/[Cl_2] samples, the [Cl_2] remains constant or slightly increases, while at high temperatures it decreases at a rate which is (apparently) described by a pseudo-first-order plot with rate constants similar to those for ClF.

Point (a) is accounted for as follows. At high temperatures the experimental quantitites $-d \ln [Cl_2]/dt$ (*i.e.*, the slope of a first-order plot) and the ratio [Cl_2]/[ClF] remain essentially constant. This means that $-d \ln [ClF]/dt$ will be essentially constant (from eq 10). At lower temperatures, [Cl_2] is observed to be essentially constant (which means $-d \ln [Cl_2]/dt$ is very small), and again $-d \ln [ClF]/dt$ appears to be constant. We do not claim that $-d \ln [ClF]/dt$ is truly constant—only that it would require rate data of very high precision in order to see the small degree of curvature.[22] The intent here is to demonstrate how ClF can apparently disappear by a first-order reaction even if the equation governing its disappearance is more complex.

The experimental observations of the fate of Cl_2 in this system make it necessary to invoke reactions other than (1). For reaction 2 to make significant contribution, k_2 must have a large value. For reaction 2 to be important in the early stages of the reaction, k_2 must be orders of magnitude larger than k_1 since at these times species other than ClF will be at low concentration. Experiments on the reaction of Cl_2 and F_2 in the shock tube over a similar temperature range (1450–2700°K), show that ClF is produced rapidly (which is not unexpected), and a distinct induction period is observed. The results are consistent with the interpretation of the low-temperature static work.[7]

Experimentally the induction period for the formation of ClF decreases with increasing temperature. It can be shown that[23] $\Delta t \propto (1/k_{-2}[Cl_2])$ where Δt = induction period. From this expression we estimate that k_{-2} is greater than 1×10^{12} cc/mol sec (*e.g.*, at 2040°K, [Cl_2] = 1.57×10^{-8} mol/cc, $\Delta t \sim 50 \times 10^{-6}$ sec).

The value of k_{-2} can reasonably be taken to be a lower limit since the proportionality constant will be larger than unity. This value of k_{-2} is certainly large enough to make reaction 2 important. Since the equilibrium constant[24] for reaction 2 is about 0.6 in this temperature range, k_2 is estimated to be $\geq 1 \times 10^{12}$ cc/mol sec. Thus, k_2 is certainly large enough to make reaction 2 important in the ClF decomposition. This large value of the rate constant, in conjunction with an assumed low activation energy for reaction 2, further explains the results.[25] At high temperatures, dissociation (*i.e.*, disappearance of *total* molecules) occurs by reactions 1 and 3, but these rates are coupled through the fast reaction 2. At lower temperatures reactions

(21) The absence of F_2 in the reacting mixture precludes reaction 4 (and thus 5) being important.

(22) Over one order of magnitude, allowing some scatter in the data, one can fit such data equally well by ln x or ln $(a + x) = kt$, where $a < x$.

(23) See, for instance, S. W. Benson, *J. Chem. Phys.*, **20**, 1605 (1952).

(24) "JANAF Thermochemical Tables," The Dow Chemical Co., Midland, Mich., June 1970.

(25) For supporting evidence see K. H. Homann, J. Warnatz, H. Gg. Wagner, and C. Zetsch, *Ber. Bunsenges Phys. Chem.*, to be published. See also A. Hoffman, K. H. Homann, and D. I. MacLean, ONR Report FRK-111, Boston College, Chestnut Hill, Mass., Jan 1971.

1 and 3 become less important relative to reaction 2 due to their higher activation energies. Thus, in our samples (large [ClF]/[Cl_2]), the ClF still disappears (*via* reaction 2) but now the [Cl_2] remains constant or even increases slightly depending on the actual temperature.

Conclusions

The thermal decomposition of ClF is complex in the temperature range 2000–2950°K, and a mechanism which adequately explains the experimental results is suggested. It is reemphasized[26] that caution is in order when inferring mechanisms from semilog kinetic plots. The results reported here also indicate that k_1 and k_3 are similar in magnitude although a more detailed study would be required to evaluate k_1 explicitly.

Acknowledgment. The authors wish to thank R. W. Anderson and H. R. Frick for the synthesis of ClF, and W. E. Eichorn for his help in obtaining some of the experimental data.

(26) A different way in which problems can arise has been demonstrated recently: M. W. Slack and E. S. Fishburne, *J. Chem. Phys.*, **52**, 5830 (1970).

Dimerization of the Perylene and Tetracene Radical Cations and Electronic Absorption Spectra of Their Dimers

by Katsumi Kimura,* Tomoko Yamazaki, and Shunji Katsumata

Physical Chemistry Laboratory, Institute of Applied Electricity, Hokkaido University, Sapporo, Japan
(Received October 5, 1970)

Publication costs assisted by the Institute of Applied Electricity, Hokkaido University

The reversible dimerizations of the perylene and tetracene radical cations in concentrated sulfuric acid have been studied spectroscopically. Equilibrium constants of the monomer–dimer equilibrium at various temperatures were determined by analyzing electronic absorption spectra. From the temperature dependences of the equilibrium constants, heats of dimerization were evaluated to be 8.8 and 5.6 kcal/mol of dimer for the perylene and tetracene cations, respectively. From the present study it has also been found that when the cation dimers are formed new absorption bands appear in the near-infrared region, and the ultraviolet and visible absorption bands shift toward shorter wavelength. The appearance of the near-infrared bands in the dimer spectra are discussed in terms of both a radical–radical charge resonance and an electronic transition between the bonding and antibonding MO's constructed for the dimer, on the basis of a symmetrical sandwich dimer structure. Interactions between the two cation radicals forming the dimer in solution are discussed.

Introduction

Recently, a considerable amount of study has been reported on the dimerization of organic free radical (neutral[1,2] or ionic[1,3–13]) in solutions. Most of the radical ions whose dimerizations have been studied so far are for substituted benzenes, while very little is known on dimerization of the radical cations and anions of catacondensed hydrocarbons. For the perylene and tetracene cations (perylene$^+$ and tetracene$^+$) it has now been found from electronic absorption studies that the dimers of these radical cations exist in equilibrium with the monomers in concentrated sulfuric acid solutions and can be detected even at concentrations as low as about 10^{-4} M at room temperature.

In previous papers, Kimura, *et al.*, have studied dimerization phenomenon of the *p*-phenylenediamine cation in solution at low temperature by analyzing electronic absorption spectra quantitatively[4] and have

(1) K. H. Hausser and J. N. Murrell, *J. Chem. Phys.*, **27**, 500 (1957).

(2) (a) M. Itoh and S. Nagakura, *J. Amer. Chem. Soc.*, **89**, 3959 (1967); (b) D. A. Wiersma and J. Kommandeur, *Mol. Phys.*, **13**, 241 (1967); (c) K. Maeda and T. Hayashi, *Bull. Chem. Soc. Jap.*, **42**, 3509 (1969).

(3) K. Uemura, S. Nakayama, Y. Seo, K. Suzuki, and Y. Ooshika, *ibid.*, **39**, 1348 (1966).

(4) K. Kimura, H. Yamada, and H. Tsubomura, *J. Chem. Phys.*, **48**, 440 (1968).

(5) H. Yamada and K. Kimura, *ibid.*, **51**, 5733 (1969).

(6) T. Sakata and S. Nagakura, *Bull. Chem. Soc. Jap.*, **42**, 1497 (1969).

(7) J. Tanaka and M. Mizuno, *ibid.*, **42**, 1841 (1969).

(8) G. Spach, H. Monterio, M. Levy, and M. Szarc, *Trans. Faraday Soc.*, **58**, 1809 (1962).

(9) E. M. Kosower and J. L. Cotter, *J. Amer. Chem. Soc.*, **86**, 5524 (1964).

carried out a theoretical calculation of the electronic spectrum of its dimer on the basis of a symmetrical sandwich structure.[14] Kimura, *et al.*, have also shown that the *p*-benzosemiquinone anion[4] in an ethanol solution and the cation radicals of several *p*-dialkoxybenzenes[5] in concentrated sulfuric acid solutions dimerize at low temperature. Our first aim was to prepare and measure spectroscopically both the anion and cation dimers of an identical alternant aromatic hydrocarbon, in order to obtain any information on difference in geometrical structures of these radical–ion dimers. In this work, although an attempt to find the anion dimer of perylene or tetracene at a low temperature was unsuccessful, we have obtained conclusive evidence for the reversible dimerizations of perylene$^+$ and tetracene$^+$ in concentrated sulfuric acid.

Experimental Section

Commercial materials of perylene and tetracene were purified by vacuum sublimation. Concentrated sulfuric acid of high purity ("Wako" 98.08%) was used without further purification. Perylene and tetracene are readily soluble in concentrated sulfuric acid, forming the cation radicals *via* the proton complexes in a considerably short time. With each of these solutions, no absorption due to neutral molecule was detected. In the solutions containing tetracene$^+$, a small amount of the proton complex of tetracene remains. This, however, does not affect the optical densities of the absorption peaks studied.

Electronic absorption spectra of these solutions were measured at various temperatures and concentrations by using a specially designed quartz Dewar with optically flat windows, quartz cells of path length of 1 and 0.1 mm being used. An ethanol–Dry Ice solution was used as a refrigerant. After recording the absorption spectrum of the equilibrated solution, the temperature of the solution was slowly raised by 5°. Absorption measurements in ultraviolet and visible regions were carried out with a Cary Model 15 spectrophotometer, and those in near-infrared region were carried out with a Hitachi EPS-2 spectrophotometer. Changes in volume of the solution with temperatures were accounted for in the calculation of extinction coefficients from optical densities.

Results and Discussion

Dimerization of the Cation Radicals. From the studies of esr[15] and electronic absorption spectra[16,17] by several workers, it is known that perylene$^+$ and tetracene$^+$ can be produced by dissolving perylene and tetracene in concentrated sulfuric acid, respectively. Changes in the absorption spectra of perylene$^+$ and tetracene$^+$ were first observed on cooling the concentrated sulfuric acid solutions in the present work. The absorption spectrum of perylene$^+$ in concentrated sulfuric acid at five different temperatures is partly depicted in Figure 1a. The changes of the absorption spectra of perylene$^+$ with concentration are shown in Figure 1b. As seen from Figures 1a and b, there exist isosbestic points in the both cases. Either at a high concentration or a low temperature, it was found that the intensities of the cation bands decrease while new absorption bands appear which may be attributed to the corresponding dimer bands as shown below.

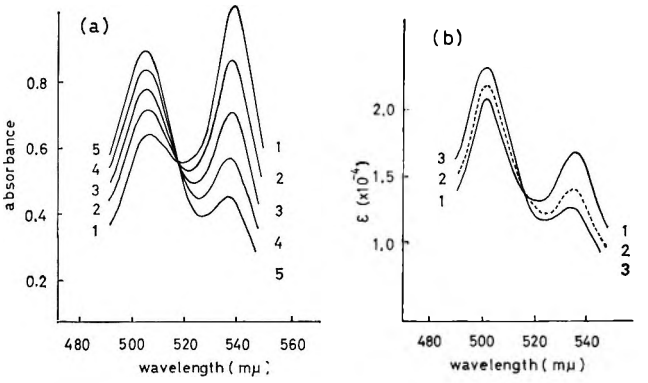

Figure 1. (a) Temperature dependence of the absorption spectrum of perylene$^+$ at $C = 3.41 \times 10^{-4}$ *M*. Curve 1, 10°; curve 2, 0°; curve 3, −10°; curve 4, −20°; curve 5, −30°. (b) Concentration dependence of the absorption spectrum of perylene$^+$ at a low temperature (−30°). Curve 1, 3.14×10^{-4} *M*; curve 2, 6.29×10^{-4} *M*; curve 3, 1.03×10^{-3} *M*.

In Figures 2 and 3, the absorption spectra obtained in this work with low-concentration solutions of perylene and tetracene, respectively, are shown by spectrum 1, essentially identical with those of perylene$^+$ and tetracene$^+$ reported by Aalbersberg, *et al.*[17] The shortest wavelength band at 223 mμ of perylene$^+$ has not been reported previously.

Since it is inferred from previous studies[4,5] that such spectral changes will be explained in terms of a dimer formation, in this work we first assumed the following monomer–dimer equilibrium for the cation A^+ (perylene$^+$ or tetracene$^+$)

$$2(A^+) \rightleftharpoons (A_2)^{2+} \qquad (1)$$

The equilibrium constant K is then given by

(10) N. Hirota and S. I. Weissman, *J. Amer. Chem. Soc.*, **86**, 2538 (1964).

(11) R. H. Boyd and W. D. Phillips, *J. Chem. Phys.*, **43**, 2927 (1965).

(12) R. Chang, *J. Phys. Chem.*, **74**, 2029 (1970).

(13) Very recently, dimerizations of the radical cations of phenothiazine and bis(dimethylamino)diphenylamine in solution have been studied spectroscopically by K. Suzuki and his coworkers at Kwansei-Gakuin University, The 23rd Annual Meeting of Chemical Society of Japan, 1970, Abstract I, pp 366, 367.

(14) K. Kimura and N. Mataga, *J. Chem. Phys.*, **51**, 4167 (1969).

(15) (a) Y. Yokozawa and I. Miyashita, *ibid.*, **25**, 796 (1956); (b) S. I. Weissman, E. de Boer, and J. J. Conradi, *ibid.*, **26**, 963 (1957); (c) E. de Boer and S. I. Weissman, *J. Amer. Chem. Soc.*, **80**, 4549 (1958).

(16) G. J. Hoytink and W. P. Weijland, *Recl. Trav. Chim. Pays-Bas*, **76**, 836 (1957).

(17) W. I. Aalbersberg, G. J. Hoytink, E. L. Mackor, and W. P. Weijland, *J. Chem. Soc.*, 3049 (1959).

$$K = (1 - \alpha)/2C\alpha^2 \quad (2)$$

where α is the fraction of the cation in the monomeric form and C is the total concentration of the cation, $C = [A^+] + 2[(A_2)^{2+}]$, that is obtained from the analytical concentration of perylene or tetracene dissolved in concentrated sulfuric acid. The observed extinction

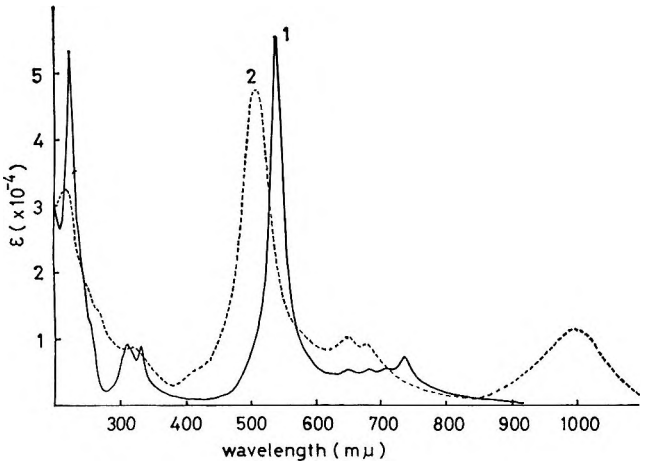

Figure 2. Electronic absorption spectra of perylene$^+$ in concentrated sulfuric acid at room temperature. Curve 1, the spectrum due mainly to the cation monomer, measured at a low concentration ($C = 5.83 \times 10^{-5}$ M); curve 2, the spectrum of the cation dimer, determined from an extrapolation of a series of concentrations.

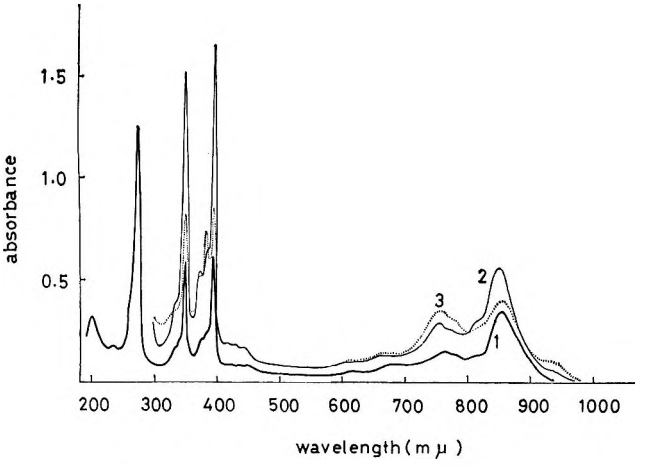

Figure 3. Electronic absorption spectra of tetracene$^+$ in concentrated sulfuric acid: curve 1, the spectrum due mainly to the cation monomer, measured at a low concentration ($C = 1.0 \times 10^{-5}$ M) at room temperature; curves 2 and 3, the spectra of the cation solution including partly its dimer, measured at a higher concentration ($C = 2.5 \times 10^{-4}$ M) at room temperature and at $-30°$, respectively.

coefficient ϵ at any given wavelength can be related to the molar extinction coefficient of the monomer ϵ_M and that of the dimer ϵ_D, respectively

$$\epsilon = \alpha\epsilon_M + (1 - \alpha)\epsilon_D \quad (3)$$

Eliminating α from eq 2 and 3 and taking logarithms, it follows that

$$y = 2x + b \quad (4)$$

where

$$y = \log \{C(\epsilon_M - \epsilon)/\epsilon_M\} \quad (5)$$

$$x = \log \{C(\epsilon - \epsilon_D)/\epsilon_M\} \quad (6)$$

$$b = \log \{2K\epsilon_M/(\epsilon_M - \epsilon_D)\} \quad (7)$$

It is seen from eq 5 and 6 that y and x are the functions of C at any given wavelength, while b is a constant, so that plots of y against x should give a straight line of slope 2 on the assumption of the monomer–dimer equilibrium.[18]

Since ϵ_D was unknown at the beginning of the present analysis, we selected suitable wavelengths (537.5 mμ for perylene$^+$ and 349 mμ for tetracene$^+$) at which to a first approximation ϵ_D may be neglected in calculating x. ϵ_M is obtained with a solution of very low concentration. Using the experimental ϵ and ϵ_M at these wavelengths and ϵ_D being neglected, linearities between y and x values were obtained which give straight lines of slope of about 2 at different temperatures (actually 1.7 and 2.1 for perylene$^+$ and tetracene$^+$, respectively) as shown in Figure 4. This indicates that these cations should be in equilibrium with their dimers in the concentrated sulfuric acid solutions.

Table I: Wavelengths and Molar Extinction Coefficients of Absorption Peaks of the Cation Monomers and Dimers

Monomer		Dimer	
λ, mμ	$\epsilon_M \times 10^{-4}$	λ, mμ	$\epsilon_D \times 10^{-4}$
	Perylene$^+$		
223	5.32		
(310)	(0.89)		
333	0.88	(275)	(1.18)
538	5.56	503	4.70
(650)	(0.51)	650	1.06
675	0.48		
(707)	(0.52)		
733	0.72		
		1000	1.18
	Tetracene$^+$		
198	2.94		
274	1.17		
349	2.18		
373	1.83		
394	5.33	384	4.76
(747)	(1.21)		
856	2.25	747	3.26
		938	2.00

(18) If we start by a more general expression of monomer–polymer equilibrium $n(A^+) \rightleftharpoons (A_n)^{n+}$, then eq 4 should be replaced by $y = nx + b$ which gives a straight line of slope of n, the degree of polymerization.

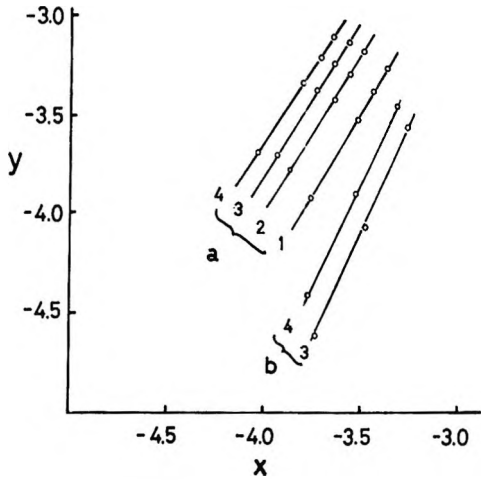

Figure 4. Initial plots of y against x for different temperatures for (a) perylene$^+$ and (b) tetracene$^+$, ϵ_D being neglected: line 1, 10°; line 2, −10°; line 3, −20°; line 4, −30°.

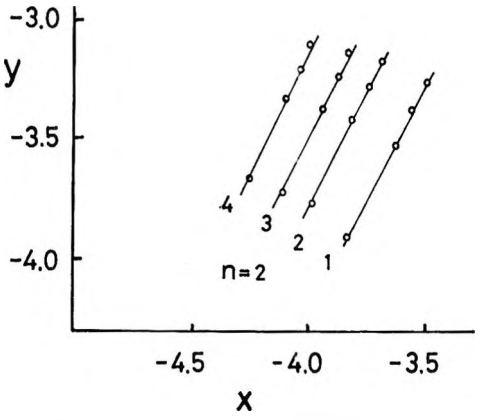

Figure 5. Final plots of y against x for different temperatures: line 1, 10°; line 2, −10°; line 3, −20°; line 4, −30°.

Once eq 4 was proved to be valid, ϵ_D's can be obtained by numerically solving eq 4 with experimental data for ϵ, ϵ_M, and C's. Values of ϵ_D's and ϵ_M's obtained in this manner are mentioned in Table I. In order to check these values, y's were recalculated and plotted against x's, as shown in Figure 5, from which it is seen that a good straight line of the slope of almost 2 is obtained through the experimental points at each of the temperatures. In Table II, equilibrium constants determined from the intercepts of the straight lines thus obtained are summarized, together with other thermodynamic quantities for the dimerization of the cations studied here. From the temperature dependence of K, heats of dimerization were evaluated to be $-\Delta H^\circ = 8.8$ and 5.6 kcal/mol for perylene$^+$ and tetracene$^+$, respectively. From these values it may be said that (perylene$_2$)$^{2+}$ is a considerably strong dimer. It is interesting to compare this with a value of 10.4 kcal/mol reported for the dimerization of the tetracyanoquinodimethane anion by Boyd and Phillips.[11]

Table II: Thermodynamic Data of Dimerization for Perylene$^+$ and Tetracene$^+$ in Concentrated Sulfuric Acid

Temperature, °C	$K \times 10^{-3}$, l./mol	ΔF°, kcal/mol	ΔS°, cal/mol deg
	Perylene$^+$		
10	2.4	−4.34	−15.8
−10	9.4	−4.56	−15.9
−20	15.3	−4.84	−15.8
−30	34.4	−5.05	−15.6
	$\Delta H^\circ = -8.8$ kcal/mol		
	Tetracene$^+$		
−10	0.32	−3.01	−10.0
−20	0.44	−3.06	−10.2
−30	0.73	−3.18	−10.1
	$\Delta H^\circ = -5.6$ kcal/mol		

Electronic Absorption Spectra of the Dimers. Hausser and Murrell[1] first pointed out that the longest-wavelength absorption band of the radical dimer in the cases of *N*-ethylphenazyl and the Würster's blue cation is attributed to a transition to a state which is an antisymmetrical combination of two charge-transfer configurations, in which all the electrons are paired. This charge-transfer mechanism has also been supported by recent polarization experiments in the crystalline states by Sakata and Nagakura[6] and by Tanaka and Mizuno.[7] However, for a considerably strong dimer such a *p*-phenylenediamine cation dimer,[19] the molecular orbital method may also be applicable. Kimura and Mataga[14] have recently carried out a molecular-orbital calculation of both the monomer and dimer of the *p*-phenylenediamine cation and showed that the observed dimer spectrum including the near-infrared band can well be explained in terms of a transition from the bonding orbital built up by two half-occupied orbitals to the corresponding antibonding orbital. Using the molecular-orbital method for the radical dimers, charge-transfer terms are naturally included with constant amount of coefficients, analogous to the ionic terms included in the molecular-orbital treatment of a hydrogen molecule, and the appearance of the longest-wavelength dimer band polarized in the out-of-plane direction may simply be explained in terms of a transition from the bonding orbital ($\varphi_m + \varphi_{m'}$) to the antibonding orbital ($\varphi_m - \varphi_{m'}$), where φ_m and $\varphi_{m'}$ denote the half-occupied MO's of two monomers. (Hereafter, two monomers forming the dimer are distinguished from each other by symbols with and without a prime.)

(19) According to the approximate calculation by Tanaka and Mizuno,[7] a moderate amount of the CT configuration (about 50%) contributes to the excited state associated with the longest-wavelength band of the *p*-phenylenediamine cation dimer, while for the tetramethyl-*p*-phenylenediamine cation dimer the CT contribution amounts to about 95%.

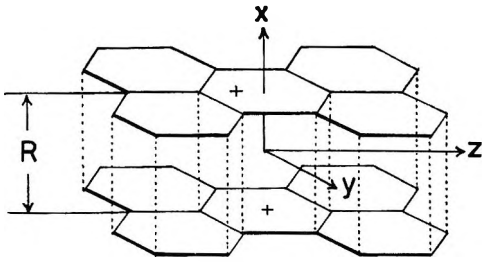

Figure 6. A symmetrical sandwich structure assumed for the dimer of perylene$^+$.

Here we will discuss the longest-wavelength bands of the cation dimers in terms of both the charge-transfer and molecular-orbital concepts. For the dimer geometries, parallel sandwich structures are assumed. The assumed model of $(\text{perylene}_2)^{2+}$ is shown in Figure 6. From the standpoint of the charge transfer (CT), the CT energy between the two component may approximately be given by[20]

$$E_{CT} = \{(\varphi_m\varphi_m|\varphi_m\varphi_m) - (\varphi_m\varphi_m|\varphi_{m'}\varphi_{m'})\}(1 - S_{mm'}^2) \quad (8)$$

where $S_{mm'}$ is the overlap integral between φ_m and $\varphi_{m'}$. Overlap integral components, $S_{\mu\nu'}$'s expressed in terms of two AO's belonging to two dimeric monomers were calculated by the following equation[21]

$$S_{\mu\nu'} = S(2p\pi_\mu \cdot 2p\pi_{\nu'}) \sin^2\theta + S(2p\sigma_\mu \cdot 2p\sigma_{\nu'}) \cos^2\theta \quad (9)$$

where θ is an angle between the axis perpendicular to the monomer plane and the line passing through two atoms, μ and ν. In Figure 7 the overlap integrals $S_{mm'}$ calculated by using the SCF–MO coefficients,[20] $c_{m\mu}$ values, of the monomers are plotted against the radical–radical separation for both $(\text{perylene}_2)^{2+}$ and $(\text{tetracene}_2)^{2+}$. The CT energies in these dimers obtained from eq 8 are shown in Figure 8. Since the interplanar separation is probably between 3 and 4 Å, the calculated CT energy values of 1.0–1.3 eV (Figure 8) seems to support the interpretation that the longest-wavelength bands of the dimers (1.2–1.3 eV) may be the so-called CT bands.[22]

From the standpoint of the molecular orbital, on the other hand, the bonding and antibonding MO's of the dimer are expressed by

$$\varphi_{m\pm} = \{2(1 \pm S_{mm'})\}^{-1/2}(\varphi_m \pm \varphi_{m'}) \quad (10)$$

and splitting in orbital energy between these two MO's may be given by[14]

$$\Delta_m = 2\sum c_{m\mu}c_{m\nu'}F_{\mu\nu'}(1 + S_{mm'}) \approx 2\langle F_{CC}\rangle S_{mm'}(1 + S_{mm'}) \quad (11)$$

where the off-diagonal Fock–Hamiltonian elements between the two monomers $F_{\mu\nu'}$'s are approximated by $\langle F_{CC}\rangle S_{\mu\nu'}$. In Figure 9 the orbital-energy splitting

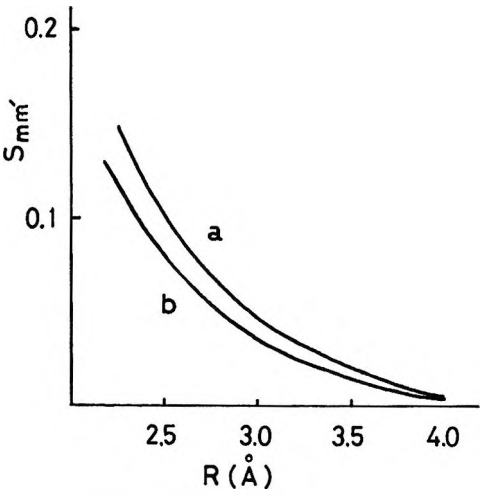

Figure 7. Overlap integral $S_{mm'}$ plotted against the interplanar distance for the cation dimers: curve a, perylene$^+$; curve b, tetracene$^+$.

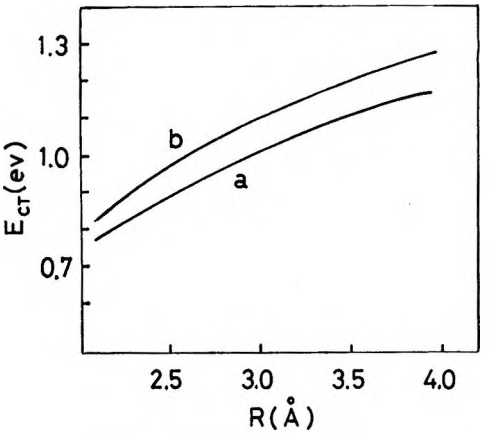

Figure 8. Charge-transfer energies E_{CT} plotted against the interplanar distance for the cation dimers: curve a, perylene$^+$; curve b, tetracene$^+$.

(20) This equation (eq 8) corresponds to eq 8 given in ref 7. We consider only the charge transfer between the two half-occupied MO's φ_m and $\varphi_{m'}$. The wave functions of the singlet ground and charge-transfer configurations are expressed by $\Psi_G = \{\varphi_m(1)\varphi_{m'}(2) + \varphi_{m'}(1)\varphi_m(2)\}/\sqrt{2(1 + S_{mm'}^2)}$ and $\Psi_{CT} = \{\varphi_m(1)\varphi_m(2) + \varphi_{m'}(1)\varphi_{m'}(2)\}/\sqrt{2(1 + S_{mm'}^2)}$. The charge-transfer energy given in eq 8 expresses the diagonal energy of the charge-transfer state relative to the ground state. The calculations of $(\varphi_m\varphi_m|\varphi_m\varphi_m)$ and $(\varphi_m\varphi_m|\varphi_{m'}\varphi_{m'})$ in eq 8 were carried out in the Pariser–Parr approximation by using a FACOM 230-60 computer of Hakkaido University. The SCF–MO calculations of perylene$^+$ and tetracene$^+$ have recently been carried out using a method of an open-shell approximation in our laboratory. The calculated results of electronic transitions of these cations will be published elsewhere.

(21) Overlap integral values of $S(2p\pi \cdot 2p\pi)$ and $S(2p\sigma \cdot 2p\sigma)$ were taken from the table given by R. S. Mulliken, C. A. Rieke, D. Orloff, and H. Orloff, *J. Chem. Phys.*, **17**, 1248 (1949).

(22) In the above treatment, the effect of solvent on the charge-transfer energy was not taken into consideration in using eq 8, since it may be considered that there is no charge distortion between the two identical components in the doubly charged dimers in the charge-transfer state as well as in the ground state, and therefore the solvent molecules seem to affect to the both states to similar extent. (The charge-transfer states in the present case might be said more properly the charge-resonance state.) This consideration may partly be supported by our experimental fact that any appreciable solvent effects of all the absorption bands of the dimers were not detected in the present work as long as concentrated sulfuric acid of 98.08, 88.27, and 83.37% were used as solvents.

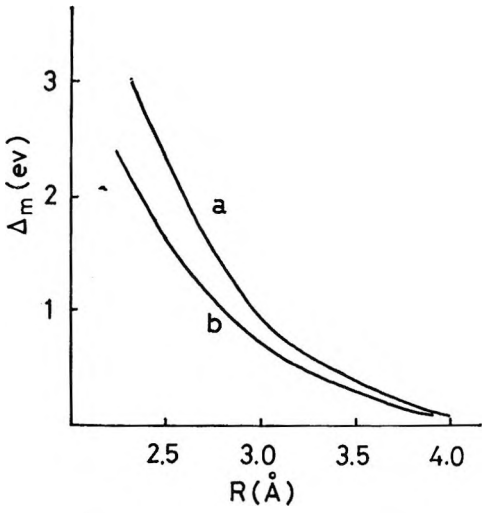

Figure 9. Orbital-energy splittings Δ_m plotted against the interplanar distance for the cation dimers: curve a, perylene$^+$; curve b, tetracene$^+$.

curves calculated with $\langle F_{CC} \rangle = -9.98$ eV[14] for perylene$^+$ ($m = 10$) and tetracene$^+$ ($m = 9$) are plotted against the interplanar separation R. These curves of Figure 9 seem to give a good picture for the changes in transition energy with R. Furthermore, it is also of interest to estimate an f value for the longest-wavelength dimer band in order to compare with the experimental value. If the distance R is assumed to be about 3 Å for the dimer of perylene$^+$, then an f value of 0.48 can be obtained from a calculation of transition moment by assuming that the ground and the first excited state are due almost to the electronic configurations χ_G and $\chi_{10+ \rightarrow 10-}$, respectively. This calculation seems fairly well to reproduce the experimental f value of 0.28 obtained from the dimer 1000-mμ band in Figure 2. Therefore, it may be reasonably considered that the present model of the parallel structure for the cation dimers well interprets the appearance of the near-infrared absorption bands of the dimers.

From symmetry consideration, it is shown that in either of these two theories the longest-wavelength band can be assigned by an electron transition with a moment along x axis perpendicular to the molecular planes.

As seen from Figures 2 and 3, except the longest-wavelength dimer bands, the monomer and dimer spectra are fairly similar to each other, and the dimerization of the cation radicals shifts each of the monomer bands toward shorter wavelength. Such blue shift of the monomer bands has also been shown in the cases of the *p*-phenylenediamine cation,[4] and interpreted by our previous theoretical study.[14] These blue shifts seem to be one of the characteristics of the dimer spectra.

On the basis of the above dimer structure (D_{2h}) and MO's, it is indicated from a symmetry consideration that transitions of $\varphi_{i\pm} \rightarrow \varphi_{k\pm}$ are allowed while those of $\varphi_{i\pm} \rightarrow \varphi_{k\mp}$ are forbidden, where $i < m < k$. Now considering that φ_{m+} and φ_{m-} are the highest occupied and the lowest vacant MO's of the cation dimers, it follows that allowed transitions in which φ_{m+} and φ_{m-} participate are only $\varphi_{m+} \rightarrow \varphi_{k+}$ and $\varphi_{i-} \rightarrow \varphi_{m-}$. This may be an origin of the blue shifts appearing in the visible and near-uv region, in which electronic excitations of relatively low energy take place. However, if we assume a twisted parallel dimer structure in which the two radical planes are rotated from each other around the x axis, then transitions $\varphi_{m+} \rightarrow \varphi_{k\pm}$ and $\varphi_{i\pm} \rightarrow \varphi_{m-}$ all should be allowed and some splitting of the absorption bands should be expected. In the dimers of substituted pyridinyl radicals, Itoh and Nagakura[2a] have recently reported splitting of uv absorption bands in addition to the appearance of strong visible CT bands between two radical components. By using an exciton model this splitting has been ascribed to such twisted dimer structure.[23] In the perylene$^+$ and tetracene$^+$ cation dimers, however, any splitting of absorption bands are not observed in the present work, as seen from Figures 2 and 3, so that it appears that the blue shifts observed in the dimer bands consistent with the symmetrical sandwich structure mentioned above.

It is also interesting to note that blue shift[24] or splitting[25] of absorption spectra are usually observed in dimerization of various planar ionic dyes. Their spectral changes have been explained by exciton theory developed for interactions among chromophores in molecular crystals[26] and dimeric monomers.[27]

Dimer Formation of the Cation Radicals in Solution. When two neutral radicals are brought together in a vacuum, the quantum-mechanical forces of attraction between them, which give rise to the radical dimers, are similar to those between two hydrogen atoms, which give rise to H_2. In the case of cation radicals, there exists an additional force of electrostatic repulsion between the cations, which probably prevent their dimer formation under a vacuum. In a polar solvent, however, the electrostatic repulsion between the two cations is greatly reduced owing to the orientation of the polar solvent molecules, while the quantum-mechanical attraction is scarcely affected, with the result that the doubly charged dimer is formed. The dielectric constant of the concentrated sulfuric acid is reported to be

(23) M. Itoh, *Chem. Phys. Lett.*, **2**, 371 (1968).

(24) E. Rabinowitch and L. F. Epstein, *J. Amer. Chem. Soc.*, **63**, 69 (1941).

(25) (a) T. Förster and E. König, *Z. Elektrochem.*, **64**, 344 (1957); (b) G. S. Levinson, W. T. Simpson, and W. Curtis, *J. Amer. Chem. Soc.*, **79**, 4314 (1957); (c) J. Lavorel, *J. Phys. Chem.*, **61**, 1601 (1957); (d) W. West and S. Pearce, *ibid.*, **69**, 1894 (1965).

(26) A. S. Davydov, "Theory of Molecular Exciton," McGraw-Hill, New York, N. Y., 1962.

(27) (a) D. S. McClure, *Can. J. Chem.*, **36**, 59 (1958); (b) M. Kasha, A. El-Beyoumi, and W. Rhodes, *J. Chim. Phys. Physicochem. Biol.*, **58**, 916 (1961); (c) H. De Voe, *J. Chem. Phys.*, **37**, 1534 (1962); (d) A. Witkowoski and W. Moffitt, *ibid.*, **33**, 842 (1960); (e) K. Bergman and C. T. O'Konski, *J. Phys. Chem.*, **67**, 2169 (1963); (f) K. K. Rohatgi, *J. Mol. Spectrosc.*, **27**, 545 (1968).

very large (ϵ = 110 at 20°).[28] The solvent having such a large dielectric constant probably plays an important role in reducing the electrostatic repulsion between the two component cations in the dimer.

Another factor of reducing the electrostatic repulsion between the two cations is the distribution of the positive charges all over the component atoms of the dimers. This kind of reduction of the electrostatic repulsion may be considered to become greater for larger planar molecular ions.

The magnitudes of ΔS observed for the dimerization of perylene$^+$ and tetracene$^+$ are about -16 and -10 cal/mol deg, respectively, as shown in the last column of Table II. It is interesting to compare these entropy values with those in the dimerization of TCNQ$^-$ in aqueous solution (-19.5 cal/mol deg at 25°).[11] Since a cation or anion in solution has an electrostriction effect on solvent molecules in its neighborhood, there may be a loss of entropy, and this loss is greater the larger the charge. As a result there may be considerable losses of entropy in the dimerization process of the cations.

Using a simple model called the double-sphere model,[29] ΔS is given by $NZ^2e^2(\partial \ln \epsilon/\partial T)_P/\epsilon R$, where N is Avogadro's number, Z the number of charges on the ion, and R is distance between the two charges. In an aqueous solution ϵ is about 80 and $(\partial \ln \epsilon/\partial T)_P$ remains constant at -0.0046 over a fairly wide temperature range.[29] In a concentrated sulfuric acid solution, although $(\partial \ln \epsilon/\partial T)_P$ is unknown, its ϵ value (about 110) is greater than that of water by 40%. This may be one of main reasons why $|\Delta S|$ of perylene$^+$ and tetracene$^+$ in concentrated sulfuric acid are smaller than that of TCNQ$^-$ in aqueous solution. From the above entropy relation, it might also be roughly said that the difference in ΔS between perylene$^+$ and tetracene$^+$ in dimerization is probably due to difference in the interplanar separation (R), since all the factors except R are equal or nearly equal to each other. This probably indicates that the interplanar separation of (tetracene$_2$)$^{2+}$ is longer than that of (perylene$_2$)$^{2+}$.

Concerning the association of aromatic hydrocarbon radical anions with alkali cations, recent studies[30] have revealed conclusive evidence for the existence of two kinds of ion pairs, *viz.* contact and solvent-separated ion pairs, in low-dielectric ethereal solvents such as THF. As far as we know, any ion-pair formation has not been reported between aromatic hydrocarbon cations and large inorganic anions such as $(ClO_4)^-$. In the systems studied in the present work, it may reasonably be considered that the perylene$^+$ and tetracene$^+$ cations hardly interact with the $(HSO_4)^-$ anion existing as a counterion, because of the bulky tetrahedral anion, and therefore are fully free from the counterions in concentrated sulfuric acid.

It has long been known that somewhat similar situations on atomic ions are encountered with the dimer of the mercury ion, $(Hg_2)^{2+}$, and that of the tellurium ion, $(Te_2)^{2-}$, stable in aqueous solution.[31] Hg and Te are odd-electron atoms.

Electronic absorption spectra of some dimer monocations have been studied at low temperature with γ-irradiated solutions of hydrocarbons by Badger and Brocklehurst[32] and those of some dimer monoanions have been studied by esr[33] and electronic spectra[34] by many workers. Very recently, Chiang and Reddoch[35] have studied the esr spectrum and heat of dissociation of (perylene$_2$)$^+$ in dichloromethylene. In the present study, however, a possibility of such dimer monocations in the concentrated sulfuric acid may be ruled out.

Acknowledgments. We would like to thank Professor H. Baba for his valuable discussion and his permission of the use of Hitachi EPS-2 spectrophotometer. Thanks are also due to the Ministry of Education for the research grant.

(28) J. C. D. Brand, J. C. James, and A. Rutherford, *J. Chem. Phys.*, **20**, 530 (1952).

(29) K. J. Laidler, "Reaction Kinetics," Vol. 2, Pergamon Press, New York, N. Y., 1963, Chapter 1.

(30) For instance, T. E. Hogen-Esch and J. Smid, *J. Amer. Chem. Soc.*, **87**, 669 (1965); **88**, 307 (1966); **89**, 2764 (1967); M. Szwarc, *Accounts Chem. Res.*, **2**, 87 (1969).

(31) (a) R. N. Gurney, *J. Chem. Phys.*, **6**, 499 (1938); (b) R. N. Gurney, "Ionic Processes in Solution," McGraw-Hill, New York, N. Y., 1953, Chapter 4.

(32) (a) B. Badger, B. Brocklehurst, and R. D. Russell, *Chem. Phys. Lett.*, **1**, 122 (1967); (b) B. Badger and B. Brocklehurst, *Trans. Faraday Soc.*, **65**, 2576 (1969); (c) *ibid.*, **65**, 2582 (1969); (d) *ibid.*, **65**, 2588 (1969).

(33) (a) I. C. Lewis and L. S. Singer, *J. Chem. Phys.*, **43**, 2712 (1965); (b) O. W. Howarth and G. K. Fraenkel, *J. Amer. Chem. Soc.*, **88**, 4514 (1966); (c) B. G. Segal, M. Kaplan, and G. K. Fraenkel, *J. Chem. Phys.*, **43**, 4191 (1965); (d) O. Edlund, P-O. Kinell, A. Lund, and A. Shimizu, *ibid.*, **46**, 3679 (1967); (e) H. van Willigen, E. de Boer, J. T. Cooper, and W. F. Forbes, *ibid.*, **49**, 1190 (1968).

(34) (a) L. R. Melby, R. J. Harder, W. R. Hertler, W. Mahler, R. E. Benson, and W. E. Mochel, *J. Amer. Chem. Soc.*, **84**, 3374 (1962); (b) M. Ito, *ibid.*, **92**, 886 (1970).

(35) T. C. Chiang and A. H. Reddoch, *J. Chem. Phys.*, **52**, 1371 (1970).

The Role of Singlet and Triplet States in Aromatic Substitution Reactions

by George F. Vesley[1]

Scientific Research Staff, Ford Motor Company, Dearborn, Michigan, and The University of North Dakota, Grand Forks, North Dakota 58201 *(Received December 30, 1970)*

Publication costs assisted by Ford Motor Company

The rate of photochemical hydrogen–deuterium exchange in *p*-hydroquinone has been measured. This rate coupled with fluorescence quenching experiments is used to elucidate the mechanism of photoinduced aromatic substitution reactions. It is concluded that both triplet and singlet states can be intermediates in photochemical electrophilic substitution reactions; however, if the aromatic compound possesses a high intersystem crossing yield, the reaction proceeds primarily *via* a triplet state. This is the case for the photochemical hydrogen–deuterium exchange in *p*-hydroquinone.

The excited state of a molecule can be considered, in terms of its reactivity, as a new and different species. Both experimental results and theoretical considerations have led to this conclusion.[2-6] These papers report the measurement of the pK values of the excited state[4,5] as well as photochemical reactions which are attributed to the increased basicity of ring positions in the excited state.[2-4] Aromatic hydrocarbons have been reported to be as much as 28 powers of ten more basic in their excited states than in their ground states.[5]

A convenient probe for the study of the acid–base reaction of the excited states is the photodeuteration of aromatic molecules.[2,4] These previous results have indicated that the lowest excited state is responsible for the photochemical aromatic substitution reactions, but there is evidence in some cases for the intermediacy of a triplet state[7,8] or a higher excited singlet.[7]

Yao and Heller have made an extensive investigation of the thermally induced multiple deuterium exchange in *p*-hydroquinine[9] (HQ-h_4) in which they developed an epr technique for measuring the quantity of exchange.[10] Analysis by this method involves the air oxidation of *p*-hydroquinone in alkaline dimethyl sulfoxide to the corresponding semiquinone radical anion. Fortunately, the epr spectra of the isomers (HQ-h_4, HQ-h_3d, etc.) are different enough to enable quantitative analysis of the relative amounts of each radical anion. These authors also showed that the amount of semiquinone radical anion was an excellent representation of the amount of original *p*-hydroquinone isomer present. This method of analysis is superior to nmr spectroscopy since the number of deuterium atoms substituted can easily be determined and other products derived from radical reactions can be observed.

The photochemical hydrogen–deuterium exchange was investigated in order to elucidate the excited states responsible for aromatic photochemical substitutions and the mechanism of these reactions, as well as to gain an understanding of the acid–base properties of excited states. *p*-Hydroquinone was chosen because the dark reaction was slow ($k = 3 \times 10^{-3}$ min^{-1} at 80°, [D$^+$] = 0.44 M),[9] and a convenient method of analysis was available.

This photochemical study was approached from three aspects: the quantum yields for monodeuterium exchange, the effect of acid on the fluorescence spectrum, and the luminescence properties of *p*-hydroquinone. The quantum yields for exchange have been studied as a function of acid concentration, and the results have been compared with the quenching of *p*-hydroquinone fluorescence by acid. Data obtained in this manner have recently been reported in support of a singlet mechanism.[11]

An investigation of the luminescence properties of *p*-hydroquinone was undertaken as part of this mechanistic study since these substitution reactions were conducted under conditions where ground–excited state interaction would be expected to be important and would decrease the efficiency of the reaction under study. This type of quenching reaction has been at-

(1) To whom correspondence should be addressed at Chemistry Department, University of North Dakota, Grand Forks, N. D. 58201.

(2) (a) E. Havinga, R. O. de Jongh, and M. E. Kronenberg, *Helv. Chim. Acta*, **50**, 2250 (1967), and references therein; (b) E. Havinga, "Reactions of the Photoexcited Organic Molecule," Proceedings of the Thirteenth Conference on Chemistry at The University of Brussels, Oct 1965, Interscience, New York, N. Y., 1967.

(3) H. E. Zimmerman and R. Sandel, *J. Amer. Chem. Soc.*, **85**, 915 (1963); H. E. Zimmerman and S. Somasekhara, *ibid.*, **85**, 922 (1963).

(4) J. P. Colpa, C. MacLean, and E. L. Mackor, *Tetrahedron Suppl. 2*, **19**, 65 (1963), and references cited therein.

(5) R. L. Flurry, Jr., and R. K. Wilson, *J. Phys. Chem.*, **71**, 589 (1967).

(6) R. L. Flurry, Jr., and P. G. Lykos, *J. Amer. Chem. Soc.*, **85**, 1033 (1963).

(7) M. R. Sandner, E. Hedaya, and D. J. Trecker, *ibid.*, **90**, 7249 (1968).

(8) R. L. Letsinger and O. B. Ramsay, *ibid.*, **86**, 1447 (1964); G. Frater and E. Havinga, *Tetrahedron Lett.*, 4603 (1969); R. L. Letsinger and R. R. Hautala, *ibid.*, 4205 (1969).

(9) H. C. Yao and H. C. Heller, unpublished results.

(10) H. C. Yao and H. C. Heller, *Anal. Chem.*, **41**, 1540 (1969).

(11) O. L. Chapman and R. D. Lura, *J. Amer. Chem. Soc.*, **92**, 6352 (1970).

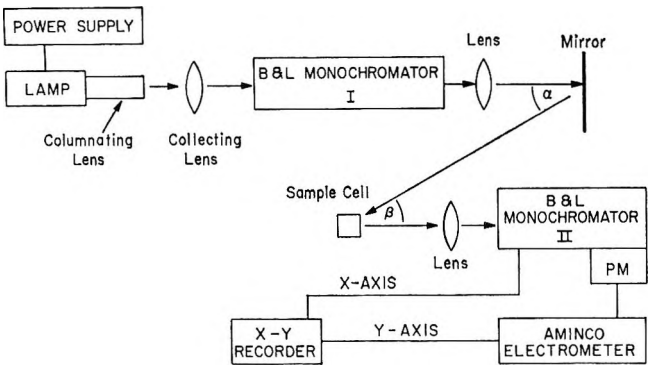

Figure 1. Front face fluorimeter.

tributed to the excited singlet state and has the effect of reducing the number of singlets available for other reactions such as singlet energy transfer or intersystem crossing, and can thereby ultimately quench singlet and triplet reactions.[12] The effect of singlet quenchers on intersystem crossing has recently been reported.[13]

Experimental Section

Materials. *p*-Hydroquinone (HQ-h_4) was obtained from Aldrich Chemical Co., and was recrystallized twice from benzene–alcohol mixtures. Merck, Sharp and Dohme 99.7% deuterium oxide and deuterium chloride and Rossville Gold Shield ethanol were used as received. Aminco spectrograde solvents were used for the low temperature emission work. The 1,3-pentadiene was obtained from Chemical Samples Co., and was distilled from $LiAlH_4$ under N_2 immediately before use.

Fluorimetry. The fluorescence spectra were measured on one of two instruments. Dilute solutions (OD < 0.05) were measured on an Aminco-Bowman spectrophotofluorimeter. If the OD of the solution is less than 0.05, an even distribution of excited states is obtained throughout the cell and the emission intensity, when viewed perpendicular to the excitation, is a linear function of the concentration. The fluorescence spectra of the more concentrated solutions were measured on an instrument (Figure 1) constructed by the author. The excitation lamp consisted of an Osram HBO 200 WL2 high-pressure Hg arc in an Oriel Optics Corp. C-60-50 lamp housing operated by an Oriel Optics Corp. C-72-20 power supply. A Bausch and Lomb SP-200 monochromator (I) using a visible-uv grating was used to isolate the excitation radiation. The monochromatic radiation is focused on the sample cell by use of the lens and mirror. The fluorescent light is resolved by a Bausch and Lomb 2000 monochromator (II). The light emerging from monochromator II is focused on a R-136 photomultiplier, the output of which is fed through an Aminco electrometer to the y input of an x–y recorder. A motor drives the grating of monochromator II and a potentiometer on the shaft of this grating generates a voltage proportional to the wavelength setting of the grating which drives the x axis of the recorder. The intensity of the lamp was stable for long periods of time.

The fluorescence intensity was shown to be linear in the following manner: a sample of HQ-h_4 in ethanol in a 1-cm square quartz cuvette was placed in the sample cell and irradiated with 3130 Å. The emission monochromator was set to detect the HQ-h_4 fluorescence, and the exciting light was attenuated with Optics Technology neutral density filters. The recorder deflections were found to be linear with excitation intensity.[14] Variation of the angles α and β did not change the slope/intercept ratio in plots of fluorescence intensity *vs.* concentration.

All fluorescence spectra and lifetimes were measured at room temperature, in air-equilibrated solutions and in 1-cm quartz cells unless otherwise specified. In some initial experiments, the fluorescence intensity and the lifetime was measured in air-equilibrated and degassed solution. The degassing was done by the freeze–thaw method. Identical cells were used for both experiments. Oxygen had no effect on the emission intensity nor on the lifetime or emission. The exciting light for all emission spectra was 3130 Å.

Decay Times. The decay times were measured using a TRW Model 31A nanosecond spectral source and 32A decay time computer. The sample compartment was modified by using an Aminco cell holder which would accept square cuvettes and baffles were added to reduce the scattered light. A deuterium lamp, pulsed at 5 kc, was used as a source of excitation. An Optics Technology 2700 Å interference was used to filter the excitation irradiation and a Corning CS O-54 was used to detect the emission. Owing to the short decay time and the noise encountered in these measurements, the TRW system was modified as shown in Figure 2. The output of the photomultiplier was sampled with a Hewlett-Packard 185B sampling oscilloscope with a 187C dual trace amplifier and stored in a CAT. The stored signal was then fed into the Tektronics 556 oscillioscope, and the decay time was matched with the decay time computer. The procedure used to zero the decay computer and obtain the decay times has been reported.[15,16] The time scale of the emission curve was calibrated before and after each run with the 500-Mc signal from the sampling scope. No change in the zero setting of the computer or in the time calibration could be detected over several hours. To test the system, a degassed cyclohexane solution of anthracene was measured, and it

(12) G. F. Vesley and G. S. Hammond, unpublished results.

(13) L. M. Stephenson, D. G. Whitten, G. F. Vesley, and G. S. Hammond, *J. Amer. Chem. Soc.*, **88**, 3665 (1966).

(14) J. Yguerabide, *J. Chem. Phys.*, **49**, 1018 (1968).

(15) "TRW Fluorimetry Handbook," TRW Instruments, El Seguendo, Calif., 1967.

(16) R. F. Chen, G. G. Vurek, and N. Alexander, *Science*, **156**, 949 (1967).

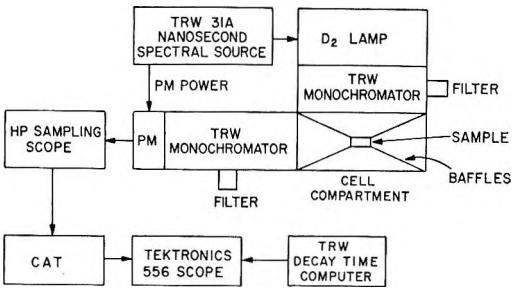

Figure 2. Decay time apparatus.

gave a decay time of 5.1 ± 0.1 nsec. The pure solvents showed no decay curve.

The phosphorescence spectra and lifetimes were measured at 77°K using the Aminco-Bowman spectrophotofluorimeter. To obtain the phosphorescence lifetimes the emission monochromator was set at the wavelength of maximum phosphorescence intensity. The output of the electrometer was displayed on a Tektronics 556 oscilloscope. Polaroid pictures of the decays were taken, and the decay time was obtained from these pictures.

Absorption Spectra. All absorption spectra were measured with a Cary Model 14 recording spectrophotometer.

Quantum Yields. All quantum yield samples were degassed by the freeze–thaw method using a forepump (2 cycles) and then a diffusion pump (3 cycles). The *p*-hydroquinone irradiations were carried out on an optional bench using an Osram HBO 200-W L2 high-pressure Hg lamp focused through a Bausch and Lomb Sp 200 monochromator. The intensity of the lamp at 2900 Å was measured by potassium ferrioxalate actinometry[17,18] before and after each run. The lamp intensity was constant within 5% over the period of irradiation. An ϵ of 1.33×10^4 M^{-1} cm^{-1} and a quantum yield of 1.24 were used. The concentrations of the *p*-hydroquinone solutions were adjusted to make sure all the light would be absorbed.

The vpc analysis of the 1,3-pentadienes was performed on a Beckman GC-4 using a 30-ft × $^1/_8$-in. column of 10% β,β'-oxydipropionitrile at 25°. The integration was done electronically with an Infotronics Digital Readout System Model CRS-11HSB/42.

An analysis for the exchange was performed on a Varian E-3 epr spectrometer. The procedure for the analysis has been reported.[10] This method of analysis gives relative concentrations to 10%.[19]

Results

Spectra. The absorption spectra of *p*-hydroquinone shows two well-defined bands corresponding to the ^1L_a band ($^1A_{1g} \rightarrow {}^1B_{1u}$ transition) at 2100 Å (log ϵ = 4.2), and ^1L_b band ($^1A_{1g} \rightarrow {}^1B_{2u}$ transition) at 2900 Å[20,21] (log ϵ = 3.6). We find this spectrum to be pH independent in the pH range 5 to −1.25. There is no evidence for ground-state complexes. Neither the shape nor the extinction coefficient of the absorption spectrum is affected in acid concentrations up to 36 N H_2SO_4. However, if the pH is greater than 7, new absorptions appear which are attributed to the anion.[21] To ensure that the undissociated species is responsible for the observed photochemistry, all work was carried out in at least 10^{-4} M hydrogen or deuterium ion.

p-Hydroquinone shows strong fluorescence, ϕ_f = 0.37 in water,[22] between 3000 and 4200 Å, maximum at 3320 Å. This fluorescence is attributed to excited monomer HQ-h_4. There is no evidence for new emissions. The width of the fluorescence spectra at half-height is constant within the experimental error over the concentration range 1.3×10^{-4} to 0.259 M. The fluorescence maximum and ϵ for HQ-h_4 are constant in the following solvents: H_2O, D_2O, EtOH, and CH_3CN.

The low temperature emission spectra (77°K) in EPA shows both fluorescence and phosphorescence. The fluorescence is identical with that observed at room temperature. The phosphorescence emission is more intense than the fluorescence and has a 0→0 band corresponding to a triplet energy of 74.3 kcal/mol.

Table I and Table II lists the emission lifetimes under various conditions. The phosphorescence[24] and fluorescence[25] are in good agreement with those previously reported.

Table I: Phosphorescence Emission Lifetime

p-Hydroquinone	In EPA 2.65 ± 0.1 sec
p-Hydroquinone	In ethanol 2.70 ± 0.2 sec
Perdeuterio-*p*-hydroquinone	In EPA 3.26 ± 0.1 sec

Concentration Studies. The effect of *p*-hydroquinone concentration on its fluorescence intensity in aqueous solution is shown in Figure 3. Each set of points

(17) G. F. Vesley, Ph.D. Thesis, California Institute of Technology, Pasadena, Calif., 1968.

(18) C. G. Hatchard and C. A. Parker, *Proc. Roy. Soc., Ser. A*, **235**, 518 (1956).

(19) G. M. Androes, *Mol. Phys.*, **15**, 291 (1968).

(20) H. H. Jaffé and M. Orchin, "Theory and Applications of Ultraviolet Spectroscopy," Wiley, New York, N. Y., 1968.

(21) L. V. Smirnov and A. I. Suprunenko, *Opt. Spectrosc. (USSR)*, **8**, 420 (1960).

(22) The fluorescence yield was obtained by measuring the area under the emission curve and comparing it to quinine bisulfate in 0.1 N H_2SO_4 (ϕ_f = 0.55).[23] The proper corrections for absorption and phototube sensitivity were made.

(23) W. H. Melhuish, *New Zealand, J. Sci. Technol.*, **B37**, 142 (1955).

(24) τ_p = 3.03 sec, B. A. Pyatritskii, *Dokl. Akad. Nauk SSSR*, **64**, 813 (1949); τ_p 2.3 sec, O. G. Zinoveva, *Zh. Eksp. Teor. Fiz.*, **20**, 132 (1950); τ_p = 2.9 sec, P. P. Bikum, A. A. Peteov, and B. Ya. Sveshnikov, *ibid.*, 21, 150 (1951).

(25) τ_f = 2 nsec, T. V. Ivanova, P. I. Kudryashov, and B. Ya. Sveshnikov, *Sov. Phys. Dokl.*, **6**, 407 (1961). This measurement was made in ethanol.

Table II:[a] Fluorescence Emission Lifetime

Compd	Solvent	τ, nsec
p-Hydroquinone	Water	1.9 ± 0.1
p-Hydroquinone	Deuterium oxide	2.1 ± 0.1
p-Hydroquinone	Ethanol	2.1 ± 0.1
p-Hydroquinone	Dioxane	2.4 ± 0.1
p-Hydroquinone	Cyclohexane	2.5 ± 0.1
p-Hydroquinone	Acetonitrile	2.5 ± 0.1
Perdeuterio-*p*-hydroquinone	Water	1.9 ± 0.1
Perdeuterio-*p*-hydroquinone	Deuterium oxide	1.9 ± 0.1
Perdeuterio-*p*-hydroquinone	Ethanol	2.2 ± 0.1

[a] [HQ-h_4] $\sim 10^{-4}$ M in all cases.

constitutes a separate run. Similar results were obtained using D_2O as a solvent. These data can be explained by a simple self-quenching mechanism. The intensity of the fluorescence can be related to the *p*-hydroquinone concentration by eq 1, where I_f is the intensity of the fluorescence, I_0 is the intensity of the

$$\frac{1}{I_f} = \left(\frac{1}{I_0 \tau_0 k_f}\right)(1 + k_{sq}\tau_0[\text{HQ-h}_4]) \qquad (1)$$

excitation radiation, τ_0 the singlet lifetime at infinite dilution, k_{sq} the rate constant for self-quenching, and k_f the rate constant for fluorescence. The ratio slope/intercept yields the Stern–Volmer constant K. Table III lists K and k_{sq}.

Table III: Self-Quenching Constants of *p*-Hydroquinone

Solvent	K, M^{-1}	k_{sq}, M^{-1} sec^{-1}
Water	7.17	$3.8 \pm 0.3 \times 10^9$
Deuterium oxide	2.88	1.4×10^9

Fluorescence Quenching by Acid. The effect of acid on the fluorescence is shown in Figures 4 and 5. Acid concentrations of 5 M or less quench the intensity of the *p*-hydroquinone fluorescence without changing the shape of this emission; the width at half-height is constant. However, in 36 N H_2SO_4 the fluorescence and phosphorescence spectra are red shifted. In sulfuric acid the fluorescence maximum occurs at 3750 Å and the 0→0 phosphorescence band is estimated at 72.6 kcal/mol. These new emissions may come from a protonated complex[6,26] or may be due to solvent effects.

The dependence of fluorescence efficiency on the acid concentration at concentrations less than 2 M can be represented by the following

$$\frac{I_{f_0}}{I_f} = 1 + k_q\tau[\text{D}^+] \qquad (2)$$

where I_{f_0} is the intensity of fluorescence in the absence of D^+, I_f is the intensity of fluorescence at a given concentration of D^+, k_q is the rate of quenching, and τ is the singlet lifetime at the given concentration of HQ-h_4. These data deviate from linearity at high acid concentrations due to nearest-neighbor quenching.[27-29] The rate constants in Table IV are calculated from the linear portion of the curve below 2 M. It is noteworthy that the concentration of HQ-h_4 does not effect the rate constant for fluorescence quenching.

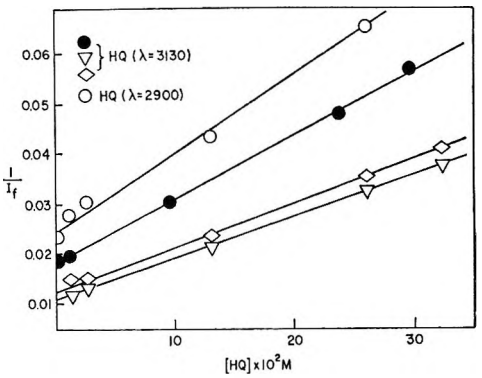

Figure 3. Dependence of *p*-hydroquinone fluorescence intensity on concentration in aqueous solution.

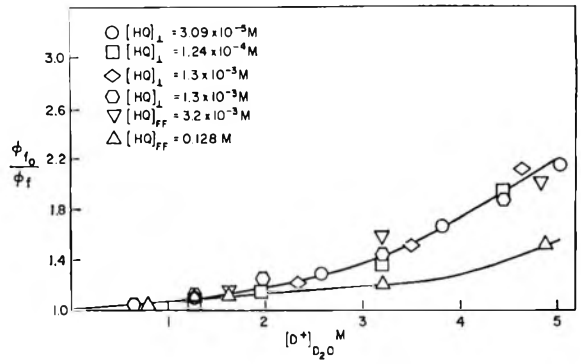

Figure 4. Quenching of *p*-hydroquinone fluorescence by D^+ in D_2O.

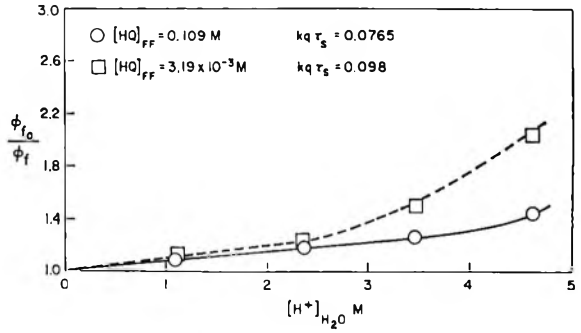

Figure 5. Quenching of *p*-hydroquinone fluorescence by H^+ in H_2O.

(26) G. Jackson and G. Porter, *Proc. Roy. Soc., Ser. A*, **260**, 13 (1961).
(27) A. Weller in *Progr. React. Kinet.*, **1**, 189 (1961).
(28) J. L. Kropp and M. Burton, *J. Chem. Phys.*, **37**, 1742 (1962).
(29) P. J. Wagner, *J. Amer. Chem. Soc.*, **89**, 5715 (1967).

Table IV: Rates of Fluorescence Quenching by Acid

Solvent	[HQ-h$_4$]	τ, nsec	k_q, M^{-1} sec^{-1}
H_3O^+	3.2×10^{-3}	1.9	5.2×10^7
H_3O^+	0.109	1.4	5.5×10^7
D_3O^+	3.2×10^{-3}	2.1	2.8×10^7
D_3O^+	0.128	1.6	3.7×10^7

The fluorescence of dilute solutions of *p*-hydroquinone is measured on an Aminco-Bowman spectrophotofluorimeter where the phototube is perpendicular to the excitation and the high concentration measurements were made on the front face fluorimeter. Table IV gives a summary of these quenching data.

Deuterium Exchange Quantum Yields. The quantum-yields for the hydrogen deuterium exchange were measured in DCl–D_2O solutions as a function of deuterium ion concentration. These quantum yields were obtained using a *p*-hydroquinone concentration of 0.13 *M* and D_3O^+ concentrations between 2 and 0.12 *M*. These data appear in Figure 6.

Intersystems Crossing Yield. To show the availability of triplets in solution, *p*-hydroquinone has been used to sensitize the isomerization *cis*- and *trans*-1,3-pentadiene.[30,31] The quantum yields for these sensitized isomerizations were measured using 0.13 *M* HQ-h$_4$ in ethanol solution. Table V summarizes these data.

Table V:[a] Quantum Yields for the Sensitized Isomerization of 1,3-Pentadiene

	$\phi_{c\rightarrow t}$	$\phi_{t\rightarrow c}$
1,3-Pentadiene	0.27 ± 0.03	0.17 ± 0.02

[a] [1,3-Pentadiene] = 5×10^{-2}, [HQ] = 0.13, ethanol was used as solvent for these reactions.

This isomerization has been shown to proceed through a triplet state. Lamola and Hammond[31] have shown that the sum of these quantum yields is equal to the intersystem crossing yield. In this case, the quantum yields must be adjusted for singlet quenching[12,32] (1,3-pentadiene quenching the singlet HQ-h$_4$), and for self-quenching (HQ-h$_4$ singlet–ground state interaction). The fluorescence of HQ-h$_4$ is very efficiently quenched by *cis*-1,3-pentadiene, $k = 1.5 \times 10^4\ M^{-1}\,\text{sec}^{-1}$. With these corrections in mind, one can obtain the following expression for the intersystem crossing yield. The intersystem crossing yield can also be obtained from 1 −

$$\phi_{ic} = \left(\frac{\phi_{f_0}}{\phi_f}\right)_{1,3\text{-pentadiene}} \left(\frac{\phi_{f_0}}{\phi_f}\right)_{sq} (\phi_{c\rightarrow t} + \phi_{t\rightarrow c}) \qquad (3)$$

$\phi_f = \phi_{ic}$. This yields an intersystem crossing of 0.63, which is in very good agreement with that obtained from eq 3 ($\phi_{ic} = 0.62$). These experiments show that *p*-hydroquinone is an efficient producer of triplets in solution and that it can be used as a triplet sensitizer.

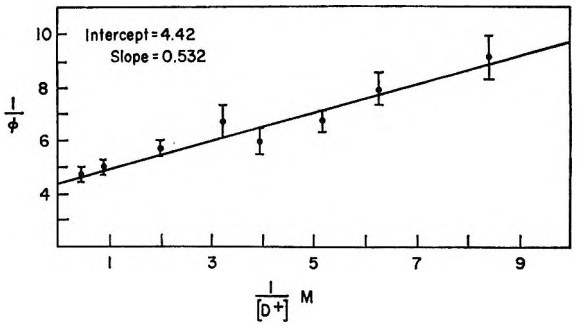

Figure 6. Quantum yield for deuterium exchange as a function of acid concentration.

Discussion

The absorption spectrum of *p*-hydroquinone clearly shows the lowest transition to be a π,π^* singlet state. The oxygen substituent shifts the absorption to the red, but no new bands due to an n,π^* transition are observed.[20] The lowest triplet is also a π,π^* state since the phosphorescence does not show the characteristic vibrational structure nor an emission lifetime of a n,π^* state. In aqueous acidic solution the hydroxyls are surely deuterated. However, this deuteration does not affect the benzene ring since the absorption spectrum is identical in various solvents.

Since the quantum yield for exchange is dependent on the acid concentration (Figure 6), it would be reasonable to assume that the initial step would involve the reaction of a *p*-hydroquinone π,π^* singlet with a deuterium ion. The singlet state has been previously credited as one of the reactants in photodeuteration.[2,4] The reaction with D^+ is therefore considered as another mode of deactivation of the excited singlet state in competition with fluorescence and intersystem crossing. The result of this collision is the formation of a σ complex.

Whether the σ complex is formed in an excited state or a vibrational level of the ground state has received some discussion.[33] It has been suggested,[2] and it would seem to hold in this case as well, that there is a strong potential barrier between the *p*-hydroquinone singlet and deuterium ion, and the σ excited state complex of the two. It is quite evident that a large barrier exists between the ground state reactants and the ground state σ complex since the rate of exchange is only measurable at elevated temperatures. It should be emphasized here that, although an emission (uniden-

(30) G. S. Hammond, *et al.*, *J. Amer. Chem. Soc.*, **86**, 3197 (1964).

(31) A. A. Lamola and G. S. Hammond, *J. Chem. Phys.*, **43**, 2129 (1965).

(32) L. M. Stephenson, Ph.D. Thesis, California Institute of Technology, Pasadena, Calif., 1968.

(33) G. Porter, R. Daudel, and G. S. Hammond, in the discussion of E. Havinga's paper in ref 2b.

tified) can be observed at extremely high acid concentrations (36 N H_2SO_4), no new emission is observed under the conditions of the photochemical exchange, $[D^+] < 1$ M. Therefore, it can be concluded that if another species is present, its concentration is not large enough to account for the high quantum yields and the σ complex is probably formed in a high vibrational level of the ground state. This process may be considered as an acid-catalyzed internal conversion. The ensuing chemistry would then be identical with ground state electrophilic substitution with the exception that the σ complex is not formed in the lowest vibrational state. (See Figure 7.)

Although no micromechanism for the formation of the σ complex is intended several speculative possibilities exist. These include intermolecular deuterium ion addition or intramolecular deuterium ion transfer from the deuterated hydroxyl.[34] The latter suggestion may be reasonable since the acidity of the hydroxyl hydrogen is increased in the excited state.[35]

With these considerations in mind the simplest mechanism which is consistent with the data is shown in Scheme I. This mechanism includes self-quenching of the p-hydroquinone singlet and deactivation *via* the ground state σ complex.

Scheme I

$$HQ\text{-}h_4 \xrightarrow{h\nu} (HQ\text{-}h_4)^1 \quad (4)$$

$$(HQ\text{-}h_4)^1 \xrightarrow{k_{ds}} HQ\text{-}h_4 \quad (5)$$

$$(HQ\text{-}h_4)^1 \xrightarrow{k_f} HQ\text{-}h_4 + h\nu \quad (6)$$

$$(HQ\text{-}h_4)^1 \xrightarrow{k_{ic}} (HQ\text{-}h_4)^3 \quad (7)$$

$$HQ\text{-}h_4 + (HQ\text{-}h_4)^1 \xrightarrow{k_{sq}} 2HQ\text{-}h_4 \quad (8)$$

$$D^+ + (HQ\text{-}h_4)^1 \xrightarrow{k_r} HQ\text{-}h_4d^+ \quad (9)$$

$$HQ\text{-}h_4d^+ \xrightarrow{k_1} HQ\text{-}h_4 + D^+ \quad (10)$$

$$HQ\text{-}h_4d^+ \xrightarrow{k_2} HQ\text{-}h_3d + H^+ \quad (11)$$

Kinetic analysis of this mechanism yields the following equations for the quantum yield for exchange and fluorescence quantum yield as a function of acid concentration.

$$\frac{1}{\phi} = \left(\frac{k_1 + k_2}{k_2}\right)\left(1 + \frac{1}{k_r\tau[D^+]}\right) \quad (12)$$

$$\frac{\phi_{f_0}}{\phi_f} = (1 + k_r\tau[D^+]) \quad (13)$$

The quantum yield data and fluorescence quenching data were obtained at concentrations of less than 1 M p-hydroquinone; τ is therefore the singlet lifetime at that concentration ($\tau^{-1} = k_{ds} + k_f + k_{ic} - k_{sq}[HQ]$). Analysis of Figure 6 according to eq 12 yields k_r = 8.32 M^{-1} and $(k_1 + k_2)/k_2 = 4.42$. The value for the intercept indicates that k_1 is greater than k_2, that is the σ complex decomposes yielding starting material approximately three times as fast as that going to the exchanged product. This kinetic isotope effect is in the opposite direction to that expected and sheds doubt on the proposed mechanism.

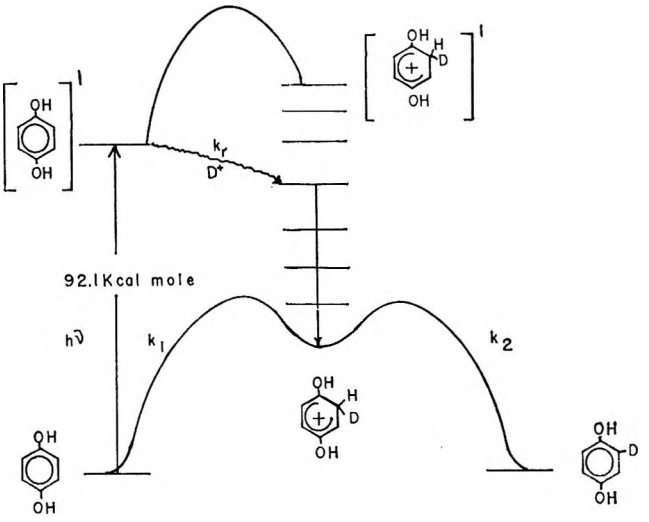

Figure 7. Energy level diagram for the hydrogen–deuterium exchange.

Previous workers[2] have explained a similar discrepancy by introducing an energy-wasting step. This step involves the deactivation of the excited hydrocarbon singlet by acid without the formation of a complex. Fluorescence quenching data with acid should reflect the importance of this step as well as a check on the proposed mechanism. A value of 0.059 M^{-1} for τk_r is obtained from the linear portion of curve in Figure 4. If the quantum yield data and this fluorescence quenching data are obtained at the same p-hydroquinone concentration, the value of τ is constant for both experiments and it can be seen that the rate of the reaction derived from the quantum yields experiments is 140 times as great as the rate of fluorescence quenching. These results clearly indicate that an energy-wasting step is not important and that a singlet mechanism is not significant in this H–D exchange.

Two other mechanisms come to mind, a radical process or a triplet intermediate. Flash photolysis of p-hydroquinone at 77°K shows the formation of radicals.[36] Radicals are also reported in the solution photolysis[37-39]

(34) O. L. Chapman, private communication.

(35) I. Arigal, J. Feitelson, and M. Ottolenghi, *J. Chem. Phys.*, **50**, 2614 (1969), $pK_a = 3.1$ for the hydroxyl hydrogen of p-hydroquinone in its excited singlet state.

(36) F. J. Land, G. Porter, and E. Strachan, *Trans. Faraday Soc.*, **57**, 1885 (1961).

(37) H. Lindschitz, J. Rennert, and R. M. Korn, *J. Amer. Chem. Soc.*, **76**, 5389 (1954).

(38) H. I. Joschek and S. I. Miller, *ibid.*, **88**, 3273 (1966).

(39) H. I. Joschek and L. I. Grossweiner, *ibid.*, **88**, 3261 (1966).

of *p*-hydroquinone. These latter authors[38,39] report oxidation of HQ-h_4 in H_2O using 2537-Å radiation. Quinone as well as polyhydroxy aromatics are reported as products. We found the efficiency of the exchange reaction is reduced when 2537-Å irradiation is used. In this experiment the solution turned yellow and upon epr analysis signals were observed which are not accounted for by the hydroquinone isomers. However, analysis of samples which has been irradiated at 2900 Å showed no evidence of new products, and the solutions remained colorless. To check the intermediacy of quinones, *p*-benzoquinone was added to solutions of *p*-hydroquinone with the result of quenching the exchange reaction. Irradiation of *p*-benzoquinone in D_2O–DCl solutions showed no exchange.

It therefore seems reasonable to analyze this reaction as a result of a triplet intermediate. This mechanism is shown in Scheme II.

Scheme II

$$HQ\text{-}h_4 \xrightarrow{h\nu} (HQ\text{-}h_4)^1 \quad (14)$$

$$(HQ\text{-}h_4)^1 \xrightarrow{k_{ds}} HQ\text{-}h_4 \quad (15)$$

$$(HQ\text{-}h_4)^1 \xrightarrow{k_f} HQ\text{-}h_4 + h\nu \quad (16)$$

$$(HQ\text{-}h_4) \xrightarrow{k_{ic}} (HQ\text{-}h_4)^3 \quad (17)$$

$$HQ\text{-}h_4 + (HQ\text{-}h_4)^1 \xrightarrow{k_{sq}} 2HQ\text{-}h_2 \quad (18)$$

$$D^+ + (HQ\text{-}h_4)^3 \xrightarrow{k_r} HQ\text{-}h_4d^+ \quad (19)$$

$$HQ\text{-}h_4d^+ \xrightarrow{k_1} HQ\text{-}h_4 + D^+ \quad (20)$$

$$HQ\text{-}h_4d^+ \xrightarrow{k_2} HQ\text{-}h_3d + H^+ \quad (21)$$

$$(HQ\text{-}h_4)^3 \xrightarrow{k_{dt}} HQ\text{-}h_4 \quad (22)$$

Quenching of the singlet *p*-hydroquinone by deuterium is omitted here since it is slow compared with intersystem crossing. The *p*-hydroquinone-sensitized isomerization of 1,3-pentadiene shows that a large number of triplets are produced in solution. Analysis of Scheme II yields the following equation for the quantum yield

$$\frac{1}{\phi} = \left(\frac{1}{\phi_{ic}}\right)\left(\frac{\phi_{f_0}}{\phi_f}\right)_{sq}\left(\frac{k_1 + k_2}{k_2}\right)\left(1 + \frac{k_{dt}}{k_r[D^+]}\right) \quad (23)$$

This equation clearly fits the data represented in Figure 6. The intercept now takes on a different meaning. If the value of the intercept is corrected for the intersystem crossing yield at 0.1 *M* *p*-hydroquinone, then $k_1 \cong k_2$. The slope to intercept ratio yields $k_{dt} = 0.12\,k_r$.

The proof of a triplet mechanism lies in the ability to sensitize or quench the reaction. However, in order to sensitize the exchange reaction, the sensitizer must have greater than 75 kcal of triplet energy, be soluble in water, have a lower singlet energy than *p*-hydroquinone, and be stable in acid. The usual sensitizers unfortunately do not meet these requirements. Similar problems are encountered in designing quenching experiments. The usual organic sensitizers and quenchers cannot be used for these reasons.

It can be concluded that both singlet and triplet intermediates can lead to photochemical aromatic substitution. However, in this case, the singlet decay is very fast and the intersystem crossing is comparable. Therefore, the singlet state does not exist long enough for much exchange to occur *via* this state. The primary path is therefore intersystem crossing to the triplet followed by reaction with D^+ resulting in the formation of a deuterated complex in a high vibrational level of the ground state which proceeds to starting material or exchanged product.

Acknowledgment. The author wishes to acknowledge the helpful discussions of Drs. H. C. Heller, H. D. Yao, and V. I. Stenberg for critically reading this manuscript. The work done at the University of North Dakota was supported by the University of North Dakota Faculty Research Grant and a grant from The Research Corp.

Crystallographic Studies on Nickel Hydroxide and the Higher Nickel Oxides

by R. S. McEwen[1]

Bell Telephone Laboratories, Murray Hill, New Jersey 07971 *(Received September 4, 1970)*

Publication costs borne completely by The Journal of Physical Chemistry

Many papers have appeared on the subject of nickel hydroxide and its oxidation products. This paper re-examines some aspects of the problem, using high resolution electron microscopy and diffraction to assist interpretation of powder X-ray patterns. No evidence has been found for correlation between layer positions in hydrated nickel hydroxide (α form) and an apparent contraction of lattice parameters within the layers has been shown to be caused by a special diffraction effect. Some comparisons are drawn between chemically prepared and electrochemically formed oxidized materials.

Introduction

Nickel hydroxide and its oxidation products are of considerable interest to electrochemists because of their use as the active material of the positive electrode of the nickel–cadmium battery. The nickel electrode is not characterized by a reversible electrode potential, and the stoichiometry of the electrode reaction has not been exactly established. However, it is generally recognized that in essence the reaction involves change of nickel valency between +2 and +3 and that hydrogen atoms diffuse in and out of the electrode material.[2-7]

Much effort has been expended in the use of X-ray powder diffraction techniques to determine the structures of the species participating in the reaction. This memorandum surveys pertinent experimental results and discusses the problem of determining structures of compounds of ill-defined stoichiometry when disorder and poor crystallinity give rise to special diffraction effects.

The paper is in two sections. The first relates to the simpler problem of the structure of the hydroxide in its reduced state, the second to the structure of the oxidized material.

1. Nickel(II) Hydroxide

Review

The first consideration is the structure of the compound $Ni(OH)_2$.[8] This structure, also adopted by the hydroxides of bivalent Ca, Mg, Fe, Co, and Cd, is usually denoted as the brucite or C6-type structure. It has a hexagonal unit cell of dimensions: $a = 3.126$, $c = 4.605$ Å, containing one formula unit of $Ni(OH)_2$. The atoms have the fractional coordinates: nickel 0, 0, 0; oxygen $^1/_3$, $^2/_3$, z and $^2/_3$, $^1/_3$, $\bar{z}$, where $z = 0.25$. Figure 1 shows several unit cells projected down the unique c axis. As indicated by the heavy lines radiating from the nickel, the metal is surrounded by six equidistant oxygen atoms, three lying above the plane of the nickel and three below. The Ni–O distance is 2.14 Å. Such layers of nickel atoms with an octahedral coordination of oxygen atoms and with the crystal z axis coincident with the $\bar{3}$ axis of the octahedron, will be termed "normal layers" in the following.

Bernal and Megaw[9] in 1935 suggested for the isomorphous $Ca(OH)_2$, that the O–H bonds lie parallel to the c axis, the hydrogen atoms being on opposite sides of the oxygen layer. The O···O distance is 3.3 Å and for that reason the possibility of hydrogen bonding was ruled out. Studies by nmr spectroscopy[10] and by neutron diffraction[11] on $Ca(OH)_2$ have confirmed that there are no hydrogen bonds between the layers.

Nickel hydroxide also exists in a modified form, which is designated α to distinguish it from the brucite form just described, often termed β. It is a loose hydrate $Ni(OH)_2 \cdot xH_2O$, where x varies between 0.5 and 0.7. It has been assigned the structure[12] shown in

(1) Address all correspondence at Department of Chemistry, Florida State University, Tallahassee, Fla. 32306.

(2) (a) G. W. D. Briggs and W. F. K. Wynne-Jones, *Electrochim. Acta*, **7**, 241, 249 (1962); (b) J. P. Harivel, P. Morignat, J. Labat, and F. J. Laurent, 5th International Power Sources Symposium, Brighton, Sept 1966.

(3) J. T. Richardson, *J. Phys. Chem.*, **67**, 1377 (1963).

(4) A. Pacault and J. Labat, *C. R. Acad. Sci. Paris*, **258**, 5421 (1964).

(5) A. Salkind and P. F. Briuns, *J. Electrochem. Soc.*, **109**, 356 (1962).

(6) D. Tuomi, *ibid.*, **112**, 1 (1965).

(7) P. C. Milner and U. B. Thomas, *Advan. Electrochem. Electrochem. Eng.*, **5** (1967).

(8) R. W. G. Wyckoff, "Crystal Structures," Vol. 1, Interscience, New York, N. Y., 1960.

(9) J. D. Bernal and H. D. Megaw, *Proc. Roy. Soc., Ser. A*, **151**, 384 (1935).

(10) D. D. Elleman and D. Williams, *J. Chem. Phys.*, **25**, 742 (1956).

(11) W. R. Busing and H. A. Levy, *ibid.*, **26**, 563 (1967).

(12) H. Bode, K. Dehmelt, and J. Witte, *Electrochim. Acta*, **11**, 1079 (1966).

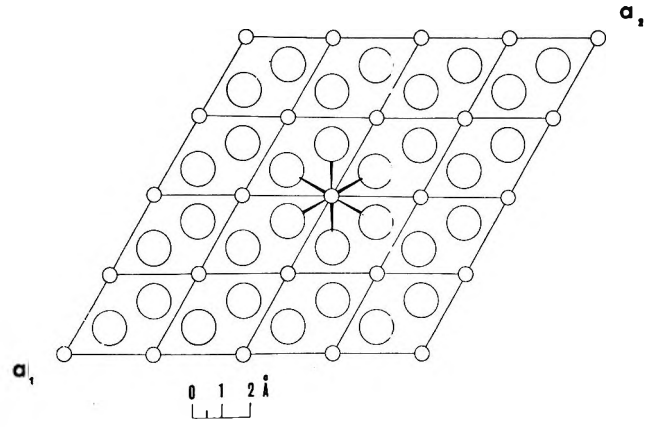

Figure 1. The structure of nickel(II) hydroxide: projection down the *c* axis. The small circles represent nickel atoms, the large circles, oxygen atoms.

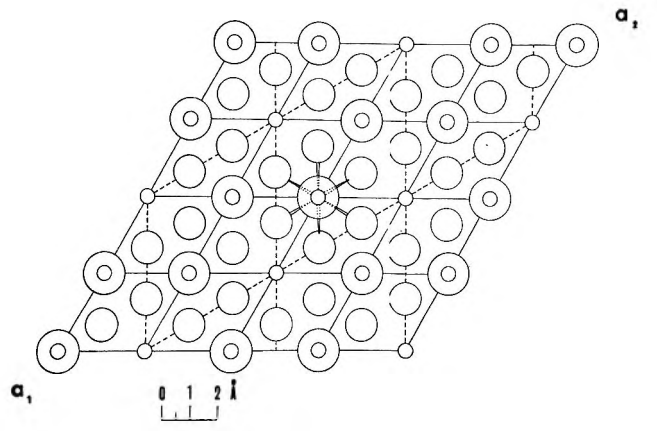

Figure 2. The structure proposed by Bode, *et al.*,[18] for the hydrated form of nickel(II) hydroxide projection down the *c* axis. The largest circles represent water molecules.

Figure 2. It differs from the anhydrous hydroxide by the presence of water molecules situated above and below some of the Ni atoms along the trigonal axis, and by the increase of the *c* axis length to about 8 Å. A different unit cell shown by dashed lines (....) has been chosen to accommodate $3Ni(OH)_2 \cdot 2H_2O$ as an idealized formula unit. The feature of interlaminar water seems well established from density measurements and chemical analysis apart from X-ray diffraction evidence. However, we have found no evidence to support the details of this structure in the present work. Another interpretation of diffraction data from our samples of hydrated nickel hydroxide will be given.

Experimental and Discussion

We decided to investigate the differences in reduced (bivalent) nickel hydroxide when it was formed and treated in four different ways. (1) The material was formed by homogeneous precipitation by electrolyzing a nickel salt solution (this is a common method for preparing thin film electrodes); (2) it was formed by controlled precipitation from a complexing solution; (3) reagent grade and electrochemically prepared nickel hydroxide were treated hydrothermally; and (4) the same materials as in 3 were subjected to compression.

When nickel salt solutions are electrolyzed, the reduction of H^+ ions [or NO_3^- ions for $Ni(NO_3)_2$ solutions] raises the pH at the cathode. This results in the homogeneous precipitation of nickel hydroxide. The diffraction patterns produced with this material depend on the rate at which electrolysis is conducted. When an electrode is made cathodic at a few mA/cm^2 current density in 1 *M* solutions of $Ni(NO_3)_2$ at room temperature, the diffraction pattern of the precipitated material differs from that of normal brucite (β form) by the presence of diffuse intensity maxima at angles corresponding to *d* spacings of around 8 and 4 Å. As the electrolysis current density is lowered, these additional reflections become more pronounced and shift to lower angles (10 and 5 Å).

These are first- and second-order diffraction maxima from normal layers whose separation has been increased from 4.605 in the brucite structure by insertion of a layer of water molecules.

Taking 1.7 Å as the radius of a water molecule, the value for the expanded *c* axis spacing would be 7.6 Å if the water molecules would be close packed with the hydroxide ions on either side. If they do not close pack, the *c* axis spacing would be larger, 4.6 + 3.4 = 8.0 Å. This value is frequently observed. A value of 10.5 Å for the expanded *d* spacing would indicate that the water layer is two molecules thick.

Two changes occur in the brucite reflections: (1) general reflections, *hkl* begin to disappear; and (2) the powder diffraction line profiles of *hk*0 reflections become asymmetric. Figures 3a and 3b show typical *hk*0 reflection line profiles from cathodically formed nickel hydroxide. These reflections are termed "two dimensional," since they arise only from layers of the structure normal to the *c* axis.

The data plotted in Figure 3a was obtained using a Siemens two circle diffractometer, using a $\theta/2\theta$ step scan. The steps were 0.1° and the time taken to accumulate 10^4 counts was measured. The powder pattern of Figure 3b was obtained as were all succeeding patterns, with a 57.3-mm radius Debye–Scherrer camera and a Jarrell-Ash recording microdensitometer.

The type of line profile observed in two-dimensional reflections from some layer structures was explained by Von Laue in 1932,[13] Warren in 1941,[14] and Wilson in 1949,[15] as due to a randomization of layer orientation relative to one another. The spacing between the parallel layers remains constant. Theoretical ex-

(13) M. Von Laue, *Z. Kristallogr.* **82**, 127 (1932).
(14) B. E. Warren, *Phys. Rev.*, **59**, 693 (1941).
(15) A. J. C. Wilson, *Acta Crystallogr.*, **2**, 245 (1949).

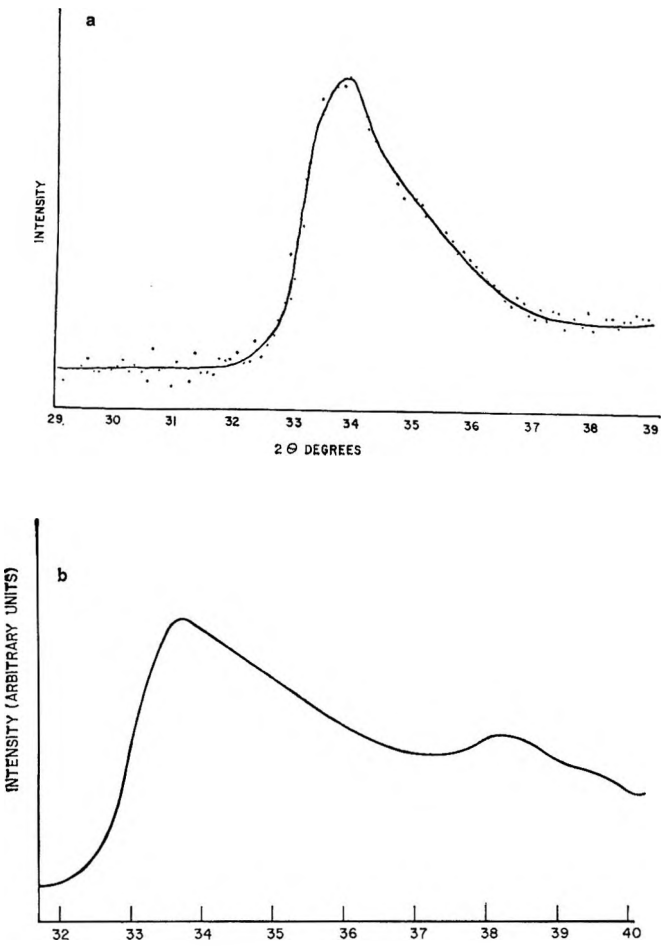

Figure 3. (a) Diffractometer trace of the line profile of the 100 reflection of hydrated nickel(II) hydroxide. (b) Microdensitometer trace of the line profile of the 100 reflection of partially hydrated nickel(II) hydroxide having regions of normal β-phase structure. The maximum between 38 and 39° in 2θ is due to the β-phase 101 reflection.

pressions for the line profile have been derived for the case in which the layers are oriented completely randomly. These expressions contain terms which depend on the size and the shape of the layers.

Other examples of random or nearly random layer lattice structures are found in certain layer minerals and in carbon black. The graphitization of carbon black was studied by Houska and Warren in 1954.[16] Departure of the observed line profile from that calculated on the assumption of completely random orientation can be interpreted as a correlation between layer positions. Houska and Warren[16] used coefficients derived from Fourier analysis of the line profiles to compute a correlation function which showed that, during heat treatment, adjacent carbon layers tend to take up positions characteristic of those in the hexagonal graphite structure. Furthermore, they were able to determine the probability of second nearest layers adopting relative orientations as in the three-layer or rhombohedral graphite structure. That is, they determined the relative probabilities of the stacking sequences: ABAB and ABCA.

Both from our microdensitometer traces and by careful visual inspection of our powder photographs, we found no evidence of lines corresponding to general reflections from a cell with expanded c spacing. In particular, the 111, 112, 113, and 114 reflections which calculate strong were noticeably absent.

On the other hand, for materials precipitated electrochemically at high current densities, there are always some general reflections from the normal brucite cell. Only material formed at low rates give diffraction patterns having no brucite general lines. These observations mean that: (1) there is no correlation between normal layers separated by water molecules which act as an amorphous "glue" joining the brucite layers; and (2) in material formed at high current densities where water layers do not necessarily alternate regularly with normal brucite layers. Therefore, it is not possible to make a clear distinction between a crystal in which water layers are interspersed at intervals between sequences of brucite layers, and separate but contiguous crystals with the brucite structure with adsorbed water.

It has been noted by several workers from Feitknecht[17] in 1936 who first observed the α form of the hydroxides, to Bode, *et al.*, in 1966[18] that when hydrated, the layers of $Ni(OH)_2$ undergo a contraction of between 0.05 and 0.10 Å in the a-axial length. However, our measurements show that this contraction is only apparent, the shifts in peak position being disorder and particle-size effects.[15] The peaks are shifted to higher angles according to $\Delta(\sin\theta) = 0.16\lambda/L$, where λ is the wavelength of the radiation used and L is the diameter of the layers of the crystallites. L was evaluated from broadening of the lines. The expression relating particle size to line breadth to half-peak intensity is the same for two-dimensional reflections as for three-dimensional crystal reflections, but the numerical factor is about twice as large for the former. The observation that there is no real lattice contraction in the α-nickel hydroxide hydrate means that the bond angles and lengths of the $[Ni(OH)_6]$ unit are unchanged on hydration.

Finally, we did not find it possible to locate molecules of the water layer on only certain of the available positions as was proposed by Bode[18] (see Figure 2). An ordered arrangement of water molecules would give rise to extra reflections and imply a correlation between nickel–oxygen octahedra layers separated by such a layer. As we have noted, no such correlation is observed. It is therefore more reasonable to locate a fraction of a molecule of water above all positions and retain the original cell in two dimensions. This makes

(16) C. R. Houska and B. E. Warren, *J. Appl. Phys.*, **25**, 1503 (1954).

(17) W. Lotmar and W. Feitknecht, *Z. Kristallogr. Mineral, Petrogr. Abt. A*, **93**, 368 (1936).

(18) H. Bode, *Angew. Chem. Int. Ed. Engl.*, **73**, 553 (1961).

all the nickel atoms chemically identical and gives the water layers a relatively structureless aspect.

Solutions of $Ni(OH)_2$ in aqueous ammonia were placed in a desiccator over sulfuric acid. By this method it was possible to obtain quite well crystallized hydroxide containing various amounts of interlayer water, but always having regions of β phase. Attempts to obtain single-crystal electron diffraction data proved unsuccessful because of the extreme tendency to dehydration and because the good thermal insulating properties of the nickel(II) hydroxide resulted in local heating and disruption of the material in the electron beam. However, some experiments in forming the mixed nickel–zinc α-hydroxide gave rather more stable and better crystallized material.

Hydrothermal treatment (discussion of the hydrothermal treatment will be given later) of $Ni(OH)_2$ in dilute NaOH gave extremely well crystallized β-phase material with a particle size in the 10-μ range.

Some metal halides and hydroxides with structures similar to that of $Ni(OH)_2$ undergo stacking sequence alterations on mechanical deformation. No such changes were observed when $Ni(OH)_2$ powders were subjected to compression in a press up to 20,000 psi.

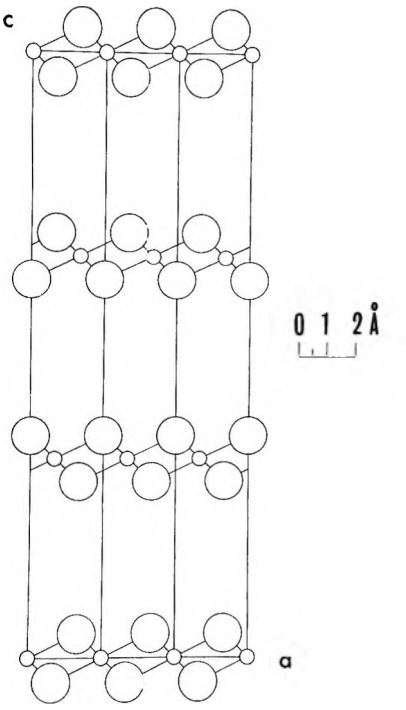

Figure 4. Atomic positions in the ordered layers of γ-nickel oxyhydroxide:[9] projection down the a axis.

2. Higher Nickel Oxides

Review

The subject of the higher oxides of nickel has a lengthy and confused history.[12,18–25] Many different formulas and structures have been proposed and refuted. The experimental facts are these. Black hydrated compounds of nickel, oxygen, and hydrogen and, depending on their mode of preparation, potassium in widely varying quantities, can be formed in which there is an excess of oxygen above that required by the formula NiO. This "active oxygen" is frequently measured by its ability to oxidize I^- in acid solution. Nickel has been inferred to be in a valency state greater than two by magnetic susceptibility measurements.[3,4]

X-Ray structural studies are complicated by special diffraction effects, but it appears that there are two basic structural forms, β and γ.

β-NiO(OH). The usual brucite modification, β-$Ni(OH)_2$ can undergo electrochemical oxidation to the +3 state with no change in the main structural features. The lattice parameters have been reported to change smoothly from $a = 3.126$, $c = 4.605$ Å in β-$Ni(OH)_2$ to $a = 2.82$, $c = 4.85$ Å in β-NiO(OH). The extent to which this structure is preserved depends on the rate of oxidation.[2]

γ-NiO(OH). The other basic structural form needed to explain all the observations is of the C19 or $CdCl_2$ type.[20] However, the cell is greatly elongated as compared with that of $CdCl_2$ itself. The lattice is rhombohedral, but Figure 4 shows the corresponding hexagonal triple cell, the height of which is equal to the long body diagonal of the rhombohedral cell. The atomic arrangement is shown in projection down one of the nonunique axes in Figure 4. Cell dimensions given by Glemser and Einerhand[20] for a compound they call γ-nickel hydroxide are $a = 2.82$, $c = 20.65$ Å.

The space between the layers of nickel atoms which retain their octahedral surrounding of oxygen atoms is occupied by disordered material giving little or no contribution to the Bragg reflections but only to the general background scatter. This interlaminar material was thought to be of the same chemical constitution as the normal, ordered layers shown in Figure 4. However, assuming that the height of the ordered layers is at least as great as in β-$Ni(OH)_2$, the space available to disordered, interlaminar material is approximately $(21 - 3 \times 4.6) = 7.2$ Å, or 2.4 Å per layer. This is insufficient for any reasonable arrangement of a layer of composition NiO(OH), but is adequate to accommodate OH^- ions or H_2O.

The basic structure as described now seems well established for a number of reasons. (1) The lattice

(19) R. W. Cairns and E. Ott, *J. Amer. Chem. Soc.*, **55**, 527 (1933).
(20) O. Glemser and J. Einerhand, *Z. Anorg. Allg. Chem.*, **261**, 26,43 (1950).
(21) W. Feitknecht, H. R. Christen, and H. Studer, *ibid.*, **283**, 88 (1956).
(22) J. Labat, *J. Chim. Phys.*, **60**, 83 (1963).
(23) L. N. Sagoyan, *Izv. Akad. Nauk SSSR, Ser. Khim.*, **17**(1), 3 (1964).
(24) F. P. Kober, *5th International Power Sources Symposium*, Brighton, Sept 1966.
(25) H. Bode, K. Dehmelt, and J. Witte, *Z. Anorg. Allg. Chem.*, **366**(1), 1 (1969).

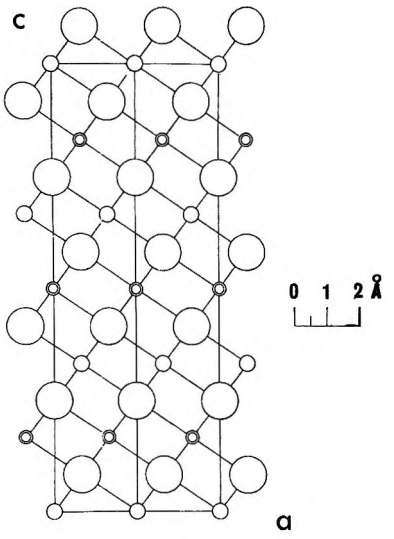

Figure 5. The structure of sodium nickelate, $NaNiO_2$[11]: projection down the a axis. The double circles represent sodium atoms.

constants are derived from powder diffraction patterns which are much sharper and richer in lines than those of the α-$Ni(OH)_2$ or β-NiO(OH). (2) The calculated X-ray densities based on cell dimensions and chemical analysis agree with observed densities.[25] (3) There is a broad measure of agreement between observed and calculated structure factors calculated on the basis of the coordinates of the ordered layers shown in Figure 4.[20] (4) γ-Nickel oxyhydroxide is formed on hydrolysis of $NaNiO_2$, the structure[26] of which is closely related to the γ-nickel oxyhydroxide structure. Figure 5 shows a projection down one of the nonunique axes of the hexagonal triple cell of the rhombohedral form of $NaNiO_2$. (This compound also exists in a slightly distorted monoclinic form.) When hydrolysis takes place, most of the sodium atoms are displaced, and a variable number of water molecules forms the disordered interlaminar material. Some oxide ions are presumably converted to hydroxide ions without any rearrangement of the oxygen positions. The γ-nickel oxyhydroxide always contains small quantities of alkali metal ions in the disordered layers, the amount depending upon the mode of preparation.

The cell dimensions vary quite widely as the oxidation value of the nickel changes. Although distinct compounds have been proposed with formulas $Ni_2O_3 \cdot 2H_2O$ and $Ni_3O_4 \cdot 2H_2O$, it seems that these ideal formulas have no special significance. Oxidation of nickel higher than +3 is possible,[18] but so far X-ray work has not yielded any useful results as the material becomes very amorphous.[20]

Experimental Section

In our experiments on higher nickel oxides, we have hydrothermally treated materials formed by bromine and by electrochemical oxidation. The materials have been examined by electron and X-ray diffraction. Materials collected from positive battery plates were also examined for comparison.

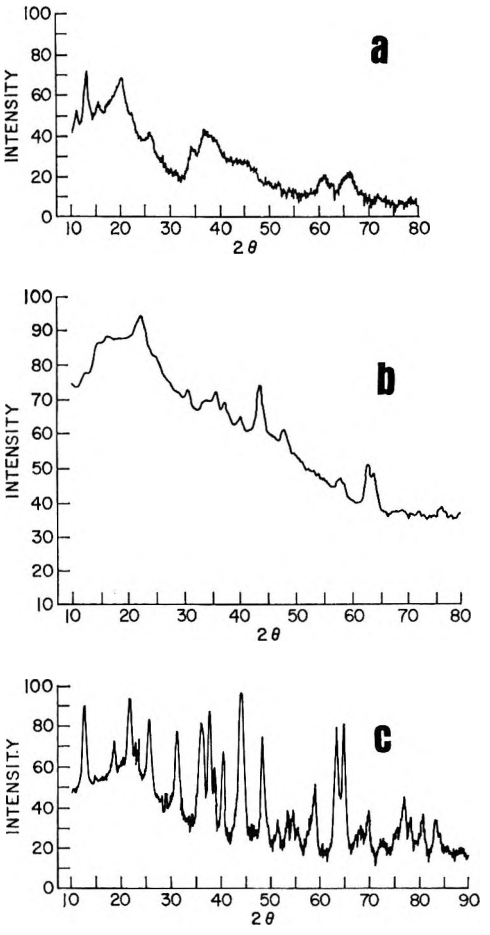

Figure 6. Microdensitometer traces of powder X-ray diffraction patterns of higher nickel oxides. (a) Oxidized form of nickel hydroxide prepared by method of Cairns and Ott.[19] (b) Active material obtained from a sintered nickel electrode cycled many times. (c) Hydrothermally treated oxide prepared by method of Cairns and Ott.[19]

An oxidized form of nickel hydroxide was prepared by the method of Cairns and Ott.[19] A solution of 47.5 g of KOH and 11 ml of Br_2 in 500 ml of water was added slowly with vigorous stirring to a solution of 50 g of $NiNO_3 \cdot 6H_2O$ in 750 g of water—the temperature being kept at 100°. Care was taken to exclude CO_2 and the water was doubly distilled in an atmosphere of nitrogen. The black precipitate was washed by filtration and centrifugation. After washing with about 10 l. of water, some of the precipitate remained in colloidal form and was not thrown down on prolonged centrifugation. The recovered product was dried at room temperature over silica gel in a vacuum desiccator. The most notable features of the X-ray diffraction pattern of the material are two comparatively sharp lines at 7.0 and 3.5 Å. The remaining lines are extremely diffuse, but

(26) L. D. Dyer, B. S. Borie, and G. P. Smith, *J. Amer. Chem. Soc.*, 76, 1499 (1954).

as far as could be judged, not asymmetric. The pattern shown in Figure 6a is in general agreement with that of the γ phase reported by Glemser and Einerhand,[20] but permitted no detailed interpretation. Depending on the extent of drying the material, the sharp lines varied in position from 7.9 and 3.8 to 6.8 and 3.4. Sometimes both pairs of values could be observed in the same sample. The lines at 7.0 and 3.5 Å can be taken as the most easily identified characteristic of the γ phase.

Fully discharged material from thin film electrodes which had been charged and discharged only a few times at the $C/2$ ($C/2$ rate is the current required to charge the electrode in 2 hr assuming 100% charging efficiency) rate showed diffraction patterns very similar to that of the reduced material β-$Ni(OH)_2$. They always included a diffuse low angle band (8–10 Å). In these cases the oxidation has proceeded within the β phase. Some "normal" layers are separated by water in both the reduced and oxidized states.

Material taken from electrodes which had undergone a large number of cycles or had failed due to flaking gave patterns containing lines of the γ phase. Usually the diffuse 8–10-Å spacing of the water-separated layers was replaced by the relatively sharp 7-Å line of the γ structure.

The oldest electrode material examined came from a sintered nickel electrode which had been deep cycled about 3000 times and its ampere-hour capacity had decreased to a nearly steady value. Most of the black active material was removed by dissolution in a hot solution of 1 M ammonium acetate in concentrated NH_4OH. A small quantity of insoluble material was washed out. The X-ray pattern showed this to be mainly metallic nickel, but a number of quite sharp lines of an unknown phase were recorded. Some of these were later shown to correspond to the pattern of the hydrothermally recrystallized nickel oxyhydroxides (Figure 6b and Table I).

Table I[a]

d_{obsd}	$1/d_{obsd}^2$	$1/d_{calcd}^2$	hkl	I_{obsd}
6.94	0.0208	0.0206	003	40
4.097	0.0596	0.0573	005	37
3.481	0.0825	0.0825	006	32
2.521	0.1573	0.1573	100	36
2.384	0.1759	0.1780	103	57
2.319	0.1860	0.1857	009	31
2.087	0.2296	0.2292	0010	25
2.094	0.2382	0.2399	106	73
2.008	0.2480	0.2490	102	24
1.709	0.3424	0.3430	109	17
1.436	0.4849	0.4874	1012	63
1.260	0.6299	0.6294	200	11
0.9072	1.2151	1.2137	217	20

[a] A number of the lines in the powder diffraction pattern of a hydrothermally recrystallized higher nickel oxide which can be indexed in terms of a cell similar to that reported by Glemser and Einerhand (see ref 20). Calculated on the hexagonal triple cell: a = 2.89; c = 20.89 Å.

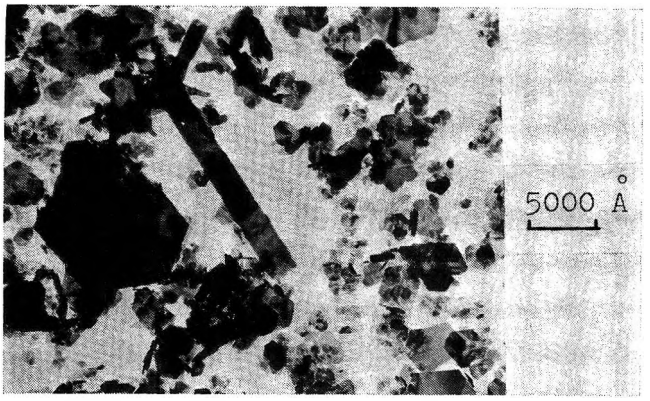

Figure 7. Electron micrograph of hydrothermally treated higher nickel oxide: magnification 20,000×.

Hydrothermal Treatment

Small quantities (0.1 g) of nickel hydroxide with 1–2 ml of 40% KOH were sealed into a $^3/_{16}$-in. diameter platinum tube. The tube was placed in a hydrothermal bomb (Tuttle cold seat cone closure type) and maintained at a temperature of 240° and a pressure of 15,000 psi for periods ranging from 4 to 14 days. At the end of a run, the bomb was cooled with ice water and the material was thoroughly washed by centrifugation.

The material was dried over silica gel under vacuum at room temperature. Samples for transmission electron microscopy and diffraction were prepared by passing a copper grid covered with a thin layer of carbon through a suspension of the material in water. The electron microscope used was a Siemens Elmiskop.

Hydrothermally treated material prepared by the Cairns and Ott[19] method gave X-ray patterns in agreement with those reported by Aia.[27] The line pattern was superimposed upon a broad band which peaked around 4 Å (Figure 6c). Electron micrographs revealed hexagonal plate crystals ranging from tenths of a micron to a few microns in size (Figures 7 and 8a). Diffraction patterns of isolated single crystals, Figures 8b and 9c showed a hexagonal reciprocal net. The a dimension of the hexagonal cell was calculated as 2.89 Å. Taking the first line in the X-ray diffraction pattern as the 003 reflection from a hexagonal triple cell, it was possible to index about half the lines as shown in Table I. The cell is thus similar to that reported by Glemser and Einerhand.[20] The intensities, however, are different.

Hydrothermally treated materials originating from electrochemical preparation also showed the γ-type cell. In addition, both X-ray powder and electron single-crystal diffraction detected a lattice of the bru-

(27) M. A. Aia, General Telephone Research Lab. Internal Report TR66-100.3, 1966.

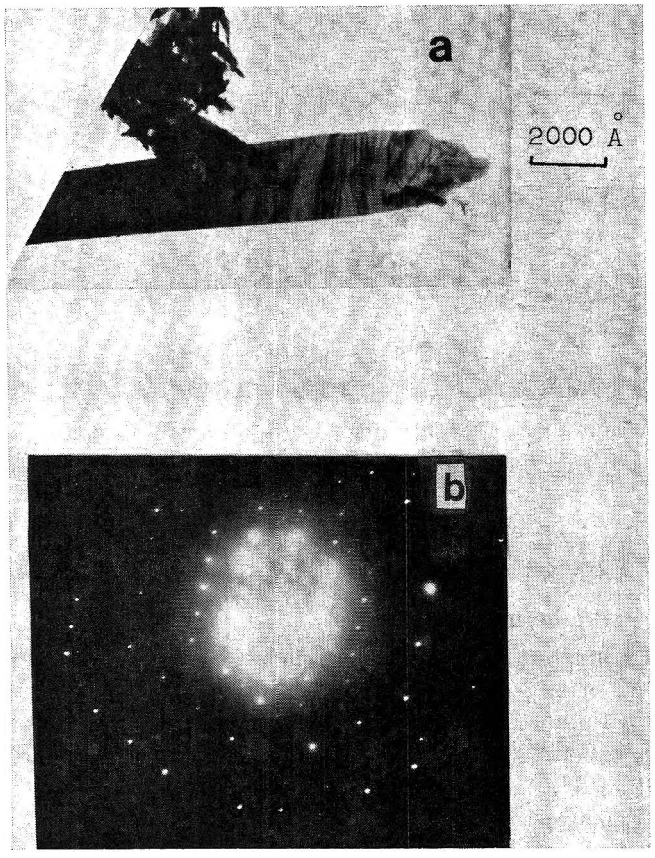

Figure 8. (a) Electron micrograph of an isolated single crystal of hydrothermally treated higher nickel oxide: magnification 60,000×. (b) Selected area transmission electron diffraction pattern of the crystal shown in Figure 8a.

cite type, and other lattices which were slight distortions from hexagonal. Figures 9a and 9b show that such samples contain crystals with different habits—hexagonal plates and flat needles. The product mixtures were so complex and the rate of crystal growth so slow—a sample hydrothermally treated for 3 weeks contained crystals of 20 μ at most—that these interesting results could not be fully explored in a reasonable time period.

In one hydrothermal run on the electrochemically prepared material, the temperature was held at 290 rather than 240°. The product mixture gave lines corresponding to NiO in the X-ray powder diagrams.

The presence of the broad band around 4 Å in the X-ray patterns of these materials showed that disorder still existed. The band was less obvious in samples treated for long periods.

Analysis by atomic absorption spectroscopy showed that the potassium content was about 0.5% after hydrothermal treatment.

The infrared spectrum of the oxidized materials run in a KBr pellet from 350 to 7000 cm^{-1} showed broad bands at 570 and 3400 cm^{-1}. The absence of bands 3650 Å and 350 cm^{-1} indicated that few OH groups were present.

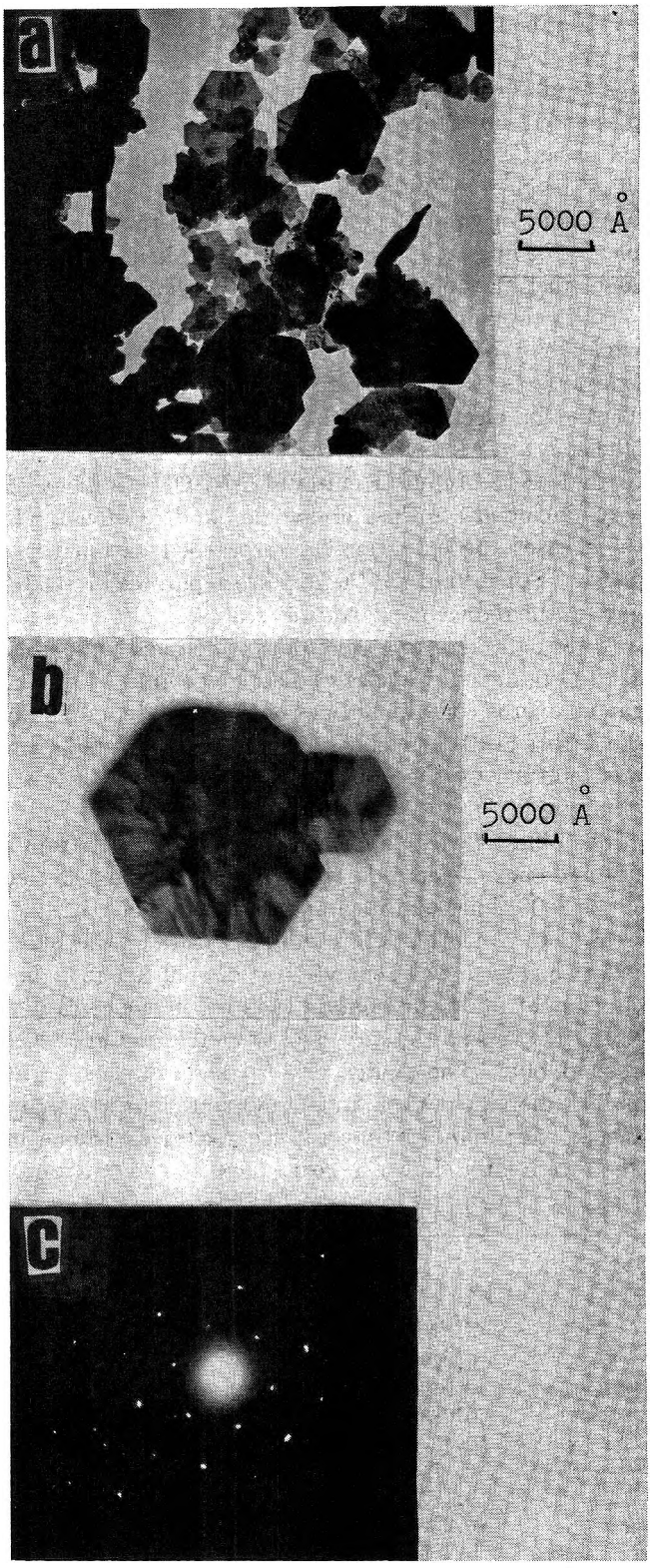

Figure 9. (a) Electron micrograph of hydrothermally treated higher nickel oxide prepared by anodic deposition from a potassium acetate/nickel sulfate solution at a current density of 55 mA cm^{-2} and a temperature of 77°, magnification 20,000×. (b) Electron micrograph of a crystal of hydrothermally treated higher nickel oxide prepared by anodic deposition, magnification 20,000×. (c) The diffraction pattern obtained from the crystal shown in Figure 9b. The net is not exactly hexagonal.

Discussion

The β-phase oxidation can most simply be summarized by the formula $NiO_x(OH)_{2-x}$ where x runs from 0 to 1. As hydrogen atoms are lost from the lattice and the oxidation number of nickel increases ($x \rightarrow 1$), the a axis of the unit cell decreases and the c axis increases in length. The values given by the various authors are subject to revision for the same reasons as described in connection with the reduced hydroxide, the line profiles frequently being asymmetric. From what results are available, however, it seems as if there is a real contraction in the xy plane on oxidation, although not as great as that shown by the uncorrected values. The c axis length is not subject to this error, and there is an increase of 0.24 Å in separation accompanying the parallel slippage of the layers. As we noted earlier, hydrogen bonding is not present in the reduced β phase, and the decreased interlayer adhesion is due only to the increase in charge on the oxygen atoms as hydrogen atoms are removed.

The γ structure is closely related to that of the alkali nickelates, $MNiO_2$ (M = Li, Na, K). The quantity of potassium in higher nickel oxides formed in the presence of potassium ions varies widely, depending on the mode of preparation. Potassium atoms are comparable in size to water molecules (radius of K = 1.33 Å, radius of water = 1.7 Å) and can to a large extent be replaced by them in the interlaminar positions. In the recently investigated structure of anhydrous potassium nickelate[28] the ratio of filled to vacant potassium sites is about 1:4. The potassium atoms adopt an ordered arrangement giving rise to superlattice reflections. If the temperature is high enough, NiO is formed and this would necessitate losing one layer of oxygen atoms for every $NiO_x(OH)_{2-x}$ layer, and a rearrangement of the stacking order. However, it would not involve much change in the overall framework, since the body diagonal of the NiO cubic cell is equal to $^1/_3$ of the hexagonal triple cell c axis of the higher nickel oxide. Furthermore, the Ni···Ni distance is the same in NiO and these higher nickel oxides. The close relationship between the structures of nickel hydroxide, higher nickel oxides, and the alkali nickelates explains their ready interconvertibility, despite their extreme insolubility, the nonexistence of a standard potential for the nickel oxide electrode, and the confusing similarity in diffraction patterns.

Summary

Nickel hydroxide is a double layer lattice structure. In certain modes of preparation, it is capable of incorporating water molecules between its layers of nickel–oxygen polyhedra. Usually only a fraction of the total number of layers separate to admit water, which then binds the crystallites tightly together at a fixed distance but with no spacial relationship in their own plane. By forming the hydroxide relatively slowly by an electrochemical precipitation method, nearly all the layers can be made to separate and admit water. Because the parallel layers are positioned randomly with respect to each other except for a fixed interlayer spacing, the structure is referred to as a random layer lattice structure. Scattering of X-rays from this type of lattice gives rise to certain special diffraction effects which necessitate corrections to be applied for the derivation of cell parameters. This has been overlooked by previous authors who have thereby concluded wrongly that lattice contractions occur on hydration.

Nickel hydroxide can be oxidized within its usual brucite-type structure by simple abstraction of hydrogen atoms. At high rates of discharge of a cell with a nickel oxide electrode, or after a large number of cycles, another phase is formed. This γ phase is closely related to the alkali nickelates. When potassium is involved, the quantity of potassium incorporated is variable since it can be replaced easily by water molecules. The potassium atoms are capable of holding the nickel oxygen polyhedra layers in a definite fixed relationship to one another.

Oxidized material which was hydrothermally recrystallized or came from aged battery electrodes gave different patterns from those obtained by chemical precipitation in the oxidized state or by electrochemical oxidation. There is evidence from the electron diffraction photographs that there exist subtle variants of the basic γ structure. It is unfortunate that the times required for equilibrium to be established during hydrothermal reaction are so long. If conditions could be established to give homogeneous products, a variety of new types of ordering might be established.

Acknowledgments. It is a pleasure to acknowledge the cooperation of Messrs. R. D. Heidenreich, R. A. Laudise, E. D. Kolb, and P. H. Schmidt in making available the equipment used in this work. We particularly wish to thank R. Sard for his assistance in the electron microscopy work. Thanks are also due to R. L. Beauchamp who supplied the cycle aged nickel hydroxide.

(28) P. N. Bitiutskii and V. I. Khitrova, *Krystallografiya*, 13, 53 (1968).

Dielectric Relaxation of 1-Butanol and 1-Decanol in Several Solvents

by J. Crossley

Department of Chemistry, Lakehead University, Thunder Bay, Ontario, Canada *(Received December 2, 1970)*

Publication costs assisted by The National Research Council of Canada

The dielectric absorption of 1-butanol and 1-decanol each at several concentrations in cyclohexane and mesitylene, and of 1-decanol in *p*-xylene, has been measured at nine microwave frequencies at 25°. Cole–Cole plots for these systems are unsymmetrical, and the data have been analyzed for two relaxation times both of which are sensitive to the nature of the solvent and solute and their concentration. The relaxation times are attributed to molecular and intramolecular relaxation processes, and their magnitude and weight factor are dependent upon the relative importance of solute–solute and solute–solvent interactions. The apparent dipole moments, which are greatest in the aromatic solvents but increase much more markedly with increased alcohol concentration in cyclohexane, are significantly less than the vapor phase and pure liquid values.

Introduction

Intermolecular hydrogen bonding in monohydric aliphatic alcohols and their solutions has been examined by all of the usual physical methods.[1,2] However, the nature and concentration of the various hydrogen-bonded species, which may include monomers and a variety of linear and cyclic multimers, is by no means established. Dielectric absorption measurements have been extensively applied to the problem, and the frequency and temperature dependence of the absorption are reasonably well established for pure liquids.[3,4] Much less dielectric work has been reported for alcohols, or indeed any aliphatic compounds, in solution. In dilute solution the dielectric absorption of aliphatic alcohols[5] appears to be similar to that for nonhydrogen-bonded aliphatic compounds which have a rotatable polar group.[6] Increased alcohol concentration has a considerable effect on the magnitude of the relaxation times and their relative contributions. The low-frequency process, which dominates the absorption of the pure liquids and is notably absent in dilute solution, becomes evident at intermediate concentrations and its emergence corresponds with an increased dipole moment.[7] The latter is readily obtained from dielectric relaxation measurements and is a useful parameter when interpreting relaxation data for hydrogen-bonded systems.

In the study reported here the effect of molecular size and the nature of the solvent are examined by measuring 1-butanol and 1-decanol, over a range of concentration in a variety of solvents, in the microwave region at 25°. These results are compared with those obtained in some similar recent studies on primary and branched-chain aliphatic alcohols in nonpolar solvents.

Experimental Section

Apparatus. The apparatus and procedure used for determining the dielectric constant (ϵ') and dielectric loss (ϵ'') at 1–2.5,[8] 9–35,[9] and 70 GHz[10] have been described previously. Static dielectric constants (ϵ_0) were measured at 2 MHz using a WTW Dipolmeter DMO1.

Evaluation of Data. The ϵ' and ϵ'' values for the solvents were measured along with the solutions and the solution data were corrected accordingly. For all the systems measured Cole–Cole plots[11] were unsymmetrical or had significant distribution factors which indicated contributions from more than one relaxation process. In view of this and previous work,[5] which suggests that in solution the dielectric absorption of alcohols may be characterized by two relaxation times, the absorption data were analyzed for two relaxation times (τ_1 and τ_2) and their weight factors (C_1 and C_2). The analyses were performed with the aid of a computer programmed to calculate the τ_1, τ_2, and C_1 values that gave the best fit to the experimental data for a given value of ϵ_∞ the high-frequency dielectric constant, using the equations[12]

$$\frac{\epsilon''}{\epsilon_0 - \epsilon_\infty} = \frac{C_1\omega\tau_1}{1 + (\omega\tau_1)^2} + \frac{C_2\omega\tau_2}{1 + (\omega\tau_2)^2} \qquad (1)$$

(1) D. Hadzi, "Hydrogen Bonding," Pergamon Press, New York, N. Y., 1959.

(2) G. C. Pimentel and A. L. McClellan, "The Hydrogen Bond," W. H. Freeman, San Francisco, Calif., 1960.

(3) S. K. Garg and C. P. Smyth, *J. Phys. Chem.*, **69**, 1294 (1964).

(4) W. Dannhauser and A. F. Flueckinger, *Phys. Chem. Liquids*, **2**, 37 (1970).

(5) G. P. Johari and C. P. Smyth, *J. Amer. Chem. Soc.*, **91**, 6215 (1969).

(6) J. Crossley, G. P. Johari, and C. P. Smyth, *ibid.*, **91**, 5197 (1969).

(7) J. Crossley, L. Glasser, and C. P. Smyth, *J. Chem. Phys.*, **52**, 6203 (1970).

(8) S. E. Keefe and E. H. Grant, *Rev. Sci. Instrum.*, **39**, 800 (1968).

(9) W. F. Hassell, M. D. Magee, S. W. Tucker, and S. Walker, *Tetrahedron*, **20**, 2137 (1964).

(10) S. K. Garg, H. Kilp, and C. P. Smyth, *J. Chem. Phys.*, **43**, 2341 (1965).

(11) K. S. Cole and R. H. Cole, *ibid.*, **9**, 341 (1941).

(12) A. Budo, *Phys. Z.*, **39**, 706 (1938).

Table II: Relaxation Times (τ_1, τ_2), Weight Factors (C_1), Static Dielectric Constants (ϵ_0), High-Frequency Dielectric Constants (ϵ_∞), and Dipole Moments (μ) for 1-Butanol and 1-Decanol at Various Mole Fractions (f_2) in Several Solvents at 25°. The Relaxation Times Are in Picoseconds and Dipole Moments in Debyes

Solute	Solvent	f_2	τ_1	τ_2	C_1	ϵ_∞	μ	ϵ_0
1-Butanol	Cyclohexane	0.05916	68	4.7	0.38	2.055	1.05	2.1234
		0.09264	75	3.9	0.46	2.064	1.16	2.1979
		0.1220	123	5.6	0.52	2.083	1.22	2.2828
		0.1508	150	5.9	0.58	2.095	1.32	2.3887
		0.1918	218	6.8	0.68	2.115	1.45	2.5878
	Mesitylene	0.04193	46	6.7	0.25	2.293	1.48	2.3775
		0.08813	60	8.0	0.35	2.322	1.45	2.4965
		0.1232	83	8.4	0.40	2.340	1.46	2.6012
1-Decanol	Cyclohexane	0.06010	73	8.8	0.40	2.060	1.03	2.1231
		0.08585	87	8.1	0.44	2.068	1.09	2.1685
		0.1187	112	9.5	0.47	2.086	1.11	2.2307
		0.1475	117	8.8	0.52	2.105	1.15	2.2920
		0.1839	153	11.3	0.53	2.120	1.20	2.3732
	p-Xylene	0.06160	43	7.9	0.37	2.286	1.46	2.4165
		0.09142	70	9.4	0.34	2.294	1.44	2.4831
		0.1266	92	10.1	0.39	2.295	1.46	2.5617
	Mesitylene	0.05645	58	10.6	0.28	2.290	1.47	2.3996
		0.08480	64	11.2	0.34	2.304	1.41	2.4547
		0.1191	84	11.4	0.39	2.304	1.44	2.5222

$$\frac{\epsilon - \epsilon_\infty}{\epsilon_0 - \epsilon_\infty} = \frac{C_1}{1 + (\omega\tau_1)^2} \frac{C_2}{1 + (\omega\tau_2)^2} \quad (2)$$

$$C_1 + C_2 = 1 \quad (3)$$

The computer calculations were repeated with several ϵ_∞ values until the best fit was obtained. The errors involved in the experimental and analytical procedures have been assessed.[13]

Apparent dipole moments were calculated from the equation

$$\mu^2 = \frac{9kT}{4\pi N} \cdot \frac{(\epsilon_0 - \epsilon_\infty)(2\epsilon_0 + \epsilon_\infty)}{\epsilon_0(\epsilon_\infty + 2)^2} \quad (4)$$

in which kT is the thermal energy and N is the number of solute molecules per milliliter of solution.

Materials. The alcohols were dried over calcium hydride and fractionally distilled using a spinning-band column. The solvents were dried over and distilled from sodium.

Results

The experimental data corrected for solvent absorption are given in Table I.[14] Cole–Cole plots drawn through the experimental points for 1-butanol and 1-decanol at 0.12 mol fraction in cyclohexane, mesitylene, and *p*-xylene are shown in Figure 1. Points calculated for the same frequencies, using the relaxation data given in Table II, are also shown and the agreement is within the error for the experimental data. Table II lists the measured values of ϵ_0, the τ_1, τ_2, C_1, and ϵ_∞ values obtained from the analyses, and the dipole moments calculated using eq 4.

Discussion

The Cole–Cole plots shown in Figure 1 are all unsymmetrical and, especially for 1-butanol, show evidence of two dispersion regions. Analyses for two relaxation times using eq 1–3 would seem to be valid in view of the good agreement between the measured and calculated points. The analyses given in Table II are self-consistent for all the solutions. For each alcohol in each solvent both relaxation times lengthen and the C_1 values show a small increase with increased alcohol concentration. Because of the smaller dipole moments, and thus smaller loss values, it was possible to measure the alcohols at much higher concentrations in cyclohexane than in the aromatic solvents. Table III gives previous relaxation data obtained for these alcohols in dilute solution,[5,7,15] and in general these results compare well with those given in Table II.

For the alcohols in dilute solution the τ_1 and τ_2 values have been interpreted[5] in terms of molecular and –OH group rotation, respectively. This seems plausible since in reasonably dilute solution, where intermolecular association is minimized, τ_1 increases with increased molecular size and τ_2, which is relatively independent of molecular size, is very similar to the relaxation times reported for –OH group rotation in phenols. In addi-

(13) M. D. Magee and S. Walker, *Trans. Faraday Soc.*, **62**, 3093 (1966).

(14) Table I will appear immediately following this article in the microfilm edition of this volume of the journal. Single copies may be obtained from the Reprint Department, ACS Publications, 1155 Sixteenth St., N. W., Washington, D. C. 20036. Remit $3.00 for photocopy or $2.00 for microfilm.

(15) J. Crossley, *Can. J. Chem.*, **49**, 712 (1971).

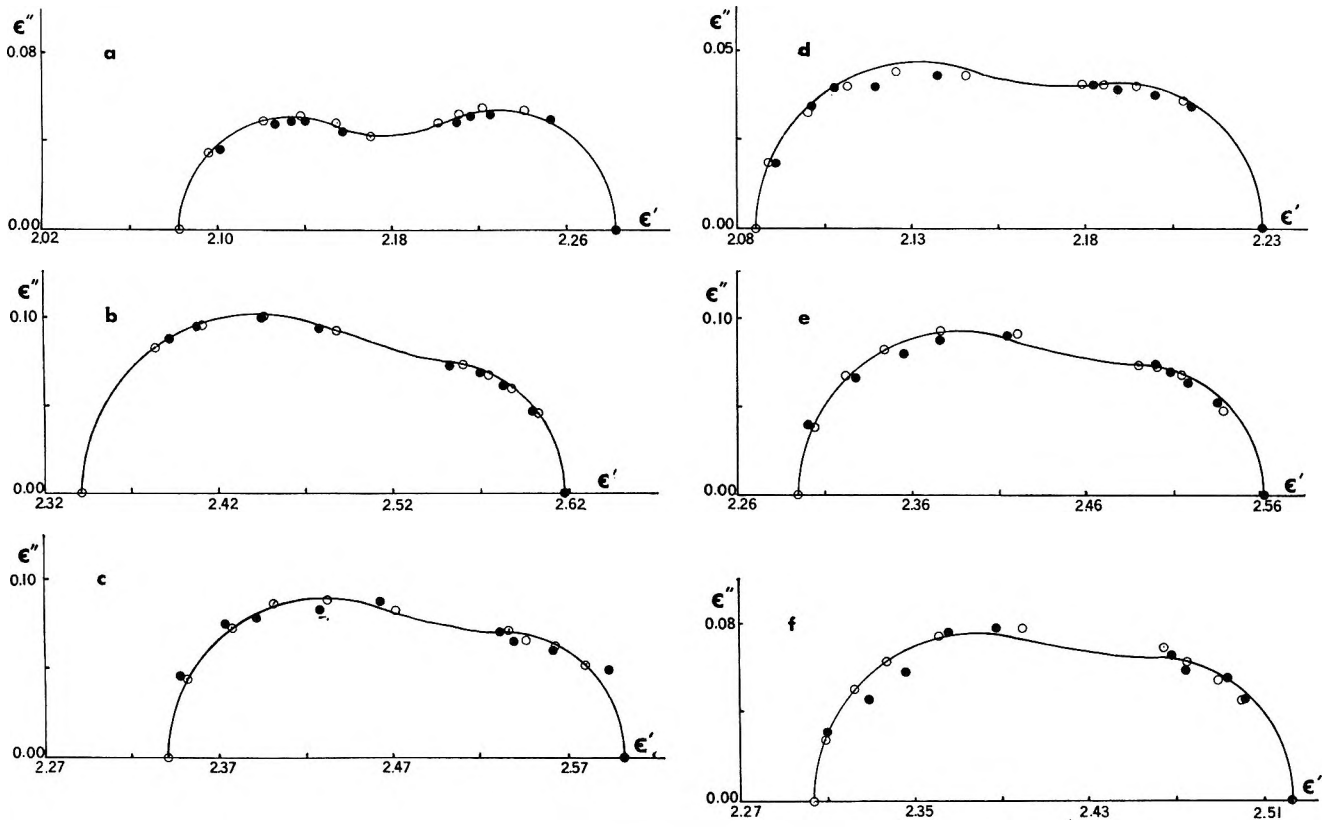

Figure 1. Cole–Cole plots for 1-butanol in (a) cyclohexane, (b) *p*-xylene,[14] and (c) mesitylene and for 1-decanol in (d) cyclohexane, (e) *p*-xylene, and (f) mesitylene at 25°. The experimental and calculated points are represented by filled and open circles, respectively. The alcohol mole fraction is about 0.12 for all the solutions.

Table III: Some Previously Reported Relaxation Data for 1-Butanol and 1-Decanol at 25°.[5,7,15] (The symbols have the same meaning as in Table II)

Solute	Solvent	f_2	τ_1	τ_2	C_1	μ
1-Butanol	*n*-Heptane	0.039	31	1.5	0.19	1.23
		0.060	44	2.5	0.35	1.12
		0.092	69	2.8	0.37	1.18
	Benzene	0.0235	19	2.9	0.23	1.46
		0.0524	22	2.9	0.23	1.60
	p-Xylene	0.04205	22	3.7	0.36	1.49
		0.06094	35	5.6	0.32	1.42
		0.09152	55	6.8	0.33	1.45
		0.1193	66	8.2	0.38	1.46
1-Decanol	*n*-Heptane	0.037	61	2.9	0.17	1.22
		0.056	95	4.0	0.23	1.15
		0.090	72	4.1	0.36	1.17
	Benzene	0.0254	35	5.0	0.29	1.50
		0.0423	33	5.2	0.35	1.48

tion the dielectric absorption for alcohols in dilute solution is remarkably similar to that for some non-hydrogen-bonded aliphatic straight-chain compounds; *n*-octylaldehyde, *n*-octylamine, and *n*-dodecyl methyl ether, also in dilute solution.[6] However, the dielectric absorption of *n*-alkyl bromides, ketones, and certain ethers do not show a separation into two dispersion regions and their data fit a Cole–Cole distribution.[6] For liquid *n*-alkyl bromides the mean relaxation time and Cole–Cole distribution parameter increase with increased molecular size.[16] This behavior has been interpreted in terms of a distribution of relaxation times, due to the rotation of different molecular segments, the extreme values corresponding to $-CH_2Br$ and molecular end-over-end rotation. It seems that for straight-chain compounds with a rotatable polar end group the dielectric absorption will be dependent upon the relative ease of rotation of the polar group about its C–X bond and rotation about the skeletal C–C bonds. If rotation of the polar group involves a lower potential barrier than rotation about the C–C bonds, then dielectric absorption, by rotation about the long axis through the carbon backbone, would be dominated by the rotation of the polar end group. For molecules in which polar group rotation occurs about a C–C bond segmental rotations, and a distribution of relaxation times, are likely. Dipole reorientation by rotation about the other two axes, molecular relaxation, is independent of segmental rotations. These modes of relaxation would be the longest of a range of relaxation times for molecules in which the polar end group rotates about a C–C bond and a distribution of relaxation times would be observed. For those molecules in

(16) K. Higasi, K. Bergmann, and C. P. Smyth. *J. Phys. Chem.*, **64**, 880 (1960).

which the polar group rotates about a bond other than a C–C bond, *e.g.*, C–O for alcohols, the data may separate into two absorption regions, due to molecular and end group rotation. However, it seems unlikely that there should be no contribution from segmental rotation in the latter cases and the τ_2 values in Tables II and III probably contain some contributions from CH_2OH or larger segments. It may be pointed out that, even for measurements at nine frequencies, analyses into two relaxation times probably at best only represent a semiquantitative picture for these systems.

In dilute solution the τ_1 process arises almost entirely from the rotation of alcohol monomers.[5] As the alcohol concentration is increased, the relaxation time τ_1 lengthens. The effect is greater in cyclohexane than in the aromatic solvents and is also greater for 1-butanol than 1-decanol. The lengthening is undoubtably due to solute–solute interaction which will be stronger for 1-butanol than 1-decanol and stronger in cyclohexane than in aromatic solvents due to the competition from solute–solvent interactions. The latter interactions are obviously weaker than solute–solute interactions since at a given concentration the relaxation times are longest in cyclohexane where solute–solvent interactions are a minimum. For the more concentrated cyclohexane solutions a good portion of the absorption is not covered by the experimental points. However, previous data for normal alcohols show the emergence of an additional low-frequency absorption at alcohol mole fractions above 0.15.[7] There is little doubt that this process, which is almost the entire absorption of pure liquid alcohols[3] and is intimately connected with multimer formation,[7] contributes to the absorption below 0.15 mol fraction, where its contribution is insufficient for an observable separation, since alcohol multimers exist even at the lowest concentrations used in this study.[17,18] Thus the τ_1 values in Table II are probably not discrete relaxation times but contain contributions from monomers and various polar multimers. The rate of formation of multimers will be greatest in cyclohexane. In the aromatic solvents the competing solute–solvent interactions are important and the solute molecules collide with each other less frequently since they tend to "stick" with the solvent. Consequently the rate of multimer formation is somewhat slower, and the contribution from the long relaxation time is less than in the aliphatic solvents. The extreme case of solute–solvent interaction is for alcohols in *p*-dioxane where a distribution of relaxation times about a short mean value is observed.[5] In this case an alcohol–dioxane complex is formed, and alcohol–alcohol multimer formation occurs at much higher alcohol concentrations than in the weaker electron donor solvents.[19]

For dilute solutions of alcohols in benzene[5] the short relaxation time τ_2 is independent of concentration and only lengthens slightly with increased molecular size, and is of the same magnitude as the –OH group relaxation time in phenols.[20,21] The τ_2 values in Table II are of the order anticipated for the rotation of an hydroxyl group about its C–O bond, but they lengthen with increased alcohol concentration in each solvent. In view of the limited accuracy of these values no significance will be given to the solvent dependency. However, the τ_2 values for the most concentrated solutions (Table II) are appreciably larger than those obtained for more dilute solutions (Table III). The –OH relaxation time in cholesterol has been shown to lengthen with increased solvent electron donor capacity.[22] This is understandable since a hydrogen-bonded (to solute or solvent) OH group will require more energy to rotate than a nonbonded group. Thus a range of hydroxyl group relaxation times is possible in any of the systems under investigation and the analyzed τ_2 values probably are a composite of relaxation times for free and hindered (by solute or solvent) hydroxyl groups.

In view of the necessarily rather vague interpretation of τ_1 and τ_2 specific discussion for the C values would be unacceptable. However, a qualitative picture of the relative importance of molecular (C_1) and intramolecular (C_2) relaxations is not unreasonable. For 1-butanol and 1-decanol C_1 is almost independent of alcohol concentration in dilute solution but increases with concentration in the stronger solutions. In addition, C_1 increases with increased tendency to form chainlike complexes for the four butanols,[15] *i.e.*, 1-butanol > isobutyl alcohol > *sec*-butyl alcohol > *tert*-butyl alcohol. Increased alcohol concentration will favor the formation of higher multimers and thereby reduce the number of rotatable hydroxyl groups and the contribution (C_2) from hydroxyl group rotation. Thus the increased contribution from τ_1 with increasing alcohol concentration is consistent with the self-association of alcohols.

For all systems the dipole moments are less than their vapor phase and pure liquid values, 1.7 and 2.7 D, respectively,[23] which suggests the presence of weakly polar multimers in the solutions. The large dipole moments for the pure liquid straight-chain alcohols probably arise from association into higher multimers, either linear chains[24] or cyclic tetramers[18,25] and pentamers.[19] In dilute solution self-association leads to the formation of weakly polar dimers and trimers. At higher concentrations the strongly polar larger multi-

(17) H. C. Van Ness, J. Van Winkle, H. H. Richtol, and H. B. Hollinger, *J. Phys. Chem.*, **71**, 1483 (1967).

(18) A. A. Fletcher and C. A. Heller, *ibid.*, **71**, 3742 (1967).

(19) J. Malecki, *J. Chem. Phys.*, **43**, 1351 (1965).

(20) M. Davies and R. J. Meakins, *ibid.*, **26**, 1584 (1957).

(21) F. K. Fong and C. P. Smyth, *J. Amer. Chem. Soc.*, **85**, 1565 (1963).

(22) M. D. Magee and S. Walker, *J. Phys. Chem.*, **74**, 2378 (1970).

(23) A. L. McClellan, "Tables of Experimental Dipole Moments," W. H. Freeman, San Francisco, Calif., 1963.

(24) W. Dannhauser, *J. Chem. Phys.*, **48**, 1911, 1918 (1968).

(25) P. Bordewijk, F. Gransch, and C. J. F. Bottcher, *J. Phys. Chem.*, **73**, 3255 (1969).

mers are formed. Thus the fact that the dipole moments in dilute cyclohexane solution are smaller than those in aromatic solvents, and show a marked increase with increased alcohol concentration, is consistent with a greater degree of alcohol self-association in cyclohexane. Solute–solvent interactions are minimal in the latter inert solvent, and alcohol self-association is the only important interaction. In the aromatic solvents solute–solvent interactions are important and have a disassociating effect on the alcohol multimers.[19] Somewhat larger dipole moments are to be expected in the aromatic solvents because of the solute–solvent interactions[26] which are absent in cyclohexane solution.

Both relaxation times appear to be a composite of several processes and it is remarkable that consistent analyses in terms of two apparently Debye-like absorptions have been possible. The situation is somewhat analogous to pure liquid water[27] and alcohols[3] both of which have a complex molecular structure but show a single Debye-type relaxation.

(26) J. Crossley and C. P. Smyth, *J. Amer. Chem. Soc.*, **91**, 2482 (1969).

(27) M. Davies, "Some Electrical and Optical Aspects of Molecular Behaviour," Pergamon Press, London, 1965.

Excimer Model for Fluorene and Dibenzofuran[1]

by Fredrick L. Minn,* Jack P. Pinion, and Nicolae Filipescu

Department of Chemistry, The George Washington University, Washington, D. C. 20006 *(Received September 21, 1970)*

Publication costs assisted by the U. S. Atomic Energy Commission

SCF–CI–MO calculations were carried out for excimers of naphthalene, fluorene, and dibenzofuran in a model which allowed relative rotational, translational, and shearing motions of the two parallel-stacked monomer molecules. Within the approximations only changes in the distance between the planes of the monomers were found to affect the predicted energy levels. An interplanar distance of ~3.5 Å was found to give agreement with experimental excimer fluorescence wavelengths. The calculated oscillator strengths for excimer emission were all small ($f < 10^{-2}$) and predicted polarizations were parallel to the in-plane long axis of monomer.

The original attempts to correlate experimentally observed red-shifted excimer emission with predictions from an acceptable theoretical model were based on exciton splitting and charge-resonance concepts.[2,3] More recent calculations involving configuration interaction between molecular-exciton and charge-resonance states gave substantially improved results.[4–6] Most previous theoretical work on excimers has been done on naphthalene.[5,7–10] Independent of Horrocks and Brown,[11] we recently observed pronounced excimer emission from dibenzofuran and substituted fluorenes.[12] Since these have lower symmetry than naphthalene or pyrene and since dibenzofuran is heteroaromatic, we were interested in testing a theoretical model on systems described by two such molecules. Here we report the results of a "supermolecule" modification to a semiempirical molecular orbital (MO) method, first suggested by Chandra and Lim,[13] applied to excimer aggregates of naphthalene, fluorene, and dibenzofuran.

Excimer Model

Since the crystalline emission of pyrene does not differ from that of its solvated excimers,[14] Barnes and Birks[15] suggested that the excimer configuration comprises two adjacent molecules in parallel planes, as in the crystalline lattice. Consequently, our model places

(1) Taken in part from the Ph.D. Thesis of J. P. P. at The George Washington University, 1970.

(2) Th. Förster, *Pure Appl. Chem.*, **4**, 121 (1962).

(3) J. Ferguson, *J. Chem. Phys.*, **28**, 765 (1958).

(4) E. Konijenberg, Dissertation, Freie Universität Amsterdam, 1963.

(5) T. Azumi and H. Azumi, *Bull. Chem. Soc. Jap.*, **39**, 1829, 2317 (1966); **40**, 279 (1967).

(6) J. N. Murrell and J. Tanaka, *Mol. Phys.*, **7**, 363 (1964).

(7) T. Azumi, A. T. Armstrong, and S. P. McGlynn, *J. Chem. Phys.*, **41**, 3839 (1964).

(8) S. P. McGlynn, A. T. Armstrong, and T. Azumi in "Modern Quantum Chemistry. Part III," O. Sinanoglu, Ed., Academic Press, New York, N. Y., 1965, p 203.

(9) B. N. Srinivasan, J. V. Russel, and S. P. McGlynn, *J. Chem. Phys.*, **48**, 1931 (1968).

(10) Th. Förster, *Angew. Chem., Int. Ed. Engl.*, **8**, 333 (1969).

(11) D. L. Horrocks and W. G. Brown, *Chem. Phys. Lett.*, **5**, 117 (1970).

(12) J. P. Pinion, Ph.D. Thesis, The George Washington University, 1970.

(13) A. K. Chandra and E. C. Lim, *J. Chem. Phys.*, **48**, 2589 (1968).

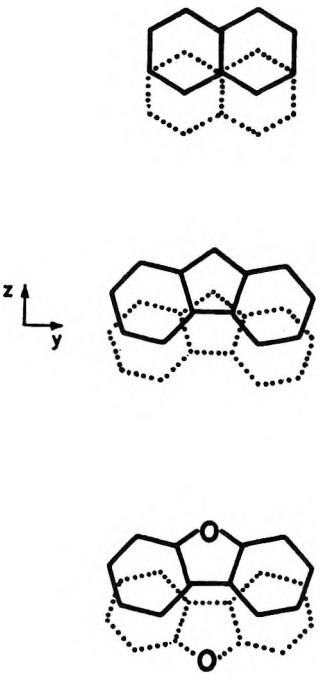

Figure 1. Assumed geometry of excimers.

the two molecules atop one another but displaced from perfect superposition, as shown in Figure 1.

Intramolecular bond distances and angles were taken from X-ray crystallographic data for naphthalene[16,17] and fluorene;[18] those of dibenzofuran were estimated by analogy with fluorene.[19]

The two parallel molecules were taken to be displaced along the short axis by about one carbon–carbon bond length, an arrangement suggested by the excimer-emitting pyrene crystal where such a geometry exists. This configuration both minimizes intermolecular π-electronic repulsion and maintains a high degree of symmetry. For dibenzofuran, the initial relative orientation of the two molecules was chosen such that their electric dipole moments were opposed. This geometry not only reduces the oxygen lone-pair repulsions but also staggers the aromatic $2p\pi$ orbitals. The effects of changes in the distance between the two photoassociated molecules and of in-plane translations and rotations on the relative disposition of energy levels in the excimer and on predicted polarization of the transition dipole moments were examined.

Method of Calculation

Energy-level diagrams for monomer and excimer, together with polarizations and oscillator strengths, were calculated by a semiempirical MO–SCF–CI procedure. For the excited dimers the π electrons of the two-component chromophores were treated as parts of a single extended system delocalized over both component molecules. The technique includes effects of local excitations and of electron transfer in a natural way. Unlike the method outlined by Chandra and Lim,[10] ours uses self-consistent-field orbitals instead of Hückel MO's as basis. We expected to obtain reliable results on fluorene and dibenzofuran with SCF–MO's without having to include a large number of interacting configurations, since SCF–MO's give the ground-state energy accurate to second order with respect to one-electron-excited configurations. Empirically in this laboratory and theoretically in others,[20] addition of more than the few lowest-energy configurations brings about very small changes in the smallest excitation energy; while the higher excited states could probably be improved by use of more extended CI, the concern of this work is with the excimer (lowest level) emission. In addition, SCF orbitals, which are better approximations to actual wave functions than are HMO's, are known to give more accurate results when used for evaluating spectral properties of heteroaromatic or nonalternant systems.[21,22] For the alternant, highly symmetrical naphthalene excimer, our results were close to those of Chandra and Lim.

The usual σ–π separation and neglect of differential overlap were assumed. Interactions between the two π systems were introduced by the electrostatic repulsions between all pairs of contributing atoms and by partial bonding between sites of the two molecules near one another. Specifically, the electron-repulsion integrals γ were evaluated by the Mataga–Nishimoto formula[23] and the nonzero bond resonance integrals β by the distance-dependent equation, $\beta = 9.811 \exp(-1.032r)$, whose form was suggested by Pariser and Parr;[24] this equation was constructed to give literature values for benzene and ethylene at their experimental C–C distances.[25,26] Inter-ring β's were further adjusted to allow for the σ interaction of the two p orbitals. Thus, denoting components of the unit vector between the two cores as x, y, and z, we have

$$\beta = x^2\beta_{\sigma\sigma} + (y^2 + z^2)\beta_{\pi\pi}$$

$$\gamma = x^4\gamma_{\sigma\sigma\sigma\sigma} + (y^2 + z^2)^2\gamma_{\pi\pi\pi\pi} + x^2(y^2 + z^2)(2\gamma_{\sigma\sigma\pi\pi} + 4\gamma_{\sigma\pi\sigma\pi})$$

(14) J. B. Birks, A. A. Kazzaz, and J. A. King, *Proc. Roy. Soc., Ser. A*, **291**, 568 (1966).

(15) R. L. Barnes and J. B. Birks, *ibid.*, **291**, 570 (1966).

(16) A. I. Kitaigorodskii, "Organic Chemical Crystallography," Consultants Bureau, New York, N. Y., 1955.

(17) J. Trotter, *Acta Crystallogr.*, **16**, 605 (1963).

(18) D. M. Burns and J. Iball, *Proc. Roy. Soc., Ser. A*, **227**, 200 (1955).

(19) The results of the calculation are insensitive to slight variations in the atomic coordinates.

(20) For example, E. Weltin, J. P. Weber, and E. Heilbronner, *Theoret. Chim. Acta*, **2**, 114 (1964).

(21) J. Fabian, A. Mehlhorn, and R. Zahradnik, *J. Phys. Chem.*, **72**, 3975 (1968).

(22) M. Tichy and R. Zahradnik, *ibid.*, **73**, 534 (1969), and references therein.

(23) M. Mataga and K. Nishimoto, *Z. Phys. Chem.*, **13**, 140 (1957).

(24) R. Pariser and R. G. Parr, *J. Chem. Phys.*, **21**, 767 (1953).

(25) M. Klessinger, *Theoret. Chim. Acta*, **5**, 236, 251 (1956).

(26) J. E. Bloor, B. R. Gilson, and N. Brearley, *ibid.*, **8**, 35 (1967).

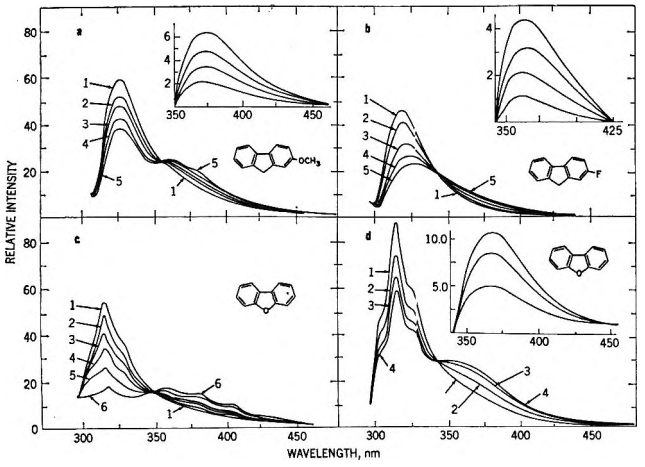

Figure 2. Total emission spectra (uncorrected). a, 2-methoxyfluorene in dioxane at 22° excited at 300 nm; 1–5, 0.05, 0.10, 0.20, 0.32, and 0.43 *M*. b, 2-fluorofluorene in dioxane at 22° excited at 293 nm; 1–5, 0.10, 0.21, 0.60, 0.81, and 1.16 *M*. c, dibenzofuran in dioxane at 22° excited at 278 nm; 1–6, 0.16, 0.21, 0.24, 0.60, 1.08, and 1.64 *M*. d, dibenzofuran in methylcyclohexane, 1.05 *M*, at different temperatures; 1–4, 31, 11, 7, and 0°, respectively. Inserts represent the excimer component of emission obtained by subtraction.

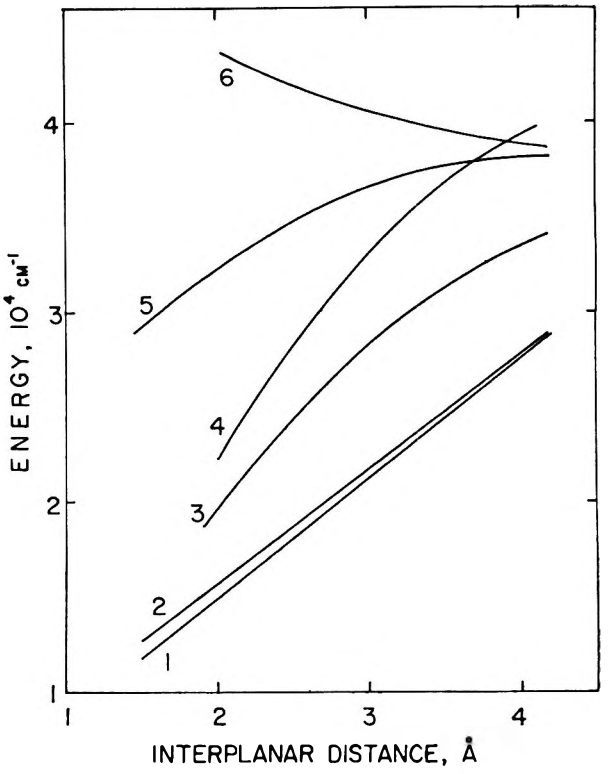

Figure 3. Variation in configuration energy with interplanar separation distance for the naphthalene excimer: 1, $\psi_{9,12} - \psi_{10,11}$; 2, $\psi_{9,11} - \psi_{10,12}$; 3, $\psi_{8,11} + \psi_{10,13}$; 4, $\psi_{8,11} - \psi_{10,13}$; 5, $\psi_{9,11} + \psi_{10,12}$; 6, $\psi_{9,12} + \psi_{10,11}$. Energies are relative to the dimer ground state.

where the subscripts designate components obtained from orbitals that point directly toward one another (σ) or are parallel to each other and perpendicular to the line of centers (π). Since numerical integration of the carbon β's gives values which differ by only a few per cent,[27] we took $\beta_{\sigma\sigma} = \beta_{\pi\pi}$; the various directional combinations of the γ's ($\gamma_{\sigma\sigma\sigma\sigma}$, $\gamma_{\pi\pi\pi\pi}$, etc.) were also taken to be equal. Carbon valence-state ionization potentials and one-center repulsion integrals for naphthalene were taken from the literature;[24] the corresponding values for fluorene and dibenzofuran were taken to be the same as those for phenanthrene.[25] For the ether–oxygen ionization potential and one-center integrals we used 33.9 and 16.2 eV, respectively.[28] The SCF ground-state wave functions were allowed to interact with the lowest six excited-state configurations. A modification to Bloor and Gilson's closed-shell SCF–CI program[29] was used on an IBM 360/50 computer.

The two parallel ring systems were displaced relative to one another by (1) variation of the interplanar distance, (2) rotation of one molecule in plane about its center, or (3) translation of one molecule along its short axis in a motion resembling shearing. The expected excimer emission energies, oscillator strengths, and polarizations were thus calculated.

Results and Discussion

The monomer and excimer emissions for 2-methoxyfluorene, 2-fluorofluorene, and dibenzofuran, as determined from variable concentration and temperature spectra, are shown in Figure 2. The inserts represent the excimer emission alone, obtained by subtraction of a dilute normalized emission of the monomer. These spectra are included mainly to exhibit the excimer emission of these compounds and to locate the wavelengths at which the two component fluorescences are found.[30–33]

Some general remarks can be made regarding the influence of relative displacements of monomer molecules on predicted excimer emission energy. The calculations indicate that both the in-plane rotation of one molecule and translation along its short axis (shearing) have only a very limited influence on the dimer energy levels. Thus, z displacements from 1.3 to 3 Å in any of the compounds tested caused a maximum shift of 2500 cm^{-1} in calculated excimer levels. In-plane rota-

(27) C. C. J. Roothaan, *J. Chem. Phys.*, **19**, 1445 (1951).

(28) M. J. S. Dewar, "The Molecular Orbital Theory of Organic Chemistry," McGraw-Hill, New York, N. Y., 1969, p 380.

(29) Quantum Chemistry Program Exchange, Indiana University, Program 71.3.

(30) The emission spectra of substituted fluorenes are used instead of that of fluorene because the excimer fluorescence of the former is far more pronounced than that of the unsubstituted molecule, which is not unusual. See, for example, ref 31–33 for a comparison of the excimer emission of naphthalene and methylnaphthalenes.

(31) Th. Förster, *Pure Appl. Chem.*, **7**, 73 (1963).

(32) B. Stevens and T. Dickenson, *J. Chem. Soc.*, 5492 (1963).

(33) J. B. Birks and J. B. Aladekomo, *Spectrochim. Acta*, **20**, 15 (1964).

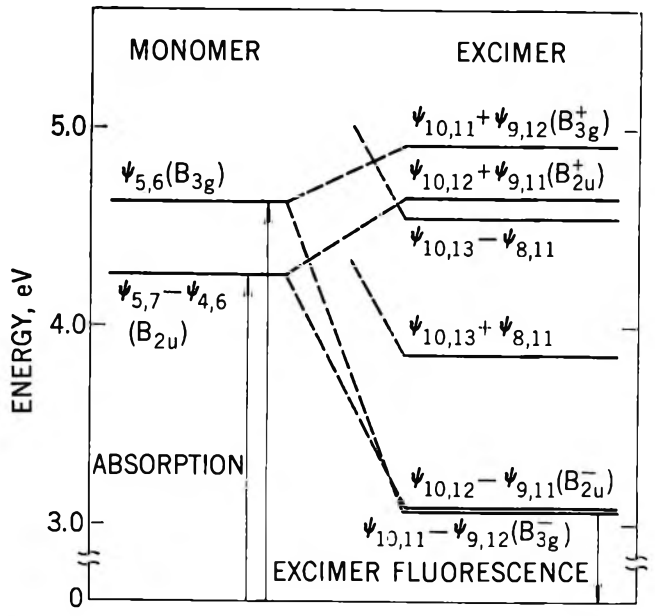

Figure 4. Correlation diagram for the naphthalene monomer–naphthalene excimer energy levels.

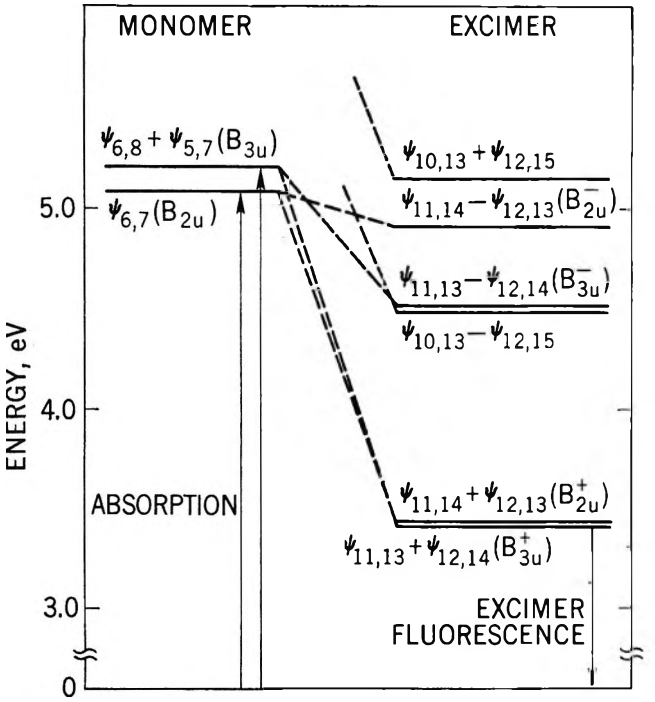

Figure 5. Correlation diagram for the fluorene monomer–fluorene excimer energy levels.

tions of up to ±45° from the staggered relative positions of Figure 1 were found to affect the energies of predicted excited states even less, no more than 800 cm^{-1}. These are principally but not completely artifacts of the calculation. The large inter-ring C–C distances, coupled with the assumptions of equal β's and γ's, give energies which are sensitive to distance but almost invariant with angle. Attempts to correct this insensitivity by altering the quantities $\gamma_{\sigma\sigma\sigma\sigma}$, $\gamma_{\sigma\pi\sigma\pi}$, and

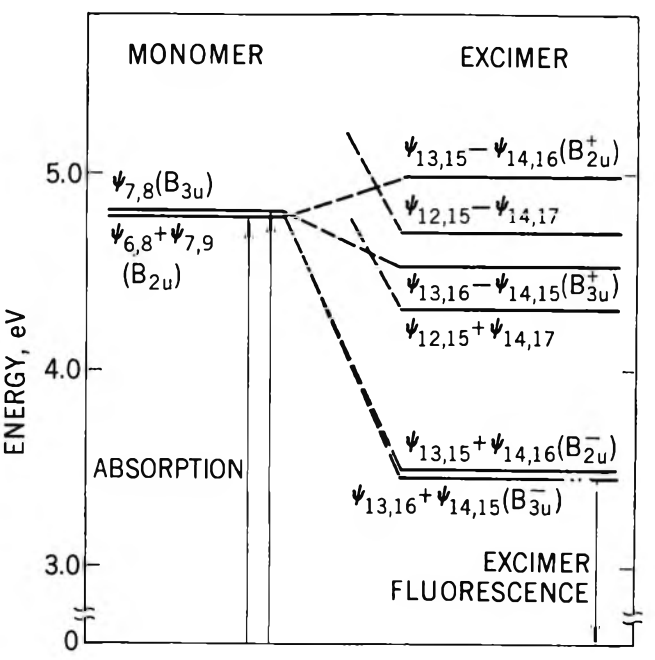

Figure 6. Correlation diagram for the dibenzofuran monomer–dibenzofuran dimer energy levels.

$\gamma_{\sigma\sigma\pi\pi}$ to make their ratio with $\gamma_{\pi\pi\pi\pi}$ roughly the same as the values obtained from carbon 4ζ wave functions[34] led to nonconvergence of the self-consistency iterations or to energies two orders of magnitude too large. We therefore settled on the equal-γ approximation given in the previous section by the following rationale. The value of $\gamma_{\pi\pi\pi\pi}$ is given by a formula depending only on distance and the value of the one-center repulsion integral, but the one-center integrals $\langle 2p_x2p_x|2p_x2p_x\rangle$ and $\langle 2p_z2p_z|2p_z2p_z\rangle$ are equal and hence the empirical formulation of any γ is probably not too different from that of $\gamma_{\pi\pi\pi\pi}$.

In contrast with the shearing and rotation motions, variation of the interplanar separation produces profound alterations in expected energy levels. Again, this was found to be the case for naphthalene, fluorene, and heteroaromatic dibenzofuran. To illustrate the magnitude of this effect, we have plotted in Figure 3 the predicted energy levels of the excimer, including the expected emission energy, as a function of the interring distance for naphthalene. Since curve 1 represents the variation of the lowest excited state, it also represents possible variations of energy for excimer fluorescence to a repulsive portion of the monomer–monomer ground state. From this diagram one can see that the experimentally observed excimer γ_{max} 380 nm corresponds to an intermolecular separation of 3.4 Å. It is interesting that the best correlation for fluorene and for dibenzofuran is found at essentially the same interplanar distance of 3.5 Å. Physically, this is indeed

(34) J. Jortner, S. A. Rice, J. L. Katz, and S.-I. Choi, *J. Chem. Phys.*, **42**, 309 (1965).

sensible, since one would expect similar types of bonding interaction. Figures 4, 5, and 6 are energy level diagrams for monomer and excimer calculated for naphthalene, fluorene, and dibenzofuran, respectively, for the geometry giving best agreement with spectral data. The SCF levels were numbered from the lowest occupied to the highest vacant orbital; CI wave functions correspond to one-electron excitations from the ground state, the first subscript designating the vacated orbital and the second the terminal. In the correlation diagrams the ground states of monomer and excimer were placed at zero energy. Excimer fluorescence was assumed to occur in times short compared to the separation motion of the repulsive ground-state monomers. Although informative, the disposition of the higher excited levels of the excimer cannot easily be verified experimentally. The present theoretical analysis also predicts that the excimer emission should be weak (near-zero oscillator strength) and that it should be polarized parallel to the in-plane long axis of the monomer.

Acknowledgment. This work was supported in part by the U. S. Atomic Energy Commission under Contract AT-(40-1)3797.

Conductance Study of Squaric Acid Aqueous Dissociation

by Lowell M. Schwartz* and Leland O. Howard

Department of Chemistry, University of Massachusetts, Boston, Massachusetts 02116 *(Received January 7, 1971)*

Publication costs borne completely by The Journal of Physical Chemistry

The primary dissociation constant of squaric acid in aqueous solution has been measured conductometrically and found to be $pK_1 \simeq 0.5$ at 25°. The precise value depends on which semiempirical equation is used to predict the dependence of equivalent conductance on concentration. Measuring pK_1 as a function of temperature yields $\Delta H_1°$ of about −1.5 kcal/mol and $\Delta S_1°$ about −7.5 cal/mol deg. These thermodynamic functions, when compared with corresponding values for the aqueous dissociation of weak organic acids, lead to the conclusion that the unusual strength of squaric acid is attributable to a relatively small entropy change accompanying the primary dissociation.

Introduction

1,2-Dihydroxycyclobutenedione, commonly known as "squaric acid" (H_2Sq), is a member of a series of cyclic oxocarbon dibasic acids whose dianions are strongly stabilized by π-electron delocalization.[1] This stability is believed to account for the unusually high acid strengths of some of these acids in aqueous solution. The primary dissociation constant of H_2Sq has been estimated from pH potentiometric measurements variously as $pK_1 = 1.7 \pm 0.3$,[2] 1.2 ± 0.2,[3] and 0.55 ± 0.15[4] at room temperature. The relatively large uncertainties in these values are due to difficulties inherent in the potentiometric method as applied to highly dissociated acids. To obtain accuracy in pK_1 by this technique requires extremely pure reagents and also highly concentrated solutions to ensure a reasonable concentration of undissociated acid. The limited solubility of H_2Sq in water precludes reaching high concentrations and consequently the pK_1 values are uncertain. In this work we seek to avoid some of these difficulties by using conductance measurements to determine pK_1. We were encouraged to attempt this approach by the results of Darken[5] working on oxalic acid which is similar to squaric acid in its aqueous dissociation.

Patton and West[6] have summarized the reported dissociation constants of the oxocarbon acid series and note that whereas Hückel molecular orbital calculations predict that squarate ion (Sq^{2-}) enjoys a greater delocalization energy than croconate ion ($C_5O_5^{2-}$), croconic acid is stronger ($pK_1 = 0.32$)[7] than squaric acid. Our determination of H_2Sq ($pK_1 = 0.55$) was done after Patton and West made their observation and this lower value, if indeed it is more reliable than those previously reported, tends to reduce the degree of discrepancy. Nevertheless, it is well established that dissociation equilibria depend in a major way on solute–solvent in-

(1) R. West and D. L. Powell, *J. Amer. Chem. Soc.*, **85**, 2577 (1963).
(2) D. T. Ireland and H. F. Walton, *J. Phys. Chem.*, **71**, 751 (1967).
(3) D. J. MacDonald, *J. Org. Chem.*, **33**, 4559 (1968).
(4) L. M. Schwartz and L. O. Howard, *J. Phys. Chem.*, **74**, 4374 (1970).
(5) L. S. Darken, *J. Amer. Chem. Soc.*, **63**, 1007 (1941).
(6) E. Patton and R. West, *J. Phys. Chem.*, **74**, 2512 (1970).
(7) B. Carlqvist and D. Dyrssen, *Acta Chem. Scand.*, **16**, 94 (1962).

teractions as well as on the energetics of the dissociating species themselves.[8] It remains to be seen to what extent these interactions are operating here.

Method

Conductance measurements were made on aqueous solutions of squaric acid at various concentrations and at various temperatures. At any given temperature the primary dissociation constant K_1 is calculable from

$$K_1 = \frac{\gamma_\pm^2[H^+][HSq^-]}{\gamma_0[H_2Sq]} = \frac{\gamma_\pm^2\alpha^2C}{\gamma_0(1-\alpha)} \quad (1)$$

where $[H_2Sq]$, $[HSq^-]$, and $[H^+]$ represent the molar concentrations of the undissociated squaric acid, bisquarate ion, and hydrogen ion, respectively, $\gamma_\pm$ is the mean activity coefficient of the singly charged species, and $\gamma_0 = 10^{0.1I}$, the activity coefficient of undissociated acid,[9] I being the ionic strength. C is the stoichiometric acid concentration and α is the fraction of this which has undergone the primary dissociation.

Ignoring for the moment the secondary dissociation, α is in principle given by

$$\alpha = \frac{\Lambda}{\Lambda_\epsilon} \quad (2)$$

where Λ is the measured equivalent conductance at concentration C and Λ_ϵ is the hypothetical equivalent conductance of the same solution but in which the acid is completely dissociated into H^+ and HSq^- ions. We assume that if such a hypothetical solution could be realized, its equivalent conductance would vary with ionic strength in the same manner as other completely dissociated electrolytic solutions. In the range of ionic strengths employed here, *i.e.*, 0.06–0.16 M, this variation must be expressed semiempirically and two alternative relationships were chosen, that of Shedlovsky[10] and used by Darken[5]

$$\Lambda_\epsilon = \Lambda^0 - (B_1\Lambda^0 + B_2)(I)^{1/2} + bI(1 - B_1(I)^{1/2}) \quad (3)$$

and that of Robinson and Stokes[11]

$$\Lambda_\epsilon = \Lambda^0 - \frac{(B_1\Lambda^0 + B_2)(I)^{1/2}}{1 + Ba(I)^{1/2}} \quad (4)$$

In these equations B_1, B_2, and B are tabulated functions of temperature (see, for example, ref 12, Appendix 7.1) and a and b are treated as adjustable parameters. Λ^0 is the equivalent conductance at infinite dilution which, because in the present case it is unknown and unrealizable, we regard as an adjustable parameter also.

Following Darken,[5] the secondary ionization is treated as a correction. Stoichiometrically this ionization adds H^+ and destroys HSq^- to the same extent which it adds Sq^{2-}. The correction to the specific conductance due to this dissociation then is

$$[Sq^{2-}](\lambda_{H^+} + 2\lambda_{Sq^{2-}} - \lambda_{HSq^-}) \equiv [Sq^{2-}]\Lambda_2$$

where λ are the equivalent conductances of the individual ions. The corrected equivalent conductance Λ_{cor} is related to the measured value Λ by

$$\Lambda_{cor} = \Lambda - \frac{[Sq^{2-}]}{C}\left(\frac{\Lambda_2}{\Lambda_\epsilon}\right)\Lambda_\epsilon \quad (5)$$

and this Λ_{cor} replaces Λ in eq 2. The ratio $\Lambda_2/\Lambda_\epsilon$ is $(\lambda_{H^+} + 2\lambda_{Sq^{2-}} - \lambda_{HSq^-})/(\lambda_{H^+} + \lambda_{HSq^-})$ which is nearly unity since λ_{H^+} is numerically the dominant term in both numerator and denominator. Reasonable estimates of the ionic equivalent conductances in this expression lead to the conclusion that the ratio is within 10% of unity. Since the correction term itself in eq 5 is less than 1% of Λ at all concentrations used here, there is little justification for further experiments to refine $\Lambda_2/\Lambda_\epsilon$ and unity is assumed.

For similar reasons there is no need to calculate $[Sq^{2-}]$ accurately. Knowing the secondary dissociation constant[4] K_2, the squarate ion concentration is calculable from

$$K_2 = \frac{\gamma_\pm[H^+]\gamma_=[Sq^{2-}]}{\gamma_\pm[HSq^-]} = \frac{\gamma_=(\alpha + [Sq^{2-}])[Sq^{2-}]}{\alpha - [Sq^{2-}]}$$

where $\gamma_= = \gamma_\pm^4$ is the activity coefficient of Sq^{2-}. With pK_2 about 3.5 and α near unity, the approximation

$$[Sq^{2-}] = \frac{K_2}{\gamma_=} \quad (6)$$

represents a satisfactory estimate.

The activity coefficients of squaric acid ionic species have not been measured and must be estimated semiempirically. We chose to use the Davies[13] equation

$$\log \gamma_\pm = -D\left(\frac{(I)^{1/2}}{1 + (I)^{1/2}} - 0.3I\right) \quad (7)$$

where D is the Debye–Hückel coefficient. It is claimed that this relationship represents $\gamma_\pm$ to within 1.6% for normal-sized ions up to 0.1 M ionic strength. The temperature variation of the activity coefficients is assumed to be included in D.

The calculational procedure must be iterative since α values needed for eq 1 stem from eq 2, which depends on Λ_ϵ, which in turn depends on I and hence α. Also this sequence itself involves the unknown parameter Λ^0. The method we adopted was to write a digital computer program to repeat the calculations for many values of Λ^0 within a specified range and to select that value which yielded the most "constant" equilibrium con-

(8) E. J. King, "Acid-Base Equilibria," Macmillan, New York, N. Y., 1965, Chapter 7.

(9) J. N. Butler, "Ionic Equilibrium," Addison-Wesley Publishing Co., Reading, Mass., 1964.

(10) T. Shedlovsky, *J. Amer. Chem. Soc.*, **54**, 1405 (1932).

(11) R. A. Robinson and R. H. Stokes, *ibid.*, **76**, 1991 (1954).

(12) R. A. Robinson and R. H. Stokes, "Electrolyte Solutions," 2nd ed (revised), Butterworths, London, 1965.

(13) C. W. Davies, "Ion Association," Butterworths, London, 1962.

stant pK_1. The program operates as follows. A separate computer run was required for each temperature. Experimental data consisting of conductance measurements and corresponding C values were given to the program along with pK_2 at the temperature in question from ref 4, values of the parameters in eq 3, 4, and 7, and the limits of the range of Λ^0 that should be tried. For each value of Λ^0 the program calculated for each solution a consistent set of γ, α, Λ_ϵ, and I by (a) initially setting $\alpha = 1$ and $I = C$, (b) calculating Λ_ϵ from the programmed eq 3 or 4, (c) calculating Λ_{cor} from Λ_ϵ according to eq 5, 6, and 7, (d) calculating improved $\alpha = \Lambda_{cor}/\Lambda_\epsilon$, and (e) calculating improved $I = \alpha C + 2[Sq^{2-}]$. For each solution the sequence (b), (c), (d), and (e) was repeated three more times. On the fourth repetition the variables differed from the third improvements by about 0.001% and so a consistent set was assured and K_1 and pK_1 could be calculated from eq 1. The mean of the pK_1 values for the various solutions and the standard deviation from the mean were computed. This entire procedure was done repetitively with Λ^0 incremented by 0.1 mho-cm²/equiv until the preset limit was reached. That value which yielded the smallest standard deviation of pK_1 was selected along with the corresponding mean pK_1.

The calculational procedure was tested with the oxalic acid conductance data reported by Darken.[5] In this test we followed Darken's procedure of using eq 3 with $b = (B_1\Lambda^0 + B_2)$ and found that his 12 high concentration data points yielded $pK_1 = 1.264$ and $\Lambda^0 = 389.9$ mho-cm²/equiv by our calculation as compared to $pK_1 = 1.271$ and $\Lambda^0 = 390$ by his own. This agreement is satisfactory considering the significant differences in the two procedures.

Experimental Section

Squaric acid purchased from Aldrich Chemical Co. was dried under vacuum at 100° and tested for purity by titrating with standardized NaOH. Acid samples whose equivalent weights were within 0.3% of theoretical were chosen and dissolved under N_2 gas in conductivity water measuring 0.7×10^{-6} mho/cm. Conductance measurements were made using a Beckman CEL-BBl dip-type conductance cell fitted into a specially fabricated sealed vessel which, when filled with solution by pipet, ensured that the solution geometry around the electrodes was fixed. The cell resistance was determined using a 1000-Hz signal balanced on a General Radio Type 1608A impedance bridge (accuracy of 0.1% claimed) and null-detected with the help of a General Radio Type 1232A tuned amplifier. Typical signal voltages at the cell electrodes were about 50 mV and conductance measurements were found to be independent of frequency up to 2000 Hz and independent of signal strength up to 2 V at the electrodes.

A particular solution was sealed in the cell compartment and measurements were taken at a series of temperatures beginning at 25°, up to 50°, down to 10°, and back to 25°. The bath temperatures were thermostated by a YSI Model 72 proportioning controller which held to 0.005° between 25 and 35° and to 0.05° outside this range. Thermal equilibrium was monitored by observing the change in cell conductance with time, and steady values were generally achieved within 25 min of changing the temperature controller setpoint.

The experimental procedure and apparatus were tested by measuring conductances of five aqueous solutions of untreated Matheson Coleman and Bell reagent grade oxalic acid between 0.025 and 0.064 M. These measurements yielded $pK_1 = 1.255 \pm 0.001$ and $\Lambda^0 = 386.4$ by the same calculation which yielded $pK_1 = 1.264$ from Darken's oxalic acid data.

After measuring the conductances of a few squaric acid solutions, it became apparent that the results were not varying as a function of concentration with the same precision we had found with the oxalic acid test solutions. We eventually concluded that the problem resulted from slow decomposition of H_2Sq inside the conductance cell compartment. Our custom had been to introduce a solution into the compartment and allow up to 3 days for equilibration of the solution with electrode surfaces before making the measurements. In spite of our precautions to exclude air from the cell, and even though the equilibration was done with the cell disconnected from the signal voltage, we noted a steady decline in the conductance of a particular solution amounting to about one part per thousand per day and continuing over a 2-week period. We suspect that H_2Sq decomposes slowly in contact with the platinized electrodes and have attempted to account for this effect by correcting all conductance values back to an initial time by adding conductance from the time of measurement at a rate of 0.1% per day. This correction increased the precision somewhat but not up to the level we enjoyed with the oxalic acid test solutions. As will be seen, the accuracy in the determination of squaric acid pK_1 is not limited entirely by this effect.

Results

The equivalent conductances of the nine squaric acid solutions measured between 10 and 50° are shown in Table I. The calculations of pK_1 at each temperature from these data were carried out using the Shedlovsky correlation (eq 3) with $b = (B_1\Lambda^0 + B_2)$ and then again using the Robinson–Stokes equation (eq 4) with the "ion-size" parameter $a = 4$ Å, a typical value for small ions.[12] The results of these calculations are given in Table II.

We note that pK_1 appears to be an increasing function of temperature between 15 and 50° but that the value at 10° deviates and perhaps signals a minimum value of pK_1 near 15°. The deviation might simply be attributable to the same random experimental error which is

Table I: Measured Equivalent Conductances of Squaric Acid Solutions

	Temp, °C							
C, M	10	15	20	25	30	35	40	50
0.05927	267.1	290.1	314.0	337.4	360.1	381.7	401.8	440.4
0.06130	264.4	287.7	311.5	334.9	356.3	377.6	398.9	436.2
0.08696	257.0	280.4	303.0	325.3	346.8	367.9	386.2	421.8
0.1035	247.4	269.2	291.6	312.9	333.2	353.1	371.6	405.6
0.1158	248.3	270.4	292.4	313.8	334.4	353.8	372.5	406.7
0.1212	246.4	268.3	290.1	311.0	331.4	350.9	369.5	403.7
0.1343	243.7	265.4	286.8	307.4	325.9	344.7	363.1	398.3
0.1430	239.4	260.9	281.7	302.4	322.3	340.7	358.7	391.4
0.1582	236.0	257.1	278.0	298.0	317.4	335.7	353.1	384.9

Table II: Calculated pK_1 and Λ^0 Values from the Conductance Data in Table I and Using the Shedlovsky Correlation Equation (3) and the Robinson–Stokes Equation (4) with Ion-Size Parameter a = 4 Å

	Calculations utilizing			
Temp,	Eq 3		Eq 4 with a = 4 Å	
°C	pK_1 ± std dev	Λ^0	pK_1 ± std dev	Λ^0
10	0.520 ± 0.023	310.1	0.503 ± 0.023	308.7
15	0.509 ± 0.024	337.8	0.492 ± 0.025	336.3
20	0.522 ± 0.022	367.6	0.504 ± 0.023	365.8
25	0.541 ± 0.021	397.6	0.523 ± 0.021	395.6
30	0.557 ± 0.021	426.3	0.540 ± 0.022	424.2
35	0.578 ± 0.022	455.2	0.562 ± 0.022	452.9
40	0.582 ± 0.018	481.0	0.567 ± 0.019	478.6
50	0.611 ± 0.021	532.3	0.612 ± 0.022	530.0

Table III: Empirical Fit of pK_1 *vs.* Absolute Temperature Data Reported in Table II to the Equation $pK_1 = A_1/T + A_2 + A_3T$ and Thermodynamic Properties of the Primary Dissociation Calculated at 25°

		Calculation utilizing	
		Eq 3	Eq 4 with a = 4 Å
Parameters[a]	A_1	−536.5	−850.7
	A_2	+2.990	+5.153
	A_3	-2.239×10^{-3}	-5.899×10^{-3}
$\Delta G_1°$ at 25°		0.738 kcal/mol	0.714 kcal/mol
$\Delta H_1°$ at 25°		−1.493 kcal/mol	−1.544 kcal/mol
$\Delta S_1°$ at 25°		−7.48 cal/deg mol	−7.57 cal/deg mol

[a] Least-squares fit of eq 8 between 15 and 40°.

reflected in the approximately ±0.02 pK standard deviation on each pK_1 value. However, because the Λ^0 values calculated from these same experimental data show no deviant behavior at 10°, we regard the high pK_1 at this temperature with some confidence.

A least-squares fit of the empirical equation[14]

$$pK_1 = \frac{A_1}{T} + A_2 + A_3T \qquad (8)$$

failed to produce an equation which followed the minimum at 15° although the result did represent all the experimental points to within their standard deviations. For the purpose of finding the slope at 25°, the 10 and 50° points were omitted from the least-squares calculation and the resulting empirical equation (see Table III) fit the data to within ±0.009 pK unit from 15 to 40°.

$\Delta H_1°$, $\Delta S_1°$, and $\Delta G_1°$, the standard enthalpy, entropy, and Gibbs free energy, respectively, of the primary dissociation at 25° were calculated from the well known thermodynamic relationships and using the empirical eq 8 for the slope. These results are shown in Table III.

The standard deviation values entered in Table II, which are typically 0.02 pK unit, represent the scatter of pK_1 values about the calculated mean. These deviations are caused by the random error in the equivalent conductance values and are due presumably to a variety of experimental reasons including the problem of the slow decomposition mentioned previously. In addition to these experimental uncertainties, the results may be inaccurate because of a number of more systematic errors introduced through the calculations. In particular, these might involve (a) the degree to which H^+-HSq^- follows the semiempirical equation used to predict the variation of Λ_ϵ with ionic strength, *i.e.*, eq 3 or 4, and (b) the degree to which the activity coefficients of these same ionic species follow the Davies correlation, eq 7. Quantitative estimates of these uncertainties are difficult to make. In the first instance, the fact that the Shedlovsky and the Robinson–Stokes correlations (the latter with a = 4 Å) produce a discrepancy of about 0.02 pK unit at 25° indicates that at least this uncertainty exists. A recalculation using the Robinson–Stokes equation with a = 5 Å yields at 25° a value of pK_1 = 0.548 and Λ^0 = 396.0 which is in better agreement with the pK_1 value calculated from the Shedlovsky equation but because the ion-size parameter a is unknown this agreement has little significance. With regard to the activity coefficients, if we venture to assume that the mean activity coefficients of H^+ and HSq^- are within 2% of the correlation, the corresponding uncertainty in pK_1 is about ±0.02 at

(14) H. S. Harned and R. A. Robinson, *Trans. Faraday Soc.*, **36**, 973 (1940).

Table IV: The Relative Constancy of $\eta^0 \times \lambda^0_{HSq^-}$ Shows That the Calculated Limiting Equivalent Conductance of HSq^- Varies with Temperature Nearly As Predicted by Walden's Rule[12]

	Temp, °C							
	10	15	20	25	30	35	40	50
$\lambda^0_{H^+}$[a]	275	300.6	324.5	349.8	373.5	397.0	419	462
$\lambda^0_{HSq^-}$	34.4	36.4	42.2	46.8	51.7	57.0	61	69
η^0 [b]	1.306	1.138	1.002	0.8903	0.7975	0.7194	0.6531	0.5467
$\eta^0 \times \lambda^0_{HSq^-}$	44.9	41.4	42.3	42.6	41.3	41.0	39.8	37.7

[a] Hydrogen ion limiting equivalent conductances.[18] [b] Viscosity of water in centipoises; see ref 12, Appendix 1.1.

25°. In summary, it appears that each of the principal sources of inaccuracy could introduce about ±0.02 pK unit of uncertainty and so the absolute pK_1 could deviate from the values in Table II by as much as ±0.06 pK unit and the corresponding $\Delta G_1°$ values in Table III by as much as ±0.08 kcal/mol. From the scatter of the pK_1 data about the eq 8 least-squares correlation, we estimate that $\Delta H_1°$ is uncertain to ±0.12 kcal/mol and hence the maximum uncertainty in $\Delta S_1°$ is ±0.7 cal/mol deg.

Discussion

This conductance study indicates that pK_1 for squaric acid at 25° is 0.54, if the Shedlovsky formula is used, and, if the Robinson–Stokes correlation is used, 0.52 to 0.55 corresponding to a reasonable range of possible values for the ion-size parameter of a = 4 to 5 Å. Each of these pK values carries an uncertainty of about ±0.06 pK unit. This result is in accord with our previous less precise measurement of pK_1 = 0.55 ± 0.15 by pH potentiometric methods[4] and substantiates the finding that squaric acid is a stronger acid than previously believed.[6]

The thermodynamic results in Table III seem to indicate that the unusual strength of squaric acid is not due directly to an increase in delocalization energy accompanying dissociation. The primary dissociation is characterized by $\Delta H°$ of about −1.5 kcal/mol and $\Delta S°$ about −7.5 cal/mol deg, whereas typical weak carboxylic acids which involve no appreciable change in delocalization energy on dissociation have corresponding $\Delta H°$ = 0 ± 1 kcal/mol and $\Delta S°$ = −25 ± 3 cal/mol deg.[15] Squaric acid is stronger than typical carboxylic acids not because its dissociation $\Delta H°$ is abnormally negative as would be expected if π-electron delocalization were increasing in the anion, but because the dissociation $\Delta S°$ is considerably less negative. A similar phenomenon has been recently reported by Kurz and Farrar[16] to be involved in the aqueous dissociation of several other strong (0.5 < pK < 1.4) organic acids. In this work the acid strengths of five haloacetic acids, oxalic acid, and sulfamic acid are attributed to entropy rather than energy effects.

It is convenient to regard the entropy change accompanying the aqueous reaction $H_2Sq + H_2O \rightarrow HSq^- + H_3O^+$ as composed of three contributions due to (a) the symmetry differences of the isolated reaction species, (b) differences in vibrational, translational, and other rotational motions of the isolated species, and (c) differences in the structure of the solvent molecules around the reactants and products. Following Benson,[17] the first contribution is

$$\Delta S_\sigma° = R \ln \frac{\sigma_{H_2Sq}\sigma_{H_2O}}{\sigma_{HSq^-}\sigma_{H_3O^+}}$$

in which the symmetry numbers of H_2Sq, H_2O, and H_3O^+ are readily assigned as 2, 2, and 3, respectively. σ_{HSq^-} would be 1 if the ion were classical and 2 if the π electrons were completely delocalized and the corresponding $\Delta S°$ would be +0.57 or −0.81 cal/mol deg, respectively, but either of these values is minor compared to the total $\Delta S°$. Similarly the contribution due to other molecular motions is equally small.[8] Apparently then, the measured $\Delta S_1°$ value of −7.5 cal/mol deg is due almost entirely to changes in the structure of the solvent water and these changes are less than those accompanying aqueous dissociation of weak organic acids. This effect may be interpreted as either (1) that the undissociated squaric acid molecule imparts an unusually high degree of structuring to the surrounding water such that relatively little additional structuring occurs upon dissociation of the charged ions, or (2) the bisquarate ion imparts an unusually small degree of structuring on the water owing perhaps to the delocalization of its negative charge.

A by-product obtained from this study is an estimation of Λ^0, the hypothetical equivalent conductance of H_2Sq dissociated into H^+ and HSq^- at infinite dilution. These values at the various temperatures are given in Table II where it is seen that the two sets of calculations yield approximately the same set of Λ^0 values. Since $\Lambda^0 = \lambda^0_{H^+} + \lambda^0_{HSq^-}$, and measured $\lambda^0_{H^+}$ values are available,[18] $\lambda^0_{HSq^-}$ may be estimated and are shown in

(15) Reference 8, Chapter 8.

(16) J. L. Kurz and J. M. Farrar, *J. Amer. Chem. Soc.*, **91**, 6057 (1969).

(17) S. W. Benson, *ibid.*, **80**, 5151 (1958).

(18) Reference 12, Appendix 6.2.

Table IV. Λ^0 at each temperature is taken as the average of the two values in Table II for the purpose of this calculation. λ^0_{HSq} increases with temperature in a reasonable way as can be seen in Table IV by multiplying each value by the viscosity of water at that temperature. The relative constancy of this product (Walden's rule)[12] is expected of ionic conductances at infinite dilution, and this finding adds confidence to the validity of the methods used in this study.

Acknowledgment. We are grateful to Professor Robert I. Gelb for his help with the experimental techniques of conductivity measurement and also to the Research Corporation for partially supporting this study.

The Salting-In of Nonpolar Gases in Aqueous Tetraalkylammonium Bromide Solutions and the Apparent Molal Volume of These Salts in Water

by Michel Lucas* and Anne de Trobriand

Department de Chimie, Centre d'Etudes Nucléaires, Fontenay-aux-Roses, France *(Received October 8, 1970)*

Publication costs assisted by the Commissariat à l'Energie Atomique, France

The apparent molal volume of tetrapropylammonium bromide in water at 5, 15, and 25°, tetrabutylammonium bromide at 5 and 25°, and tetraethylammonium bromide at 5° have been measured at various concentrations. The experimental variation of the salting-out constants with the molality of the solution and the temperature has been compared to the variation calculated according to the scaled particle theory for some nonpolar gases. The calculated and experimental constants both have a similar concentration dependence, though their actual values are quite different. The discrepancy may be ascribed to the influence of dispersion forces which are not taken into account in our calculations.

Introduction

The salting-out constant k for a gas in an aqueous salt solution is given by the equation

$$\log \frac{S^\circ}{S} = km \qquad (1)$$

Here S° is the solubility of the gas in water and S its solubility in the salt solution of molality m. The salting-out constants calculated from data in the literature for tetraalkylammonium bromide solutions[1] show rather large variations with the salt molality. To compare the experimental constants with those calculated from the scaled particle theory,[2-4] the apparent molal volumes of the salts are required. Most but not all of these apparent molal volumes can be found in the literature.[5]

To complete the salt series, the apparent molal volumes of tetrapropylammonium bromide in water at 5 and 15° and those of tetrabutyl- and tetraethylammonium compounds were determined at 5°.

Experimental Section

Chemicals. The tetraethyl- and tetrabutylammonium bromides, Carlo Erba, polarographic grade, were dried at 70° *in vacuo* before use. The tetrapropylammonium bromide, Eastman Kodak, was purified according to the procedure given in ref 5.

Measurements. Density measurements were made with 25-ml pycnometers, standardized with doubly distilled water. The procedure of Weissberger was followed.[6] Density measurements were reliable to within ±0.00005. The corresponding precision for the apparent molal volume was ±0.3 ml/mol for m smaller than 0.3 and ±0.1 ml/mol for higher molalities. The water bath was maintained at ±0.02° at all temperatures.

Results

The apparent molal volumes of the salts at various temperatures are listed in Table I. They were calculated from the density data by means of the equation

(1) W. Y. Wen and J. Hung, *J. Phys. Chem.*, **74**, 170 (1970).
(2) S. K. Shoor and K. E. Gubbins, *ibid.*, **73**, 448 (1969).
(3) M. Lucas, *Bull. Soc. Chim. Fr.*, 2994 (1969).
(4) W. L. Masterton and T. P. Lee, *J. Phys. Chem.*, **74**, 1776 (1970).
(5) W. Y. Wen and S. Saito, *ibid.*, **68**, 2639 (1964).
(6) A. Weissberger, "Physical Methods of Organic Chemistry," Vol. I, 2nd ed, part I, Interscience, New York, N. Y., 1949.

Table I: Apparent Molal Volumes of Tetraalkylammonium Bromides in Aqueous Solutions at 5, 15, and 25° (units of ml/mol)

Concn, m	$(C_4H_9)_4NBr$ 5°	$(C_4H_9)_4NBr$ 25°	$(C_3H_7)_4NBr$ 5°	$(C_3H_7)_4NBr$ 15°	$(C_3H_7)_4NBr$ 25°	$(C_2H_5)_4NBr$ 5°
0.05			236.0		239.3	
0.1	293.7	299.9	235.6	237.0	238.8	171.7
0.15			235.4	236.7	238.4	
0.2	293.3	298.9	235.2	236.5	238.1	171.2
0.25			234.9	236.2	237.8	
0.3	292.3	298.2	234.5	236.0	237.5	170.8
0.4	291.5	297.6	233.8	235.3	237.0	170.6
0.5	290.7	297.0	233.0	234.7	236.6	170.2
0.6	Limit of solu-	296.5	232.4	233.9	236.2	170.0
0.7	bility		231.7	233.5	235.7	169.8
0.8		295.8	231.3	232.9	235.3	169.6
0.9			230.8	232.6	234.8	169.4
1.0		295.5	230.3	232.3	234.4	169.2
1.2		295.4	229.5	231.5	233.7	168.8
1.4		295.1	228.7		233.0	168.5
2.0			227.2		231.6	167.5

$$V_2 = \frac{1}{m}\left(\frac{1000 + mM_2}{d} - \frac{1000}{d^\circ}\right) \qquad (2)$$

where d° is the density of pure water, M_2 the molecular weight of the salt, d the density of the solution, and m its molality. The shape of the curves obtained when V_2 is plotted against m is very similar to that reported by Wen,[5] but at 25° there are some differences between his values and ours for tetrabutylammonium bromide.

Discussion

We have plotted the experimental values of the apparent molal volume V_2 of a given salt and of the salting-out constant for a given gas against the square root of the molality of a solution of the salt at a given temperature. Figure 1 shows the plots for methane and tetrabutylammonium bromide. The values of V_2 decrease with increasing molality, and a minimum is found near $m = 1.4$. The values of k increase with increasing molality, and there is a maximum near $m = 0.9$. Both sets of curves are somewhat similar in shape; but variations are opposite in sign.

Figure 2 shows the corresponding plots for propane and tetrapropylammonium bromide. In this case the values of V_2 decrease with increasing m values and breaks in the curves are observed at 5 and 15° but not 25°. Similar characteristics are shown by the k curves. The variation is always opposite in sign. Figures 3 and 4 show the data for methane, ethane, and propane in aqueous ammonium or tetrahydroethylammonium bromide solutions.

In those cases, V_2 increases with increasing m, and k varies in the opposite direction. Also small variations of k with the molality and the temperature correspond to small variations of V_2. (Data for V_2 are taken from ref 7 for $(EtOH)_4NBr$ and calculated for NH_4Br on the assumption that the relation $V_2 = V_2^\circ + S_v m^{1/2}$ holds

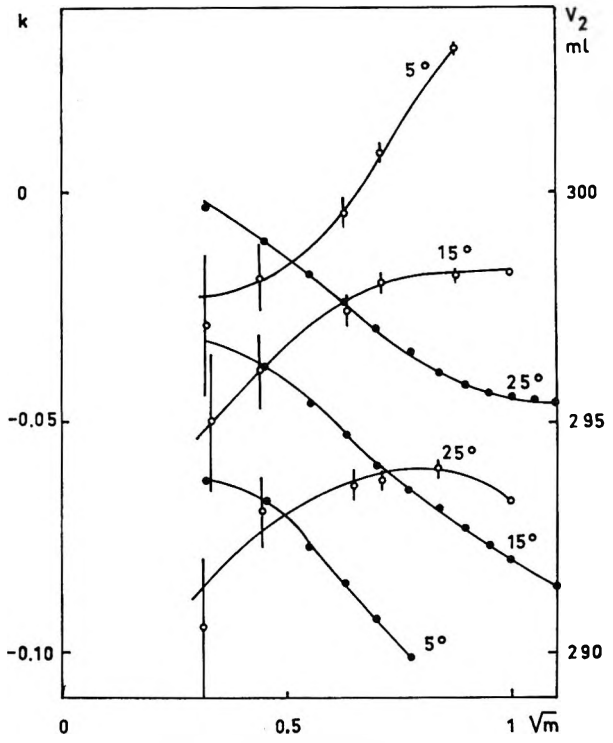

Figure 1. Salting-out constant for methane and apparent molal volume of salt in aqueous tetrabutylammonium bromide solutions: open circles, k; black circles, V_2.

up to $m = 1$ with V_2° taken from ref 8 and S_v from ref 9.)

Now we should compare the experimental results with those predicted from the scaled particle theory. Pierotti[10] has divided the process of solution of a non-

(7) W. Y. Wen and S. Saito, *J. Phys. Chem.*, 69, 3569 (1965).

(8) K. Fajans and O. Johnson, *J. Amer. Chem. Soc.*, 64, 676 (1942).

(9) H. S. Harned and B. B. Owen, "The Physical Chemistry of Electrolytic Solutions," 3rd ed, Reinhold, New York, N. Y., 1958, pp 360–370.

(10) R. A. Pierotti, *J. Phys. Chem.*, 69, 281 (1965).

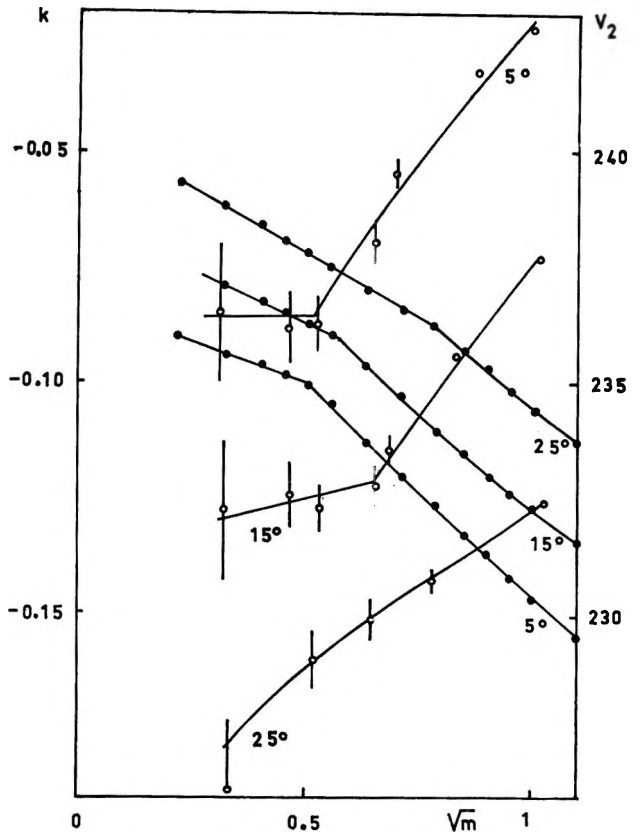

Figure 2. Salting-out constant for propane and apparent molal volume of salt in aqueous tetrapropylammonium bromide solutions: open circles, k; black circles, V_2.

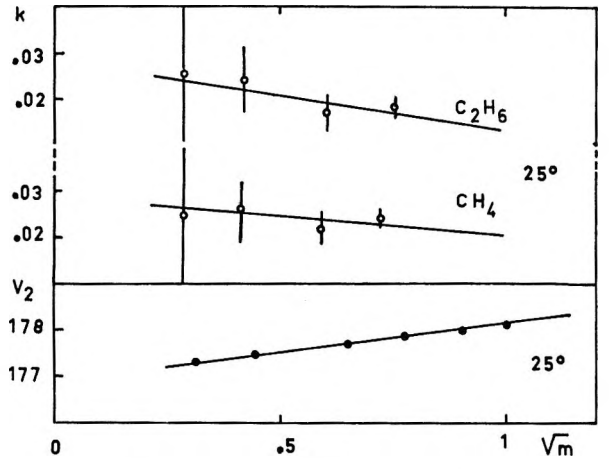

Figure 3. Salting-out constant for methane and ethane and apparent molal volume of salt in aqueous $(EtOH)_4NBr$ solutions: open circles, k; black circles, V_2.

polar gas in water into two steps. First, a cavity has to be made in the solvent to accommodate the solute particle. Its diameter is exactly the hard-sphere diameter of the gas. This is referred to as the cavity formation process. The scaled particle theory allows the computation of the free energy involved in this step which for a mole of solute is G_c.

The second step is to consider the interactions of the

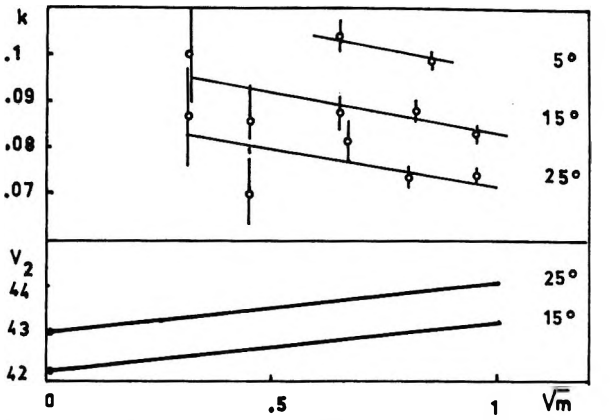

Figure 4. Salting-out constant for butane and apparent molal volume of salt in aqueous NH_4Br solutions: open circles, k; black circles, V_2.

solute with the solvent particles through dispersion forces, polarizability, etc. The free energy associated with this step is G_i.

The solubility of a gas is described by the Henry constant

$$K = \frac{p}{x} \tag{3}$$

where p is the partial pressure of the gas over the solution and x its molar fraction in the solution. Pierotti states that K is related to the free energies G_c and G_i and the molar volume of the solvent by the equation

$$RT \ln K = G_c + G_i + RT \ln \frac{RT}{V} \tag{4}$$

where T is the absolute temperature.

The quantity $G_c + RT \ln RT/V$ may be calculated for a very slightly soluble gas in a mixture of solvents by means of the equations given by Lebowitz and Rowlinson.[11]

We shall write these equations on a molal basis. The same symbols as in ref 11 are used.

Let us consider i particles constituting the solvent. ρ_i is the number density and R_i the hard-sphere diameter for a given particle. For a mixture of i particles, the quantities ξ, X, and Y are defined as

$$\xi = \frac{\pi}{6} \sum \rho_i R_i^3; \; X = \frac{\pi}{6} \sum \rho_i R_i^2; \; Y = \frac{\pi}{6} \sum \rho_i R_i \tag{5}$$

The value of G_c for a solute of diameter D is given by

$$\frac{G_c}{RT} = -\ln (1 - \xi) + \frac{3D^2Y}{1 - \xi} + \frac{9X^2D^2}{2(1 - \xi)} + \frac{3DX}{1 - \xi} \tag{6}$$

Now consider a solvent which is an aqueous salt

(11) J. L. Lebowitz and J. S. Rowlinson, *J. Chem. Phys.*, **41**, 133 (1964).

solution. On a molal basis, there are 55.5 mol of water (1000 g) for m mol of the salt. The apparent molal volume of the salt is given by eq 2. It follows then that the density of the solution is given by the relation

$$d = \frac{55.5M_{H_2O} + mM_2}{55.5V_{H_2O} + mV_2} \quad (7)$$

where M_{H_2O} is the molecular weight of water and V_{H_2O} the molar volume of pure water. The number density ρ_{H_2O} of the water in the aqueous salt solution is

$$\rho_{H_2O} = \frac{55.5Nd}{1000 + mM_2} = \frac{55.5N}{55.5V_{H_2O} + mV_2} \quad (8)$$

where N is the Avogadro number.

The number density of one of the two ionic species is

$$\rho_+ = \rho_- = \frac{mN}{55.5V_{H_2O} + mV_2} \quad (9)$$

Now if a, b, and c are the hard-sphere diameters of the water and of the anion and cation of the salt, from eq 5, 8, and 9, it follows that

$$\xi = \frac{N\pi}{6}\frac{55.5a^3 + m(b^3 + c^3)}{55.5V_{H_2O} + mV_2} \quad (10)$$

Similar relations are found for X and Y except that a^3, b^3, and c^3 are replaced by a^2, b^2, and c^2 or a, b, and c.

In addition, the volume V in eq 4 is given by the equation

$$V = \frac{55.5V_{H_2O} + mV_2}{55.5 + 2m} \quad (11)$$

Then the value of G_c may be calculated by means of eq 6, 10, and 11.

Now if $K°$ is the Henry constant for the gas in pure water, the salting-out constant is given by

$$k = \frac{1}{2.3m}\left(\frac{G_c - G_c°}{RT} + \ln\frac{V°}{V}\right) + \frac{1}{2.3m}\left(\frac{G_i - G_i°}{RT}\right) \quad (12)$$

$k = k_c + k_i$ with

$$k_c = \frac{1}{2.3m}\left(\frac{G_c - G_c°}{RT} + \ln\frac{V°}{V}\right) \quad (13)$$

$$k_i = \frac{1}{2.3mRT}(G_i - G_i°) \quad (14)$$

Here $G_i°$, $G_c°$, and $V°$ are the corresponding values for G_i, G_c, and V, when the molality is equal to zero.

It should be outlined that k_c is a function of the constants D, a, b, c, and V_{H_2O} for a given salt and solute and of the variables m and V_2. This is apparent from eq 6, 10, 11, and 13; then a relation between k_c and V_2 can be given, but it is rather complex.

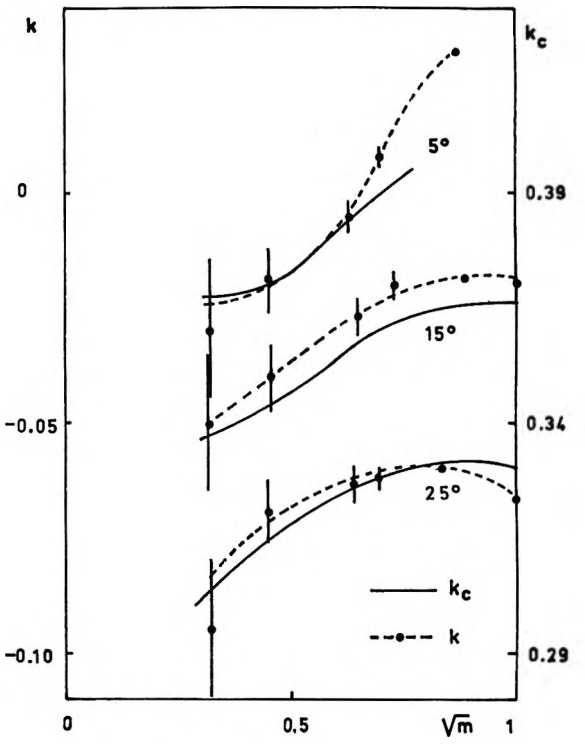

Figure 5. Plots of experimental and calculated salting-out constants against $m^{1/2}$ for methane and aqueous tetrabutylammonium bromide solutions.

For the calculation of k_c, the values of a, b, c, and D are required. From ref 10, a is equal to 2.76 Å for water; b is chosen equal to the crystal ionic diameter of Br^-, that is, 3.92 Å. In ref 12 the values given, respectively, for the cations tetrapropyl- and tetrabutylammonium are 8.7 and 8.0 Å. The values for methane and propane are, respectively, 3.8 and 5.1 Å.[13]

The calculation of G_i may be done by means of the equations given in the literature.[2,3] However this calculation rests upon the assumption that G_i, the free energy of interaction, is equal to H_i, the enthalpy of interaction.[10] We had shown that this assumption leads to an inconsistency,[14] except when the solvent has an expansivity coefficient equal to zero or very small, which is the case only for pure water and not for aqueous salt solutions. Then H_i and G_i can no longer be considered as equal quantities, and at present we cannot evaluate G_i and k_i. We shall only compare k and k_c.

The values for k_c have been calculated for methane and aqueous tetrabutylammonium bromide solutions and for propane and tetrapropylammonium bromide at 5, 15, and 25°.

Figure 5 shows the plots of k_c for methane and tetra-

(12) B. E. Conway, R. E. Verrall, and J. E. Desnoyers, *Trans. Faraday Soc.*, 62, 2738 (1966).

(13) J. O. Hirschfelder, C. F. Curtiss, and R. B. Bird, "Molecular Theory of Gases and Liquids," Wiley, New York, N. Y., 1967, p 1110.

(14) M. Lucas and A. Feillolay, *Bull. Soc. Chim. Fr.*, 1267 (1970).

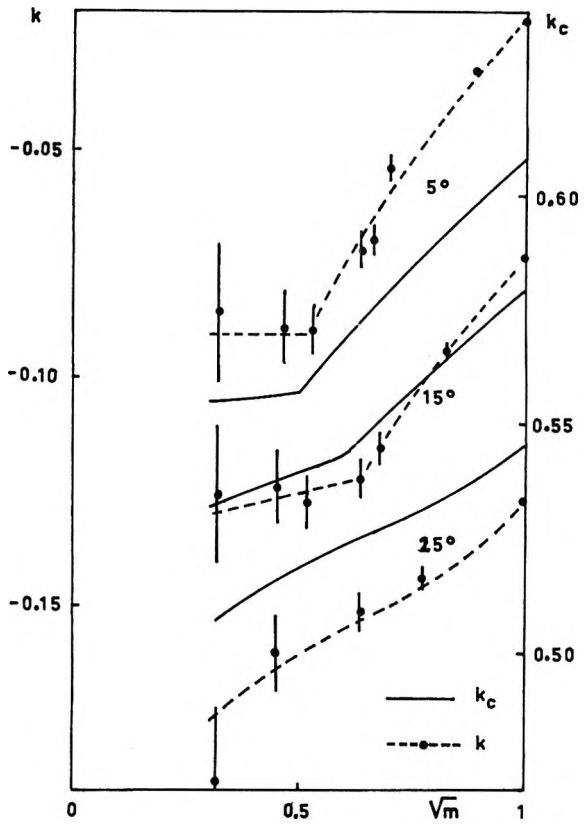

Figure 6. Plots of experimental and calculated salting-out constants against $m^{1/2}$ for propane and aqueous tetrapropylammonium bromide solutions.

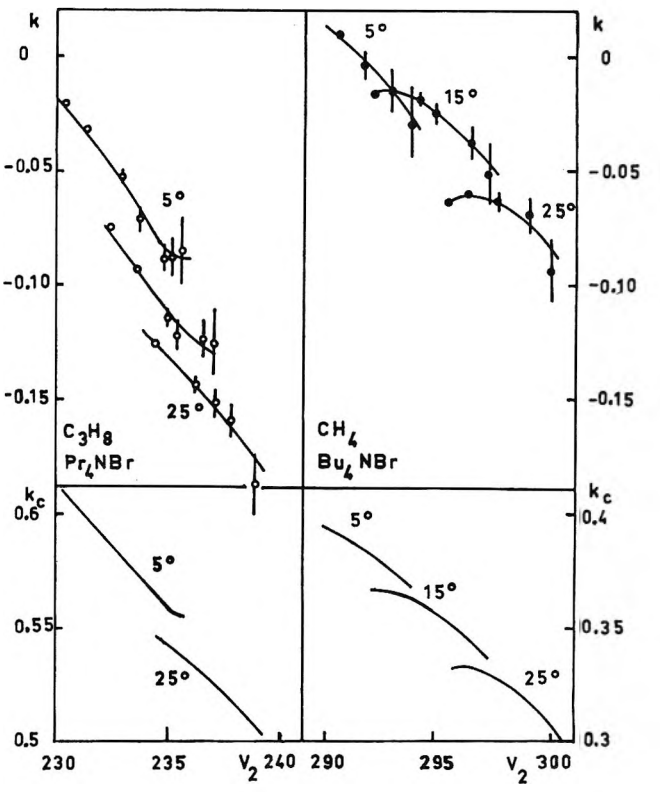

Figure 7. Plots of k and k_c against the apparent molal volume of the salts for methane and aqueous tetrabutylammonium bromide solutions and for propane and aqueous tetrapropylammonium bromide solutions.

butylammonium bromide solutions against $m^{1/2}$. The experimental values for k are plotted on the same figure. The main features of experimental curves are reproduced by the calculated ones.

Figure 6 shows similar plots for propane and tetrapropylammonium bromide. Both sets of curves are similar, especially as the existence of breaks at 5 and 15° is shown.

The only discrepancy is that in the last case the variation of k_c with the temperature and the salt molality is smaller than the experimental one. The values taken for the gas and the cation diameters are mainly tentative and may be slightly in error. However, in both cases, the variation of k with the temperature and the salt molality is consistent, at least qualitatively, with the variation calculated according to the scaled particle theory, even if the possible variation of k_i with the same parameters has been ignored.

The values of k_i are always negative, as the interaction forces always cause salting-in. Therefore the values of k_c are strongly in excess of the experimental ones. In any event the data necessary for the calculation of k_i are lacking, and all that we can do is to compare the variations of k and k_c and not the magnitude of calculated and experimental salting-out constants.

Finally the plots of k and k_c against V_2 are shown in Figure 7. The dependence of k and k_c on V_2 is rather complex, although in some cases it may be described approximately by a linear relation.

Self-Association of Methanol Vapor. Evidence for Dimers and Tetramers

by Aaron N. Fletcher

Chemistry Division, Research Department, Code 6052, Naval Weapons Center, China Lake, California 93555
(Received July 1, 1970)

Publication costs assisted by the Naval Weapons Center, China Lake

In an attempt to help resolve conflicting interpretations as to the major self-association species of alcohols, a spectrophotometric study of methanol vapor has been made from 2.5 to 3.0 μm taking measurements every 0.1 nm. The interdependence of the absorption of monomer and polymers was determined making use of absorption spectra integrated over 501 different wavelength regions. Particular attention was given to the problem of band overlap in the assignments of absorption to the various species. After computer subtraction of the monomer spectra, polymer bands at about 2.775 and 2.950 μm were found to show second- and fourth-order relationships with the monomer concentration, respectively. The wavelength region from 2.80 to 2.90 μm, intermediate to the two bands, consisted only of overlaps of these bands. These results are interpreted as evidence for dimers and tetramers as the major self-association polymers of methanol vapor.

Introduction

Previous workers, using heat capacity,[1] PVT,[2] and infrared absorption data,[3] concluded that the most probable major self-association species of methanol vapor were the dimer and the tetramer. This 1–2–4 model also has been used to explain heat capacity data of a number of other alcohols in the gas phase.[4-10] Recently, however, Tucker, *et al.*,[11] have reported that their data could be best explained by the existence of only monomer, trimers, and octamers of methanol in both the gas phase and in nonpolar solvents.

The usual approach for the selection of models of self-association is to use some form of a material-balance equation. Material-balance equations, however, have an inherent limit to their range of application evoked by the saturation pressure in the gas phase and the neat-solution concentration in the liquid phase. Furthermore, condensation upon the walls of the container increases the possibility of significant experimental bias in the concentration range of greatest interest in self-association studies of vapors, *i.e.*, the pressures just below saturation.

The purpose of the present study is to determine all the significant n-mers (n is the number of monomer units contained in each polymer molecule) formed in the self-association of methanol in the gas phase without using material-balance equations. By examination of both monomer absorption and polymer absorption in the wavelength region 2.5 to 3.0 μm, five major advantages will be achieved. First, it will be possible to determine monomer–polymer mathematical relationships at low concentrations where material-balance equations would be sensitive only to the monomer and thus provide a wider range of measurements. Second, it will be possible to check for interference in the determination of the monomer concentration by the presence of polymeric species. Retention of a mathematical relationship between the monomer absorbance and a polymer absorbance, from low concentrations to high, will be used as evidence of an insignificant amount of polymer end-group absorbance at the wavelengths used to measure the monomer. Third, examination of all of the available polymer absorption wavelength region allows a comparison of polymer absorption at different concentrations and thus the detection of any new polymer species. This procedure detects wavelength regions (if they exist) where only polymers having the same value of n are found. This ensures not only that all measurable n-mers have been detected, but it also ensures against the introduction of a more complicated model which gives a better "fit" to the monomer–polymer relationship. Fourth, the relationships between the monomer and the n-mers can be determined for each individual sample. Thus, it is possible to determine the constancy of the equilibrium quotients over a wide range of absorbance values, temperatures, and concentrations. And fifth, since the quantitative measurements of the methanol are not used in the determination of the self-association polymers, wall condensation errors are not a problem.

(1) W. Weltner, Jr. and K. S. Pitzer, *J. Amer. Chem. Soc.*, **73**, 2606 (1951).

(2) C. B. Kretschmer and R. Wiebe, *ibid.*, **76**, 2579 (1954).

(3) R. G. Inskeep, J. M. Kelliher, P. E. McMahon, and B. G. Somers, *J. Chem. Phys.*, **28**, 1033 (1958).

(4) G. M. Barrow, *ibid.*, **20**, 1739 (1952).

(5) J. F. Mathews and J. J. McKetta, *J. Phys. Chem.*, **65**, 758 (1961).

(6) N. S. Berman and J. J. McKetta, *ibid.*, **66**, 1444 (1962).

(7) E. T. Beynon, Jr. and J. J. McKetta, *ibid.*, **67**, 2761 (1963).

(8) J. L. Hales, J. D. Cox, and E. B. Lees, *Trans. Faraday Soc.*, **59**, 1544 (1963).

(9) N. S. Berman, C. W. Larkam, and J. J. McKetta, *J. Chem. Eng. Data*, **9**, 218 (1964).

(10) N. S. Berman, *AIChE J.*, **14**, 497 (1968).

(11) E. E. Tucker, S. B. Farnham, and S. D. Christian, *J. Phys. Chem.*, **73**, 3820 (1969).

Experimental Section

Equipment. Spectral measurements were made with a Cary 14RI spectrophotometer with the monochromator grating blazed for maximum efficiency at 1.6 μm and having a Cary 1490090 Universal %T Slidewire. The Universal Slidewire has the capability of expanding any 5, 10, 20, 50, or 100% transmission (%T) full scale starting at any specified integral %T within the range of 0–100%T. The output of slidewire was transferred to a 1000 unit digital readout, making a theoretical output scale of 20,000 units. In practice, noise–time considerations limited the system to a maximum sensitivity of the 10%T range (10,000 units). The absolute value of the %T scale was checked at 5 different points with calibrated rotating sector disks (Beckman Instruments) and found to be within the 0.2% error rating. Measurements were made every 0.1 nm and both the wavelength and the slidewire output were punched onto paper tape. The calculated spectral resolution was 2 cm^{-1} at 3.0 μm and less than 1 cm^{-1} at 2.5 μm. The instrument was continuously flushed with dried air. An insulated stainless-steel gas cell with an 18.9-cm light path was used to take spectral measurements. The spectrophotometer cell used four calcium fluoride windows with an evacuatable separation between the end windows. A Lauda Type N constant-temperature bath was used to pump Union Carbide UCON HTF-10 fluid to a jacket around the length of the spectrophotometer cell. A Hewlett-Packard quartz thermometer was used to measure the temperature of the UCON HTF-10 in the cell jacket and inside the main constant-temperature bath. The outer portion of the spectrophotometer cell was insulated with polyurethane foam and epoxy-fiberglass. Quantitative measurements of gas concentration were made by breaking sealed glass ampules of methanol inside an additional chamber connected to 0.15-, 1-, and 9-l. tanks. The tanks and addition chamber were calibrated by weighing distilled water into them (using a 3-kg capacity balance accurate to 1 mg). Repeat measurements gave differences on the order of 0.02% relative error. Hoke stainless-steel bellow valves were used throughout the system. Except for a heated $^1/_8$ in. o.d. stainless-steel tube connecting to the spectrophotometer cell, the remaining portions of the all stainless-steel system (in contact with methanol) were submerged in a 50-gallon constant-temperature bath containing UCON HTF-10 bath fluid. A Bayley Inst. Co. Precision temperature controller (Danville, Calif.) allowed temperature control of the main bath in the range of ± 0.001 to 0.01° depending upon the absolute temperature. The spectrophotometer-cell temperature variation was $\pm 0.3°$. Pressure could be measured by a means of a Pace Differential Gage (submerged in the oil bath) sensitive to 0.01 psi full scale. The Pace Gage drove a Texas Instrument Co. No. 150 LPC pressure controller. The gas pressure was measured with a Texas Instrument Co. 0–3000 Torr Quartz Precision Pressure Gage (readable to 0.01 Torr).

Material. Spectroquality methanol from Matheson Coleman and Bell was distilled from calcium hydride at slightly greater than atmospheric pressure. Distillation and all transfers were made in the absence of air. The flask of methanol was cooled with solid CO_2 and the pressure reduced to partially degas the methanol before its transfer by distillation to the glass ampules. Matheson Prepurified Grade (99.998% min) argon was used to preflush the distillation equipment and to pressurize the methanol system.

Procedure. Weighed portions of methanol (corrected for air-density effects) were introduced into the evacuated stainless-steel system yielding a known concentration of methanol in the 1- and 9-l. tanks. Both tanks were in turn pressurized with argon so that expansion of either into the spectrophotometer cell would result in a total pressure of 2400 Torr. A 100-W heater was wrapped around the two tanks to create a hot band. Although 1 hr of mixing with the hot band appeared sufficient, quantitative measurements were always made with a minimum of 15 hr of mixing. Some of the nonquantitative high-concentration runs were mixed in the spectrophotometer cell by raising its temperature 20 to 30°. A number of successive runs were made from a single weighing of methanol by expanding the known concentration of methanol in the 9-l. tank into the evacuated 1-l. tank. Evacuation to better than 10^{-5} Torr measured with a Veeco Discharge Pressure Gage was possible. Spectrophotometric calibration runs were made for every two sample runs. Because of some of the high scale sensitivity—high pen dampening, some spectrophotometric runs from 3.0 to 2.5 μm required up to 4 hr to perform. In order to make full use of the %T scale expansion, a series of runs was necessary to obtain a complete absorption spectrum, *e.g.*, 60 to 80%T combined with a 80–100%T run were common. Also, mixed-range runs were performed giving priority to values on the more sensitive range, *e.g.*, 80–100%T combined with a 0–100%T run. These combinations as well as most of the other manipulations of the data were performed on a Univac 1108 computer.

Results and Discussion

Measurement of the Monomer Concentration and Spectra. Quantitative measurements of the formal methanol concentration were made only high enough to ensure that Beer's law was applicable and to determine when the formal[12] polymer concentration was significant, *i.e.*, was high enough so as to make more than a

(12) The term formal (*F*) is used to express the mathematical concentration of the added material without consideration of any chemical reaction within the solution. Molar (*M*) is used to express known (tentative or real) concentrations.

possible 1% error in the determination of the monomer concentration. Since over $^1/_2$ million absorption measurements were recorded and used in calculations, it was necessary to transform the data to a reduced form. The spectral absorbance values of data measured up to and including ± 0.5 nm from each integral nanometer were integrated using the trapezoid formula and associated with the integral nanometer. This transformation reduces the 5011 absorption measurements used for each run down to 501 integrated absorbance values, I_λ. Figure 1 shows a semilog plot of these condensed values for the monomer of methanol at 80°. The condensed spectrum has the appearance of that expected from an instrument of lower spectral resolution.

In order to test for the applicability of Beer's law, the relationship

$$I_\lambda = b \times E_\lambda \times A_0 \quad (1)$$

can be written where E_λ is the formal absorptivity observed at wavelength λ, A_0 is the formal added methanol concentration in moles liter^{-1}, and b is the cell length. At low alcohol concentrations

$$E_\lambda \longrightarrow \epsilon_\lambda(1) \text{ as } A_0 \longrightarrow A_1 \quad (2)$$

where $\epsilon_\lambda(1)$ is the molar absorptivity of the monomer at wavelength λ and A_1 is the monomer concentration in moles liter^{-1}. If E_λ is a constant for a range of formal alcohol concentrations when the polymer concentration is low, we can then use Beer's law to determine the monomer concentration, A_1, at all concentrations.

It was found convenient to make use of the sum of the integrated absorbance units, I_λ, for ten successive λ values in this and other tests. A unit $\gamma(\lambda)$ is defined

$$\gamma(\lambda) = \sum_{\lambda-9}^{\lambda} I_{\lambda(\text{nanometers})} \quad (3)$$

where λ is measured in nanometers as a subscript and in micrometers in the parentheses. Values of $\gamma(2.67)/A_0$ along with other basic data are presented elsewhere.[13] These ratios at 40, 80, and 120° were observed to be constant at low concentrations confirming that our spectrophotometer–computer system had the resolution needed to make use of Beer's law and thus measure the monomer concentration.

Although Beer's law may be valid at low concentrations, absorption from the nonhydrogen-bonded O–H proton of acyclic polymers, if they are present, could interfere with the determination of A_1 at higher concentrations. Bellamy and Pace[14] have shown by differential spectroscopy that the polymer end-group absorption peak of methanol in CCl_4 is shifted to 2.750 μm from the monomer peak at 2.745 μm. In order to reduce the chances of end-group interference, all monomer determinations in the present study were made on the R-rotational band in the wavelength region 2.65 to 2.70 μm. It should be noted that no assumption is made here as to the absence of end-group absorption.

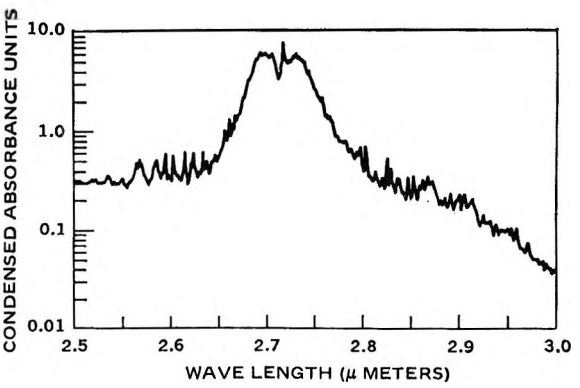

Figure 1. Condensed absorbance curve for 0.0033 mol l.$^{-1}$ of methanol vapor at 80°.

A test will be described in a later section, however, that indicates a negligible interference is possible when shifting monomer determinations over the 2.65–2.70-μm spectral region. Because of the great emphasis to obtain monomer measurements free from end-group absorption, a major portion of this study was performed at concentrations where the polymers represented only a small proportion of the total methanol present. At higher concentrations, where the polymer concentration was significant, the monomer absorption was too intense for accurate measurement in the wavelength region where end-group absorption would be expected. For this reason it was not possible, with the present spectrophotometer cell, to determine whether absorption of acyclic species was present near the Q band.

The monomer concentrations were measured, where possible, with $\gamma(\lambda)$ values in the prime range of 10 to 100 (corresponding to average absorbance values of 0.1 to 1.0) shifting to different wavelength regions as necessary. The validity of this procedure was confirmed by the constancy of $\gamma(\lambda)$ ratios,[13] *e.g.*, a relative error of 0.36% was found for 14 values of $\gamma(2.67)/\gamma(2.66)$ for the prime results of 80°. Values outside the prime region are still usable as the ratios using $\gamma(\lambda)$ values from 1 to 230 were in reasonable agreement with those in the prime region of 10 to 100.

Determination of Polymer Absorbance from 2.75 to 3.00 μm. The absorbance at wavelength λ can be expressed by

$$I_\lambda = b[\epsilon_\lambda(1) \times A_1 + \epsilon_\lambda(2) \times A_2 \ldots + \epsilon_\lambda(n) \times A_n] \quad (4)$$

by applying Beer's law for each possible self-association species. $\epsilon_\lambda(n)$ is the apparent molar absorptivity of all polymers made up of n monomer units at wavelength

(13) Tables of basic data and statistical correlations will appear following these pages in the microfilm edition of this volume of the journal. Single copies may be obtained from the Reprint Dept., ACS Publications, 1155 Sixteenth St., N.W., Washington, D. C. 20036. Remit $4.00 for a photocopy or $2.00 for microfiche.

(14) L. J. Bellamy and R. H. Pace, *Spectrochim. Acta*, 22, 525 (1966).

λ. Equation 4 can also be expressed using the mass-law equilibrium constant, $K_{1,n}$, relating the concentration of the monomer, A_1, with the concentration of each n-mer, A_n

$$I_\lambda = b[\epsilon_\lambda(1) \times A_1 + \epsilon_\lambda(2) \times K_{1\,2} \times A_1^2 \ldots + \epsilon_\lambda(n) \times K_{1,n} \times A_1^n] \quad (5)$$

By using one of the low-concentration monomer curves (0.00058 F at 120°, 0.0012 F at 80°, and an average composite at 40°) expanded so that its absorbance matches the monomer absorption [usually $\gamma(2.68)$] of the sample of interest, it is possible to subtract the monomer absorption. The polymer absorption curves can be represented by

$$\Delta_\lambda = I_\lambda - b \times \epsilon_\lambda(1) \times A_1 = b[\epsilon_\lambda(2) \times K_{1,2} \times A_1^2 \ldots + \epsilon_\lambda(n) \times K_{1,n} \times A_1^n] \quad (6)$$

An example of a plot of Δ may be seen in Figure 2 where two prominent absorption peaks at 2.775 and 2.950 μm are found for methanol vapor at 40°. The region from 2.65 to 2.75 μm is illustrative of the efficiency of this procedure. All of this region is reasonably flat except for the very sharp spike of the Q band at 2.716 μm showing very little change in the shape of the monomer absorption band over a wide range of absorbance values.

Determination of the First Significant n-Mer and Testing for End-Group Interference. Since a major problem in the evaluation of infrared data for self-associating species is to ensure that absorption is really caused by the species ascribed to it, the absorption data of this report were examined in several ways. Figure 1 shows that the monomer absorbs throughout the 2.5–3.0-μm region. That the spectra were due to the monomer was confirmed by the constancy of band shapes using overlays of log absorbance plots at different low concentrations. A trial subtraction of the "monomer" absorption using eq 6 results in the Δ(2.75 to 2.80) values shown in Figure 3. Of the results at the three different temperatures, the 120° curves showed essentially no 2.95-μm absorption, the 80° curves showed 2.95-μm absorption at the higher concentrations, and the 40° curves showed the 2.95-μm peak only at the two highest concentrations. We are concerned with this 2.95-μm absorption region, since end-group absorption, associated with it, if there is some, *might* absorb in the 2.75–2.80-μm region. Since the slope of the data in Figure 3 remains the same for data both with and without 2.95-μm absorption, however, it would appear safe to conclude that any high-polymer end-group absorption is not significantly affecting absorption from 2.75 to 2.80 μm.

The presence of measurable polymer end-group absorption at wavelengths where the monomer was determined would cause A_1 values to be too large. This would in turn cause Δ to be smaller and A_1^n to be larger than their true values. Both effects would have caused measured Δ/A_1^n values to become smaller at high concentrations than at low. No such trend is observed in Figure 3 as the data do not show curvature, *i.e.*, Δ/A_1^n = constant.[13] Since the data fit a second-order line we appear to be observing the first (and only the first) term in eq 6. The 2.775-μm band is consequently assigned to the dimer. Note should be taken that the constancy of Δ/A_1^n does not show that no end-group absorbance occurs from 2.65 to 2.70 μm. The lowest concentrations were measured where at least 99% of the formal concentration was monomer so that no measurable end-group absorption could have been seen. These results consequently only show that any end-group absorption was not sufficient to change the Δ/A_1^n relationship from the lowest to the highest concentrations examined remembering that we sometimes shifted wavelengths in order to use prime absorption values.[13]

There are four factors that reduce the end-group absorption by methanol polymers in the gas phase in the wavelength region 2.65 to 2.70 μm. First, the increased mass of the polymers reduces the intensity of the rota-

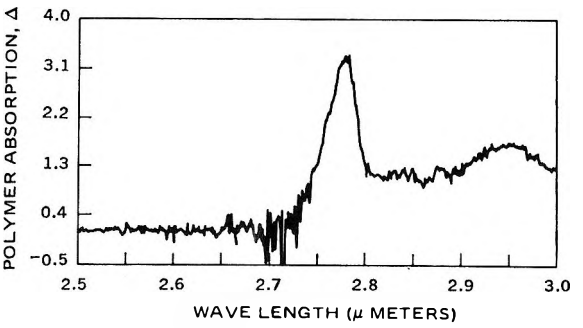

Figure 2. Polymer absorption of methanol vapor at 40°.

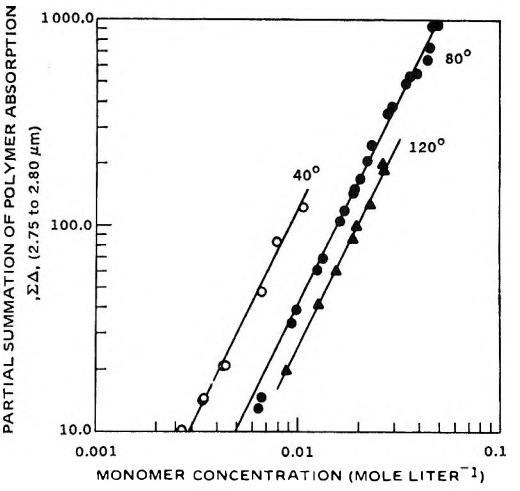

Figure 3. Determination of the n-mer responsible for the 2.775-μm absorption band. Solid lines are second order in monomer concentration.

tional P and R bands compared with those of the monomer. A loss of rotational bands occurs in Figure 2 although experimental "noise" may not make this too apparent. Second, the change in electron density of the O–H group caused by hydrogen bonding has been observed to shift the end-group absorption of the polymer to longer wavelengths in the liquid-phase study of Bellamy and Pace.[14] Third, some of the polymeric material may be cyclic and consequently introduce no end-group absorption. Fourth, the polymer *must* have reduced end-group absorption from that of the equivalent formal amount of monomer units since at least $n - 1$ monomer units must be involved in the hydrogen bonds that hold the polymer together. Thus, the tetramer *at the very most* would have $^1/_4$ the end-group absorption of the four monomer molecules from which it is formed. The first three factors would act to reduce even further the end-group absorption at the wavelengths used to determine the monomer in the present study.

On the basis of the frequency shift and band width of mixed dimers, Reece and Werner[15] also concluded that the 2.775-μm band (which they measured as peaking at 2.778 μm for methanol vapor) was due to the dimer. Similar arguments were made by Murty[16] for the existence of dimers of methanol and other alcohols in the liquid phase. Starting with this band-position information as evidence for the existence of the dimer, then the constancy of the $\Delta(2.75 \text{ to } 2.80)/A_1^2$ data serves to confirm the validity of the mass-action equations, the applicability of the spectrophotometer–computer system to separate absorption curves of the self-association species of methanol vapor, and the absence of end-group interference in the determination of all of the A_1 values in this study.

The 120° absorbance values for Δ at wavelengths greater than 2.8 μm were found to be quite low when the formal polymer concentration was measurable.[13] Hence, not only is the 2.775-μm peak formed by a dimer but its concentration is large enough to be detected by material-balance equations at 120°. Since the dimer equilibrium quotient should increase with decreasing temperature, and since its absorption band was still quite significant at 40° (Figure 2), it is concluded that the dimer is a significant species for a general model of the self-association of methanol vapor over a range of temperatures.

The Ratio Test and Determination of the Second Significant n-Mer. Studies of hydrogen bonding of mixed dimers in solution show that the bound O–H$\cdots$ has a shift from the wavelength of the monomer towards longer wavelengths with increasing heats of reaction.[17–20] A simplified explanation for this is: The stronger the hydrogen bond, the weaker the O–H bond, and hence the shift of the O–H stretch vibration to longer wavelengths. The recent evidence by Barnes and Hallam[21,22] on alcohols in an argon matrix strongly

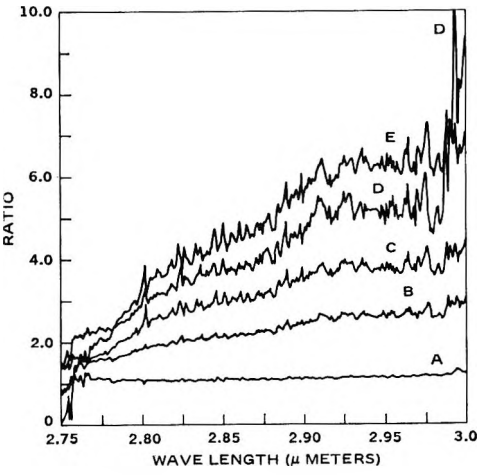

Figure 4. Example of ratio of polymer absorbances, Δ, 80°. Results labeled by monomer concentrations: curve A, 0.0358/0.0343; curve B, 0.0358/0.0284; curve C, 0.0390/0.0284; curve D, 0.0358/0.0238; curve E, 0.0440/0.0284.

favors an acyclic form of the dimer. If the dimer were cyclic, the marked wavelength separation from the higher polymers could be attributed to a weak, bent, hydrogen bond. But an acyclic dimer far removed from the wavelength position of the higher polymers suggests a marked sensitivity of the O–H bond strength to the relative location of the O–H group within the self-association polymer. Thus the acyclic tetramer should have four different "types" of O–H groups which should absorb in four different wavelength regions.[23] It is consequently unlikely that the band position of the smaller self-association polymers would be identical.

In order to test whether wavelength regions, in addition to the dimer, exist where only a single polymer absorbs, a ratio of Δ values for two different concentrations of monomer was made from 2.75 to 3.0 μm. In wavelength regions where absorption of a single n-mer is predominant, the ratio of two Δ values from eq 6 reduces to

$$\Delta(j)/\Delta(k) = [A_1(j)/A_1(k)]^n = \text{constant} \qquad (7)$$

where the letters in the parentheses designate different concentrations. As the hydrogen bonds are expected

(15) I. H. Reece and R. L. Werner, *Spectrochim. Acta* **24A**, 1271 (1968).
(16) T. S. S. R. Murty, *Can. J. Chem.*, **48**, 184 (1970).
(17) M. D. Joesten and R. S. Drago, *J. Amer. Chem. Soc.*, **84**, 3817 (1962).
(18) K. F. Purcell and R. S. Drago, *ibid.*, **89**, 2874 (1967).
(19) G. Sellier and B. Wojtkowisk, *J. Chim. Phys. Physicochim. Biol.*, **65**, 936 (1968)
(20) E. M. Arnett, L. Joris, E. Mitchel, T. S. S. R. Murty, T. M. Gorrie, and P. v. R. Schleyer, *J. Amer. Chem. Soc.*, **92**, 2365 (1970).
(21) A. J. Barnes and H. E. Hallam, *Trans. Faraday Soc.*, **66**, 1920 (1970).
(22) A. J. Barnes and H. E. Hallam, *ibid.*, **66**, 1932 (1970).
(23) A. N. Fletcher and C. A. Heller, *J. Phys. Chem.*, **71**, 3742 (1967).

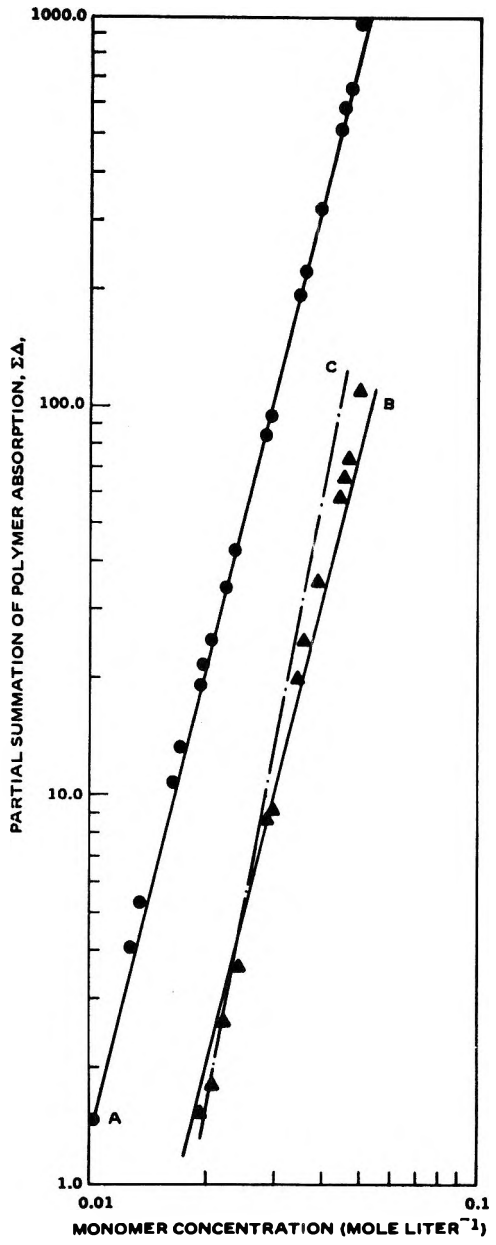

Figure 5. Determination of the n-mer responsible for the 2.95-μm absorption band. Curve A, ●, summation of Δ values from 2.90 to 2.985 μm, solid line is fourth order in monomer. Curve B, ▲, summation of Δ values for 2.985 to 3.00 μm, solid line is fourth order while dashed line C is fifth order in monomer.

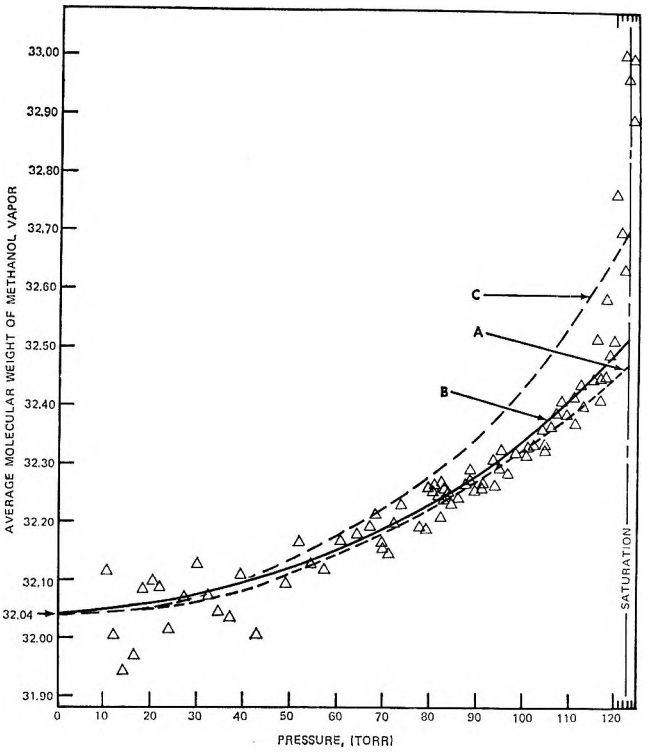

Figure 6. Data of Cheam, Farnham, and Christian[25] for methanol vapor at 25°. Curve A has a root mean square deviation (RMSD) of 0.047 for data up to 90 Torr using the trimer model with a $K_{1,3}$ of 4.38×10^{-7} Torr^{-2}. Curve B has a RMSD of 0.048 for data up to 90 Torr using the monomer–dimer–tetramer model with a $K_{1,2}$ of 3.5×10^{-5} Torr^{-1} and $K_{1,4}$ of 2.0×10^{-9} Torr^{-3} (personal communication from S. D. Christian, 1970). Curve C is calculated using the equilibrium quotients reported by Tucker, Farnham, and Christian[11] for the monomer–trimer–octamer model.

to increase in strength with an increasing amount of self-association,[14] the higher polymers are expected to be observed at increasingly longer wavelengths. Figure 4 shows a range of constant ratios of Δ values with the higher ratios, corresponding to the higher value of n in eq 7, found at the longer wavelengths. The intensities of the small "peaks" common to the ratios in Figure 4 do not change enough to be an indication of new species. They are believed to be artifacts due to the use of a common monomer "blank." Disregarding these experimental errors, a region showing little change in the Δ ratio values with changing wavelengths is observed from 2.90 to 2.985 μm in Figure 4. This range defines the region where primarily a single n-mer absorbs in addition to the monomer if the assumption about the wavelength sensitivity of small self-association species holds. A log plot of Δ against A_1 is given in Figure 5 where it is seen that a fourth-order plot fits the data over a 1000-fold range of $\Sigma_{2900}{}^{2985}\Delta_\lambda$ values. It is concluded that the tetramer is the second significant n-mer.

Evidence for the Rejection of the Trimer as a Major Self-Association Species of Methanol Vapor. A curve-subtraction technique for the dimer was used in the same fashion as for the removal of the monomer absorption. The wavelength region from 2.80 to 2.90 μm was then found to have about the same ratio as from 2.900 to 2.985 μm. After two curve subtractions, we are making an appreciable demand upon the accuracy of the spectrophotometric results to then perform a ratio test. One of the better ratio tests gave an average estimated standard deviation of 0.64 for the 201 ratio values from 2.80 to 3.0 μm with an average ratio

of 2.6. Although the deviations were high, they were random, so it is concluded that no significant absorption occurs within the region 2.80 to 2.90 μm that cannot be attributed to the dimer or the tetramer absorption bands. This lack of trimer absorption band is in agreement with previous material balance studies[11,23] where it was not found possible to fit equations that included the trimer along with the dimer and tetramer. The polymer spectra indicate that the trimer is present only in concentrations too low to be detected by the present system.

The lack of a flat region for high concentration ratios from 2.75 to 2.80 μm is the result of subtracting two very large measurements from each other and then taking a ratio of two sets of these subtractions. It appears that a portion of the original I_λ curves reached the maximum absorbance values that could be measured with a %T instrument near 2.75 μm and that part of the high polymer band absorbs near 2.80 μm.

The plot in Figure 5 for $\Sigma_{2985}^{3000}\Delta_\lambda$ suggests the possibility of an n-mer higher than fourth. As this wavelength region has a low total absorption (Figures 1 and 2), it is subject to increased experimental errors as is evidenced by the cross-over of curves D and E of Figure 4. A *small* amount of a higher n-mer cannot be rejected, however, from the 2.985–3.000-μm results.

Testing for n-Mers Using a Power Series. Values of $\gamma(\lambda)$ from the 80° results were tested every 50 nm from 2.80 to 3.0 μm and at 2.78 μm using the equivalent of eq 5.[13] The purpose of this was to double check the curve-subtracting techniques. All combinations of fits using the monomer and up to two n-mers were examined going up to sixth order comparing the integrated absorbance values, $\gamma(\lambda)$, with the monomer concentration. The least-squares computer program used for this test has been described previously.[23] A number of combinations of n-mers using as high as five in addition to the monomer were also tested. Except for a few cases of the 1–2–4–6 model, all models with more than three terms showed one or more negative coefficients. Using the F-test[24] to compare variances of the valid (no negative coefficients) regression equations, all models other than the dimer were rejected for the $\gamma(2.78)$ values.[13] In a similar fashion, it was found that all models other than the monomer–tetramer had to be rejected using $\gamma(2.95)$ at 80° if only 1–n models were considered (as is suggested by the lack of band shape change from 2.90 to 2.985 μm shown by the ratio test).

Rejection of the Monomer–Trimer–Octamer Model. Using a vapor-density balance that compensates for wall condensation (except near saturation pressure), Cheam, *et al.*,[25] have recently reported evidence favoring the trimer as the major self-association polymer for methanol vapor up to 90 Torr at 25°. They found an insignificant difference between the fit of the 1–3 model from the fit of the 1–3–8 model at pressures up to 116 Torr. This insignificance places particular doubt upon the previous PVT evidence for the octamer.

As shown in Figure 6, a plot using the equilibrium quotients for the 1–3–8 model reported by Tucker, *et al.*,[11] does not fit the vapor-density data. This writer suspects that condensation of methanol upon the container walls introduced a significant experimental error into the results of Tucker, *et al.* The present study, of course, indicates that the monomer–dimer–tetramer model should be given preference to the monomer–trimer model. Certainly the results of Cheam, *et al.* (Figure 6), do not present any evidence to the contrary.

Acknowledgment. The computer programming performed by James R. Nichols, John B. Garber, and John E. Anderson is gratefully acknowledged. I also wish to thank Professor Hans B. Jonassen for a helpful criticism of the manuscript and Professor S. D. Christian for supplying his 1–2–4 equilibrium quotients and RMSD values for the data of Cheam, *et al.*[25]

(24) P. G. Hoel, "Introduction to Mathematical Statistics," 2nd ed, Wiley, New York, N. Y., 1954.

(25) V. Cheam, S. B. Farnham, and S. D. Christian, *J. Phys. Chem.*, **74**, 4157 (1970).

Vapor Pressure Isotope Effects in Methanol

by J. L. Borowitz*[1] and F. S. Klein

The Weizmann Institute of Science, Rehovoth, Israel *(Received September 18, 1970)*

Publication costs borne completely by The Journal of Physical Chemistry

The relative volatilities of the systems methanol-^{18}O–methanol-^{16}O and methanol-^{13}C–methanol-^{12}C have been measured in CH_3OH, CH_3OD, CD_3OH, and CD_3OD. The measurements were made with the aid of an adiabatic distillation column using a kinetic technique. The deuterated methanols were synthesized: CH_3OD by hydrolysis of dimethyl carbonate; CD_3OD by heterogenous catalysis from CO and deuterium; and CD_3OH by isotopic exchange between CD_3OD and NH_4NO_3. Isotopic analysis for deuterium was made by nmr. The ^{18}O and ^{13}C contents of methanol samples were determined mass spectrometrically after decomposing the samples to CO. The results are summarized in Table II. The temperature dependence of the $^{18}O/^{16}O$ relative volatility has led to conclusions concerning the effect of deuterium substitution on the intermolecular forces. Within the temperature range measured, the following can be stated: (a) the intermolecular forces are greater in CD_3OH and CD_3OD than in CH_3OH and CH_3OD, respectively; (b) isotopic substitution by ^{13}C or D in the methyl group causes an increase in the vapor pressure of methanol; (c) this increase is mainly due to changes in the intramolecular vibrational frequencies on condensation; (d) isotopic substitution by ^{18}O or D in the hydroxyl group causes a decrease in the vapor pressure of methanol; (e) while the deuterium substitution appears to affect the hydrogen-bond strength, substitution of ^{13}C and ^{18}O does not. These conclusions are borne out by spectroscopic observations.

Introduction

Isotope effects in vapor pressure have been shown[2a] to be of considerable usefulness in the investigation of intermolecular forces in liquids. This paper describes the measurements of the relative volatilities of a number of isotopic methanols. The relative volatility α of (two components in) a liquid mixture is defined by the equation

$$\alpha = \frac{n}{1-n} \Big/ \frac{N}{1-N} \qquad (1)$$

where n and N are the mole fractions of one component in the vapor phase and in the liquid phase of the system, respectively.

In the case of an ideal mixture of liquids, the vapors of which are ideal gases, α may be shown to be equal to the ratio of the vapor pressures of the pure liquids. The corrections for nonideality are very small in the case of isotopic mixtures, and have been discussed by Rozen[2b] among others.

Applying the Wigner quantum correction to the partition function of the liquid, Herzfeld and Teller[3] showed that the theory of isotope effects on the vapor pressure of liquids requires in a first approximation that the logarithm of the relative volatility α be inversely proportional to the square of the absolute temperature T. It has been observed, however, that in many cases ln α changes sign at a given temperature. The expression of ln $\alpha = f(T)$ must therefore contain at least one other term. Topley and Eyring[4] showed that this term is of the form B/T and that it is associated with a shift in the internal frequency of the component on condensation. The relative volatility may then be given in the form

$$\ln \alpha = A/T^2 - B/T \qquad (2)$$

It has furthermore been shown[2a] that theories which relate isotope effects to changes of mass only fail in the interpretation of experimental results and that structural parameters, such as the relative shift of centers of force *vs.* mass with isotope substitution, have to be considered.

Methanol, being the first member of the alcohol series, was chosen as a comparatively simple molecule for the study of intermolecular bonding in alcohols. The dependence of the intermolecular forces on the distribution of mass between the alkyl and hydroxyl groups as well as the contribution of each of these two groups to the intermolecular bonds were investigated by examining the effect of carbon and oxygen isotope substitution, respectively, on the vapor pressure of deuterium-substituted methanols. The results of these investigations also indicate the form and extent of the effect of isotopic substitution of hydrogen on the intermolecular forces.

Experimental Section

The relative volatilities of methanols were measured by a distillation method taking transient and equilib-

(1) To whom correspondence should be addressed at Soreq Nuclear Research Centre, Yavne, Israel.

(2) (a) Reviewed by J. Bigeleisen, *J. Chem. Phys.*, **34**, 1485 (1961); (b) A. M. Rozen, "Theory of Isotopic Separation in Columns," Office of Technical Services, U. S. Dept of Commerce, Washington 25, D. C.

(3) K. F. Herzfeld and E. Teller, *Phys. Rev.*, **54**, 912 (1938).

(4) B. Topley and H. Eyring, *J. Chem. Phys.*, **2**, 217 (1934).

rium data. This limited the number of pure isotopic species required to four, *viz.* CH_3OH, CH_3OD, CD_3OH, and CD_3OD, and obviated the need for the pure ^{18}O and ^{13}C forms of each of these materials.

The distillations were carried out under total reflux, with zero feed and product rates, in a column with a large boiler and no distillate or feed reservoir. The materials distilled had ^{18}O and ^{13}C concentrations of approximately natural abundance, so that each could be considered as if it were part of a binary system.

The relative volatility of the $^{18}O/^{16}O$ pairs, such as $CH_3{}^{18}OH$–$CH_3{}^{16}OH$, was calculated from the initial rate of change in the isotopic composition of the vapor at the top of the column during a distillation run and from the final composition, *i.e.*, the steady-state enrichment attained in the run. This method has been described by Bigeleisen and Ribnikar.[5] It uses two sets of data to determine the number N of theoretical plates in the column and $\epsilon = \alpha - 1$. The first set is the initial isotope enrichment in the column. The experimental enrichment as a function of time is given by the expression

$$(Q_t - 1)^2 = 2\pi N\epsilon^2 Lt/H \qquad (3)$$

where Q_t is the enrichment at time t of the experiment, L is the liquid flow rate in the column, and H is the liquid hold-up of the column. Equation 3 is a limiting expression for $t \to 0$.

The second set of measurements is the final enrichment Q_∞ at steady state given by the equation

$$Q_\infty = e^{\epsilon N} \qquad (4)$$

ϵ and N can then be evaluated from eq 3 and 4. The $^{12}C/^{13}C$ relative volatility was determined by comparing final enrichments of $^{18}O/^{16}O$ and $^{13}C/^{12}C$ for the same experimental conditions, on the assumption that the number of theoretical plates in the column is the same for both species

$$\epsilon_c = \epsilon_o \ln Q_{\infty\,\text{carbon}}/\ln Q_{\infty\,\text{oxygen}}$$

There are not sufficient data available to check this assumption for methanol. Using an empirical formula due to Murch[6] one can show that the difference between the number of theoretical plates of a column distilling H_2O or D_2O under similar conditions is not more than 2.5%. Since isotope effects in methanol are even smaller than those in water, it can be assumed that the number of theoretical plates of a given column is practically independent of whether CH_3OH, CD_3OD, or any other isotopic methanol is being distilled.

The column (Figure 1) used in these experiments is an adiabatic, packed column, designed according to a suggestion by Dostrovsky.[7] The column A itself is a Pyrex tube of 1-cm i.d., which is packed with "Helipak 3012" stainless-steel packing to a height of 2 m. It is surrounded by a glass vacuum jacket B for insulation. In order to minimize heat losses across the vacuum

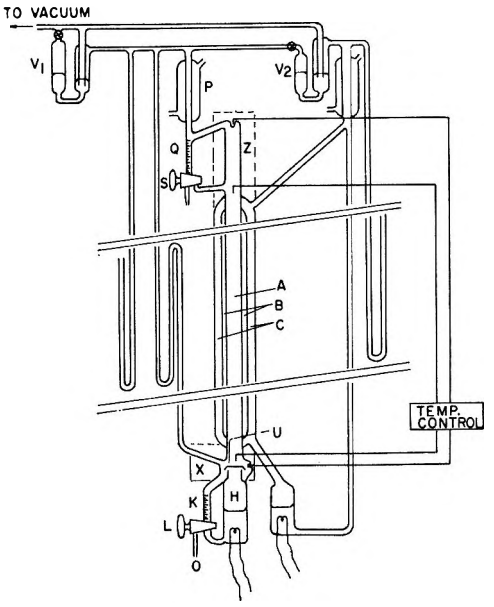

Figure 1. Scheme of column.

jacket it is surrounded by a third tube C in which methanol vapor is circulated at the same pressure as that at the top of the distillation column. The top of the column is connected to the condenser P, the return line of which is equipped with a buret Q which is used to measure the liquid flow from the condenser. The two-way buret valve S is also used for extracting samples of the distillate. The region between the top of the column packing and condenser P is surrounded by a heating element Z which serves both to eliminate heat losses and to preheat the liquid leaving the condenser to the temperature of the top of the packing. At the bottom of the column the vapor is separated from the liquid by means of a cap U, over the vapor line coming from the boiler H. The liquid flow from the column into the boiler is measured in the vacuum-jacketed buret K, by closing the two-way valve L for short periods. The region between the boiler and the column is also surrounded by a heating element X.

The pressure in the column is controlled by a manostat V_1. The pressure in the vapor jacket is controlled by the manostat V_2, which, in turn, is controlled by V_1. The heating elements X and Z are controlled by a thermistor sensing circuit which keeps the temperature on the outside wall of the region equal to that of the vapor on the inside.

The materials investigated were the isotopic methanols: CH_3OH, CH_3OD, CD_3OD, and CD_3OH.

The CH_3OH (Methanol Puriss. p.a., Fluka) was dried by reaction with magnesium in the presence of iodine to less than 0.01% moisture content, as determined by Karl Fischer reagent. This was necessary in

(5) J. Bigeleisen and S. Ribnikar, *J. Chem. Phys.*, **35**, 1297 (1961).
(6) D. P. Murch, *Ind. Eng. Chem.*, **45**, 2616 (1953).
(7) I. Dostrovsky, private communication.

order to minimize any possible effect of water on the relative volatility of the methanol.

CH_3OD was prepared by the hydrolysis of dimethyl carbonate after Streitwieser, Verbit, and Stang.[8] Using D_2O with a deuterium content of over 99.5% the methanol obtained contained over 98% deuterium in the hydroxyl group, as determined by nmr spectroscopy. This material was dried on "Drierite" and distilled in the column to over 99% deuterium content in the hydroxyl before starting measurements.

CD_3OD was synthesized from CP carbon monoxide (The Matheson Co.) and 99.8% pure deuterium gas (General Dynamics) on Harshaw zinc chromite Zn 0314 1/4-in. catalyst. The synthesis was carried out at a pressure of 4 atm absolute in a glass system similar to that used by Beersmans and Jungers.[9] The product methanol contained over 99% deuterium in both the methyl and hydroxyl groups, as determined by nmr spectroscopy, and less than 0.01% moisture.[10]

CD_3OH was prepared from CD_3OD by exchange with ammonium nitrate (ACS purity). The ammonium nitrate was dried before use to constant weight over P_2O_5 in a vacuum desiccator. CD_3OD (76 g) was vacuum distilled onto ammonium nitrate (17 g). The salt was allowed to dissolve, and the CD_3OD was then vacuum distilled onto a further batch of ammonium nitrate. Solution[11] and distillation were repeated until the hydroxyl deuterium content fell to below 1%, as determined by nmr spectroscopy. CD_3OH was obtained with a yield of about 95%. The moisture content of the product was less than 0.1%.

Methanol samples from the distillation experiments were analyzed by mass spectrometer for the ^{13}C and ^{18}O content. The samples (approximately 0.2 ml for a distillate sample, and 0.5 ml for a boiler sample) were decomposed on a platinum filament at approximately 900° to carbon monoxide and hydrogen in a decomposition vessel. This vessel was equipped with a silver–palladium thimble through which the hydrogen was removed as it was formed.[12] The abundance ratios

$$\frac{\text{mass 28}}{\text{mass 29}} \quad \text{and} \quad \frac{\text{mass 30}}{\text{mass 28} + \text{mass 29}}$$

in the CO formed were measured on an Atlas M 86 mass spectrometer. The ^{13}C and ^{18}O concentrations were calculated from these ratios by comparison with the respective ratios obtained from a standard sample of CO. The measured ratios were reproducible to ±0.5% on a single sample. The standard deviation of the average of the ratios obtained from six identical samples of methanol was ±0.1%.

In the calculation of enrichments the contribution of $^{12}C^{17}O$ to the mass 29 peak had to be taken into account. This was done by assuming that the ^{17}O enrichment in a distillation experiment is 1/2 of the ^{18}O enrichment. An error of 10% in this estimate leads to an error of only 0.1% in the calculated ^{13}C enrichment.

Results

An example of the operating conditions and the results of a single experiment are given in Table I.

Table I: Experimental Parameters of a Typical Distillation Experiment

CH_3OH at 430 Torr	
Flow rate of liquid, ml/min	0.99 ± 0.02
Hold-up, ml	8.3 ± 0.1
Boiler content, ml	50.0
Pressure drop across column, Torr	16.0 ± 3
$N\epsilon^2$	2.49×10^{-3}
Final ^{18}O enrichment, $Q_{^{18}O}$[a]	1.77
$N\epsilon$	0.572
$\epsilon_{^{18}O}$ ($\epsilon = \alpha - 1$)	4.22×10^{-3}
Number of theoretical plates, N	132.0
Final ^{13}C enrichment, $Q_{^{13}C}$	0.948
$\epsilon_{^{13}C}$	-4.2×10^{-4}

[a] Q = (isotope concentration in boiler)/(isotope concentration in condenser) at steady-state conditions.

At least three such experiments were done at each pressure and for each of the isotopic methanols (except for CD_3OH). In some cases, up to seven experiments were carried out on a single material at one pressure in order to increase the precision of the results.

Assuming that the number of theoretical plates N in the column is not dependent on the isotopic composition of the methanol being distilled, the results for N can be averaged over all the experiments at any single pressure. The average $\bar{N}$ was thus used to calculate ϵ_o and ϵ_c from the Q_∞ data for each experiment. The ratio R of the final enrichments Q_∞ of the ^{13}C and ^{18}O isotopes was averaged over all the experiments at one pressure for a given material. This ratio was then used to obtain the relative volatility for ^{13}C from the ^{18}O result for the same material and pressure.

Table II presents the average values of the relative volatilities as a function of the vapor pressure P for all four ^{18}O–^{16}O and ^{13}C–^{12}C methanol pairs. The errors given in the table are standard deviations.

Discussion

Summarizing the present results we observe that the vapor pressure of methanol increases with ^{13}C substitution in the methyl group and decreases with ^{18}O substitution in the hydroxyl group.

(8) A. Streitwieser, Jr., L. Verbit, and P. Stang, *J. Org. Chem.*, 29, 3706 (1964).

(9) J. Beersmans and J. C. Jungers, *Bull. Soc. Chim. Belg.*, 56, 72 (1947).

(10) J. L. Borowitz, *J. Catal.*, 13, 106 (1969).

(11) The repeated solution of ammonium nitrate in the methanol was necessary because it was found that hydrogen exchange takes place only with the dissolved salt, albeit quickly, while exchange between dissolved and undissolved salt at room temperature was too slow to be detectable over a period of 24 hr.

(12) J. L. Borowitz, A. Raviv, P. Ronah, D. Sadeh, D. Samuel, and F. Klein, *J. Label. Compounds*, 1, 259 (1965).

Table II: Average Relative Volatilities

$\epsilon = \alpha - 1$

Pressure, Torr	Temp, °C	CH_3OH	CH_3OD	CD_3OH	CD_3OD
		$\epsilon_{^{18}O} \times 10^3$			
760	64	2.6 ± 0.3	2.2 ± 0.2	1.7 ± 0.5	1.0 ± 0.3
420	51	3.7 ± 0.2	3.4 ± 0.2	3.2 ± 0.5	2.6 ± 0.2
250	39	4.6 ± 0.2	4.3 ± 0.3		3.8 ± 0.3
200	35	5.0			

Pressure, Torr	CH_3OH	CH_3OD	CD_3OH	CD_3OD
	$\epsilon_{^{13}C} \times 10^4$			
760	-2.8 ± 0.5	-2.9 ± 0.6	-3.4 ± 1.0	-2.0 ± 0.6
420	-3.4 ± 0.3	-4.1 ± 0.3	-4.2 ± 0.8	-4.7 ± 0.4
250	-3.3 ± 0.4	-4.7 ± 0.6		-6.1 ± 0.5
200	-3.6 ± 0.4			

The effect of isotope substitution of ^{18}O in the hydroxyl group is about one order of magnitude greater than that of ^{13}C substitution in the methyl group. (Similar relative effects were observed for D-substitution in the hydroxyl and methyl groups.[9])

Our results for ϵ_o and ϵ_c of CH_3OH are generally in fair agreement with previous measurements[13-16] (see Table III). Only the ϵ_c value of Zelvenski differs significantly from the present value, but Rozen's recalculation brings this result more into line.

Table III: Comparison of Results at Atmospheric Pressure with Those of Previous Workers

$\epsilon_o \times 10^3$	$\epsilon_c \times 10^4$	Ref
3.0	−2.0	14
2.9	−5.0	15
1.5	−2.3	16
2.6	−2.8	Present paper for CH_3OH at 760 Torr

The relative volatility data, ϵ_o and ϵ_c, were fitted to the equation $T\epsilon = A/T + B$, using the least-squares method. The calculated constants A and B are given in Table IV. Figure 2 shows plots of this function for the oxygen data.

The above equation was given by Bigeleisen, *et al.*,[17] in the following form

$$\ln \alpha = \frac{A}{T^2} - \frac{B}{T} \tag{5}$$

The term A/T^2 results from the quantum correction[18] to the partition function of a monoatomic liquid–vapor system. A is given by

$$A = \frac{h}{24k^2}[\overline{F_1^2}/M_1 - \overline{F_2^2}/M_2] \tag{6}$$

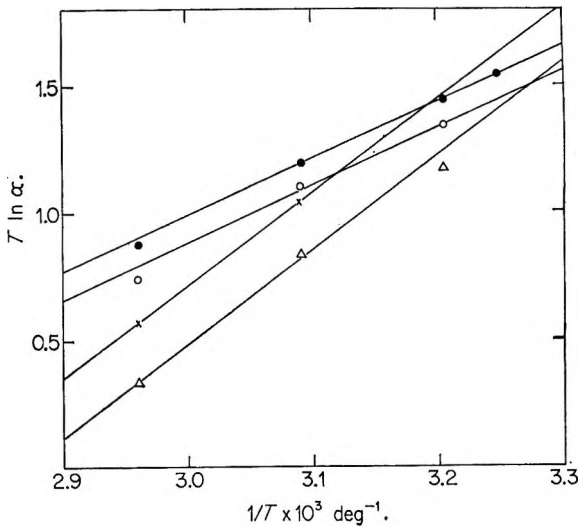

Figure 2. Temperature dependence of ^{18}O relative volatilities: ●, CH_3OH; ×, CD_3OH; ○, CH_3OD; △, CD_3OD.

where $\overline{F^2}$ is the mean square force[19] on an atom (or a molecule, as a first approximation, as in our case). M is the molecular weight.[20] The constant B,[22] given by

$$B = \frac{h}{2k}\left(\sum_1^{3n-6} (\nu_{\text{gas}_1} - \nu_{\text{liq}_1}) - \sum_1^{3n-6} (\nu_{\text{gas}_2} - \nu_{\text{liq}_2})\right) \tag{7}$$

corrects for changes in the internal frequencies ν_T on condensation.

Comparing CH_3OH and CH_3OD (Table IV), we see that the values of A are equal within experimental error. The same is true of the pair CD_3OH and CD_3-

(13) I. Dostrovsky, E. D. Hughes, and D. Llewellyn, *Bull. Res. Counc. Isr.*, **1**, 133 (1954).

(14) P. Baertschi, H. Kuhn, and W. Kuhn, *Nature*, **171**, 1018 (1953).

(15) Ya. D. Zelvenski, V. E. Sokolov, and V. A. Shalygin, *Nauch. Dokl. Vyssh. Shk., Khim. Khim. Technol.*, 388 (1958).

(16) Reference 2b, p 487.

(17) J. Bigeleisen, M. J. Stern, and W. A. van Hook, *J. Chem. Phys.*, **38**, 489 (1963).

(18) L. D. Landau and E. M. Lifshitz, "Statistical Physics," Pergamon Press, London, 1958, p 293.

(19) $\overline{F^2}$ is normally *not* assumed to change with isotopic substitution as it is a function of electronic interactions only. Deuterium substitution, however, is known to affect interatomic distances,[23] so that in this case $\overline{F^2}$ must change on deuterium substitution. ^{18}O substitution in methanol is therefore a useful tool to study these changes in $\overline{F^2}$.

(20) In the case of polyatomic molecules the moments of inertia should be taken into account. Friedmann[21] incorporated the moments of inertia of a linear molecule into an "effective mass," which is substituted for the mass M in eq 6. In order to examine the effect of intermolecular librations, methanol was considered as a linear molecule with moment of inertia equal to the average of the moments of inertia about the two principal axes nearly perpendicular to the CO bond. Replacing the masses in eq 6 by effective masses did not however alter the conclusions of the present discussion and for the sake of simplicity the ordinary mass, M, is therefore used in this discussion.

(21) H. Friedmann, *Advan. Chem. Phys.*, **4**, 225 (1962).

(22) M. J. Stern, W. A. van Hook, and M. Wolfsberg, *J. Chem. Phys.*, **39**, 3179 (1963).

Table IV: Values of Coefficients A and B of Equation 5[a,b]

$$\ln \alpha = \frac{A}{T^2} - \frac{B}{T}$$

	CH_3OH	CH_3OD	CD_3OH	CD_3OD
		^{18}O		
$A \times 10^{-3}$	2.2 ± 0.4	2.5 ± 0.4	4.1 ± 0.4	3.5 ± 0.6
B	-5.6 ± 1.3	-6.7 ± 1.1	-11.6 ± 1.6	-9.9 ± 1.8
		^{13}C		
$A \times 10^{-3}$	-0.3 ± 0.05	-0.3 ± 0.05	-0.2 ± 0.2	-0.5 ± 0.1
B	0.7 ± 0.2	0.7 ± 0.15	0.5 ± 0.5	1.3 ± 0.3

[a] See ref 17. [b] Relative volatilities for ^{18}O isotope substitution in deuterated methanols.

OD. However, the values of A for the second pair are greater than those of the first pair.

Using expression 6 for A and neglecting the small difference in $\overline{F^2}$ on ^{18}O substitution,[20] *i.e.*, $\overline{F_1}^2 = \overline{F_2}^2$, we calculate

$$\frac{A_{CH_3OH}}{A_{CH_3OD}} = \left(\frac{1}{32} - \frac{1}{34}\right)\overline{F^2}_{CH_3OH} \Big/ \left(\frac{1}{33} - \frac{1}{35}\right)\overline{F^2}_{CH_3OD} = \frac{2.20}{2.51}$$

i.e.

$$\frac{\overline{F^2}_{CH_3OH}}{\overline{F^2}_{CH_3OD}} = 0.83 \pm 0.2$$

We find that the intermolecular force in CH_3OH is smaller than that in CH_3OD. The fact that CH_3OH is more volatile than CH_3OD may thus be at least partly due to differences in the intermolecular forces in the two liquids. There should also be an intramolecular contribution to ln α because we are dealing with molecules and not with atoms, but it is apparently smaller in this case than the intermolecular contribution. The same, again, holds for the pair CD_3OH–CD_3OD where $\overline{F^2}_{CD_3OH}/\overline{F^2}_{CD_3OD} = 0.88 \pm 0.2$.

However, when considering the pair CD_3OH–CH_3OD, we obtain similarly to the above

$$\overline{F^2}_{CD_3OH}/\overline{F^2}_{CH_3OH} = 2.2 \pm 0.2$$

that is the intermolecular force is greater in CD_3OH than in CH_3OH, and similarly, the intermolecular force is greater in CD_3OD than in CH_3OD.

In these two cases, however, the heavier molecules are *more* volatile.[9] Clearly, the intramolecular contribution to the relative volatility is greater than the intermolecular contribution in the methyl-deuterated molecules. The fact that the B term for the methyl-deuterated methanols is larger than that for the methyl-unsubstituted molecules supports this conclusion. An accurate analysis of the intramolecular contribution is not warranted at present, considering the given accuracy of the data.

The respective values of A and B for isotopic carbon substitution (Table IV) are about one order of magnitude smaller and of opposite sign than the analogous oxygen values. The analysis of these values is, however, less straightforward than that of the oxygen values. The reason for this is that the isotope effects here may include additional factors neglected in the treatment of the ^{18}O results. This is discussed further below.

The above conclusions on the intermolecular forces in deuterated methanols are borne out by spectroscopic data. The O–H out-of-plane bending vibration of frequency ν_T is a good indicator of the strength of the intermolecular force.[23] In the liquid this vibration replaces the internal rotation about the C–O bond in the gas. The frequency increases sharply on condensation (see Table V) and is also strongly isotope dependent. Clearly, the larger this frequency in the liquid, the stronger is the intermolecular force. We see from Table V that ν_T is always larger in the deuterio-methyl molecule than in the protium-methyl methanol.

With regard to the intramolecular effects, we consider the frequencies, ν_s and ν_b, of the OH stretching and the inplane bending vibrations, respectively. These frequencies change markedly on condensation. Their values in the liquid phase have been used as measures of hydrogen bonding.[23] Table V shows that the sum of these frequencies, again, is larger in the CD_3 molecules than in the CH_3 molecules.

We see, therefore, that the spectroscopic data confirm the conclusions drawn from the ^{18}O results; the B term is always larger in a heavy molecule (see Table IV), *i.e.*, intramolecular effects are larger in a heavier molecule. In general, we can conclude that, in methanol, when the heavier molecule is more volatile than the light, this is due to domination of the relative volatility by intramolecular effects.

The vapor pressure of the deuterated methanols increases in the order CH_3OD, CD_3OD, CH_3OH, CD_3-

(23) G. C. Pimentel and A. L. McLellan, "The Hydrogen Bond," W. H. Freeman, San Francisco, Calif., and London, 1960, p 75.

Table V: Vibrational Frequencies of Methanol[a,b] in Wave Numbers (cm^{-1})

	CD_3OH		CH_3OH		CD_3OD		CH_3OD	
	Gas	Liquid	Gas	Liquid	Gas	Liquid	Gas	Liquid
ν_s	3690	3310	3682	3337	2724	2474	2720	2485
$\Delta\nu_s$	380		345		250		235	
ν_b	1297	1391	1346	1420	776	818	863	942
$\Delta\nu_b$	−94		−74		−42		−79	
ν_T	270	665	270	655	213	483	213	475
$\Delta\nu_T$	−395		−385		−270		−262	

[a] M. Falk and E. Whalley, *J. Chem. Phys.*, **34**, 1554 (1961); M. Margottin-Maclou, *J. Phys. Radium*, **21**, 634 (1960). [b] $\Delta\nu = \nu_{gas} - \nu_{liquid}$.

OH.[9] This sequence is the same as that in which the sum $\nu_s + \nu_b$ increases, and opposite to the order of increase in ν_T. It would appear that the changes in the vapor pressures of the deuterated methanols are directly correlated with the changes in hydrogen-bond strength on isotopic substitution.

The ^{18}O and ^{13}C effects, on the other hand, decrease in the order of the molecular weights, *i.e.*, in the order CH_3OH, CH_3OD, CD_3OH, CD_3OD. This indicates that these effects are not related to the changes in the hydrogen bond strength on isotopic substitution.

The ^{13}C and CD_3 relative volatilities are an order of magnitude smaller than those of the ^{18}O and hydroxyl-deuterium substituted species. This means that, for the methyl-substituted species, the inter- and intramolecular contributions almost balance one another. Thus small effects which do not affect the ^{18}O result significantly (to the accuracy of the present measurements) may make up a significant part of the ^{13}C relative volatility. Such effects may be changes in the intermolecular force constants with temperature.[24] The fact that the ^{13}C effects are so much smaller than the ^{18}O effect can be ascribed, in part, to the position of the methyl group with regard to the hydrogen bond in the liquid. Following Friedmann,[21] we note that increasing the mass of the methyl group moves the center of gravity of the molecular away from the center of interaction, thus increasing the zero-point energy of the molecule in the liquid phase, and thereby decreasing the intermolecular contribution to the isotope effect.

In the case of ^{18}O substitution the center of gravity moves in the opposite direction and the intermolecular contribution is increased. We see that with ^{13}C substitution inter- and intramolecular contributions tend to balance, whereas with ^{18}O substitution a large isotope effect will be observed.

(24) J. N. Finch and E. R. Lippincott, *J. Chem. Phys.*, **24**, 908 (1956); *J. Phys. Chem.*, **61**, 894 (1957).

Self-Diffusion Studies of Gel Hydration and the Obstruction Effect

by Alan G. Langdon[1] and Henry C. Thomas*

Department of Chemistry, University of North Carolina, Chapel Hill, North Carolina 27514 *(Received December 7, 1970)*

Publication costs assisted by the Petroleum Research Fund

By modifying the capillary method there has been obtained a moderately rapid and quite accurate means of measuring trace diffusion coefficients in chemically equilibrated gels. Trace diffusion coefficients have been obtained for the anions chloride and iodide at various gel compositions and total salt concentrations. The dependence on gel composition is linear and independent of electrolyte concentration below 0.1 *M*. Trace cation diffusion coefficients for sodium showed a similar behavior over the concentration range 0.05 to 0.5 *M*. The results are adequately accounted for in terms of a model picturing the gel as a collection of randomly oriented and heavily hydrated needles.

Introduction

Agar gels have long been of interest as diffusion media.[2] In recent years investigation of their properties has been motivated by the advent of gel filtration chromatography, gel electrophoresis, and attempts to use gels in precise methods for measuring aqueous diffusion coefficients.[3-5]

One recent study[3] sought to determine the extent to which the effect of the macromolecules in an agar gel could be described as mechanical obstructions in the paths of diffusing ions. Such a description appeared adequate for sodium and cesium diffusion in gels of up to 0.04 weight fraction of agar. The diffusion coefficients varied linearly with gel composition according to

$$D_g/D_s = 1/F = 1/(1 + \alpha w) \qquad (1)$$

where D_g = diffusion coefficient in gel, D_s = diffusion coefficient in pure aqueous solution, F = a quantity considered to be the square of the path lengthening relative to pure solution, w = weight fraction of anhydrous agar in gel, α = slope of the plot of D_g against w divided by D_s. An extrapolation to $w = 0$ allowed an estimate of D_s.

In subsequent investigations[6,7] with equilibrated gels, eq 1 was found inadequate at concentrations lower than 5.0×10^{-2} *M* for strontium, sodium, and cesium diffusion. It was suspected that the deviations resulted from the small but significant cation exchange capacity of agar.[8,9] Anion diffusion should be much less affected. We thus sought to test further the usefulness of the obstruction effect concept by studies of anion diffusion that would indicate whether additional complicating effects, *e.g.*, a change in macromolecular geometry with electrolyte concentration, were present. Providing such effects were absent, it should be possible to use the diffusion data to reveal something about the macromolecular structure and hydration of the gel.

The majority of previous cation studies were performed using the chloride salts. Fortunately a suitable chlorine isotope, Cl^{36}, is available for tracer studies. A soft β emitter, Cl^{36} could not be used in the continuous monitoring methods designed for hard γ emitters. A new technique was needed, and for this the adaption of a capillary method offered the advantage of being an absolute method, which for a diffusion medium such as agar should be capable of high accuracy. The small volume of gel involved in each measurement would minimize problems of quenching during liquid scintillation counting, the most convenient method of estimating soft β activity. Because the method could be used for all radioactive isotopes, it would also provide a means of checking the previous results and extending the range of observations to low concentrations.

Experimental Section

The Capillary Method. The capillary method[10,11] was adapted for use with gelatinous media. Agar gels of compositions greater than about 0.5% by weight agar were found ideal for the study of diffusion by this method. The sharp boundaries formed by slicing at the ends of the capillary showed no evidence of deterioration after prolonged contact with solution or upon immersion and removal from solution.

The capillary tubes were 1.3–3.5-cm sections of uniform bore, thick wall capillary tubing, with internal diameter of *ca.* 0.6 mm and volumes of 0.012–0.019 cc

(1) Visiting Post Doctoral Research Associate.

(2) F. Voigtlander, *Z. Phys. Chem.* (*Leipzig*), **3**, 316 (1889).

(3) A. L. Slade, A. E. Cremers, and H. C. Thomas, *J. Phys. Chem.*, **70**, 2840 (1966).

(4) G. F. Allen, H. Schurig, A. L. Slade, and H. C. Thomas, *ibid.*, **67**, 1402 (1963).

(5) G. Spalding, *ibid.*, **73**, 3389 (1969).

(6) I. H. Doetsch, Ph.D. Thesis, The University of North Carolina at Chapel Hill, 1970.

(7) R. J. Passarelli, Ph.D. Thesis, The University of North Carolina at Chapel Hill, 1968.

(8) C. Araki, *Bull. Chem. Soc. Jap.*, **29**, 543 (1956).

(9) T. Currie, *Chem. Ind.* (*London*), **5**, 116 (1955).

(10) J. S. Anderson and K. Saddington, *J. Chem. Soc.*, S381 (1949).

(11) A. C. Wahl and N. A. Bonner, "Radioactivity Applied to Chemistry," Wiley, New York, N. Y., 1951, Chapter 4.

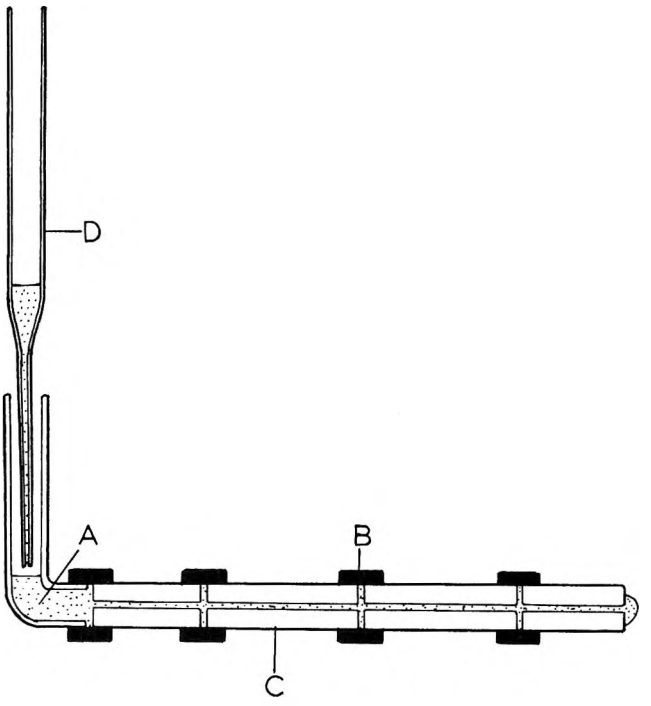

Figure 1. Apparatus for filling capillary tubes: A, agar solution; B, rubber seal; C, capillary tubing; D, medicine dropper.

(calibrated by the weight of mercury needed to fill them).

Filling procedure was as follows. The tubes were placed end to end on a strip of adhesive tape (wide enough to wrap halfway around the tubes), the gaps between the tubes were sealed with a small section of rubber tubing, at one end a glass elbow was attached, and the melted gel was added through it (see Figure 1). Solidification of the gel during filling was prevented by thermostating the apparatus at *ca.* 60°. The filled tubes were left at room temperature for 5 min for the gel to become firm. They were then separated by slicing through gel and adhesive tape (in that order) with a sharp razor blade. With a little practice, this operation could be performed to leave a clean gel boundary and a column of agar gel with a length accurately defined by the length of the glass capillary tubing.

Diffusion runs were started by suspending the tubes in a 2000-ml flask filled with a solution at the appropriate concentration, magnetically stirred, and thermostated at 25.0 ± 0.1°. At the end of a run, usually after the activity had diminished to about one-third, the tubes were removed and the gel extracted into 20-ml counting vials by air pressure or centrifugation. Finally the liquid content of each vial was made up to 1.0 ± 0.1 ml with NaCl solution.

Counting Procedures. A 14-ml aliquot of a scintillation fluid, prepared from 60 g of naphthalene, 100 ml of methanol, 20 ml of ethylene glycol, and 4 g of BBOT (Packard) diluted to 1 l. with dioxane,[12] was added to each sample. Cl^{36} was counted by a Mark 11 Nuclear-Chicago three-channel liquid scintillation counter, quenching effects being checked by the channel ratios method. (The presence of the aqueous solution in the scintillation fluid caused some overall quenching, but this was constant to within ±0.1% for all samples when water contents did not vary by more than 0.1 g.)

Na^{22} and I^{131} were counted in a well counter with a 3-cm NaI(Tl) crystal and a Packard Auto-Gamma spectrometer. Na^{22} and Cl^{36} in double labeling experiments could not be discriminated adequately by liquid scintillation counting. However, from the combined liquid scintillation count and the Na^{22} count from crystal scintillation counting, the activities of Na^{22} and Cl^{36} were resolved allowing the simultaneous study of Na^+ and Cl^- self-diffusion in the same gel sample in some experiments.

Calculations. The solution of the diffusion equation for diffusion from a capillary open at both ends and immersed in an infinite volume of solution is

$$\frac{C_t}{C_0} = \frac{8}{\pi} \sum_{n=0}^{\infty} \frac{1}{(2n+1)^2} \times \exp[-(2n+1)^2\pi^2 Dt/4(a/2)^2] \quad (2)$$

where C_t = average concentration (of radioactive isotope) at time t, C_0 = initial concentration, D = self-diffusion coefficient of ion in gel, a = length of capillary, t = time of diffusion. The ratio, C_t/C_0 (= Q_t/Q_0, where Q_t = activity at time t = t and Q_0 = activity at time t = 0) was estimated from the capillary volume and the activity per unit volume of the agar used to fill the tube. The latter was determined from the activity of a weighed amount of the labeled agar.

Preparation of Gels. Gels were prepared from "Difco certified" purified agar using 0.1 *M* solutions of Analytical reagent NaCl and NaI. They were dialyzed at the appropriate concentrations with daily changes of solution for 7 days. Samples were then transferred to 2-ml test tubes and equilibrated with "spiked" solutions of the same total concentration as solutions used in dialysis. After 24 hr the supernatant solution was withdrawn, and the gel was melted and injected into the capillaries with a medicine dropper.

Results

Experimental Error. The diffusion coefficient data of Tables I, II, and III include mean deviations between observations, the number of these being given in the parentheses. Mean deviations of up to 1% probably result from small unavoidable variations in preparation and manipulation of the gels.

Preliminary Investigations. In preliminary experiments Na^{22} self-diffusion results showed no significant

(12) G. A. Bray, *Anal. Biochem.*, 1, 279 (1960).

Table I: Sodium Self-Diffusion Coefficients at Various Stirring Rates; NaCl Concentration = 0.01 *M*

Stirring rate	$D_g \times 10^6$					Mean	
Unstirred	1.052	0.985	0.986	1.021	1.027	1.008 (5)	0.024
250 rpm (0.5-in. magnetic stirring rod)	1.093	1.063	1.096	1.112	1.113	1.095 (5)	0.014
250 rpm (1-in. magnetic stirring rod)	1.130	1.136	1.144	1.129	1.135	1.135 (5)	0.004
400 rpm (1-in. magnetic stirring rod)	1.152	1.147	1.132	1.151	1.141	1.155 (5)	0.010
600 rpm (1-in. magnetic stirring rod)	1.144	1.121	1.138	1.133	1.129	1.133 (5)	0.006
						1.141	0.007

Table II: Sodium Self-Diffusion Coefficients at Various NaCl Concentrations

c, mol/l.	100*w*	$D_g \times 10^6$	Mean
2.0	0.67	1.097	0.015 (3)
	1.0	1.051	0.046 (3)
	2.0	1.056	0.013 (3)
	3.0	1.011	0.017 (3)
	4.0	1.017	0.016 (3)
0.5	0.33	1.278	0.009 (2)
	1.0	1.209	0.017 (3)
	2.0	1.208	0.001 (3)
	3.0	1.157	0.005 (5)
	4.0	1.110	0.015 (4)
0.1	0.5	1.315	0.007 (5)
	1.0	1.247	0.018 (5)
	2.0	1.232	0.026 (5)
	3.0	1.196	0.009 (5)
	4.0	1.147	0.006 (4)
0.0056	0.5	1.295	0.014 (5)
	1.0	1.236	0.020 (4)
	2.0	1.224	0.017 (4)
	3.0	1.186	0.002 (3)
	4.0	1.151	0.007 (4)
0.01	0.67	1.204	0.008 (5)
	1.0	1.197	0.010 (4)
	2.0	1.133	0.010 (5)
	3.0	1.080	0.004 (2)
	4.0	1.042	0.004 (4)
0.001	0.5	1.305	0.010 (6)
	1.0	1.113	0.015 (5)
	2.0	1.081	0.040 (9)
	3.0	1.029	0.014 (2)
	4.0	1.014	0.037 (4)
0.0004	0.67	1.006	0.042 (3)
	1.0	0.995	0.016 (3)
	2.0	0.901	0.009 (2)
	3.0	0.856	0.016 (3)
	4.0	0.781	0.007 (2)
0.0001	0.67	0.882	0.010 (2)
	1.0	0.851	0.026 (3)
	2.0	0.814	0.009 (2)
	3.0	0.719	0.049 (2)
	4.0	0.648	0.021 (2)
0.00001	0.33	0.936	0.058 (3)
	1.0	0.773	0.023 (5)
	2.0	0.624	0.022 (4)
	3.0	0.497	0.013 (3)
	4.0	0.444	0.034 (3)

Table III: Chloride Self-Diffusion Coefficients at Various NaCl Concentrations

c, mol/l.	100*w*	$D_g \times 10^6$	Mean
1.0	0.67	1.709	0.008 (3)
	1.0	1.685	0.025 (3)
	2.0	1.677	0.001 (3)
	3.0	1.655	0.008 (3)
	4.0	1.636	0.008 (2)
0.5	0.33	1.836	0.036 (2)
	1.0	1.799	0.060 (7)
	2.0	1.787	0.020 (8)
	3.0	1.780	0.045 (8)
	4.0	1.761	0.016 (9)
0.1	0.5	1.927	0.013 (5)
	1.0	1.870	0.025 (5)
	2.0	1.830	0.025 (5)
	3.0	1.781	0.012 (5)
	4.0	1.735	0.014 (4)
0.01	0.67	1.983	0.008 (3)
	1.0	1.931	0.012 (5)
	2.0	1.862	0.010 (5)
	3.0	1.814	0.035 (4)
	4.0	1.791	0.016 (3)
0.001	0.67	2.007	0.011 (3)
	1.0	1.960	0.006 (4)
	2.0	1.921	0.013 (4)
	3.0	1.852	0.020 (5)
	4.0	1.834	0.015 (5)
0.0004	0.67	2.015	0.025 (4)
	1.0	2.034	0.036 (4)
	2.0	2.022	0.030 (2)
	3.0	1.922	0.020 (5)
	4.0	1.842	0.017 (4)

variations with gel samples that had been equilibrated for more than 48 hr. The importance of adequate stirring was clearly demonstrated. (Note: the variation with stirring rate (Table I) reflects behavior expected according to the Nernst stationary film concept.) An estimate of the thickness of the effective surface film can be calculated according to the equation[13]

$$\frac{Q_t}{Q_0} \simeq 1 + \frac{\epsilon}{d} - \frac{2}{d}\sqrt{(Dt/\pi)} \qquad (3)$$

where $\epsilon = bD_g c_g / D_{film} c_{film}$, $d = a/2$, b = thickness of effective surface film. For example, the estimated Nernst film thickness according to eq 3 for diffusion

(13) H. C. Thomas, *Proc. Natl. Acad. Sci. U. S.*, **42**, 909 (1956).

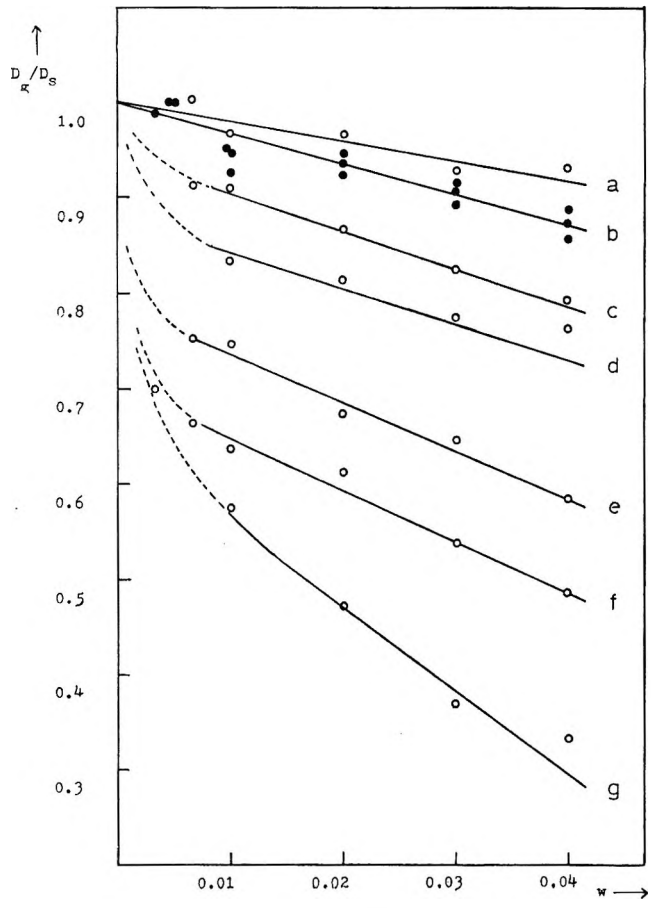

Figure 2. "Obstruction effect" for sodium self-diffusion in agar gels: a, 2.0 *M*; b, 0.5, 0.1, 0.056 *M*; c, 0.01 *M*; d, 0.001 *M*; e, 0.0004 *M*; f, 0.0001 *M*; g, 0.00001 *M*.

into the unstirred solution was 0.04 cm. At the faster stirring rates the film effect became negligible, and there was insignificant variation in the diffusion coefficient at stirring rates of 250, 400, and 600 rpm.

Self-Diffusion of Sodium Cations. The variation of D_g with w (see Figure 2) allowed least-squares extrapolation to pure aqueous solution diffusion coefficients at electrolyte concentrations above 0.05 *M*. At the lower concentrations, although the results over the range of gel compositions accessible to experiment were still linear, D_s values obtained by extrapolation were much too low.

Self-Diffusion of Chloride Anions. Diffusion data for chloride self-diffusion (Table III) were much less affected by the electrolyte concentration. Good estimates of aqueous solution diffusion coefficients could be obtained at electrolyte concentrations as low as 0.0004 *M*. However, it appeared that the gel environment changed at very high concentrations (above 0.5 *M*). The obstruction effect as indicated by D_g/D_s values was quite significantly reduced. Further examination of the sodium diffusion data revealed a similar effect for the 2.0 *M* run, a result unlikely to be due to adsorption effects at such high electrolyte concentration.

Self-Diffusion of Iodide Anions. Iodide self-diffusion results were obtained at 0.1 and 0.001 *M* NaI concentrations (see Table IV). The results were very similar to those for chloride diffusion.

Table IV: Iodide Self-Diffusion Coefficients

c, mol/l.	100w	$D_g \times 10^5$	Mean
0.1	0.67	1.840	0.005 (5)
	1.0	1.868	0.010 (4)
	2.0	1.793	0.006 (5)
	3.0	1.746	0.029 (5)
	4.0	1.737	0.010 (4)
0.001	0.67	2.020	0.030 (3)
	1.0	1.936	0.005 (3)
	2.0	1.922	0.003 (2)
	3.0	1.860	0.012 (2)
	4.0	1.780	0.010 (2)

Table V summarizes values of α, along with the extrapolated values (D_{ext}) where appropriate, and also literature (D_{lit}) and limiting law (D_{lim}) values. Figures 2 and 3 were prepared with D_{ext} values used for D_s when these were within experimental error of literature values. Otherwise the latter were used.

Table V

Ion	c	α	$D_{ext} \times 10^5$	$D_{lit} \times 10^5$	$D_{lim} \times 10^5$
Na^+	2.0	2.0	1.093	1.130[a]	0.955
	0.5	3.2	1.293	1.279[a]	1.144
	0.1	3.2	1.315	1.280[b]	1.253
	0.056	2.8	1.295	1.289[b]	1.306
	0.01	4.1	1.240	1.312[b]	1.314
	0.001	...	...	1.327[c]	1.320
	0.0004	...	...	1.333[c]	1.330
Cl^-	1.0	1.2	1.714	1.772[d]	1.660
	0.5	1.0	1.829	1.854[d]	1.770
	0.1	2.7	1.937	1.952[d]	1.875
	0.01	2.8	1.996	...	1.996
	0.001	2.5	2.024	...	2.016
	0.0004	2.7	2.060	...	2.022
I^-	0.1	2.4	1.896	1.87[e]	1.875
	0.001	2.8	2.013	...	2.025

[a] J. H. Wang and S. Miller, *J. Amer. Chem. Soc.*, **74**, 1611 (1952). [b] R. Mills, *J. Phys. Chem.*, **61**, 1631 (1957). [c] R. Mills and E. W. Godbole, *J. Amer. Chem. Soc.*, 82, 2395 (1960). [d] J. H. Wang, *ibid.*, **74**, 1612 (1952). [e] J. H. Wang and J. W. Kennedy, *ibid.*, **72**, 2060 (1950).

Discussion

The demonstration that the obstruction effect for chloride and iodide self-diffusion is independent of electrolyte concentration up to concentrations of 0.1 *M* provides evidence of a constant macromolecular geometry over this concentration range. Anion exclusion

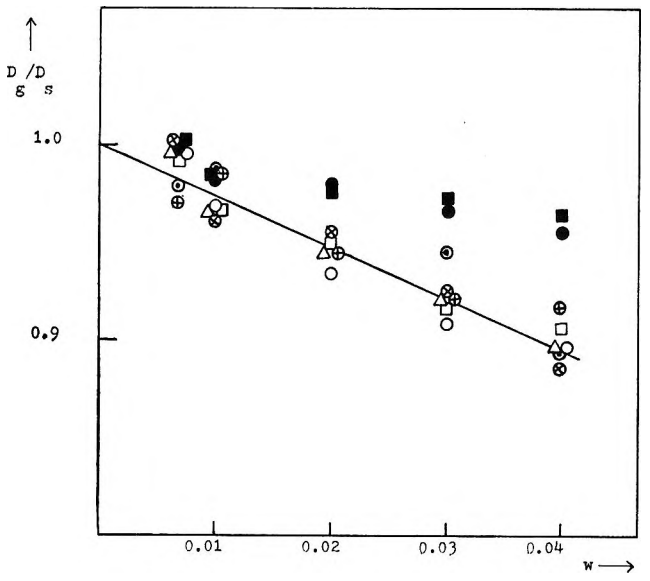

Figure 3. Obstruction effect for anion self-diffusion in agar gels: ●, 1.0 *M*; ■, 0.5 *M*; △, 0.1 *M*; ○, 0.01 *M*; □, 0.001 *M*; ⊙ 0.0004 *M*, chloride; ⊕, 0.1 *M*; ⊗, 0.001 *M*, iodide.

effects are judged to be unimportant as otherwise the variation of anion exclusion with electrolyte concentration would have been reflected in the diffusion data. The possibility that the effects due to varying exclusion are compensated by changes in gel structure seems remote.

It was not the intended purpose of this communication to consider in detail the results for cation diffusion. Adsorbed cations presumably migrate with a lower mobility than free cations, causing the diffusion coefficients in gels to decrease when electrolyte concentrations are such that a significant fraction of the ions present in the gel are adsorbed. At the higher concentrations, cation and anion diffusion can be expected to be similar though it seems that the gel offers slightly greater obstruction to cation diffusion ($\alpha = 3.1 \pm 0.1$ for sodium compared with $\alpha = 2.7 \pm 0.2$ for chloride) possibly because of the greater hydrated size of the sodium cations.

Sufficient is known of the gel structure to allow further discussion. Recent study of the gel–water relationship by nuclear magnetic resonance spectroscopy,[14] water adsorption isotherms,[15] and dielectric properties[16] has indicated that gelling is associated with a phenomenon described as an "organizing effect" and consistent with extensive hydrogen bonding. Electron microscopy[17] has shown the macromolecules of an evaporated solution of agarose (a major constituent of agar) to exist as long and relatively straight threads. A gel structure of loosely interwoven, extensively hydrogen-bonded polysaccharide macromolecules is suggested.

A random three-dimensional network of rod-shaped particles has been used to interpret the exclusion of molecules from the gel in gel filtration.[18] The extensive literature on the transport properties of heterogeneous media is useful in the consideration of diffusion through such a structure. A gel represented by a random, three-dimensional network of rods could be approximated by a random suspension of prolate spheroids, especially if the spheroids were elongated to approach needle shape. Such a system was included as a special case of Fricke's treatment of the conductivity of disperse systems.[19]

The appropriate equation can readily be modified[20] for the case of diffusion, yielding

$$D_s/D_g = 1 + \rho(\beta - 1) = F \qquad (4)$$

where ρ = effective volume fraction of gel macromolecules and β = shape factor ($= {}^5/_3$ for needles).

A value of 1.6 g/ml for the density of anhydrous agar (estimated from that of sucrose) in eq 4 gives

$$F = 1.0 + 0.42w$$

compared to the experimental value (for chloride diffusion) of

$$F = 1.0 + 2.7w$$

Although frictional and electrostatic effects may contribute, the major cause of this difference seems most likely to be the hydration of the agar macromolecules. An estimate of this hydration can be made according to[21]

$$\rho = m(1/d_a + H/d_w) \qquad (5)$$

where m = agar content of gel (g of anhydrous agar/ml of gel), d_a = density of anhydrous agar, d_w = density of water of hydration (it was assumed that the density of the water of hydration was the same as pure water), and H = hydration (g of water/g of anhydrous agar). Equation 5 can be written as

$$\rho = (1/d_a + H/d_w)/[1/d_a + (1/d_w)(1 - w)/w] \qquad (6)$$

so that for $w \ll 1$

$$D_s/D_g \simeq 1 + (1/d_a + H/d_w)(\beta - 1)w \qquad (7)$$

The value of 3.4 g of water/g of anhydrous agar obtained indicates very extensive hydration (approximately 56 water molecules/monomer unit).

Some additional support for this finding is provided by the data on water self-diffusion in agar[22] treated ac-

(14) C. Sterling and M. Masuzawa, *Makromol. Chem.*, **116**, 140 (1968).

(15) M. Masuzawa and C. Sterling, *J. Appl. Polym. Sci.*, **12**, 2023 (1968).

(16) M. Masuzawa and C. Sterling, *Biopolymers*, **6**, 1452 (1968).

(17) T. G. L. Hickson and A. Polson, *Biochim. Biophys. Acta*, **165**, 43 (1968).

(18) T. C. Laurent, *ibid.*, **136** (2), 199 (1967).

(19) H. Fricke, *Phys. Rev.*, **24**, 575 (1924).

(20) E. Schantz and M. A. Lauffer, *Biochemistry*, **1**, 658 (1962).

(21) J. H. Wang, *J. Amer. Chem. Soc.*, **76**, 4755 (1954).

(22) F. S. Nakayama and R. D. Jackson, *J. Phys. Chem.*, **67**, 932 (1963).

cording to the method of Wang.[21] The water of hydration is considered immobilized, and the amount estimated according to a model essentially the same as above is 3.6 g of water/g of anhydrous agar.

A gel hydration model can also explain the reduced obstruction effect at high salt concentrations (above 0.5 *M*). At such concentrations gel hydration can be expected to be less because of the combined effects of competition with the sodium ions for available water molecules and the structure breaking by ions that penetrate the hydration sheath.

Conclusion

The adaption of the capillary method is a useful addition to the techniques for studying diffusion in gels. It is particularly suitable for use with any radioactive isotope of appropriate half-life, including soft β emitters. Measurements can be extended to very low concentrations.

It has been shown that for anion diffusion (chloride and iodide), in contrast to cation diffusion (sodium), the variation of diffusivity is linear with gel composition and independent of electrolyte concentration up to concentrations of 0.1 *M*. Extrapolation to zero gel content gives values for diffusion coefficients in good agreement with literature values for pure solution.

Analysis of the results in terms of Fricke's equation suggested that the obstruction to diffusion is caused not so much by the agar macromolecules themselves as by an immobilized sheath of "bound" water molecules.

Acknowledgment. Acknowledgment is made to the donors of the Petroleum Research Fund, administered by the American Chemical Society, for support of this research. We are also indebted to the National Science Foundation for aid in preparing this paper.

Glass Transitions in Molecular Liquids. I. Influence of Proton Transfer Processes in Hydrazine-Based Solutions

by E. J. Sutter and C. A. Angell*

Department of Chemistry, Purdue University, Lafayette, Indiana 47907 *(Received November 23, 1970)*

Publication costs assisted by the Office of Saline Water, U. S. Department of the Interior

As a first stage in a study of the physicochemical consequences of proton-transfer processes in solutions, the composition regions of a number of protonic acid + hydrazine binary systems in which macroscopic samples can be obtained in the vitreous state have been determined. The glass transition temperatures T_g within these regions have been determined, and are compared with those determined for solutions in the $Ca(NO_3)_2 + CH_3NH_2$ system. Correlations of the magnitude of T_g at a given composition with hydrogen-bonding ability and basicity of the anion are presented. In addition, the glass temperatures of structurally related small-molecule liquids are presented and an interpretation of the relative magnitudes of T_g values in terms of structural and molecular interaction parameters is given. Also presented are the "ideal" glass transition temperatures, T_0, for these liquids predicted from thermodynamic data, and the consistency of T_g values with these predicted T_0 values is discussed.

Introduction

Recently some advances in the understanding of concentrated electrolyte solution behavior have come from studies which include detailed examination of solutions at temperatures below their normal thermodynamic crystallization temperatures.[1-3] The experimental limit on such studies of liquid properties is set by the glass transition. The temperature associated with this proves to be a valuable indicator of particle interactions and, in the case of aqueous solutions, has led to the differentiation of effects due to the breakdown of water structure, increases in Coulombic energy, and more subtle but important effects on the liquid cohesive energy due to postulated hydration sphere water-to-anion hydrogen bonding.[3] Generally parallel effects may be expected for solutions of ionic salts in nonaqueous solvents of reasonably high dielectric constants.

(1) C. A. Angell, *J. Phys. Chem.*, **70**, 2988 (1966); *ibid.*, **69**, 2137 (1965).

(2) C. A. Angell, E. J. Sare, and R. D. Bressel, *ibid.*, **71**, 2759 (1967).

(3) C. A. Angell and E. J. Sare, *J. Chem. Phys.*, **52**, 1058 (1970).

Hydrazine is a nonaqueous solvent with a number of strikingly water-like physical characteristics. Chemically, however, it is distinguished by its more strongly basic character. Advantage can be taken of this fact to study facets of solution behavior not easily studied with aqueous systems, and it is this aspect of the chemistry of hydrazine and some related solvents which has motivated the present research. For instance, weak acids such as acetic and formic acids, which in water dissolve with little dissociation, form salts by proton transfer when dissolved in hydrazine. From such acid–base-type interactions an ionic liquid may be generated from two molecular liquids with little change in size of the original particles.

The advantage of the systems we discuss in this paper over such obvious proton-transfer salts as NH_4Cl is that the salt is soluble in each of the parent liquids, and the solutions supercool readily over wide composition regions. Thus the effects of proton transfer on solution properties can be studied by following the behavior of the glass transition temperature with changing composition in these binary systems, and the effects of different chemical characteristics of the interacting molecules can be evaluated.

Insofar as the "turning-on" of a Coulomb interaction without other major changes in the molecular system under study is an important factor in the solution behavior, these studies find a parallel in the interesting work of Lind and coworkers,[4,5] who studied liquids of quasispherical molecules and molecule ions in which charge was introduced by substituting group 3 and group 5 atoms for group 4 atoms at the molecular centers. To the extent that the particles of Lind and coworkers' studies can be regarded as charged or uncharged hard spheres, their liquids have a simplicity missing from those of the present work. On the other hand, the consequences of incomplete proton transfer, and the related possibility of imposing directional character on the interparticle interactions through hydrogen bonding, which are of interest in solution chemistry, may be studied with the present systems.

The solution studies also make possible by short extrapolations estimation of glass transition temperatures for the pure solvents which are not directly measurable because pure liquids crystallize rapidly. As a subsidiary investigation we have therefore performed some solution studies involving the related solvent, methylamine, and shall use these data with solution and thermodynamic data from the literature for H_2O_2, and CH_3OH, to make correlations of glass temperatures with chemical and structural features for this series of small-molecule liquids.

Experimental Section

Purification of Reagents. Because hydrazine is a powerful reducing agent, attacked by such oxidizing agents as atmospheric oxygen, it was found necessary to purify the hydrazine and prepare the solutions under high-vacuum conditions. Hydrazine (N_2H_4), anhydrous, 97%, was purified by a procedure used by Lucien,[6] which involves drying over calcium hydride, and vacuum fractionation of the filtrate. The sample was collected at $-20°$. The hydrazine so purified was found to have a specific conductivity of 1.94×10^{-6} mho cm^{-1} at 0° (literature value 1.1 to 2.0×10^{-6} mho cm^{-1} at 0°).[7] Because of its sensitivity to impurities, this property was used as the criterion for purity of the solvents used.

Both formic and acetic acids were purified in a similar manner, anhydrous oxalic acid being used as the dehydrating agent instead of CaH_2. Their specific conductivities agreed with the literature values within the same limits as did the hydrazine; for acetic acid we found 1.6×10^{-8} mho cm^{-1} at 25° (literature value 1.1×10^{-8} mho cm^{-1} at 25°)[8a] while for formic acid we obtained 6.5×10^{-5} mho cm^{-1} at 25° (literature value 6.4×10^{-5} mho cm^{-1} at 25°).[8b]

Commercially available reagent grade salicylic acid and hydrazinium dihydrochloride were used without further treatment. Hydrazinium monobromide (N_2H_5Br) and hydrazinium phosphate ($N_2H_5PO_4$) were prepared by mixing stoichiometric amounts of anhydrous hydrazine and the corresponding aqueous acid and recrystallizing the salt from 95% ethanol.

Preparation of Solutions. Solutions were prepared under vacuum conditions, and the concentrations were determined by weighing. The solutions were withdrawn from the preparation flask by means of a syringe through a side arm capped by a serum stopple and were injected into 5-mm capillary tubes. The tubes were immediately quenched in liquid nitrogen. This procedure reduced solution decomposition to a minimum.

Because of the high vapor pressure of methylamine at room temperature, solutions of calcium nitrate in methylamine were prepared directly in specially constructed 5-mm capillary tubes with recessed thermocouple wells. Anhydrous calcium nitrate was added to the sample tube, the tube was attached to the vacuum line and evacuated, and the methylamine was added by allowing the gas to condense in the evacuated tube held at $-196°$. The tube was then sealed off. After the T_g values were determined, the tube was weighed, then broken, and the methylamine was allowed to evaporate. The tube was again weighed and the calcium nitrate was removed by washing with distilled water. From these data the mole concentrations of the solutions could be determined.

(4) G. Morrison and J. E. Lind, Jr., *J. Chem. Phys.*, **49**,53 10 (1968).

(5) S. W. Rudich and J. E. Lind, Jr., *ibid.*, **50**, 3035 (1969).

(6) H. W. Lucien, *J. Chem. Eng. Data*, **7**, 541 (1962).

(7) P. Walden and N. Hilgert, *Z. Phys. Chem., Abt. A*, **165**, 241 (1933).

(8) (a) M. Rabinovich, *Z. Phys. Chem.*, **119**, 64 (1926); (b) H. I. Schlesinger and C. Coleman, *J. Amer. Chem. Soc.*, **38**, 272 (1916).

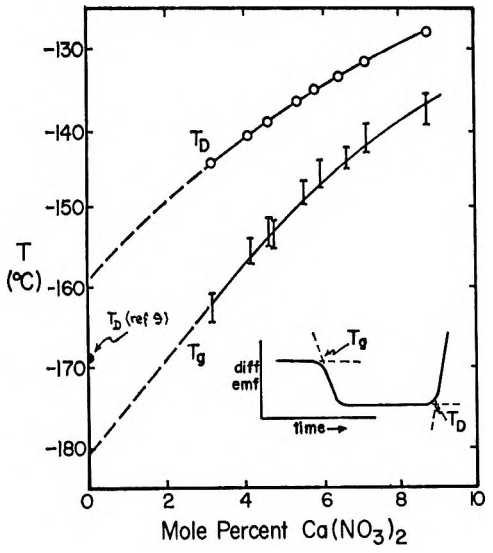

Figure 1. Glass temperatures (T_g) and devitrification temperatures (T_D) for $Ca(NO_3)_2$–CH_3NH_2 solutions. Devitrification temperature for vapor-deposited CH_3NH_2 of deNordwall and Staveley.[9]

Glass Transition and Devitrification Temperatures. The technique of differential thermal analysis (DTA) as described by Angell and Sare[3] was used to determine glass transition temperatures by detection of the change of heat capacity during warmup at constant heating rate (6.5° min^{-1}). T_g and T_D, the temperature at which irreversible crystallization commences, are defined as shown in Figure 1 inset. With the exception of calcium nitrate–methylamine solutions (see preparation of solutions) the sample containers were open 5-mm capillary tubes.

Density Measurements. Density measurements on solutions of formic acid + hydrazine were made using standard dilatometric techniques.

Results

Glass temperatures and devitrification temperatures during warmup are shown as a function of composition for solutions of $Ca(NO_3)_2$ in CH_3NH_2 in Figure 1. Also included is the "devitrification" temperature measured for vapor deposited amorphous CH_3NH_2 by deNordwall and Staveley.[9] In Figure 2a the glass temperatures for N_2H_4–HCOOH solutions are shown superimposed on the phase diagram determined in this study. We note that the melting point of $N_2H_6(OOCH)_2$ obtained in this work (148°) is substantially higher than the literature value (128°). Elemental analysis confirmed the stoichiometry of this salt which was purified by vacuum sublimation. Since the salt was prepared under vacuum conditions, by mixing stoichiometric amounts of carefully purified hydrazine and formic acid, it is likely that the higher melting point reflects a higher purity of the compound prepared in the present work.

Figures 2b and c show the molar volumes and expansion coefficients for these solutions found in this work.

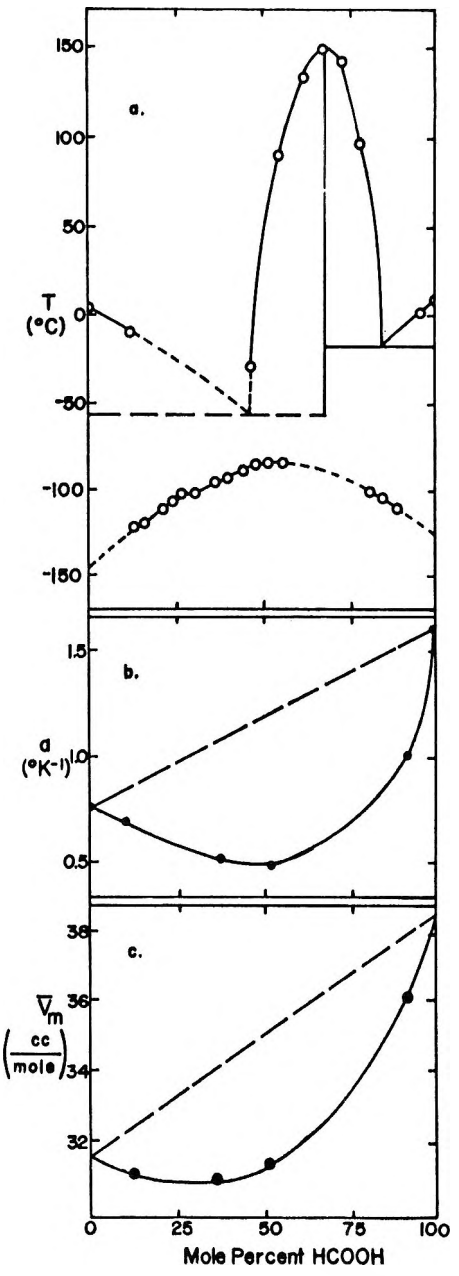

Figure 2. (a) Phase diagram and glass temperatures for N_2H_4–HCOOH solutions. Broken line on phase diagram indicates region where system did not crystallize under any conditions. Broken line on glass transition curve indicates region where system did not vitrify under any conditions. It should be noted that T_g is not a thermodynamic transition temperature and, while characterized by changes in thermodynamic properties, is only defined at a fixed heating rate. (b) Thermal expansivity for N_2H_4–HCOOH solutions; $\alpha = 1/V_m(dV/dT)$. (c). Molar volume at 273.15°K for N_2H_4–HCOOH solutions; $\bar{V}_m = (X_1m_1 + X_2m_2)/\rho$.

The density data from which the volume and expansivity plots were constructed are collected in Table I in the form of linear density–temperature equations.

In Figure 3 glass temperatures for N_2H_4–CH_3COOH solutions are shown against the liquidus line according to

(9) H. J. deNordwall and L. A. K. Staveley, *Trans. Faraday Soc.*, 52, 1207 (1956).

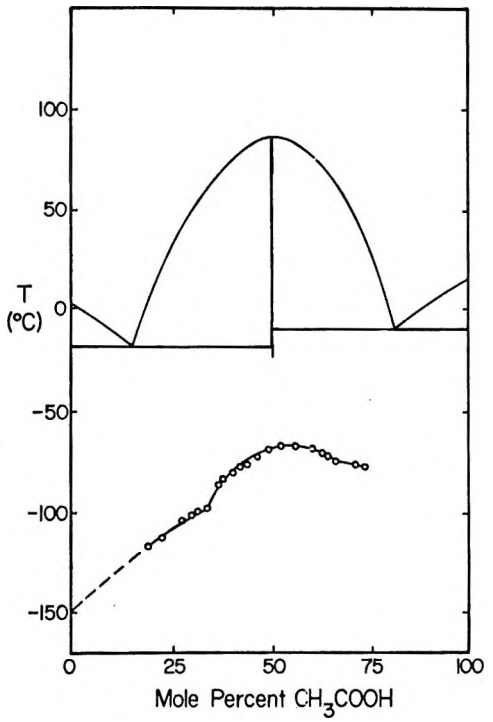

Figure 3. Glass temperatures for N_2H_4–CH_3COOH solutions against the liquidus line.[10]

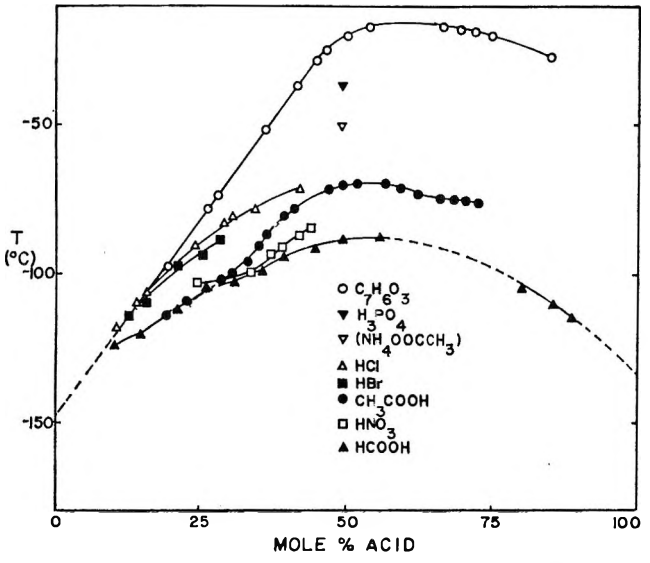

Figure 4. Glass temperatures for various acids in hydrazine: $C_7H_6O_3$, salicylic acid; (NH_4OOCCH_3), acetic acid in ammonia.

Semishen.[10] Figure 4 summarizes T_g–composition relations for solutions of various other acids in hydrazine.

Discussion

Our discussion of this work divides itself into two parts. In part I we combine the information on N_2H_4 and CH_3NH_2 derived from the present work with literature data on several structurally related molecular liquids to provide the basis for a correlation of glass transition temperatures with structural and molecular interaction parameters in small-molecule liquids. In part II we discuss the methylamine and hydrazine-based solutions, and attempt to interpret the physicochemical consequences of the acid–base process which accompanies the dissolution of various simple acidic molecular liquids in hydrazine.

Table I: Equations for the Temperature Dependence of Density for Solutions of Formic Acid in Hydrazine

Mol % formic acid	Density equation, T in °K	Temperature range, °K
00.00	$\rho = -1.221 \times 10^{-3}T + 1.558$[a]	273.15–298.15
11.22	$\rho = -7.827 \times 10^{-4}T + 1.3099$[c]	253.15–298.15
37.30	$\rho = -6.437 \times 10^{-4}T + 1.3791$	238.15–298.15
53.20	$\rho = -6.184 \times 10^{-4}T + 1.4411$	243.15–298.15
95.27	$\rho = -1.221 \times 10^{-3}T + 1.5962$	263.15–298.15
100.0	$\rho = -8.72 \times 10^{-4}T + 1.3635$[b]	273.15–298.15

[a] Reference 7. [b] J. B. Garner, B. Saxton, and H. O. Parker, *Amer. Chem. J.*, **46**, 236 (1911). [c] The number of significant figures indicates the high internal precision of these measurements. The densities are accurate to ±0.1%.

I. Glass Temperatures of Structurally Related Small-Molecule Liquids

The molecules H_2O_2, N_2H_4, CH_3OH, CH_3NH_2, and CH_3CH_3 form an interesting set, all involving the covalent single-bonded linkage of pairs of periodic table first row atoms, in each case the remaining valences being satisfied by hydrogen atoms. While the protons are submerged to different degrees in the different electronegative atom charge clouds, all these molecules can be regarded as having the same general dumbbell configuration. Differences in their physical properties should in this case be mainly attributable to differences in the mode of interaction of molecules with their neighbors in the condensed state. Effects dependent on molecular interactions are seen most clearly at low temperatures where the disordering effect of temperature is reduced to a minimum. A comparison of their glass temperatures should therefore be informative. Unfortunately none of these liquids is easily vitrified and only for CH_3OH has a glass temperature been directly measured. Faucher and Koleske[11] obtained a T_g from mechanical measurements on quenched methanol-soaked paper strips. The result, 110°K, was later refined by the calorimetric study of Sugisaki, *et al.*,[12] of the vapor-deposited glass, which yielded T_g = 103°K. Short extrapolations of the glass temperature–composition relations of Figures 1 and 4 yield glass temperatures for CH_3NH_2 and N_2H_4 of 91 and 125°K, respectively, those values being considered reliable to ±5°K. An

(10) V. I. Semishen, *Zh. Obshch. Khim.*, **13**, 633 (1943).

(11) J. A. Faucher and J. V. Koleske, *Phys. Chem. Glasses*, **7**, 202 (1966).

(12) M. Sugisaki, H. Suga, and S. Seki, *Bull. Chem. Soc. Jap.*, **40**, 2984 (1967).

Table II: Temperature Data and H Bonds for Structurally Related Small-Molecule Liquids

Molecule	T_g, °K	$T_{0(cal)}$, °K	T_l, °K[18]	T_b, °K[18]	R(A···H-A)[19]	H bonds per molecule	T_b/T_g
HO-OH	139		272.7	423.4	2.76	2	3.05
H_2N-NH_2	125	106	274.6	386.7	3.19, 3.30	2	3.10
H_3C-OH	103	68	178.3	338.2	2.65	1	3.13
H_3C-NH_2	91	86	179.6	266.9	2.18, 3.27	1	2.94
H_3C-CH_3	~46			184.6		0	4.0

extrapolation of the T_g–composition relation observed in the H_2O–H_2O_2 system by Ghormley[13] yields a T_g of 139°K. Finally, a T_g value of 46°K for the unsubstituted hydrocarbon ethane, which completes the CH_3OH, CH_3NH_2, CH_3CH_3 sequence, may be obtained from the empirical relation for hydrocarbon liquids noted by Stearns, *et al.*,[14] $T_g = {}^1/_4T_B$.

Before considering the source of the differences between these values it is of considerable interest to check their consistency against predictions from thermodynamic data. The prediction is based on the postulate that the glass transition is a direct reflection of the approach of the molecular system to a configurational ground state at which the configurational contributions to the total entropy vanish. The data necessary for this estimate are the entropy of fusion and the heat capacities of crystalline and liquid states for the substance. Such data are available for N_2H_4, CH_3NH_2, and CH_3OH.[15]

The estimate, which is best made graphically as described in detail elsewhere,[16] involves finding the lowest temperature, designated T_0, to which the liquid could be supercooled before its total entropy would become equal to the crystal value at that temperature. The heat capacity decrease which must in principle occur at T_0, if not before, is seen experimentally at the glass temperature, T_g, at which the liquid falls out of equilibrium due to the rapidly increasing relaxation times encountered as T_0 is approached,[17] *i.e.*, T_g, which typically occurs 20–30° above T_0, refers to a nonequilibrium process. The T_0 and T_g values for the present series of liquids, summarized in Table II,[18,19] are in general accord with these requirements. Independent evaluation of T_0 from conductance measurements on hydrazine solutions (to be described separately) also yield T_0 approximately 20° below T_g.

Also included in Table II are structural data which enable us to understand the sequence of T_g values. From the great difference in T_g between ethane and the other molecules it seems clear that the polymerizing effect of the hydrogen bonds which can form in the latter cases is a dominant effect. However, the sequence of hydrogen bond strengths, judged by the bond length R(A···H-A) measured in the respective crystal structures, is not the sequence of T_g values. A rational sequence is, however, obtained when it is recognized that H_2O_2 and N_2H_4 are distinguished by having two proton acceptor sites per molecule compared with one each for CH_3OH and CH_3NH_2, and accordingly may mutually bind at both ends of the molecule with a decrease in flexibility of the polymeric structure. The increase from one to two bond sites per molecule is accompanied by a T_g increment of ~25°K and seems considerably more important than the very large increase in single bond strength seen in passing from methylamine to methanol. No molecule in this series forms three dimensional networks. The smallest molecule with the ability to form such continuous polymeric structures is H_2O itself. In the case of water, however, the appropriate value of the glass temperature is problematical.[20]

It is notable, from Table II, that the T_b/T_g ratio for the hydrogen-bonded liquids is different from that for the van der Waals-bonded hydrocarbons.[14]

II. Solution Behavior

1. Calcium Nitrate in Methylamine. Although the dielectric constant of methylamine is less than that of water, $Ca(NO_3)_2$ dissolves readily, and the change with composition of the solution T_g values is similar to that observed for solutions in water, *viz.* a rapid initially linear (~5°/mol %) increase in T_g with increasing concentration. The slope above 5 mol % is markedly smaller in the present case, however, possibly indicative of more extensive ion pairing or clustering. The increase in the case of aqueous solutions has been interpreted in terms of increasing Coulomb energy of the liquid and contribution to cohesion from hydrogen

(13) J. A. Ghormley, *J. Amer. Chem. Soc.*, **79**, 1862 (1957).

(14) R. S. Stearns, I. N. Duling, and R. H. Johnson, *Ind. Eng. Chem., Prod. Res. Develop.*, **5**, 306 (1966).

(15) N_2H_4, O. W. Scott, G. D. Oliver, M. E. Gross, W. N. Hubbard, and H. M. Huffman, *J. Amer. Chem. Soc.*, **71**, 2293 (1949); CH_3NH_2, J. G. Aston, C. W. Silley, and G. H. Messerly, *ibid.*, **59**, 1743 (1937); CH_3OH, K. K. Kelley, *ibid.*, **51**, 180 (1929). The heat capacity anomaly at solid transition ($C_I \rightarrow C_{II}$) is accounted for by use of the effective first order transition entropy given by Kelley.

(16) C. A. Angell, *J. Chem. Educ.*, **47**, 583 (1970).

(17) G. Adam and J. H. Gibbs, *J. Chem. Phys.*, **43**, 139 (1965).

(18) R. C. Weast, Ed., "Handbook of Chemistry and Physics," 49th ed, Chemical Rubber Co., Cleveland, Ohio, 1968.

(19) G. C. Pimentel and A. L. McClellan, "The Hydrogen Bond," W. A. Freeman, San Francisco, Calif., 1960.

(20) C. A. Angell and E. J. Sare, *Science*, **168**, 280 (1970).

bonding of cation-solvated water molecules to near-neighbor proton-accepting anions.[3]

2. Solutions of Acids in Hydrazine. (*a*) *Glass-Forming Composition Regions.* The composition regions in which formation may occur in the present systems are, as commonly found, largely dictated by the relation of the temperature below which the homogeneous liquid becomes thermodynamically unstable (*i.e.*, the liquidus temperature, T_l) to the glass transition temperature. In the present work glasses have in some cases been observed to form in 0.2 cc quantities when T_l/T_g is as high as 2.0, probably due to the solution preparation procedure. The relationship between T_l/T_g and glass-forming ability has been explained by Turnbull.[21]

(*b*) *Glass Temperatures and Molecular Interactions in Solution.* It is seen in Figure 4 that striking increases in glass temperatures, and hence in cohesive interactions between species in solution, accompany the addition of acidic molecules to hydrazine, the effect being almost as marked as that accompanying the dissolution and ionization of an equivalent amount of $Ca(NO_3)_2$ in methylamine. Since this effect was anticipated as a consequence of the formation of ionic species by a proton-transfer reaction, most attention in this study has been given to a binary system in which each component has a large enough dielectric constant to serve as an ionizing solvent for the reaction products. The dielectric constant of formic acid is 58 at 16°[22] compared with, for instance, 6 at 20° for acetic acid[8a] and 51.7 at 25° for hydrazine.[23] Thus our initial discussion of what proves to be a complex interaction problem will be based on our study of the hydrazine–formic acid system. Electrical conductance measurements have also been made on these solutions and will be reported in a separate article.

In the hydrazine–formic acid system T_g rises to a maximum at about 55 mol % which, according to a "bond lattice" theory for the glass transition,[24a-c] implies a maximum energy separation of configurational states at this composition. Correlated with the maximum in T_g is a maximum negative deviation from additivity in the isothermal molar volume of the solutions, and a minimum in the expansion coefficient (Figures 2b and c). These observations imply that in contrast with a case such as water[24b] low-energy states are also low-volume states. This is the situation expected for a system with Coulombic interactions, and is thus consistent with the notion that the important energetic event on mixing these molecular liquids is the formation of $N_2H_5^+$ and $HCOO^-$ ionic species. The concentration of such ions would reach a maximum at 50 mol %. Such results would compare with Morrison and Lind's observation that most (but not all) of the difference in viscosity between the molecular liquid $C[C(CH_3)_3]_4$ and the corresponding fused salt $N[C(CH_3)_3]_4^+B[C(CH_3)_3]_4^-$ at a given temperature could be ascribed to the smaller volume of the salt, a consequence of electrostriction.

Conflicting with this simple interpretation, however, is the fact that formic acid, in contrast with acetic acid, is powerful enough to protonate the second acceptor site on N_2H_4, and form the compound $N_2H_6^{2+}(HCOO^-)_2$. In fact this is the only compound known to form in the binary system. It has a relatively high melting point, 148° (Figure 2a), and is responsible for the gap in glass-forming compositions in this region. The structures of other salts containing this cation, *e.g.*, $N_2H_6Cl_2$[25] and $N_2H_6(H_2PO_4)_2$,[26] have been determined, and it is clear that the $N_2H_6^{2+}$ cation is a well-defined species with a somewhat shorter N–N distance than either the N_2H_4 molecule or the $N_2H_5^+$ cation. The maximum in electrostatic charge density, hence Coulombic energy, should therefore be reached near 67 mol %. According to interpolations of measurements from lower and higher concentration range measurements, however, this composition does not correspond with maxima in T_g, although our limited molar volume data suggest it may be close to the composition of maximum deviation from molar volume additivity. In the acetic acid–hydrazine system, by contrast, a sharp density maximum is found at 50 mol %.[10]

Study of the crystal structures of N_2H_4,[27] N_2H_5Cl,[28] and $N_2H_6Cl_2$[25] suggests that the modifying influence is the N···H–N hydrogen bond. This bond in pure crystalline hydrazine links hydrazine molecules into spiral chains with N···H–N distances of 3.19 and 3.30 Å,[26] and similarly links the $N_2H_5^+$ cations in crystalline N_2H_5Cl.[27] In the latter case the bonds are shorter (N–H···N distances of 2.95 Å), and the chains are electrostatically cross-linked by the chloride ions. In passing to $N_2H_6Cl_2$, however, the relatively strong H-bonded chain structure is lost, the $N_2H_6^{2+}$ species (which now have no proton acceptor sites) occurring as individual cations "linked in a three dimensional network"[27] by weaker $N–H^+\cdots Cl^-$ hydrogen bonds.

Since H-bonded $N_2H_5^+$ chains, with the same N···H–N distance as the above, are found in the related crystals N_2H_5Br,[29] $N_2H_5H_2PO_4$,[26] and $N_2H_5HC_2O_4$, we interpret the decrease in T_g and increase in $\bar{V}_m$ beyond 55 mol % HCOOH in Figure 2 in terms of the predominance of a tight-chain breakdown effect over a

(21) D. Turnbull and M. H. Cohen, *J. Chem. Phys.*, **29**, 1049 (1958).

(22) P. Drude, *Z. Phys. Chem.*, **23**, 267 (1897).

(23) P. Jonnasch and C. Stephan, *Chem. Ber.*, **37**, 1980 (1904).

(24) (a) C. A. Angell and J. Wong, *J. Chem. Phys.*, **53**, 1058 (1970); (b) C. A. Angell, submitted for publication in *J. Phys. Chem.*; (c) K. J. Rao and C. A. Angell, 3rd International Conference on Physics of Non-Crystalline Solids, Sheffield, England, 1970.

(25) J. Donahue and W. N. Lipscomb, *J. Chem. Phys.*, **15**, 115 (1947).

(26) R. Liminga, *Ark. Kemi*, **28**, 483 (1968).

(27) R. L. Collin and W. Lipscomb, *Acta Crystallogr.*, **4**, 10 (1951).

(28) K. Sakurai and Y. Tomiie, *ibid.*, **5**, 289 (1952).

(29) K. Sakurai and Y. Tomiie, *ibid.*, **5**, 293 (1953).

Coulomb energy build-up. The important influence of the length of chain structures on glass temperatures in liquids has been seen in a variety of other chemical systems,[30] although the competition with the Coulomb energy in the present case is novel.

The recognition of the importance of hydrogen bonding in fixing T_g in these liquids leads to some predictions for related systems which are generally fulfilled. For instance, if the *anion* in a liquid of stoichiometry $N_2H_5^+X^-$ has proton acceptor sites, then its cross-linking function may be expected to raise T_g in proportion to (a) the basicity of the site, and (b) the number of bonds per anion that can form—as seen, for instance, in part I of this discussion. Thus T_g values for salts with nitrate and formate anions should underlie T_g for the salt with the more basic acetate anion as is found (Table III). Finally, hydrazinium(+1) salts derived from

Table III: T_g Values and H-Bond Types for Various Hydrazinium Salts

	T_g, °C	Types of H bonds
$N_2H_5(C_7H_5O)_3$	−16	$N^+\cdots H\text{-}N$, $N^+\text{-}H\cdots O^-$, $O\text{-}H\cdots O^-$
$N_2H_5H_2PO_4$	−37	$N^+\cdots H\text{-}N$, $N^+\text{-}H\cdots O^-$, $O\text{-}H\cdots O^-$
N_2H_5Cl	−63 (extrap.)	$N^+\cdots H\text{-}N$, $N^+\text{-}H\cdots Cl^-$
N_2H_5OAc	−68	$N^+\cdots H\text{-}N$, $N^+\text{-}H\cdots O^-$
N_2H_5Br	−73 (extrap.)	$N^+\cdots H\text{-}N$, $N^+\text{-}H\cdots O^-$
$N_2H_5NO_3$	−78 (extrap.)	$N^+\cdots H\text{-}N$, $N^+\text{-}H\cdots O^-$
N_2H_5OOCH	−88	$N^+\cdots H\text{-}N$, $N^+\text{-}H\cdots O^-$
$N_2H_6(OOCH)_2$	−100 (extrap.)	$N^+\text{-}H\cdots O^-$

polyprotic acids will contain *anions* with active protons, and thus the anions may hydrogen bond to themselves. In these salts an additional hydrogen bond is possible, namely, $O\text{-}H\cdots O^-$, and the salts will contain $(N_2H_5)_n^+$ chains crosslinked by $N^+\text{-}H\cdots O$ hydrogen bonds, while the anions will themselves be held together by $O\text{-}H\cdots O^-$ hydrogen bonds. One such salt, which the crystallographic data of Liminga[26] have shown to contain all three of these hydrogen bonds, is $N_2H_5H_2PO_4$. As anticipated, T_g for this salt is much higher (−37°) than for hydrazinium salts derived from monoprotic acids. Another salt of this type is hydrazinium salicylate, $N_2H_5C_7H_5O_3$, with a T_g of −16° (Figure 4), the highest value measured in the hydrazinium(+1) series studied in this work.

All T_g values measured for hydrazinium(+1) salts are compiled, together with information on hydrogen bond types, in Table III.

To dispel the notion that all can be understood in terms of numbers and strengths of hydrogen bonds, however, we must point out two unexplained features of the glass transition temperature curves in Figure 4. One is that the HNO_3–, CH_3COOH–, and HCOOH–hydrazine systems exhibit a change in slope toward lower T_g values at 33 mol % acid. We note that this composition represents the stoichiometry of the monosolvated salt, $N_2H_5X\cdot N_2H_4$. A second feature is the anomalous position of the hydrazinium chlorides and bromides with respect to the oxyanions. Particularly in the latter case, no cohesion can be gained from H bonding, and one must look again to small anion size and, indirectly, Coulomb energy. A similar inversion is found when T_g values for the hydrazinium salts are compared (Table IV) with those for the corresponding ammonium salts,

Table IV: T_g and T_m for Various Ammonium Hydrazinium Salts

	T_g, °C	T_m, °C
NH_4OAC	−47	114
NH_4NO_3	−67	169
N_2H_5OAC	−68	97
$N_2H_5NO_3$	−78	70 (α polymorph)

in which the cations no longer form H-bonded chains but, on the other hand, yield ionic assemblages of greater charge density by virtue of their smaller sizes. Clearly both Coulomb energy and H-bonding factors are important, and which dominates in a particular situation presumably depends on subtle geometrical factors involving anion symmetry and bond site location, and overall packing efficiency.

Summary

It has been found that the glass transition temperature is a useful physical parameter for understanding the nature and kinds of interactions in the liquid state. The study of the concentration dependence of T_g in solutions of acids in hydrazine has led to the realization that, in addition to increased cohesive energy in these liquids arising from the introduction of Coulombic interactions, hydrogen bonding plays an important, and at times even dominant, role in determining the nature and strength of the intermolecular interactions. In hydrazine-rich solutions both Coulomb and hydrogen-bond interactions operate in concert to increase the cohesive energy of the systems. In acid-rich solutions, despite increasing Coulomb energy up to 67 mol % acid, the cohesive energy of the system decreases due to the disintegration of hydrogen-bonded cation polymer chains. Addition of acid beyond this concentration serves to dilute the Coulombic interaction, further decreasing the cohesive energy of the solution. These studies have led to speculation and experimentation on proton-

(30) (a) J. H. Gibbs and E. A. Dimarzio, *J. Chem. Phys.*, **28**, 373 (1958); (b) A. Eisenberg and T. Sasada, *Phys. Non-Cryst. Solids*, 99 (1956); (c) A. J. Easteal and C. A. Angell, *J. Phys. Chem.*, **74**, 3987 (1970).

transfer and hydrogen-bonding effects on the glass transition in aqueous systems. These interesting results will be discussed in a future paper.

Acknowledgment. We wish to thank the Office of Saline Water, U. S. Department of the Interior, for their support of this project.

Some Studies of Diamond Growth Rates

by R. H. Wentorf, Jr.

General Electric Research and Development Center, Schenectady, New York 12301 *(Received November 30, 1970)*

Publication costs assisted by the General Electric Co.

Carbon can be transported along a temperature gradient in a bath of molten catalyst metal such as iron, nickel, etc. When the bath is essentially saturated with carbon at pressures high enough for diamond stability, diamond can dissolve from a source in a region at a higher temperature and crystallize on a diamond seed crystal in a region at a lower temperature. In this way the diamond growth process may be somewhat regulated and studied by controlling the carbon flux and bath characteristics. The crystals grow layer by layer and impurities may be trapped under rapidly advancing layers. The rate of desorption of impurities controls some growth. Sometimes graphite or spurious diamond crystals may form. Gravity also affects the operation of the process.

A. Introduction

During the past few years the continuing development of high-pressure, high-temperature techniques has permitted the controlled growth of diamond over long periods of time, *e.g.*, 1 week. It has thus become possible to grow good quality crystals of sizes up to about 5 mm (1 carat) and to study growth rates, growth mechanisms, the incorporation and effects of impurities, etc. This paper and the one by Strong and Chrenko which follows it describe some of the methods and results of this work. In this work we generally used diamond as the source of carbon.

By contrast, nowadays most synthesized diamonds are grown from graphite or similar forms of carbon. Typical operating ranges for diamond growth are indicated by the diagonally striped region in Figure 1. At the synthesis pressures, diamond is the stable form, and with the help of catalyst metals such as iron, nickel, etc., it crystallizes in various habits and at rates determined by both the local pressure and the temperature.[1-3] The actual transformation takes place through a thin metal film and is difficult to control, especially for long periods of time. Several years ago Strong and Tuft[4] used this process to make onion-like diamonds of 1 to 3 carat size by growing successive layers of new diamond on a seed crystal, but each layer of growth required a separate run at high pressure, and the method was slow and tricky. Many inclusions were trapped between the layers of growth so that the diamonds, though large, were not particularly beautiful nor useful. At that point it seemed appropriate to look more at slightly different diamond-growing methods.

Laboratories rich in diamonds might consider using diamond as a source of carbon for growing diamonds. One possible method is indicated in Figure 1. Diamond is supposed to dissolve in a hot region and crystallize in a cool region of a suitable bath. The entire system is at diamond-stable pressure and the driving force for recrystallization is provided by the solubility difference resulting from the temperature difference. In principle this process ought to be easier to control than when diamond forms from graphite under the combined influences of both temperature and pressure. Our early experiments along this line were only partially successful; *i.e.*, the diamond dissolved well enough, but graphite crystallized instead, due to kinetic factors, even though thermodynamic considerations forbade it. However, diamond seed crystals placed in the cool region often grew larger. (This tendency for graphite to appear where it is not stable can be observed at pressures as high as 140 kbars.)[5,6]

(1) H. P. Bovenkerk, F. P. Bundy, H. T. Hall, H. M. Strong, and R. H. Wentorf, Jr., *Nature*, **184**, 1094 (1959).

(2) H. P. Bovenkerk, *Progr. Very High Pressure Res., Proc. Int. Conf.*, 58 (1961).

(3) R. H. Wentorf, Jr., *Advan. Chem. Phys.*, **9**, 365 (1965).

(4) H. M. Strong and R. E. Tuft, private communication.

(5) F. P. Bundy, *J. Chem. Phys.*, **38**, 631 (1963); *Science*, **137**, 1057 (1962).

(6) R. H. Wentorf, Jr., *Ber. Bunsenges. Phys. Chem.*, **70**, 975 (1966).

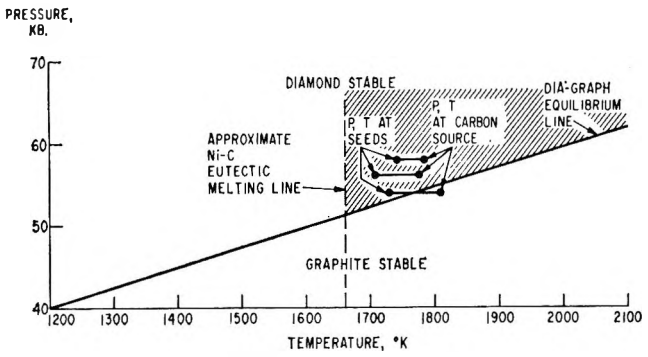

Figure 1. A portion of the pressure–temperature phase diagram for carbon.

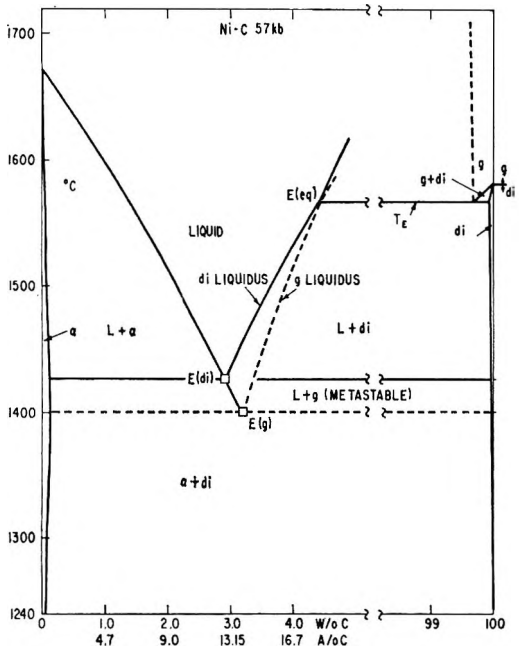

Figure 2. The nickel–carbon phase diagram at 57 kbars, according to Strong and Hanneman.[7,8]

Figure 2 is a nickel–carbon phase diagram at 57 kbars, as worked out by Strong and Hanneman.[7,8] Here one can see how the solubilities of diamond in nickel, and of nickel in diamond and graphite, vary with temperature. A temperature interval of about 60° is available for dissolving and crystallizing diamond at this pressure in this system. Actually only practical considerations, such as growth rate or insulation failure, prevent the use of arbitrarily high temperatures for dissolving the carbon from diamond or graphite, but of course the diamond must crystallize where it is stable.

B. Experimental Techniques

A convenient way to study these systems is to arrange the carbon and catalyst metal as indicated in Figure 3. This reaction cell can be compressed in a "Belt" high-pressure apparatus.[9] The heat generated in the carbon tube resistance heater flows out of the cell in such a way that useful axial temperature gradients exist in the tube.

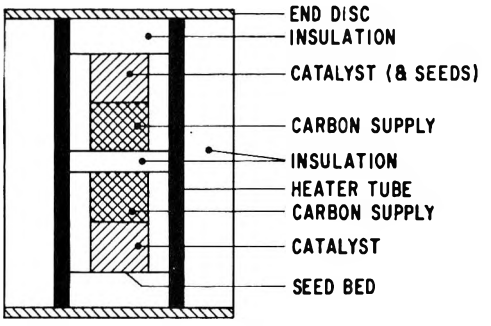

Figure 3. High-pressure cell for diamond growth.

The nutrient carbon, usually a densely packed mixture of diamond and graphite, occupies the hotter midlength region. (The graphite changes to diamond early in the operating period and is added to increase the average density of the starting mixture so as to minimize cell distortion and pressure loss.) Two cooler regions, one near each end of the cell, are available for diamond growth out of the catalyst metal baths, and diamond seed crystals are placed at these cool ends. After the cell is assembled and placed in the pressure apparatus, it is compressed to the desired operating pressure, usually around 55–60 kbars, and then heated to bring the midlength to say 1450° and the seed regions typically to about 1420°. Thermocouples may be used to monitor the cell temperatures[10] and to detect significant pressure changes within the cell.

C. Results and Discussion

1. Transient States and Seeds. While the cell is warming up, several interrelated phenomena occur which stem from carbon flux and gravity.

The solubility of carbon in say the nickel–carbon or iron–carbon eutectic is higher at 55 kbars than at 1 atm.[6,7] Therefore, even a bath which is made of metal saturated with carbon at 1 atm will not be saturated with carbon when it melts in the reaction cell. The extra carbon is supplied from the nutrient carbon and also from the seeds. The density of the bath falls with increasing carbon concentration.

During the initial heating period the top bath (Figure 3) stirs itself by convection from the thermal and carbon concentration gradients, and carbon from the nutrient mass rapidly saturates the entire molten bath. In the bottom bath the main temperature and carbon concentration gradients act to oppose convection, and carbon from the nutrient mass moves downward into the bath by the relatively slower process of diffusion. An hour or more may be required to reach a steady state there, according to our studies.

(7) H. M. Strong, *Acta Met.*, **12**, 1411 (1964).

(8) H. M. Strong and R. E. Hanneman, *J. Chem. Phys.*, **46**, 3668 (1967).

(9) H. T. Hall, *Rev. Sci. Instrum.*, **31**, 125 (1960).

(10) R. E. Hanneman and H. M. Strong, *J. Appl. Phys.*, **36**, 523 (1965); **37**, 612 (1966).

Archimedes' principle still operates at very high pressures, and many substances including diamond and graphite float in the metal bath. The central nutrient mass remains in place by virtue of its rough surface against the container walls, but a few crystals of diamond which are loosened by dissolution may float upward to the cool end of the top bath to become visiting seed crystals. Thus the top bath rarely starves for seeds.

The cool end of the bottom bath is more suitable for growing only a few crystals because both seed and impurity populations tend to be lower there. The seed crystals are mechanically embedded in the bottom insulation so that they and any new growth upon them will not float up and dissolve. The problem is to have suitable seeds available when the steady state is finally reached. If the seed is too small or too exposed to the bath, it may dissolve entirely or float away during warm-up, and if no seeds remain, diamond growth, if any, will be erratic and based on diamond made *in situ* from precipitated graphite or diamonds nucleated spontaneously by a large carbon supersaturation. On the other hand, if the seed is too large, the new growth tends to be of poor quality because a relatively large, necessarily etched seed surface bears many active growth sites which, like barnacles on a ship, do not usually act in harmony. Extremely small variations in bath composition as well as the etching of the seed during warm-up ensure that a large crystal which is grown in one experiment will not be a flawless seed for the bath in a second experiment. Each crystal is an individual, with its own faults, adjusted to its environment, and the same crystal may not fare well in a slightly different environment. The etching problem would not be bothersome if something besides diamond (or graphite newly converted to diamond *in situ*) could be used as seeds, but so far only diamond has been found to be effective.[6]

2. Carbon Transport. In a given catalyst–metal system, the flux of carbon depends mainly upon the temperature gradient and can be estimated from the total amount of carbon found to be transported to the cool end in a known time interval. In the top bath, thermal convection aids diffusion, and carbon fluxes of 3×10^{-4} g sec^{-1} cm^{-2} or more are observed with temperature gradients of about 100° cm^{-1}. In the bottom bath the temperature gradient does not favor convection and the carbon fluxes are about 10^{-4} g sec^{-1} cm^{-2} through the liquid. It is easy to maintain carbon fluxes greatly in excess of what growing crystals can accommodate.

3. Nucleation. If the diamond nuclei present are kinetically unable to absorb the imposed carbon flux, graphite nucleates spontaneously, despite its thermodynamic instability, and grows as large, shiny flakes.[5] In the immediate vicinity of a diamond crystal grown well within the range of diamond stability no graphite is found, as shown in Figure 4. Here one looks at the cool end of an iron bath. The diamond crystal resting on the circular surface was pried from the cavity near it.

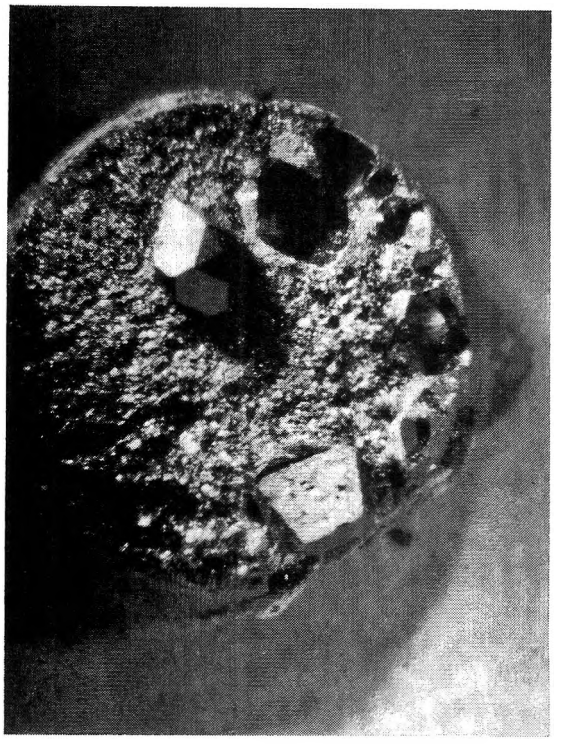

Figure 4. Cool end of iron bath with new diamond.

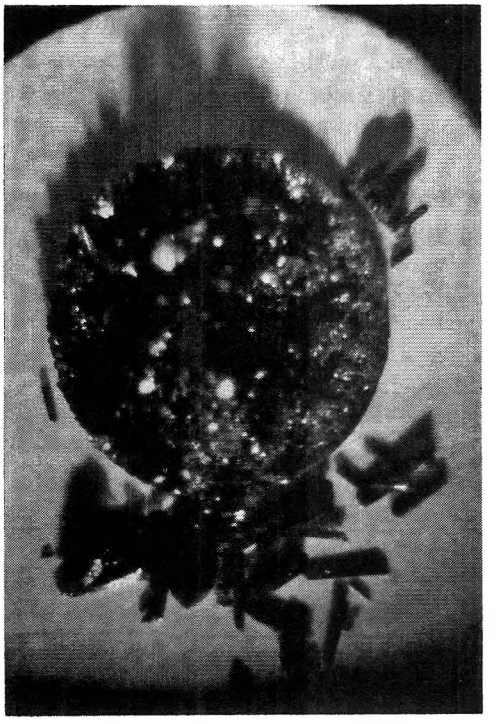

Figure 5. Prolific diamond growth on seed bed.

Figure 5 shows a prolific seedbed of diamond which, by virtue of its many active growth sites and large area, was able to accept as diamond all the carbon fed to it. One notes that certain crystals, usually twins,

grow faster than others, and, like the tallest trees in a forest, shadow their fellows.

It is possible for graphite which has been deposited from solution to change into diamond. This change is favored by higher operating pressures or by thermal cycling which may stress the graphite mechanically or produce a temporary supersaturation great enough to form locally imperfect graphite which is more easily converted to diamond because of its greater thermodynamic instability.

4. Crystal Growth. The diamond growth process appears to take place as follows. First, a tiny patch of a new layer—one might call it a "layer nucleus"—forms on say a crystal edge. Second, the layer spreads out as an advancing step to cover the face of the crystal. The thickness, number density, and frequency of formation of layer nuclei increase with supersaturation. To nucleate a layer requires a higher supersaturation than to make it spread.

Figure 6 is a photograph of the growing surface of a diamond crystal. The growth layers, a few microns thick, are typical. The layers originate from nucleation sites which usually lie near the edges of a crystal; these edges represent the vestiges of the most rapid-growing or easily nucleated crystal faces, as determined mainly by chemical bonding densities.

The advancing layer step perpetuates itself because its base or inside corner cannot advance as rapidly as the top corner. The top corner region has a better supply of fresh carbon atoms and the inside corner has a higher concentration of impurities accumulated in front of the advancing step. (See Figure 7.) The desorption and diffusing away of these impurities probably are the limiting rate factors in growing sound crystals. If the carbon is supplied too rapidly, the step is roofed over, and impurities and bath are trapped in the crystal.

Usually a growing crystal face bears many "difficult" regions over which new growth proceeds very reluctantly and near which growth layer steps tend to pile up. To avoid trapping impurities at such regions, new layers must not be nucleated faster than old ones are completed. If the area of difficult regions remained constant, regardless of crystal size, then the allowable radial growth rate of large crystals would be the same as for small crystals and would be much higher than is observed. However, if the area of difficult regions were proportional to the face area, then the time for a layer to traverse the face would be proportional to the face size, and since the growth layers seem to be all about the same thickness, the radial growth rate of the crystal would be inversely proportional to its average diameter.

Out of many experiments on diamond growth, some happened to be conducted at the maximum sound growth rate for the particular size crystal obtained, and a consideration of these data supports the analysis given above, although perhaps other growth mechanisms

Figure 6. Photomicrograph (350×) of growing surface of diamond crystal, showing stepped layers of growth.

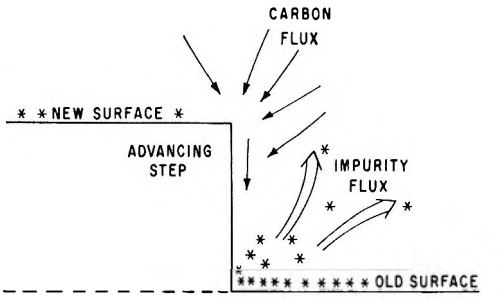

Figure 7. Sketch of processes occurring near a growth step.

could operate to produce the same result. Thus one may write

$$2srb = 1$$

where s is an average diameter, in mm, of the crystal; r is the maximum sound growth rate, in mm/hr; b is a parameter related to the particular conditions of growth. In this study, b often appears to be about 2.5 hr mm^{-2}. It varies somewhat for different baths.

Then the time to grow to a size L, growing always as fast as possible, is

$$T(L) = \int_0^L ds/r = \int_0^L 2bsds = bL^2$$

From this expression one may deduce that a high-quality, inclusion-free 3-mm crystal requires 22.5 hr, or a 6-mm crystal 90 hr, in typical transition metal–catalyst systems.

In practice it is not simple to adjust the supersaturation and layer nucleation and growth rates continuously so as to match the crystal size, and it is easier to

grow the entire crystal at a rate set by the final size. Then one finds that a 3-mm crystal would require about 55 hr, a 5-mm crystal 167 hr, etc. These values agree generally with experience in our laboratory; *i.e.*, a 5-mm (1 carat) gem quality crystal can be grown in about a week.

The value of the parameter b changes slightly with the composition of the bath. It would also be expected to fall with increasing temperature as impurity diffusion would be hastened, but the limited temperature range available to us in these studies has not permitted confirmation on this point. So far the average growth rates for diamond appear to be slightly below those obtained for quartz, garnets, ZnS, etc., from molten solvent systems.

5. Chemical Effects. More or less controlled amounts of certain impurities may be added to the bath by alloying them with the bath metal or placing them between the metal and nutrient. Many interesting reactions and effects may occur. For example, Ca or Sr are converted to their carbides and may gather some nitrogen as cyanamides. Other active metals such as Ti or Cr tend to form carbides—which may crystallize in the cool end of the bath and oxides, etc., which are more insoluble. Easily reduced oxides such as Fe_3O_4 are reduced and the product CO diffuses about in the cell. Si or Al can combine with excess O or reduce CO. S or P simply dissolve in the bath. It is difficult to be sure about anything with H because of its extreme mobility. Nitrogen is taken up by the growing diamond. Ordinary carbon, iron, nickel, etc. contain enough nitrogen to color the diamond yellow and produce other effects in the crystals. Excess nitrogen added as azide, cyanide, melamine, etc., produces green diamonds. Too much nitrogen, oxygen, or sulfur seriously interferes with diamond growth. Zr, Ti, or Al combine with N and the resulting diamonds are colorless. B also combines with N but the resulting diamonds are blue and semiconducting.[11] Either B or Al can be incorporated into growing diamonds in limited amounts depending, in part, on their concentration in the melt.

Although some of these diamond-growing baths appear to be chemically more pure than those in nature, it is very difficult to approach semiconductor standards of purity currently achieved in intrinsic silicon or germanium. Fortunately, the growing diamond does not always accept all the impurities present.

6. Further Considerations. At the moment it is not economical to use this method to grow gem crystals for sale. However, the method is technologically useful for growing many interesting kinds of diamond crystals in sizes large enough for studies of their properties.

Acknowledgment. I wish to express my thanks to W. A. Rocco for his help in this work.

(11) R. H. Wentorf, Jr., and H. P. Bovenkerk, *J. Chem. Phys.*, **36**, 1987 (1962).

Further Studies on Diamond Growth Rates and Physical Properties of Laboratory-Made Diamond

by H. M. Strong and R. M. Chrenko

General Electric Research and Development Center, Schenectady, New York 12301 *(Received November 30, 1970)*

Publication costs assisted by the General Electric Co.

Diamond crystals up to 1 carat size were grown in the Fe–C and Fe–Ni–C systems at ~57 kbars. In the Fe–C binary systems, Fe_3C is stable to 1688°K, preventing diamond growth below this temperature. Additions of Ni lower the melting temperature of Fe_3C and widen the temperature range for diamond growth. Carbon diffusivity at 57 kbars in molten Fe is about 4×10^{-5} cm²/sec, and diamond growth rates of 1 to 2.5 mg/hr were obtained. Depending on the nature of the bath metal used, crystal shapes obtained included cuboctahedra or crystals with {113}, {110} faces in addition to {111} and {100} faces. N and B, which occupy substitutional positions in diamond, are preferentially absorbed in certain directions producing interesting color patterns. Laboratory-made diamonds have comparable mechanical and electrical properties with natural diamond. The thermal conductivities of laboratory diamonds were ~5 times the conductivity of Cu at room temperature.

I. Introduction

Thousands of carats of industrial abrasive diamond are produced every day by the catalytic process in which graphite is transformed to diamond through a molten layer of metal such as iron or nickel. In this method, the driving force for the formation of diamond is derived from the difference in thermodynamic stability between the two phases of carbon. Other methods were discovered for the direct conversion of graphite to diamond at pressures exceeding 140 kbars.[1-3] These methods have produced considerable quantities of diamond in both the cubic and the more recently recognized hexagonal modification of diamond.[3,4] Due to the rapidity of the direct conversion processes, the crystals are no larger than a few hundred ångstroms. Even the melt freeze process, which requires the extreme conditions of 4000°K at 140 kbars, has been used successfully to produce a few milligrams of tiny diamond crystals.[5] None of these laboratory methods has yet successfully demonstrated a feasibility for sustained growth of diamond over sufficiently long time periods to form large diamonds.

The process by which nature has produced large gem diamonds has been speculated about[6,7] but it is not assuredly understood. Experiments on transporting carbon in molten silicates, in which natural diamonds were assumed to have grown, were failures. Laboratory experiments may sometimes reproduce natural conditions in respect to the thermodynamic variables but can be at a disadvantage in respect to the time variable.

Wentorf[8] has described in the preceding paper a process which sustains stable diamond growth over longer time periods than in previously reported laboratory experiments to produce larger diamonds in a reasonable time span. This process uses molten group VIII metal baths in which to transport carbon in a temperature gradient. These are complex systems to control satisfactorily for the growth of large perfect diamond crystals. In this report, the nature of some of these systems and how they were used to obtain good quality single diamond crystals in the 1 carat size range will be described. Some of the interesting physical properties of these diamonds will be described also.

II. Transition Metal–Carbon Systems for Diamond Growth

Long experience on the part of crystal growers has shown that the best media for forming large well faceted perfect crystals in the shortest times and without excessive nucleation of interfering crystals are those in which the nutrient dissolves to the extent of 10 to 60%. Crystallization will take place at temperatures a little above the eutectic for the mixture. There are rough guidelines for finding such media and the locations of their eutectics.[9] It is usually true that the most favorable conditions are achieved when the melting points of nutrient and growth media are as nearly alike as possible in order that the eutectic compositions will be in the desired range.

These guidelines applied to carbon–metal systems

(1) F. P. Bundy, *Science*, **137**, 1057 (1962).

(2) P. S. DeCarli and J. C. Jamieson, *ibid.*, **133**, 1821 (1961).

(3) E. I. du Pont de Nemours & Co., Netherlands patent release 6506395 (1965).

(4) R. E. Hanneman, H. M. Strong, and F. P. Bundy, *Science*, **155**, 995 (1967).

(5) F. P. Bundy, *J. Chem. Phys.*, **38**, 631 (1963).

(6) R. H. Wentorf, Jr., and H. P. Bovenker, *Astrophys. J.*, **134**, 995 (1961).

(7) G. C. Kennedy and B. E. Nordlie, *Econ. Geol.*, **63**, 495 (1968).

(8) R. H. Wentorf, Jr., *J. Phys. Chem.*, **75**, 1833 (1971).

(9) G. T. Kohman and D. H. Andrews, *ibid.*, **29**, 1317 (1925).

indicate that carbon should be used with one of the refractory metals. Systems of this type have very high melting ranges (stable carbides are a problem also) which are difficult to support at diamond stable pressures[10] for prolonged periods. It is not presently feasible to use these metals in the gradient diamond growth process. The choice of bath metals is thus narrowed to the lower melting ferrous metals and their alloys, whose eutectic compositions were < 10% carbon. The performance in diamond growth of these ferrous metal alloys has not matched, by a wide margin, that of nature's system which has produced a long list of fabulous gem diamonds.

In using the lower melting point metals, the problems which arise are those of excessive nucleation and development of flaws from entrapment of veils of metal. The growth rates must be kept low to avoid these difficulties. The method of using these alloys was described by Wentorf in the preceding paper.[8]

The iron–carbon system forms a base for mixtures of metals used in diamond growth. At 57 kbars this system is quite different from the system at 1 atm. Melting points have shifted upward; carbon appears in two stable phases and Fe_3C has a region of stability. The resulting system, Figure 1, has three eutectics, only one of which (the Fe–Fe_3C eutectic) is stable. The Fe–d and Fe–g eutectics fall at lower temperatures and are unstable with respect to Fe_3C (experimental details to be published.) Diamond growth is restricted to the region between the diamond–graphite equilibrium at 1830°K and the melting of Fe_3C at 1688°K. Note that in the presence of Fe, the diamond–graphite equilibrium is shifted downward in temperature from the pure carbon equilibrium.[11] At temperatures lower than 1688°K, diamond gives way to the greater stability of Fe_3C which rapidly consumes the diamond. Crystals grown in the Fe–C system develop slowly and often with flaws.

In the liquid range where diamond growth is possible, the gradients of temperature and carbon concentration are ~50°/cm and ≈6 × 10^{-3} g/cm³ cm, respectively.

An equilibrium rarely seen in nature occurs in the Fe–C system. At 52.5 kbars and 1680°K, there is a fourfold equilibrium or quadruple point between diamond, graphite, Fe_3C and liquid. This is in accord with the Gibbs phase rule.

The nickel–carbon system has characteristics similar to the iron–carbon system, except for the absence of a stable carbide.[11] The nickel–diamond liquid eutectic at 57 kbars lies at a lower carbon concentration and at a higher temperature than for the iron–diamond system. However, due to the stable Fe_3C phase, the effective operating temperatures for the two systems are nearly the same.

The ternary Fe–Ni–C system has advantages over the two binary systems because the stability of Fe_3C is reduced and the liquid–diamond equilibrium spans a wider temperature range. A section of the ternary system at 57 kbars and 1400° is shown in Figure 2.

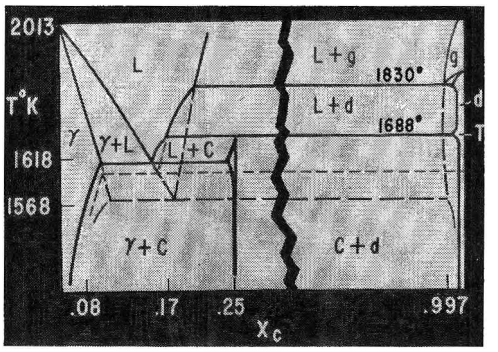

Figure 1. Fe–C system at 57 kbars.

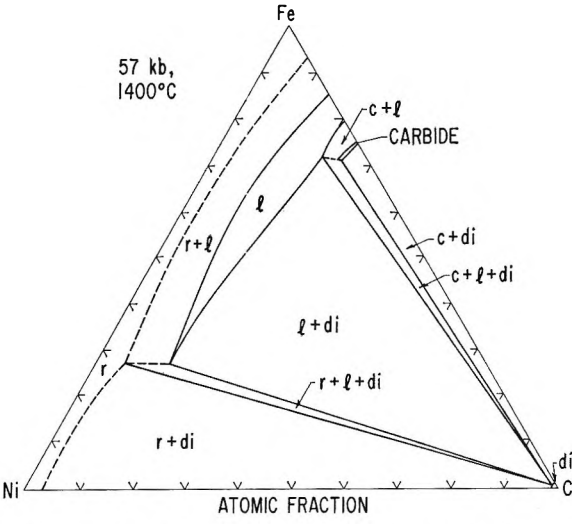

Figure 2. Fe–Ni–C ternary system at 57 kbars, 1673°K.

The Fe–Al–C system has also been used effectively. It was known from foundry practice that Al can suppress carbide formation in iron. The same property operates at 57 kbars to reduce the melting point of the system to <1600°K.

III. Carbon Diffusivity in Molten Transition Metals

The growth rates of large diamond crystals are consistent with a carbon diffusivity of ~4 × 10^{-5} cm²/sec. A diffusion rate in the range 2 × 10^{-5} to 4 × 10^{-5} was observed in two other types of experiments relating to diamond growth. These were: (1) measurements on the rate of advance of the melting line between carbon saturated liquid and solid metal, from carbon source downward toward the seed end of the bath metal; and (2) measurements on the rate of growth of diamond on a large (111) seed face through a thin molten Ni film.[11] The 1-atm diffusivity of carbon in liquid iron in the

(10) F. P. Bundy, H. P. Bovenkerk, H. M. Strong, and R. H. Wentorf, Jr., *J. Chem. Phys.*, **35**, 383 (1961).

(11) H. M. Strong and R. E. Hanneman, *ibid.*, **46**, 3668 (1967).

temperature range 1400 to 1800°K was measured by Morgan and Kitchener[12] and Hillert and Lange.[13] Their diffusivities ranged between 4×10^{-5} and 8×10^{-5} cm²/sec. At 1570–1670°K, the temperature level at which diamond studies were conducted at high pressure, Hillert and Lang obtained diffusivities of 6.0×10^{-5} to 6.7×10^{-5} cm²/sec. High-pressure diffusivities will be lower than 1-atm diffusivities when there is a positive activation volume, ΔV, of diffusion. In this case, the ratio of high-pressure diffusivity to low-pressure diffusivity is about 4.0:6.7 or 0.6. The decrease in diffusivity at high pressure arises from the additional $P\Delta V$ work of activation so that

$$0.6 \approx e^{-P\Delta V/RT}$$

from which $\Delta V \approx 1$ cm³/mol. This value of ΔV is consistent with the model of interstitial diffusion of carbon in molten iron.

IV. Single Crystal Growth

A number of methods have been devised for obtaining single crystal growth. Basically, the carbon flux must be restricted so that spontaneous nucleation has a low probability. Initially, it is difficult for the seed to adsorb all of the flux. If pressure and temperature conditions are not too far into the diamond stable region, graphite rather than diamond will deposit in an annular ring surrounding the seed diamond to accommodate the excess carbon flux. Because of the radial temperature gradient in the growth region, the graphite ring can act as nutrient for the seed growth when the latter has progressed far enough to accommodate a higher flux rate. The seed will not dissolve in the bath metal during the warm-up period if the temperature is brought up in such a way that the carbon flux from the nutrient reaches the bottom of the cell before the seed is appreciably attacked.

Growth periods may run for several days during which time temperature, pressure, and temperature gradient are held constant. Growth rates obtained are 1 to 2.5 mg/hr, overall average. The initial growth rate is a little less than the average.

Laboratory diamonds are illustrated in Figures 3–5.

V. Impurities in Diamond

The environment for diamond growth both in nature and in the laboratory contains a number of ubiquitous impurities, some of which become incorporated in diamond, a few in substitutional positions, others as micro-inclusions. While diamonds have been produced with quite low levels of impurity in the laboratory and in nature, no crystals have been observed that had impurity levels as low as in the highest purity germanium and silicon crystals.

A wide variety of impurities are found in diamond but the most interesting in terms of reported effects on diamond properties are those believed to occupy substitutional positions, nitrogen, aluminum, and boron.[14–25]

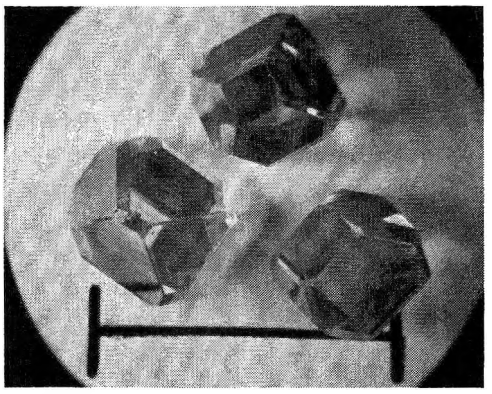

Figure 3. Yellow laboratory grown diamonds, 0.75 to 0.9 carat size. Line is 1 cm long.

Nitrogen is a major impurity in both natural and synthesized diamond, but it assumes different forms in the two kinds of diamond. Nitrogen in the majority of natural diamonds has been identified in the form of platelets lying in (100) planes[15–17] in concentrations up to several times 10^{20} atoms/cm³. Platelet nitrogen imparts a characteristic infrared absorption and alters somewhat the mechanical properties of diamond. Platelet nitrogen in moderate concentrations does not affect the color of diamond.

The nitrogen in synthesized diamond is atomically dispersed,[18–19] can be detected by paramagnetic resonance, and occurs in concentrations up to 10^{20} atoms/cm³. In concentrations of a few parts per million or more, this paramagnetic nitrogen imparts a yellow color and a characteristic infrared absorption at 1130 cm^{-1}. Diamonds in this class usually have very high electrical resistivities (the energy level of the electron on the N donor atom lies about 4 eV below the conduction band) and somewhat modified mechanical properties. The crystals have a generally cuboctahedral shape with small {110} and {113} faces, Figure 3.

(12) D. W. Morgan and J. A. Kitchener, *Trans. Faraday Soc.*, **50**, 51 (1954).

(13) M. Hillert and N. Lange, *J. Iron Steel Inst. London*, **203**, 273 (1965).

(14) W. Kaiser and W. L. Bond, *Phys. Rev.*, **115**, 857 (1959).

(15) R. J. Elliott, *Proc. Phys. Soc., London*, **76**, 787 (1960).

(16) M. Takagi and A. R. Lang, *Proc. Roy. Soc. Ser. A*, **281**, 310 (1964).

(17) T. Evans and C. Phaal, *ibid.*, **270**, 538 (1962).

(18) W. V. Smith, P. P. Sorokin, I. L. Gelles, and G. J. Lasher, *Phys. Rev.*, **115**, 1546 (1959).

(19) H. B. Dyer, R. A. Raal, L. Du Preez, and J. H. N. Loubser, *Phil. Mag.*, **11**, 763 (1965).

(20) W. V. Smith, I. L. Gelles, and P. P. Sorokin, *Phys. Rev., Lett.*, **2**, 39 (1959).

(21) A. T. Collins, P. J. Dean, E. C. Lightowlers, and W. F. Sherman, *Phys. Rev. A*, **140**, 1272 (1965).

(22) R. H. Wentorf, Jr., and H. P. Bovenkerk, *J. Chem. Phys.*, **36**, 1987 (1962).

(23) E. C. Lightowlers, *Anal. Chem.*, **34**, 1398 (1962); **35**, 1285 (1963).

(24) A. T. Collins, private communication, also to be published in *Ind. Diamond Rev.*, in press.

(25) E. C. Lightowlers, private communication.

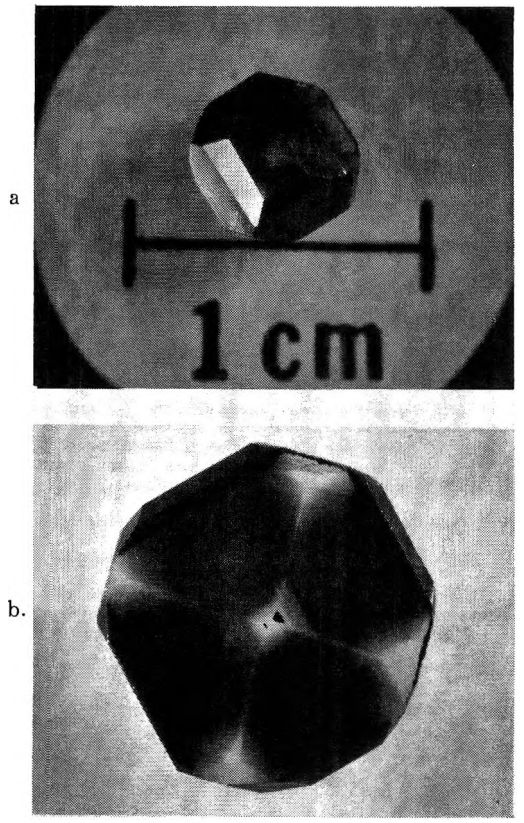

Figure 4. (a) A blue laboratory diamond of 0.9 carat. B is concentrated in dark quadrant regions. (b) Cross sectioned B-doped laboratory diamond. The dark regions are blue. Crystal is 5 mm across.

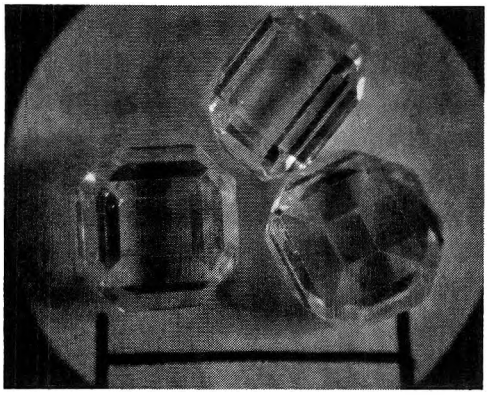

Figure 5. Colorless laboratory-grown diamonds of 0.8 to 0.9 carat size. Line is 1 cm long.

The effects of aluminum and boron in diamond are at present not perfectly clear. While it has been reported formerly[21] that aluminum was responsible for an acceptor center in conducting diamond at 0.373 eV and a characteristic absorption at 2800 cm^{-1}, recent work has shown that these properties may be due to boron.[24,25] The experiments reported here on large-diamond growth suggest that aluminum is an important getter for nitrogen but that boron is mainly responsible for conduction in diamond. Boron also imparts a blue color to nitrogen-free diamond, Figure 4.

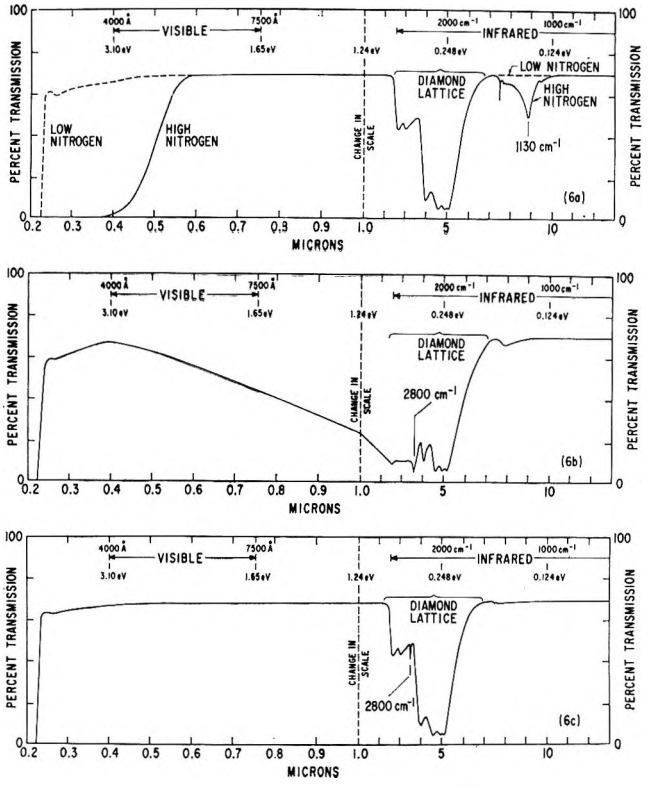

Figure 6. Absorption spectra of large laboratory-grown diamonds: (a) diamonds containing high and low nitrogen concentrations; (b) diamond doped with aluminum and boron; (c) diamond doped with aluminum only.

Some of the characteristic absorption spectra of large laboratory-grown diamond crystals are shown in Figure 6. Figure 6a illustrates spectra for diamonds containing high and low nitrogen concentrations. Figure 6b shows the spectrum of a diamond doped with aluminum and boron. The spectrum of a diamond doped with Al only is shown in Figure 6c. The assignment of the 2800-cm^{-1} absorption band to Al is now being questioned. In this work, the intensity of the 2800-cm^{-1} band did not correlate with concentration of aluminum in diamond as determined by activation analyses.

The impurities in synthesized diamond are subject to some control through selection of the bath metal. Diamonds grown in most ferrous and platinum metal alloys have a rather pleasing deep yellow color that has been identified with dispersed paramagnetic nitrogen in concentrations of 10^{18} to 3×10^{19} atoms/cm^3. The nitrogen content can be lowered by adding a nitrogen-getter to the bath metal—for example, titanium which forms a very stable nitride. Aluminum will also getter nitrogen and has been reported to be a compensator for nitrogen,[21] but the latter is now doubtful. When the nitrogen is lowered to about 10^{17} atoms/cm^3 or less, the crystals lose visible traces of yellow color.

Attractive blue-white diamonds were made by adding a few micrograms of boron to the bath metal. It has been possible to reproduce the spectroscopic characteris-

tics of the blue Hope diamond, but the resemblance ended there. In addition to the esthetic appeal of the blue crystals they do have valuable semiconducting properties.

VI. Effect of Impurities on Diamond Growth

Impurities and the nature of the bath metal have an important influence on the growth rates and morphology of diamond. Because an absolutely pure crystal has not been grown in the laboratory, there is at present no reference by which to judge quantitatively the influence of specific impurities on the growth rate. However, it has been observed that the fastest growth rates of large crystals free from visible flaws, ~2.5 mg/hr overall average, were achieved in bath metals which introduced 10^{18} to 10^{19} atoms/cm^3 dispersed paramagnetic N into diamond. When diamond was grown in baths that restricted the N concentration to less than 10^{17} atoms/cm^3, the growth rate had to be restricted to $\leqq 1.5$ mg/hr to avoid bath metal inclusions.

The Bravais[26] rule in crystal growth states that the crystal faces having the higher reticular density tend to grow more slowly than the faces of low reticular density. The faces of low reticular density then grow rapidly and disappear in a point or edge, while the slow-growing faces remain and form the crystal's facets. The rule has been justified on the grounds of minimizing surface energy. There are many exceptions to this rule which are caused by impurities or unusual properties of the growth medium, but it seems to apply quite well to diamond. The {111} faces of diamond have the highest reticular density and it is these faces which are most frequently seen in both natural and synthesized diamond. Other low index faces having relatively high reticular densities are the {100} and {110} faces. Synthesized diamond characteristically displays {111} and {100} faces while {111} and {110} are more common to natural diamond. There is little doubt that impurities in the growth environment influence crystal shape through absorption on specific crystal faces, affecting the growth rates of those faces.

Impurities tend to segregate along certain planes or directions in laboratory diamonds. An example of nitrogen segregation is seen in Figure 7 which shows a cross section of a large yellow cuboctrahedron. The dark regions (actually deep yellow) associated with the {111} planes contain 100 ppm of dispersed paramagnetic N as determined from its 1130-cm^{-1} absorption band.[27] The lighter regions contain only 5–7 ppm of N. The preference for absorption of nitrogen along the {111} planes may have helped slow the growth of these faces sufficiently to make this crystal have a predominantly octahedral shape.

In the B-doped diamond illustrated in Figure 4a, the absorption at 2800 cm^{-1} is several times as strong in the blue quadrant areas as in the light diagonal zones. The quadrant areas showed the highest B level in B activation analyses. Figure 4b shows a cross-sectional B-doped diamond.

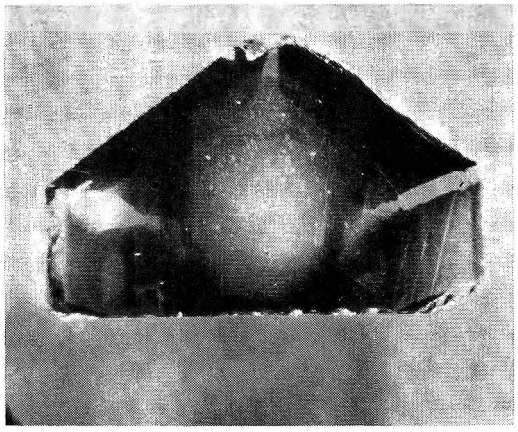

Figure 7. Cross section of a 0.6 carat laboratory-grown cuboctahedron on a (110) plane. The light regions contain 5–7 ppm of N. Sharp boundary light regions lie in approximate ⟨113⟩ directions.

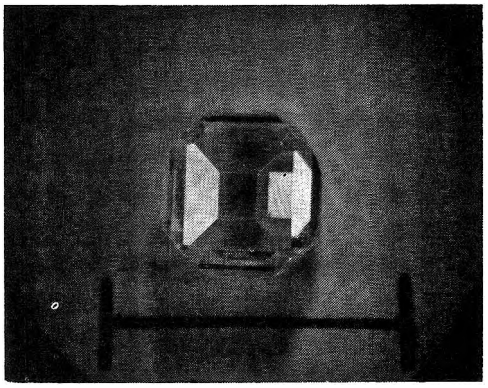

Figure 8. A many-faceted colorless crystal with its original faces. Some of the original faces were polished slightly to remove the frostiness produced by the metal crystals in the bath metal as the metal freezes when the heating power is turned off.

In the growth of colorless diamond, the ⟨110⟩, ⟨113⟩, and sometimes ⟨117⟩ directions have retarded growth rates so that the corresponding faces appeared. Crystals of this type with their multifaceted exteriors are quite attractive and somewhat more sparkly than the simple cuboctrahedra. An example of an as grown multifaceted crystal is shown in Figure 8.

VII. Mechanical Properties of Diamond

Aside from its eye appeal as a gem, the real value of diamond is in its remarkable combination of physical properties. First and foremost is its hardness which is several times that of other very hard materials. Because of this property, expensive diamond is often the cheapest cutting material to use.

Just as the physical properties of steel are altered in

(26) M. A. Bravais, *J. Ecole Polytech.*, 167 (1851).

(27) R. M. Chrenko, H. M. Strong, and R. E. Tuft, *Phil. Mag.*, in press.

countless variety by the dispersal of a little carbon, or other elements in it, so are the properties of diamond modified by dispersal of N, Al, and B in its lattice. The diamond structure has intrinsically different strength and hardness qualities in different crystal directions.[28] Impurities incorporated in diamond under laboratory growth conditions tend to segregate along particular crystal directions so that the combination of intrinsic and impurity effects in diamond can be quite complicated. Not all impurity effects have been explored, but a few are described below.

The effect of nitrogen is somewhat dependent on the form in which it enters diamond, platelet or dispersed. The presence of platelet nitrogen in {100} planes, tends to prevent the movement of dislocations, thus reducing the plastic flow[29] of diamond and increasing its apparent indentation hardness. The presence of dispersed nitrogen seems to decrease the indentation hardness and resistance to rough abrasion as measured on the {100} planes. Laboratory diamonds are capable of wearing away 30–100 ft³ of corundum wheel per gram of diamond consumed. Natural diamonds probably have about the same capability, but the ones tested in this work had abrasion resistances in the low end of this range.

Published work on the thermal conductivity of natural diamond (in ref 28) showed that nitrogen-free diamond had higher thermal conductivities than those containing platelet nitrogen. The thermal conductivities of a 1-carat flawless nitrogen-free laboratory diamond and of a $^3/_4$ carat yellow laboratory diamond containing 100 ppm of nitrogen were measured by Slack.[30] Published data on diamonds and those of Slack in this laboratory are shown in Figure 9. Note that at room temperature, the thermal conductivities of the yellow and of the colorless laboratory diamonds were, respectively, 4.4 and 5 times that of copper at room temperature.

The degree of crystal perfection in laboratory-made diamonds is presently being studied with etching and X-ray diffraction techniques.

The mechanical properties of diamonds, even those modified by impurities, are still at some of the extreme limits of properties produced by nature. Thus, unsupported diamond anvils, even impure ones, are capable of squeezing other substances up to pressures of nearly 200 kbars for X-ray diffraction studies on high-pressure structures, or an impure diamond phonograph needle will last for several years. A diamond gem lasts unscathed for many lifetimes.

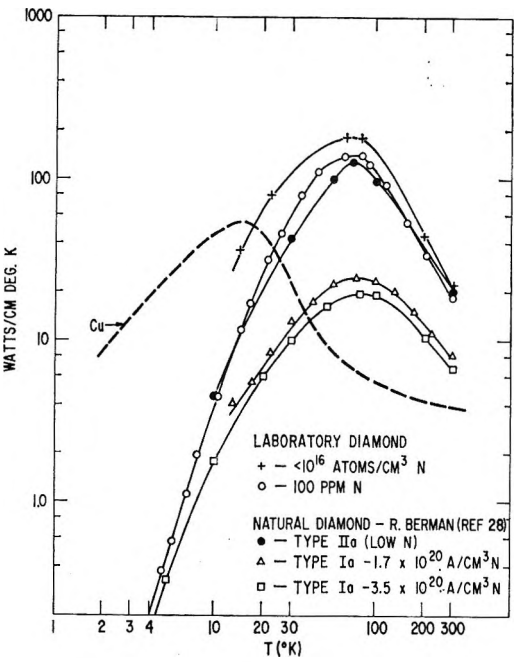

Figure 9. Thermal conductivity *vs.* absolute temperature for laboratory and natural diamond.

The possibility of growing large diamonds in the laboratory with controlled impurity content offers the opportunity for improved understanding of impurity effects in diamond. These studies are in progress.

Acknowledgments. We wish to thank R. E. Tuft for his highly skilled help and patience in growing many large diamond crystals and K. A. Darrow for his valuable help in shaping some of the diamonds for physical tests as well for performing some of those tests.

(28) "Physical Properties of Diamond," R. Berman, Ed., Clarendon Press, Oxford, 1965, contains articles by several authors on mechanical and abrasion properties. Thermal properties: Chapter 14.

(29) T. Evans and R. K. Wild, *Phil. Mag.*, 12, 479 (1965).

(30) G. A. Slack, private communication.

Potential Energy Surfaces for Atom Transfer Reactions Involving Hydrogens and Halogens[1]

by Christopher A. Parr

Chemistry Department, University of Toronto, Toronto, Canada

and Donald G. Truhlar*

Chemistry Department, University of Minnesota, Minneapolis, Minnesota 55455 *(Received October 5, 1970)*

Publication costs borne completely by The Journal of Physical Chemistry

Potential energy surfaces (PES) for the reactions $X + HD \underset{2}{\overset{-2}{\rightleftharpoons}} HX + D \underset{3}{\overset{-3}{\rightleftharpoons}} DX + H$, where X is a halogen, are reviewed. Reactions involving two or three halogen atoms are also discussed. Many calculations have been performed using semiempirical variations of the London PES equation (LEPS methods) which was originally developed for treating the $H + H_2$ reactions. There are many problems in extending this treatment to the halogen reactions and some of these, including excited electronic states, p orbitals, relativistic effects, and possibilities for nonlinear transition states, are mentioned. Furthermore, the London equation and its variations are found to be pathologically sensitive to the input coulomb ratios, both when these are semiempirical and when they are theoretical. The use of transition state theory to relate postulated potential energy surfaces to experimental data causes further errors, especially for reaction 2 when X = Br or I. More importantly, rate data in thermal bulk-gas systems are insufficient to determine most PES features. Experiments which measure scattering angles and internal energies of the products combined with single-collision scattering theory interpretations will provide more critical conditions on trial PES topography. *A priori* calculations of potential energy surfaces will also be useful in some cases. For some cases, features such as reaction barrier height and location and width of the barrier can presently be assigned satisfactory qualitative values. However, the depth and even the existence of potential wells in many of the systems is uncertain. In cases where wells are known to exist, it is found that the semiempirical LEPS methods fail to reproduce observed force constants. The transferability of the Sato parameters in the LEPS methods from system to system is not promising, but it is possible that a single set of Sato parameters will serve well for both reactions 2 and 3 for a single X. New transition state isotope effects for reaction −2 with X = Br are presented. Although they give results closer to experimental values than do previous calculations, it is shown why little confidence can be placed in the absolute accuracy of the PES leading to these predictions.

I. Introduction

Ever since the classic experiments of Bodenstein, Farkas, and coworkers,[2] the gas phase reactions of hydrogen and halogen atoms and molecules with one another have provided an important testing ground for the development of ideas about chemical dynamics. Unfortunately, the hydrogen–halogen systems are too complex for a rigorous quantum mechanical study of their dynamics. Furthermore, it is only very recently that these reactions have been investigated in molecular beams.[3-7] For these and other reasons, there are still many gaps in our understanding of the dynamics of even these simple chemical systems. In this article, we review some of the recent studies of these reactions with emphasis on one aspect of the problem—the potential energy surfaces for these reactions. We will concentrate our attention on the reactions

$$H + H_2 \longrightarrow H_2 + H \quad (1)$$

$$H + HX \longrightarrow H_2 + X \quad (2)$$

$$X + H_2 \longrightarrow XH + H \quad (-2)$$

$$H + XH \longrightarrow HX + H \quad (3)$$

that is, special cases of

$$A + BC \longrightarrow AB + C \quad (4)$$

where X is a halogen atom. Other triatomic systems including hydrogen and halogen atoms will be consid-

(1) EDITOR'S NOTE. It has been suggested that it would be useful to publish in the Journal, from time to time, a review article dealing with a specific subject of strong interest to a large number of physical chemists, and of sufficient complexity that a clarifying review might be timely and helpful. The editors would seek to identify such topics and to invite appropriate colleagues to contribute such reviews. We present in this issue the second such review article; we would be grateful for comment and reactions from readers of the Journal.

(2) (a) M. Bodenstein and S. C. Lind, *Z. Phys. Chem.*, **57**, 168 (1906); M. Bodenstein and H. Lütkemeyer, *ibid.*, **114**, 208 (1924); M. Bodenstein, *Trans. Faraday Soc.*, **27**, 413 (1931); (b) A. Farkas, *Z. Phys. Chem.*, **B10**, 419 (1931).

(3) R. B. Bernstein, *Science*, **144**, 141 (1964); E. F. Greene and J. Ross, *ibid.*, **159**, 587 (1968); M. Karplus in "Structural Chemistry and Molecular Biology," A. Rich and N. Davidson, Ed., W. H. Freeman & Co., San Francisco, Calif., 1968, p 837.

(4) S. Datz and E. H. Taylor, *J. Chem. Phys.*, **39**, 1896 (1963).

(5) W. L. Fite and R. T. Brackman, "Proceedings of the Third International Conference on the Physics of Electronic and Atomic Collisions," M. R. C. McDowell, Ed., North-Holland Publishing Co., Amsterdam, 1964, p 955; W. L. Fite and R. T. Brackman, *J. Chem. Phys.*, **42**, 4057 (1965).

ered in less detail. We will see that the combination of present experimental and theoretical findings still leaves wide uncertainties in the possible topography of the potential surfaces for reactions 2 and 3. The surface for reaction 1 is better understood.

While this article is essentially a review, in some cases additional calculations have been carried out and are presented where appropriate.

II. Potential Energy Surfaces

As usual in treating molecular mechanics, we make a separation of electronic and nuclear motions to a good approximation.[8] For each fixed set of relative nuclear coordinates, we solve for the energy states of the electronic system. The energy of each of these electronically adiabatic states as a function of the positions of the nuclei can be considered as a hypersurface in coordinate-energy space. Each hypersurface is the effective potential energy for motion of the nuclei when the system is in that electronic state. We will generally be interested only in the lowest potential energy surface. The suggestion that chemical reactions do not involve more than one such surface was first put forward by London[9] and is sometimes called London's adiabatic hypothesis. Although reactions which violate that hypothesis are known,[10] many reactions taking place at moderate temperatures involve only ground electronic states.[11] The most important case where we expect more than one surface to be important is when there is a degeneracy (such degeneracies occur, *e.g.*, in the H_2X systems discussed below). Except where otherwise stated, we will assume that the adiabatic hypothesis applies to the reactions discussed in this article, and we will consider only the lowest electronic state.

The determination of the reaction dynamics from an assumed surface is much more straightforward than the reverse problem of reconstructing the potential energy surface from experimental chemical rate data. Thus the latter is usually accomplished by trial and error. For want of a purely empirical method for the determination of potential surfaces, semiempirical and *a priori* methods are usually employed. Potential energy surfaces for chemically reactive systems can be calculated by the superposition of configurations procedure (called configuration interaction or CI). To achieve chemical accuracy, *i.e.*, potential energies accurate to a few kilocalories per mole, it is necessary to use very many configurations,[12] and accurate wave functions have not yet been obtained for most systems.[13]

One way of selecting configurations for a CI calculation is the valence-bond (VB) method.[14,15] In particular, we can obtain the "complete" nonionic VB theory by selecting all the linearly independent configurations in which the electrons are assigned to some unique set of atomic orbitals.[16] Such calculations neglect configurations corresponding to partially occupied orbitals (polarization orbitals and expanded orbitals) and to ionic states. However, the complete nonionic VB wave function for a reacting system corresponds closely to a simple picture of bond breaking and bond making[17] and lends itself readily to *semiempirical* treatment for systems with a small number of *valence* electrons.

The nonorthogonality of the atomic orbitals used to construct VB configurations has made *a priori* calculations by this method impractically difficult until quite recently. However, some accurate valence bond wave functions have been obtained,[18,19] and it is probable that many more will be carried out in the next few years due to improved computing techniques and modified VB procedures.[12,20] At present, however, although

(6) (a) Y. T. Lee, J. D. McDonald, P. R. LeBreton, and D. R. Herschbach, *ibid.*, **49**, 2447 (1968), Cl + Br_2, Br + I_2. (b) J. B. Cross and N. C. Blais, *Bull. Amer. Phys. Soc.*, **14**, 315 (1969); *J. Chem. Phys.*, **50**, 4108 (1969), Cl + Br_2; *Bull. Amer. Phys. Soc.*, **15**, 347 (1970), Cl + I_2; *J. Chem. Phys.*, **52**, 3850 (1970), Cl + Br_2. (c) H. J. Loesch and D. Beck, "Sixth International Conference on the Physics of Electronic and Atomic Collisions," I. Amdur, Ed., M.I.T. Press, Cambridge, Mass., 1968, p 587, Cl + Br_2, Cl + I_2, Cl + BrI, Br + I_2, Br + ICl. (d) Y. T. Lee, P. R. LeBreton, J. D. McDonald, and D. R. Herschbach, *J. Chem. Phys.*, **51**, 455 (1969), Cl + BrI, Br + ClI. (e) See also ref 88 for F + D_2.

(7) J. Geddes, H. F. Krause, and W. L. Fite in I. Amdur, ref 6c, p 635; *J. Chem. Phys.*, **52**, 3296 (1970), D + H_2.

(8) M. Born and R. Oppenheimer, *Ann. Phys.*, **84**, 457 (1927); M. Born and K. Huang, "Dynamical Theory of Crystal Lattices," Clarendon Press, Oxford, 1954, Secton 14.

(9) F. London, "Probleme der Modernen Physik-Sommerfeld Festschrift," S. Herzel, Leipzig, 1928, p 104.

(10) See, for example (a) B. A. Thrush, *Chem. Britain*, **2**, 287 (1966); (b) M. C. Moulton and D. R. Herschbach, *J. Chem. Phys.*, **44**, 3010 (1966); (c) W. Brennen and T. Carrington, *ibid.*, **46**, 7 (1967); (d) D. W. Naegeli and H. B. Palmer, *ibid.*, **48**, 2372 (1968).

(11) B. A. Thrush, "Chemische Elementarprozesse," H. Hartmann, Ed., Springer-Verlag, Berlin, 1968. For reaction 2, there are exothermic processes which lead to electronically excited X. However, P. Cadman and J. C. Polanyi *J. Phys. Chem.*, **72**, 3715 (1968), have found that most (>98%) of the reactive collisions lead to ground state X, when X = I. Thus the adiabatic hypothesis may be a good one even for reaction 2 at thermal energies.

(12) Configuration interaction wave functions for which the orbitals as well as the configuration weights are optimized should be particularly useful. See, for example, G. Das, *J. Chem. Phys.*, **46**, 1568 (1967); R. C. Ladner and W. A. Goddard, III, *ibid.*, **51**, 1073 (1969). One such method [W. A. Goddard, *Phys. Rev.*, **157**, 81 (1967); W. E. Palke and W. A. Goddard, *J. Chem. Phys.*, **50**, 4524 (1969)] provides a natural extension of the valence-bond method.

(13) There are, of course, some noteworthy exceptions to this gloomy statement. We will consider one in the next section on the H + H_2 reaction; see also M. Krauss *Ann. Rev. Phys. Chem.*, **21**, 39 (1970).

(14) A good review of valence-bond theory is given by M. Kotani, K. Ohno, and K. Kayama in "Encyclopedia of Physics," Vol. 37, S. Flügge, Ed., Springer-Verlag, Berlin, 1961, Part II, p 1.

(15) J. C. Slater, *Phys. Rev.*, **38**, 1109 (1931).

(16) L. Pauling, *J. Chem. Phys.*, **1**, 280 (1933).

(17) See, for example, R. N. Porter and L. M. Raff, *ibid.*, **50**, 5216 (1969).

(18) F. A. Matsen and J. C. Browne, *J. Phys. Chem.*, **66**, 2332 (1962); P. L. Moore, J. C. Browne, and F. A. Matsen, *J. Chem. Phys.*, **43**, 903 (1965).

(19) L. C. Allen, R. M. Erdahl, and J. L. Whitten, *J. Amer. Chem. Soc.*, **87**, 3769 (1965); L. C. Allen, A. M. Lesk, and R. M. Erdahl, *ibid.*, **88**, 615 (1966); F. E. Harris, *Int. J. Quantum Chem.*, **1S**, 329 (1967); R. Kapral, *J. Chem. Phys.*, **46**, 2317 (1967); J. F. Harrison, *J. Amer. Chem. Soc.*, **91**, 807 (1969); T. G. Heil, S. V. O'Neil, and H. F. Schaefer, *Chem. Phys. Lett.*, **5**, 253 (1970).

(20) G. G. Balint-Kurti and M. Karplus, *J. Chem. Phys.*, **50**, 478 (1969).

there has been recent interest[21] in using semiempirical molecular orbital-type methods for predicting potential surfaces of organic systems not containing H_2, the only calculations on the potential surfaces for reactions 2 and 3 have involved the semiempirical VB method.[22]

In this review we concentrate on the semiempirical techniques which have actually been applied to reactions 1–3 rather than on the most promising *a priori* techniques.

III. Hydrogen Exchange Reactions

Although the potential surface for reaction 1 has been treated by sophisticated and accurate techniques,[23] it is important to review the application to this system of the techniques commonly applied to more complicated systems. Many of these techniques were developed in studies of reaction 1, and their application to other reactions is less straightforward. An earlier review of semiempirical surfaces for reaction 1 is that of Laidler and Polanyi.[24]

There are three electrons in the H + H_2 system, and for the separated atoms each one is in an s atomic orbital. The VB theory is particularly simple for the case of three ^2S atoms, each with one electron or one electron outside a closed shell. For H_3 an analytic expression for the VB energy of the lowest electronic state in terms of the basic integrals over the orbitals is easily obtained.[25] These basic integrals are Q_{ij}, J_{ij}, and S_{ij}—the coulomb, exchange, and overlap integrals involving the diatomic pairs ij (*i.e.*, AB, BC, and AC of reaction 4)—and J_{ABC}—a multiple exchange integral involving all three orbitals. By neglecting J_{ABC} and all the S_{ij}, the energy expression reduces to the simple form

$$E_{ABC} = Q_{AB} + Q_{BC} + Q_{AC} - [{}^1/_2(J_{AB} - J_{BC})^2 + {}^1/_2(J_{AB} - J_{AC})^2 + {}^1/_2(J_{BC} - J_{AC})^2]^{1/2} \quad (5)$$

Equation 5 was first derived by London[26] and is called London's equation. Since the neglected integrals are not all small, this equation cannot be considered a good approximation to the VB potential energy surface. It is, however, of a form well suited to semiempirical treatment. Under approximations analogous to the above, the VB energy for the ground and lowest triplet state of a diatomic molecule ij, composed of two s electrons, becomes

$$E_{ij} = Q_{ij} \pm J_{ij} \quad (6)$$

One can calculate these integrals as functions of interatomic distance by comparison of eq 6 with diatomic potential functions obtained spectroscopically or for the H_2 molecule from accurate *ab initio* calculations of the potential curves. If one makes the assumption that the empirical integrals Q_{ij} and J_{ij} have the same values for a given interatomic distance in a polyatomic system containing ij as they have in the free molecule ij itself, then one can compute the approximate potential energy surface, eq 5, for the reactive system.

Eyring and Polanyi[27] developed a calculational procedure (called the LEP method) along these lines. They assumed that E_{ij} for the ground state is given by a Morse function[28] and that the ratio of Q_{ij} to J_{ij} is independent of internuclear distance R_{ij} (constant coulomb ratio approximation). When applied to any case with three s electrons, *e.g.* reaction 1, the LEP method generally predicts that all points along the reaction path correspond to linear configurations of the three atoms. Since all of the semiempirical and *a priori* calculations carried out on this system yield their minimum energies for the collinear geometries, we will only consider head-on collisions throughout this section. The ratio of Q_{ij} to J_{ij} may be set at such a value ($Q_{ij}/J_{ij} = 0.25$) that the difference in potential energy between the saddle-point and the bottom of the reactant valley, *i.e.*, the reaction "barrier height," is approximately equal to the experimentally observed Arrhenius activation energy. When this was done for reaction 1, Eyring and Polanyi obtained the potential energy surface shown in Figure 1.

This LEP surface for reaction 1 is seen to contain an obviously spurious deep well at very small values of x and y. It has no physical significance, but it will not influence classical trajectories as access to this region is blocked by a high energy ridge. The deep well causes the surface to have an interesting stalagmite-like feature at slightly larger x, y values. Of more importance for thermal reaction dynamics is the depression in the top of the reaction path. This small well is visible in Figure 1, but it shows up even more clearly in Figure 2. As discussed below, it is now believed that the true potential energy surface for reaction 1 does not contain such a well. The LEP method with the constant coulomb ratio approximation has been criticized for other reactive surfaces also.[29,30]

(21) See, *e.g.*, G. W. Dine and R. Hoffman, *J. Amer. Chem. Soc.*, **90**, 3227 (1968); R. Hoffman, R. Gleiter, and F. B. Mallory, *ibid.*, **92**, 1460 (1970); R. Hoffman, S. Swaminathan, B. G. Odell, and R. Gleiter, *ibid.*, **92**, 7091 (1970); and also L. Salem, *ibid.*, **90**, 553 (1968).

(22) A semiempirical molecular orbital calculation (by the CNDO/2 method) has been carried out for symmetric HFH at small internuclear separation. See J. A. Pople and G. A. Segal, *J. Chem. Phys.*, **44**, 3289 (1966).

(23) I. Shavitt, R. M. Stevens, F. L. Minn, and M. Karplus, *ibid.*, **48**, 2700 (1968).

(24) K. J. Laidler and J. C. Polanyi, *Progr. React. Kinet.*, **3**, 1 (1965).

(25) See, for example, R. N. Porter and M. Karplus, *J. Chem. Phys.*, **40**, 1105 (1964).

(26) F. London, *Z. Elektrochem.*, **35**, 552 (1929).

(27) H. Eyring and M. Polanyi, *Z. Phys. Chem.*, **B12**, 279 (1931).

(28) E. U. Condon and P. M. Morse, "Quantum Mechanics," McGraw-Hill, New York, N. Y., 1929, pp 71, 72. See also ref 36.

(29) J. G. Davy, C. R. Guerra, H. S. Johnston, C. E. Weaver, and C. E. Young, *J. Chem. Phys.*, **41**, 1517 (1964).

(30) H. S. Johnston and C. A. Parr, *J. Amer. Chem. Soc.*, **85**, 2544 (1963).

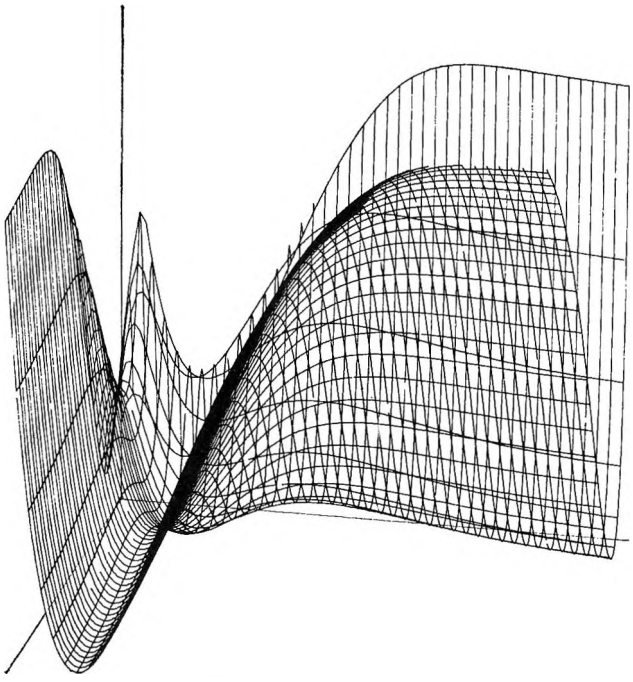

Figure 1. LEP potential surface for collinear H + H_2 → H_2 + H. $Q_{HH}/J_{HH} = 1/4$; $\theta = 70°$; $\phi = 13°$. (θ and ϕ are the spherical polar viewing angles.) The x and y axes of the cartesian coordinate system are internuclear distances R_{12} and R_{23} where 1, 2, and 3 are the atoms. The ranges of R_{12} and R_{23} do not extend to 0 but rather to where the potential equals about 4 eV.

One reason for the incorrect topography of the LEP surface for H + H_2 is that the actual ratios of the Q_{ij} to J_{ij} integrals are *not* independent of internuclear distance R_{ij}.[31] By computing these ratios from the basic electronic integrals involved, it has been found[32] that the shape and the presence or absence of wells in the potential energy surface for the R_{ij} in the regions of interest is extremely sensitive to the quantitative values of the Q_{ij} to J_{ij} ratio since, for these R_{ij}, these ratios are steep functions of distance. The ratios are in turn very sensitive to the number and nature of the approximations used in their evaluation, *e.g.*, the choice of orbital exponents[33] and the choice of zero-order correction.[34] Thus, even the use of theoretical coulomb ratios and experimental ground state potential energy curves does not appear to be a fruitful semiempirical approach. Because the LEP surface is sensitive to the values of these integrals, and the values to be used for the integrals are generally uncertain, surfaces constructed using the various established rules for LEP calculations (and the LEPS modification discussed in the next paragraph) must be viewed as strictly empirical representations whose accuracy must be tested, not assumed. Many workers have taken this approach.

Sato[35] suggested an alternative method of evaluating the Q_{ij} and J_{ij} integrals. His procedure uses eq 6 with estimates of *both* the ground[36] and lowest triplet[37] potential energy curves. By this method, it is found that the Q_{ij} to J_{ij} ratio is a strong function of R_{ij}.[38-40] Sato also modified the London eq 5 by inserting an adjustable constant k. The resultant equation cannot be obtained from the VB energy equation by making any series of approximations. It must be considered to be an arbitrary functional form. Weston[39] adjusted the Sato parameter k to fit the barrier height in the Sato (LEPS) surface for reaction 1 to the experimental activation energy. The surface obtained in this way is shown in Figure 2, right, and it has no wells. However, it is not difficult to make small modifications in the LEPS equations which produce wells for H_3 by this method also.[32]

The most accurate potential energy surface available for the H + H_2 reaction is that computed by Shavitt, Stevens, Minn, and Karplus[23] in an *a priori* configuration interaction calculation. The energies along the reaction path on this surface are believed[23] to be accurate to within 2 kcal/mol, although there is still some question as to whether the calculated barrier is too thin.[41-44] This surface is shown in Figure 3. It compares well[23] with the LEPS surface (Figure 2, right). This good agreement is one of the reasons why the LEPS method has been used for other systems. The surface of Shavitt, *et al.*, agrees with other recent *a priori* CI calculations[45] in predicting the transition

(31) Y. Sugiura, *Z. Phys.*, **45**, 484 (1927).

(32) D. G. Truhlar, unpublished.

(33) See, *e.g.*, J. O. Hirschfelder and J. W. Linnett, *J. Chem. Phys.*, **18**, 130 (1950).

(34) See, *e.g.*, H. Margeneau and P. Rosen, *ibid.*, **21**, 394 (1953); E. A. Mason and J. O. Hirschfelder, *ibid.*, **26**, 173 (1957).

(35) S. Sato, *Bull. Chem. Soc. Jap.*, **28**, 450 (1955); *J. Chem. Phys.*, **23**, 592, 2465 (1955).

(36) J. Hirschfelder, H. Eyring, and B. Topley, *ibid.*, **4**, 170 (1936).

(37) Sato (ref 35) used a diatomic triplet energy function which can be derived from the VB energy for H_2^+. This is called an anti-Morse curve. Its extension to H_2 is known to be inaccurate, and it has not been well tested in other cases; see ref 30 and 35, and R. W. Keyes, *J. Chem. Phys.*, **29**, 523 (1958); *Nature*, **182**, 1071 (1958).

(38) J. K. Cashion and D. R. Herschbach, *J. Chem. Phys.*, **40**, 2358 (1964).

(39) R. E. Weston, Jr., *ibid.*, **31**, 892 (1959).

(40) Cashion and Herschbach (ref 38) applied this method of obtaining Q_{ij} and J_{ij} (but with accurate potential curves instead of Morse and anti-Morse curves) to the London equation for H_3. Their surface contains no wells. For H_3, their method is equivalent to Ellison's method of diatomics-in-molecules; see F. O. Ellison, *ibid.*, **41**, 2198 (1964).

(41) I. Shavitt, *ibid.*, **49**, 4048 (1968).

(42) A. A. Westenberg and N. deHaas, *ibid.*, **47**, 1393 (1967).

(43) See, for example, M. Salomon, *ibid.*, **51**, 2406 (1969), and references therein.

(44) The calculations which have been directed to this question have used transition state theory with approximate corrections for tunneling through the one-mathematical-dimensional classical potential energy barrier. It has been shown [see D. G. Truhlar and A. Kuppermann, *J. Amer. Chem. Soc.*, **92**, 1840 (1970); *Chem. Phys. Lett.*, in press] that this method is not accurate enough to answer such questions about the shape of the potential energy barrier.

(45) J. Hirschfelder, H. Diamond, and H. Eyring, *J. Chem. Phys.*, **5**, 695 (1937); S. F. Boys and I. Shavitt, University of Wisconsin Naval Research Laboratory Technical Report WIS-AF-13 (1959); H. Conroy and B. L. Bruner, *J. Chem. Phys.*, **47**, 921 (1967); C. Edmiston and M. Krauss, *ibid.*, **49**, 192 (1968); H. H. Michels and F. E. Harris, *ibid.*, **48**, 2371 (1968).

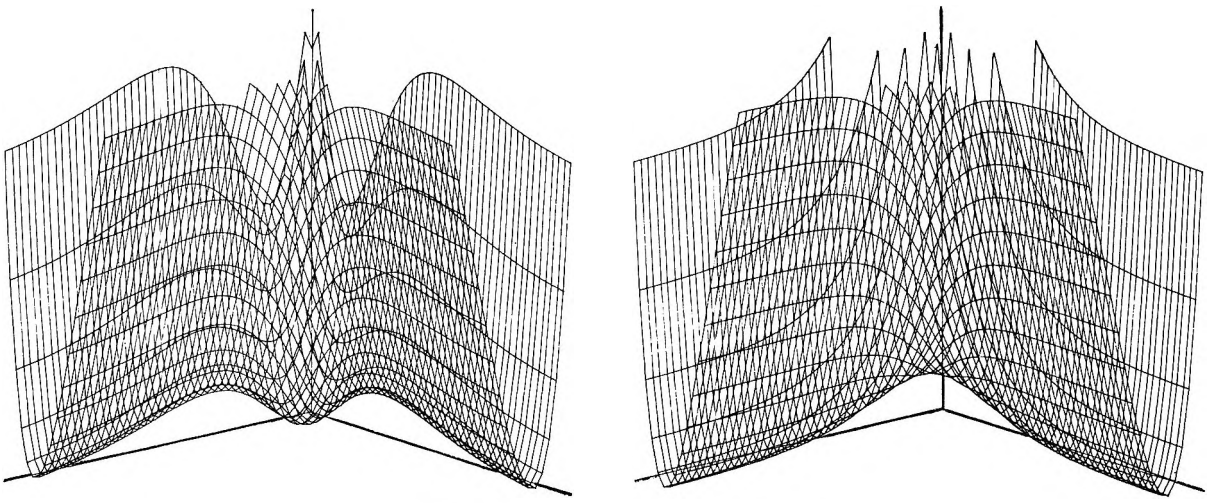

Figure 2. Potential surfaces for collinear H + $H_2 \rightarrow H_2$ + H; $\theta = 75°$; $\phi = 50°$. Left, LEP surface $Q_{HH}/J_{HH} = 1/4$; right, Weston's LEPS surface. See Table I for further details of Figures 2–15.

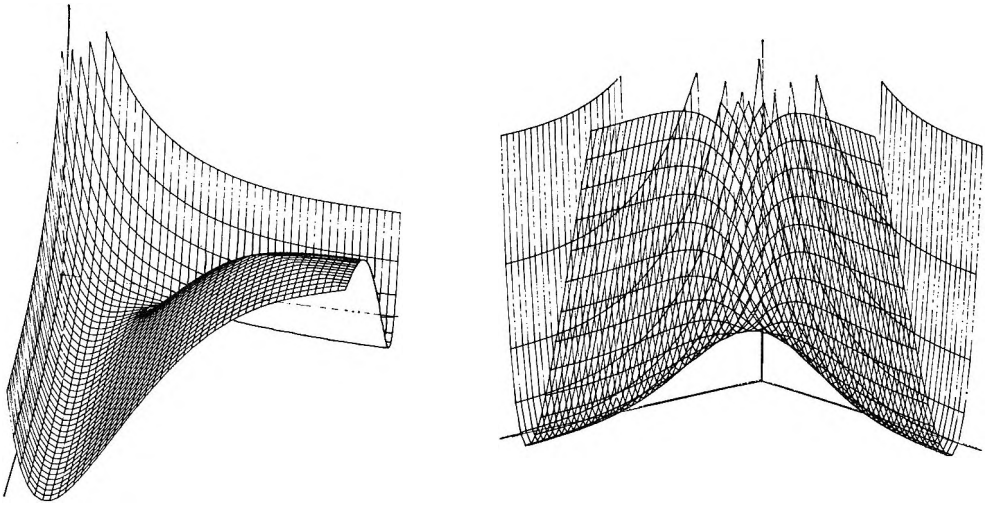

Figure 3. Two views of the *a priori* potential surface for collinear H + $H_2 \rightarrow H_2$ + H from CI calculation of Shavitt, Stevens, Minn, and Karplus. Left, $\theta = 50°$, $\phi = 9°$; right, $\theta = 75°$, $\phi = 50°$.

state is linear and that the surface has a simple barrier (*i.e.*, no wells).[45a]

A modification of the LEPS method due to Polanyi[46] adds the flexibility of using different Sato parameters k_{ij} for different atomic pairs. These parameters expand the range of surface topography available through this technique. The various surface features (reaction path curvature, energy barrier height and location, saddle point force constants, etc.) are still coupled to one another in this modification. The number of free parameters was increased not to decouple these quantities but to multiply their combinations while allowing the London equation (5) to govern their interrelations. Such extended LEPS surfaces will be considered in the next section.

One important feature of potential energy surfaces, ignored by even these subtle modifications of the London equation, is the existence of long-range dispersion interactions.[47] These interactions produce shallow wells in the potential near the reaction path at large reactant (and product) separations. Sometimes wells appear in extended LEPS surfaces, but they are in no way related to the dispersion forces. The dispersion forces may be calculated through second-order perturbation theory,[47] and their effects could be (but have not been) included in the diatomic potentials of eq 6.

(45a) NOTE ADDED IN PROOF. At the Conference on Potential Energy Surfaces in Chemistry (Aug 10–13, 1970, University of California, Santa Cruz), A. D. McLean reported calculations by B. Liu on collinear H_3 which are believed to give the barrier correct to within 0.5 kcal/mol. These calculations give a barrier of 10.1 kcal/mol, as compared to 11.0 from ref 23 and Shavitt's estimate[41] from experiment of 9.8.

(46) J. C. Polanyi, *J. Quant. Spectrosc. Radiat. Transfer*, **3**, 471 (1963).

(47) J. O. Hirschfelder, C. F. Curtiss, and R. B. Bird, "Molecular Theory of Gases and Liquids," Wiley, New York, N. Y., 1954, pp 29, 30, 960–966.

However, the use of the resultant Q_{ij} and J_{ij} integrals would not have the desired effect. For example, in one such approximate treatment, the long-range wells would then appear on the high energy plateau in the potential energy surfaces, while the (chemically) more important valleys would be hardly affected. In this paper, we confine our attention to the shape of the potential near the saddle point (or in the short-range well, if there is one). We assume we may safely ignore the long-range forces. In the region of the saddle point, the valence interactions are much larger than the dispersion interactions. The valence interaction dominates the potential in this region, and a qualitative picture of the surface may be obtained from the first-order valence interactions parametrized in the valence bond scheme.

In addition to actual calculations of the potential energy surface, some generalizations may be made from simple quantum chemical arguments and applied intuition. *E.g.*, since the transition state has partially broken and partially made bonds, the force constants (or potential surface curvatures) associated with these bond directions are expected to be smaller than those associated with the stable reactants and products.[48] Also we expect the transition state configuration to be in the reactant valley for an exothermic reaction and in the product valley for an endothermic reaction.[49,50a,b] Indeed, strong correlations can be found between the location of energy barriers along the reaction path and the barrier heights.[50b] Weaker correlations exist between barrier heights and the heats of reaction.[50b,c,d] Finally, because of this tendency, potential energy barriers for thermoneutral or nearly thermoneutral reactions are expected to be higher[50d] and sharper (*i.e.*, for thermoneutral reactions, thinner)[50e] for reactions with small or zero net energy changes than those for reactions with large net energy changes. These arguments must play an important role in surface determination even though they have been hard to quantify.

IV. The Reactions of a Halogen Atom with the Hydrogen Molecule

For atoms past the first row elements, relativistic effects upon the electronic motion become important. The halogen atoms, for example, have a low-lying excited state $^2P_{1/2}$ which is nondegenerate with the ground state $^2P_{3/2}$ due to spin-orbit coupling. Such effects are ignored in the non-relativistic Hamiltonian, but the $^2P_{1/2}$ excitation energies in bromine and iodine[51] are much too large to neglect with "chemical" accuracy. Spin-orbit coupling also affects molecular states such as the $^3\Pi_1$ and $^3\Pi_{0^+}$ states of HX.[52] Relativistic effects on bond energies can be very large.[53] The omission of relativistic effects in semiempirical valence bond calculations constitutes a severe approximation, the accuracy of which is not well documented.

A halogen atom has the valence electronic configuration s^2p^5. Since the complete nonionic VB method becomes more complicated rapidly as the number of electrons increases, it is easier to consider only the single unpaired p electron in the halogen's electronic shell structure. In this approximation, one treats H_2X, HX_2, and X_3 as pseudo-s^2p, -sp^2, and -p^3 systems, respectively. Magee[54] applied the s^2p VB theory to a model for H_2F by making approximations to the necessary integrals. In addition to wells as deep as 30 kcal/mol for linear HHF and HFH, his calculations predicted triangular H_2F to be most stable. These deep wells, like the deep wells which can be obtained for H_3 by applying a similar parametrization technique, are artifacts of the approximation scheme. However, most workers have used equations like the London equation which predict the linear geometries to be lowest in energy. Walsh's rules do not yield an unambiguous prediction for HXH and XYZ where X, Y, and Z are halogens but since the highest occupied molecular orbital favors the linear configuration[55] the prediction is that both types of species are linear. Pople and Segal[22] treated HFH in a less severe approximation as an s^2p^5 system. Their calculations, which have proven to be very accurate for the determination of equilibrium bond angles in bound triatomics, show H_2F to be linear. Muckerman and Newton did *ab initio* molecular orbital calculations on HHF which predict the minimum energy reaction path is always linear.[56] These results provide some justification for using the various modifications of the s^3 London equation (eq 5) as empirical representations of H_2X surfaces. These various s^3 equations generally predict the most stable transition states to be for linear geometries; thus their use for non-s^3 systems often constitutes an assumption, not a conclusion, that linear configurations are lowest in energy. One excep-

(48) See, *e.g.*, H. S. Johnston, "Gas Phase Reaction Rate Theory," Ronald Press, New York, N. Y., 1966, pp 72–83. The discussion in this reference is in terms of bond order, which is smaller for partial bonds than for completely unbroken bonds.

(49) H. Eyring, R. Lumry, and J. D. Spikes in "A Symposium on the Mechanism of Enzyme Action," The Johns Hopkins Press, Baltimore, Md., 1954, p 123; G. S. Hammond, *J. Amer. Chem. Soc.*, **77**, 334 (1955). Some earlier, less pertinent references which consider special classes of reaction are M. G. Evans and M. Polanyi, *Trans. Faraday Soc.*, **34**, 11 (1938); E. T. Butler and M. Polanyi, *ibid.*, **39**, 19 (1943).

(50) (a) J. C. Polanyi, *J. Chem. Phys.*, **31**, 1338 (1959); (b) M. H. Mok and J. C. Polanyi, *ibid*, **51**, 1451 (1969); (c) Johnston, ref 48, pp 207–209; (d) R. A. Marcus, *J. Phys. Chem.*, **72**, 891 (1968); see also A. O. Cohen and R. A. Marcus, *ibid.*, **72**, 4249 (1968), and R. A. Marcus, *J. Amer. Chem. Soc.*, **92**, 7224 (1969); (e) R. A. More O'Ferrall and J. Kouba, *J. Chem. Soc., B*, 985 (1967).

(51) These energies in kcal/mol are F 1.16, Cl 2.52, Br 10.54, and I 21.74 as given in C. Moore, "Atomic Energy Levels," U. S. Government Printing Office, Washington, D. C., 1949.

(52) R. S. Mulliken, *Phys. Rev.*, **51**, 316 (1937).

(53) W. C. Mackrodt, *Mol. Phys.*, **18**, 697 (1970).

(54) J. L. Magee, *J. Chem. Phys.*, **8**, 677 (1940).

(55) (a) A. D. Walsh, *J. Chem. Soc.*, 2260, 2266 (1953); (b) G. Herzberg, "Molecular Spectra and Molecular Structure," Vol. 3, Van Nostrand, Princeton, N. J., 1966, p 319.

(56) J. Muckerman and M. Newton, private communication.

tion to the s^3 London equation-type treatment predicting linear configurations to be most stable (a predicted I–H_2 complex) is discussed below.[57]

The excited electronic states for reaction 1 are fairly high in energy. For almost all other reactions there will be an excited electronic state at lower energy than for reaction 1. Lower energy excited electronic states are more liable to play a role in chemical reactions than higher energy ones, and their existence makes the Born–Oppenheimer approximation less justifiable. Nevertheless it has been usual to ignore their presence in the reactions under consideration here. Cadman and Polanyi[58] studied reaction 2 with X = I at 300°K and found that less than 2% of the product I atoms were produced in the electronically excited state. They also showed that the yield of excited I is small in the reactions of D, Cl, and Br with HI. However, these results do not exclude more significant participation of excited electronic states at small internuclear separations of all three atoms or at higher energies.

In their historic paper on the LEP method, Eyring and Polanyi,[27] applied the s^3 London equation to calculate a potential energy surface for the reaction

$$H + HBr \longrightarrow H_2 + Br \qquad (7)$$

This was calculated with all $Q_{ij} = 0$ and predicted a saddlepoint elevation of 26 kcal/mol. This is much too high, but the result is not surprising since setting all $Q_{ij} = 0$ in the LEP method for H_3 yields a barrier of 32 kcal/mol which is about 22 kcal/mol too high. Ellison and Patel[59] made calculations on H_2X for X = Cl, Br, and I using diatomics-in-molecules theory[59] (an LEP-like approximation[40]). They used triplet state potential energy curves calculated by the constant coulomb ratio assumption and obtained some very strangely shaped surfaces with basins. They found that their H_2Cl surface had a well at the same energy as H_2 + Cl if one set of potential curves was used but that the well disappeared if another set was used. This is consistent with our above discussion of the sensitivity of the LEP method to the potential curve data. Wheeler, Topley, and Eyring carried out s^3 LEP calculations with the constant coulomb ratio approximation ($Q_{ij}/J_{ij} = 0.25$) for the Cl + H_2 and Br + H_2 reactions.[60,61] For the former they found the collinear saddle point to have the geometry: R_{HH} = 1.40 Å, R_{ClH} = 1.30 Å. Since the reactant has R_{HH} = 0.74 Å and the product has R_{HCl} = 1.27 Å, the transition state is predicted to be located past the corner in the reaction path (*i.e.*, in the product valley) and to be very much like Cl–H...H where the dash denotes a normal bond and the dotted line denotes a weak partial bond.[62] Transition state theory calculations[60] based on this surface predict[63] isotope effects on the rate constants much smaller than those observed experimentally. This may be because the transition state predicted by the surface has too large a "symmetric stretching" frequency (2496 cm^{-1}). This large frequency vibration is only a slightly perturbed HCl vibration (the HCl molecule vibrational frequency is 2990 cm^{-1}) because of the position of the saddle point. Hence the failure of the LEP method in this case apparently lies in the incorrect prediction of the geometry for the transition state. (Wheeler, Topley, and Eyring's transition state theory calculations[63,64] for the Br + H_2 reaction were in better agreement[60] with experiment but were still wrong by about a factor of 2. A contour map of their Br–H–H surface has a simple barrier in the product valley; the potential energy along the reaction coordinate decreases monotonically on both sides of the barrier.) The Br + H_2 reaction is discussed in more detail below. While the early failures discussed above are understandable in the light of what we now know about the sensitivity of the London equation to approximate integrals, the semiempirical surfaces considered in the rest of this section were constructed using methods which are usually considered to yield more qualitatively correct results.

Sato applied his LEPS procedure to some systems containing halogen atoms.[35] He found the contrast that the LEPS surfaces for H_2X systems had no wells, whereas the LEP treatment had wells. Sato felt that both the H_3 and H_2X calculations were empirical justifications for his method since no experimental evidence for wells such as the LEP wells was then available and *a priori* calculations on H_3 predicted a simple barrier. For X_3 systems his LEPS calculations predicted wells

(57) Another exception is LiH_2^+; see A.-J. Wu and F. O. Ellison, *J. Chem. Phys.*, **47**, 1458 (1967).

(58) P. Cadman and J. C. Polanyi, *J. Phys. Chem.*, **72**, 3715 (1968).

(59) F. O. Ellison and J. C. Patel, *J. Amer. Chem. Soc.*, **86**, 2115 (1964).

(60) A. Wheeler, B. Topley, and H. Eyring, *J. Chem. Phys.*, **4**, 178 (1936).

(61) See also J. C. Morris and R. H. Pease, *ibid.*, **3**, 796 (1935).

(62) A contour plot of their surface shows the potential energy along the reaction coordinate for collinear collisions rises to a local maximum of 9 kcal/mol as Cl approaches H_2, drops to a minimum of 6 kcal/mol at R = 0.8 Å, and R_{HCl} = 1.4 Å, and then rises to the 13-kcal/mol transition state. (The reaction is 3 kcal/mol endothermic.)

(63) Some derivations of transition state theory [*e.g.*, R. A. Marcus, *J. Chem. Phys.*, **46**, 959 (1967), and references therein] assume adiabaticity in the nonreactive vibrational modes. J. C. Polanyi and W. H. Wong, *ibid.*, **51**, 1493 (1969), concluded that the adiabaticity criterion for the detailed application of transition state theory is not well met for reactions with "late" (product valley) transition states. This is due to a dynamic effect; vibrationally cold reactants have a very small probability of passing over the energy barrier in these cases. The failure of quasiclassical trajectory calculations to agree with this adiabaticity criterion is more serious for the later transition states. The barrier is apparently past the "corner" (the point of maximum curvature of the "reaction" path) for Cl + H_2, even later for Br + H_2, and very late for I + H_2. This means that the detailed results of transition state theory calculations on these reactions might be seriously in error. The transition state theory rates (for the usual Boltzmann average over all possible initial states) are apparently more accurate but in any case are an interesting property of the surface. L. M. Raff, L. B. Sims, D. L. Thompson, and R. N. Porter, *J. Chem. Phys.*, **53**, 1606 (1970), find that for the surfaces they did quasiclassical trajections on, this dynamic effect is important for I + H_2 and Br + H_2 but not for Cl + H_2.

(64) W. M. Jones, *J. Chem. Phys.*, **19**, 78 (1951); J. Bigeleisen and M. Wolfsberg, *ibid.*, **23**, 1535 (1955).

about 6 kcal/mol deep. At present there is evidence that molecular systems like XHX[65] and X_3[66] may indeed be weakly bound. This evidence is discussed in the next section.

Bigeleisen, Klein, Weston, and Wolfsberg[67] made a more extensive study of the application of the LEPS method to the reaction

$$Cl + H_2 \longrightarrow HCl + H \qquad (8)$$

On their surface, the saddle point is closer to the corner in the reaction path than the saddle point on the LEP surface is (R_{HCl} is increased by about 0.1 Å and R_{HH} is decreased by about 0.4 Å), and the symmetry stretching frequency at the transition state is lowered to about 1350 cm^{-1}. This improves the predicted isotope effects. However, the LEPS method predicts that the barrier is much narrower than the one in the LEP surface and that, in consequence, there is much more quantum mechanical tunneling through the LEPS barrier. Transition state theory calculations are in better agreement with experiment when the wider barrier is used. As the accuracy of presently used methods for calculating transmission coefficients for transition state theory are uncertain, tunneling cannot be used for a quantitative determination of a surface, especially when tunneling is large. Bigeleisen, *et al.*,[67] concluded that there was not enough information from the experiments to determine whether the transition state is linear or triangular.

Persky and Klein[68] applied the extended LEPS method with two different Sato parameters (k_{HH} and k_{HCl}) to reaction 8. They determined an optimal pair of Sato parameters by comparing the surface-dependent predictions of transition state theory with their data on isotope effects on rate constants. Their extended LEPS surface (called "Sato II" by them) for this endothermic reaction appears in the stereoscopic pair, Figure 4. This surface shows no new or abnormal features. At the transition state R_{HCl} = 1.35 Å, R_{HH} = 1.11 Å, and the symmetric stretching frequency is 1615 cm^{-1}. The barrier is almost as narrow as the one on the earlier LEPS surface with a single Sato parameter. Persky and Klein also reported that preliminary calculations on a generalized LEPS surface predicted H–H–Cl is linear. Reaction 8 has also been studied by Westenberg and deHaas[69] using flow systems with esr detection. These authors searched for an optimal LEPS surface with a single Sato parameter. Their choice is shown in Figure 5. As can be seen by comparison of Figures 4 right and 5, the Westenberg–deHaas surface for reaction 8 differs imperceptibly from the Persky–Klein one. Indeed, their barrier height and location differ by less than 1 kcal/mol and 0.14 Å, respectively—well within the usual bounds of "chemical" accuracy.[70]

A collision between the reagents in reaction 8 can have only two chemically different outcomes: (a) no reaction, or (b) the abstraction of an H atom by Cl. A collision between the products, however, may result in (a) no reaction, (b) abstraction of H to form molecular hydrogen, or (c) the exchange of hydrogen atoms

$$H + ClH \longrightarrow HCl + H \qquad (9)$$

In the latter case, (c) could be distinguished from (a) by using different hydrogen isotopes. Since the classical potential surface should be independent of the *direction* of the reaction, either the Persky–Klein (Figure 4) or Westenberg–deHaas (Figure 5) surface should be adequate for the reaction

$$H + HCl \longrightarrow H_2 + Cl \qquad (-8)$$

But any real collision of H and HCl will also involve reaction 9, as the incident H atom may interact with either end of the HCl molecule. Furthermore, an incident H atom is influenced by both ends of the molecule during the course of a single trajectory since the molecule may rotate. (It is obvious that we are speaking now of noncollinear trajectories.) Thus, the potential surface for H + HCl must satisfactorily represent the energies at both H–H–Cl and H–Cl–H type configurations.

Thus, we apply the LEPS surfaces (Figures 4 and 5), calibrated for Cl–H–H, to other configurations of the three atoms, including the linear exchange geometry H–Cl–H. When this is done, we obtain[71] Figures 10 and 11 for the collinear potential energy surfaces *a propos* reaction 9. (The parameters of the LEPS surfaces shown in Figures 2–15 are listed in Table I.) The surface in the stereo pair, Figure 10, comes from the Persky–Klein Sato parameters discussed above. This surface predicts (a) that there is no potential barrier for the exchange reaction 9, and (b) that the "molecule" HClH is stable by more than 9 kcal/mol with respect to dissociation into H and HCl! Similarly, the surface (nonstereo, Figure 11) with the Westenberg–deHaas Sato parameter shows (a) negligible reaction barriers (there are barriers at about 3 Å out in both valleys; they are each about 0.035 kcal/mol high), and (b) HClH bound by almost 5 kcal/mol. (The Cl + H_2 surface of Wheeler, *et al.*,[60] has also been applied to

(65) Y. Nelson and G. C. Pimentel, *J. Chem. Phys.*, **47**, 3671 (1967).

(66) P. N. Noble and G. C. Pimentel, *ibid.*, **49**, 3165 (1968).

(67) J. Bigeleisen, F. S. Klein, R. E. Weston, and M. Wolfsberg, *ibid.*, **30**, 1340 (1959).

(68) A. Persky and F. S. Klein, *ibid.*, **44**, 3617 (1966).

(69) A. A. Westenberg and N. deHaas, *ibid.*, **48**, 4405 (1968); see also A. A. Westenberg, *Science*, **164**, 381 (1969).

(70) Very recently, M. Solomon, *Int. J. Chem. Kinet.*, **2**, 175 (1970), has used a modified LEPS method on reaction 8 to obtain another thin barrier, this time with a symmetric stretch frequency of 2301 cm^{-1}. Solomon also constructs surfaces for other reactions discussed in this review and compares them to experiment using transition state theory.

(71) The figures are arranged for interhalogen comparisons. Figures 4 through 9 represent XHH surfaces, while the corresponding HXH surfaces are numbered 10 through 15.

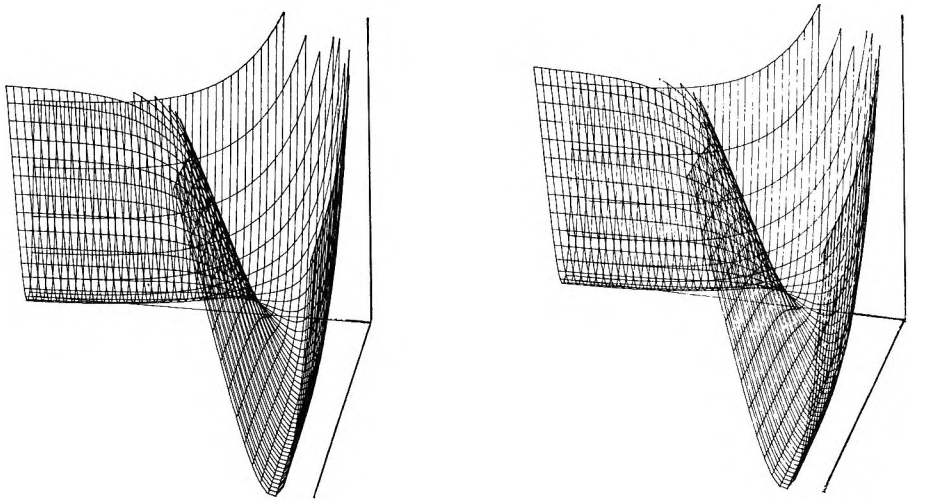

Figure 4. Stereo view of Persky and Klein's potential surface II for collinear Cl + H_2 → HCl + H; θ = 60°. Left, ϕ = 100°; right, ϕ = 104°.

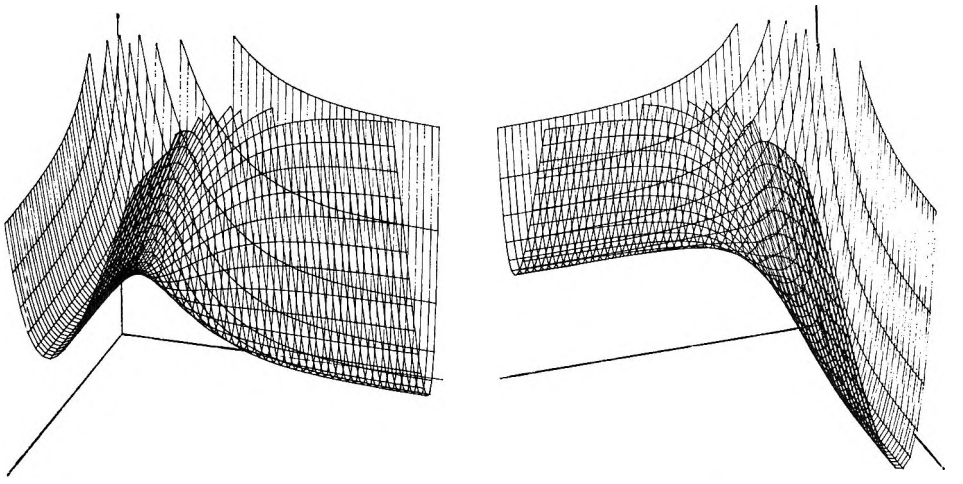

Figure 6. Two views of Timmons and Weston's potential surface for collinear Br + H_2 → HBr + H; θ = 65°. Left, ϕ = 20°; right, ϕ = 70°.

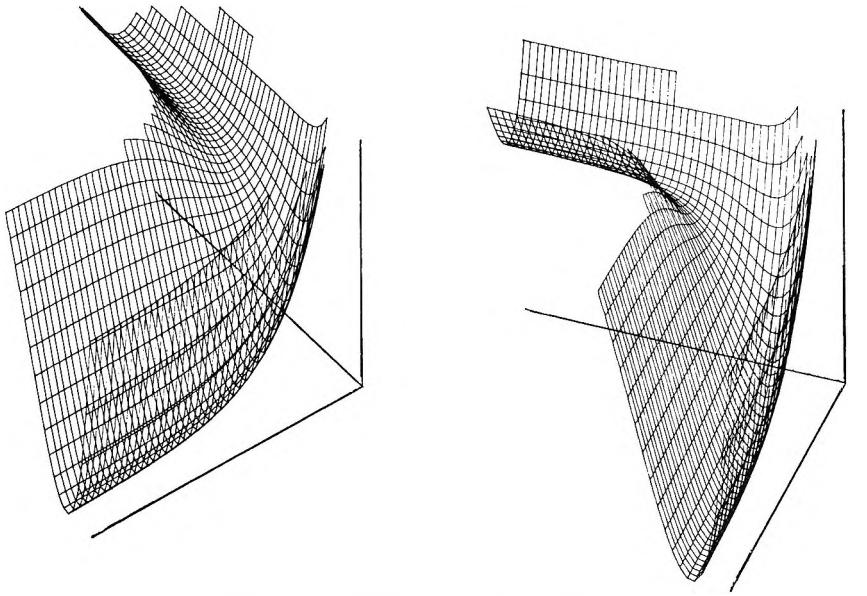

Figure 8. Two views of Sullivan's potential surface for collinear I + H_2 → HI + H. Left, θ = 45°, ϕ = 143°; right, θ = 51°, ϕ = 110°.

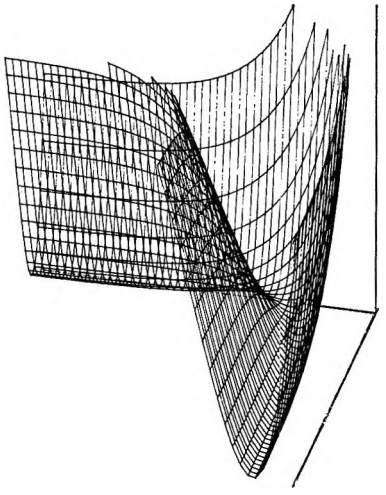

Figure 5. Westenberg and deHaas: potential surface for collinear Cl + H_2 → HCl + H; $\theta = 60°$; $\phi = 104°$.

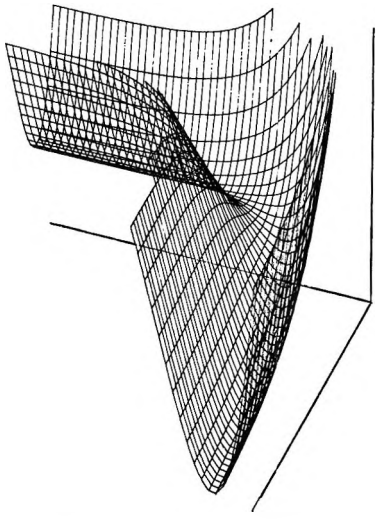

Figure 7. Parr and Kuppermann's potential surface for collinear Br + H_2 → HBr + H; $\theta = 51°$; $\phi = 110°$.

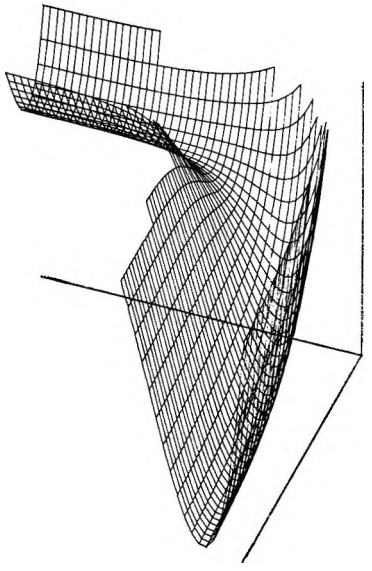

Figure 9. Parr and Kuppermann's potential surface for collinear I + H_2 → HI + H; $\theta = 51°$; $\phi = 110°$.

Table I: Sato Parameters for the LEPS Surfaces Shown in the Figures[a]

Figure	A	B	k_{HX}	k_{HH}	ΔR(H–X)
2, right	H	H	...	0.1475	...
4	Cl	H	0.247	0.107	1.05–2.25
5	Cl	H	0.188	0.188	1.05–2.25
6	Br	H	0.2	0.2	1.2–2.4
7	Br	H	0.076	0.225	1.2–2.4
8	I	H	0.2	0.2	1.4–2.6
9	I	H	0.0915	0.225	1.4–2.6
10	H	Cl	0.247	0.107	1.05–2.70
11	H	Cl	0.188	0.188	1.05–2.70
12	H	Br	0.2	0.2	1.2–2.85
13	H	Br	0.076	0.225	1.2–2.85
14	H	I	0.2	0.2	1.4–3.05
15	H	I	0.0915	0.225	1.4–3.05

[a] The surfaces are potential energies for the collinear reaction A + BH → AB + H, where A and B are H or a halogen (X). For Figures 2–9 the H–H distance varies in the range 0.5–2.5 Å. The range of H–X distances shown in Figures 4–15 is given in the column headed ΔR(H–X) in Å. The viewing angles (θ,ϕ) are given in the figure captions.

reaction 9.[72] This crude LEP surface predicts 5-kcal/mol barriers in the valleys and a 17.5-kcal/mol well for symmetrical HClH.)

Bound halogen triatoms are not unknown. Pimentel and coworkers[65,66] have observed the ir spectra of Cl-HCl and Cl_3 trapped in rare gas matrices. Although no such evidence for the existence of HClH has been reported, there is also insufficient evidence to challenge this LEPS prediction. Nevertheless, since HClH has never been observed, the predicted well is probably at least anomalously deep. We find that if the Sato parameters are altered to remove the well in the LEPS potential surface for HClH, the potential barrier to reaction 8 becomes about 10.6 kcal/mol, which is at least 3 kcal/mol too high. It must, of course, be borne in mind that the wells predicted for HClH may be an artifact of the LEPS approximation just as the H_3 well was in the original and some of the modified LEP methods.

In the limit of a free diatom, the Sato parameters bear a formal resemblance to the square of atomic orbital overlap integrals S_{ij} in the complete nonionic VB treatment. Since the S_{ij} are functions of molecular geometry,[25] the assumption of constant Sato parameter must be looked upon with some suspicion. Clearly, the Sato parameters which adequately describe the HHCl transition state may be inappropriate for the HClH one. This would not exclude transition state theory calculations as the parameters could simply be set independently for each saddle point. However, such a failure of the LEPS procedure would be fatal to classical and

(72) See W. Steiner and E. K. Rideal, *Proc. Roy. Soc., Ser. A*, 173, 506 (1939); S. Glasstone, K. J. Laidler, and H. Eyring, "The Theory of Rate Processes," McGraw-Hill, New York, N. Y., 1941, pp 226–228.

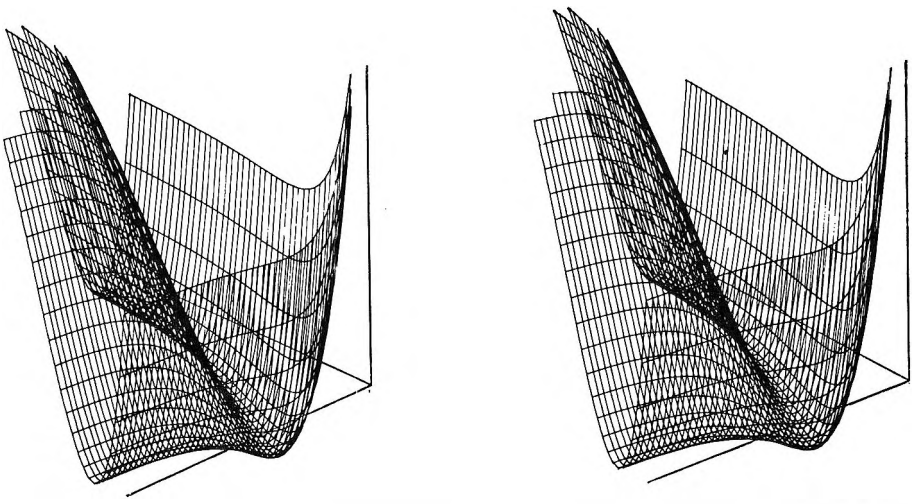

Figure 10. Stereo view of Persky and Klein's potential surface II for collinear H + HCl → HCl + H; $\theta = 64°$. Left, $\phi = 136°$; right, $\phi = 140°$.

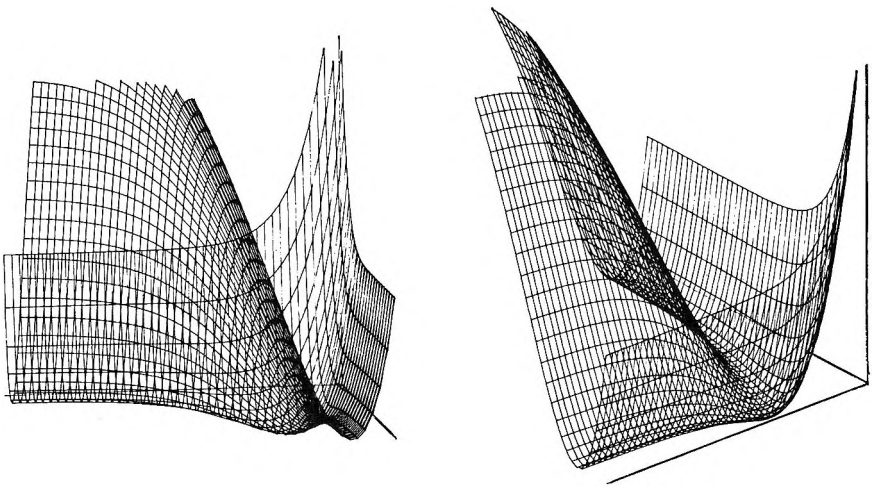

Figure 12. Two views of Timmons and Weston's potential surface for collinear H + HBr → HBr + H. Left, $\theta = 81°$, $\phi = 81°$; right, $\theta = 64°$, $\phi = 140°$.

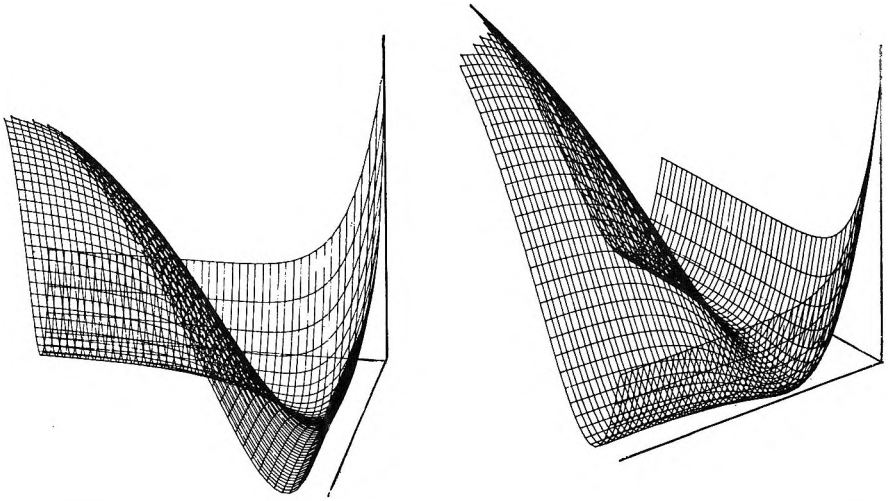

Figure 14. Two views of Sullivan's potential surface for collinear H + HI → HI + H. Left, $\theta = 67°$, $\phi = 100°$; right, $\theta = 64°$, $\phi = 140°$.

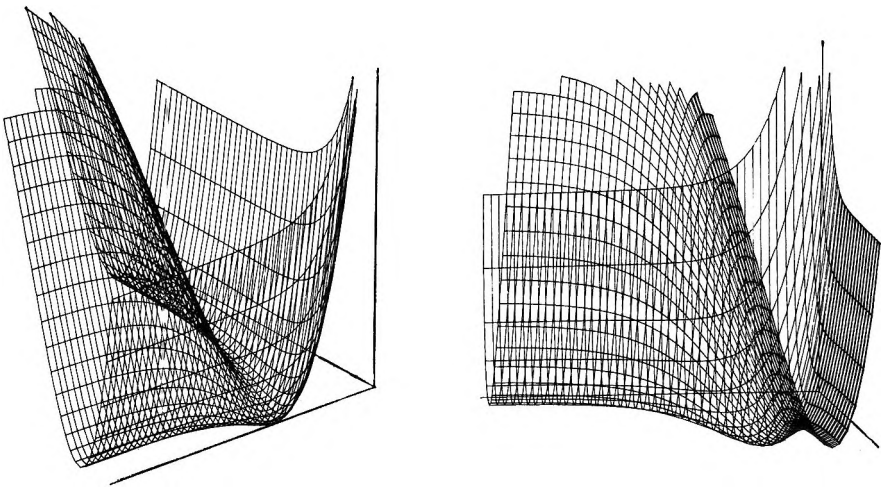

Figure 11. Two views of Westenberg and deHaas's potential surface for collinear H + HCl → HCl + H. Left, $\theta = 64°$, $\phi = 140°$; right, $\theta = 81°$, $\phi = 80°$.

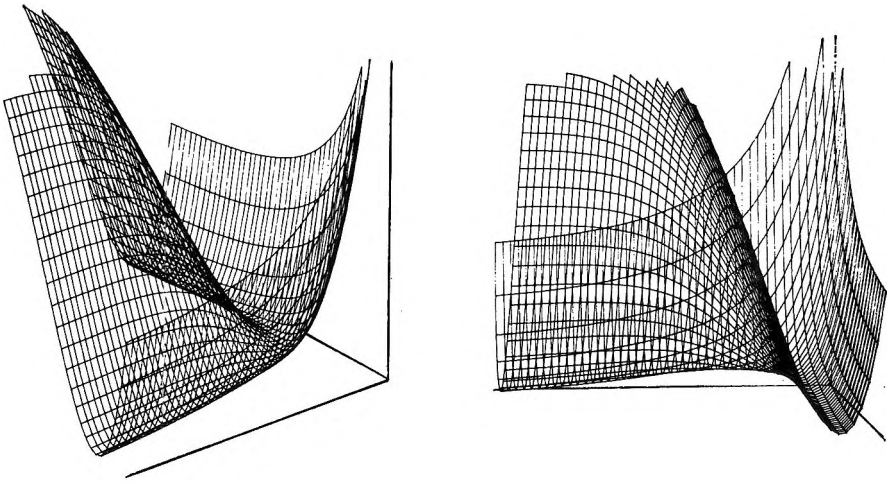

Figure 13. Two views of Parr and Kuppermann's potential surface for collinear H + HBr → HBr + H. Left, $\theta = 64°$, $\phi = 140°$; right, $\theta = 81°$, $\phi = 81°$.

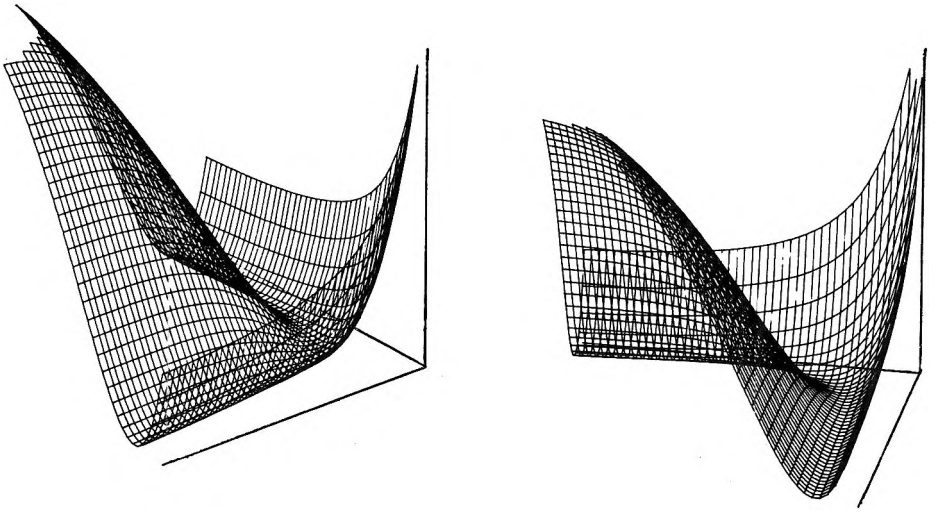

Figure 15. Two views of Parr and Kuppermann's potential surface for collinear H + HI → HI + H. Left, $\theta = 64°$, $\phi = 140°$; right, $\theta = 67°$, $\varphi = 100°$.

quantum mechanical scattering theory calculations which utilize the full energy surface.

The bromine homolog to reaction 8

$$Br + H_2 \longrightarrow HBr + H \qquad (10)$$

has been studied by Timmons and Weston.[73] They found that their isotope effects could not be predicted to within 40% from their transition state theory calculations using any single-parameter LEPS surface. It is unknown whether this is a failure of the surface or a failure of the transition state theory. Their "best" choice for such a surface is shown in the (nonstereo) pair, Figure 6. Note that the HX valley is not as deep for this case as for reaction 8 since this reaction is more endothermic. We may extend the Timmons–Weston surface to include the exchange reaction

$$H + BrH \longrightarrow HBr + H \qquad (11)$$

Then the LEPS prediction for HBrH is as shown in Figure 12. As for HClH, there are no barriers to the exchange reaction 11, and the HBrH molecule is predicted to be stable by more than 5 kcal/mol with respect to H + HBr. (The crude LEP surface with $Q_{ij}/J_{ij} = 0.25$ of Wheeler, *et al.*,[60,74] yields 3-kcal/mol barriers in the valleys and a 15-kcal/mol well for symmetrical H–Br–H.) However, there have been some studies of reactions like (11) which tend to dispute this picture of HBrH.

White, Persky, Kuppermann, and coworkers[75] have used photochemical experiments to determine the relative rates of the abstraction reaction

$$H + DBr \longrightarrow HD + Br \qquad (12)$$

and the exchange reaction

$$H + BrD \longrightarrow HBr + D \qquad (13)$$

Their finding is that at thermal energies the abstraction rate constant is over an order of magnitude larger than the exchange one. (This is inconsistent with transition state theory calculations using the full Timmons–Weston LEPS surface which would have predicted the reactions to have about equal rates since its barriers to abstraction and exchange are much smaller than thermal average energies.[76]) Accordingly, a new multiparameter LEPS surface[77] was produced with the requirement that it give an accurate value for k_{12}/k_{13} as computed from transition state theory. That portion of this new surface *a propos* reactions 10 and 12 is shown in Figure 7. It bears a close resemblance to the Timmons–Weston surface (Figure 6), although their barrier heights and locations differ by more than 1.6 kcal/mol and 0.47 Å, respectively. Some characteristics of these surfaces are compared in Table II to demonstrate the range of our ignorance. The new surface[77] gives rise to transition state theory isotope effects[78] which are much closer to the data[73] than those from the single-parameter surface of Timmons and Weston.[73] These are shown in Figure 16. More surprising, however, is the comparison of the surfaces *a propos* reactions 11 and 13. The new surface for these exchange reactions is given in Figure 13. Instead of a 5-kcal/mol well (Figure 12) this surface has a 4-kcal/mol *barrier!* Classical trajectory[77] and transition state calculations[78] on the new surface both predict that with increasing H + DBr collisional energies the exchange reaction 13 eventually dominates abstraction 12. There are ex-

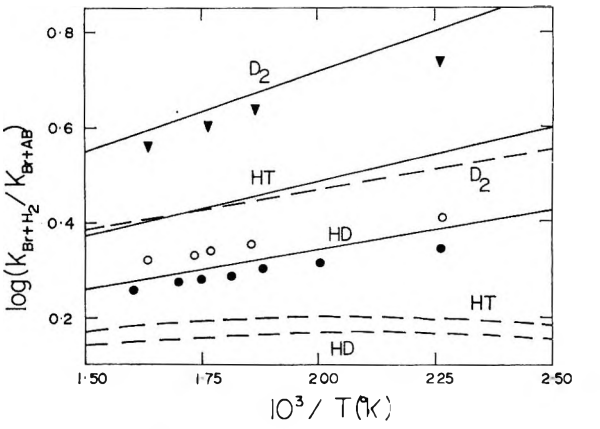

Figure 16. Logarithms of ratios R of rate constant for the reaction Br + H_2 to the rate constants for Br + D_2, Br + HT, and Br + HD as functions of temperature. Triangles (D_2), open circles (HT), and filled circles (HD) are experimental values.[73] Calculated values: ——, present; – – –, Timmons and Weston.[73]

Table II: Properties of the H–H–Br Linear Transition State for Reaction 10

Surface	R_{HH}, Å	R_{HBr}, Å	Stretching frequencies: Symmetric, cm⁻¹	Stretching frequencies: Asymmetric, cm⁻¹
Wheeler–Topley–Eyring	1.50	1.41	2326	758i
Timmons–Weston	1.62	1.42	2472	178i
Parr–Kuppermann	1.15	1.49	1420	1034i
H_2 molecule	0.74		4395	
HBr molecule		1.41	2650	

(73) R. B. Timmons and R. E. Weston, Jr., *J. Chem. Phys.*, **41**, 1654 (1964); see also R. E. Weston, Jr., *Science*, **158**, 332 (1967).

(74) See W. Steiner, *Proc. Roy. Soc., Ser. A*, **173**, 531 (1939), and Glasstone, *et al.*, ref 72, pp 231–233.

(75) J. M. White, J. Betts, D. Davis, A. Persky, and A. Kuppermann, unpublished.

(76) The abstraction barrier is about 0.1 kcal/mol, and the exchange one is less than 0.0001 kcal/mol.

(77) C. A. Parr and A. Kuppermann, to be published.

(78) All the transition state theory calculations carried out for this article use the formulas of H. S. Johnston, "Gas Phase Reaction Rate Theory," Ronald Press, New York, N. Y., 1966, pp 188–190, except that the partition functions for the transition state bend were corrected for a quartic term in the potential energy. The quartic corrections affect the values for log R in Figure 16 by less than 0.01. For pure harmonic bends the rate constants for I + D_2 in Table III would increase by more than 70% and would be in greater disagreement with experiment. The techniques used for the quartic corrections will be published elsewhere by the authors.

perimental indications[75] that this may be true in the iodine system. The quantitative and qualitative successes of the multiparameter LEPS surface suggest that it is possible for a single set of Sato parameters to describe both ABC and ACB.

This possibility is bolstered by results on the iodine system. Sullivan[79] studied absolute rates and isotope effects in the reaction

$$I + H_2 \longrightarrow HI + H \qquad (14)$$

His search for a best single-parameter LEPS potential resulted in a compromise surface shown in Figure 8. This surface gives transition state theory rates about an order of magnitude too low. It is not known how much of the error is due to transition state theory and how much is due to the surface. When Sullivan's Sato parameter is used for the exchange reaction

$$H + IH \longrightarrow HI + H \qquad (15)$$

the surface shown in Figure 14 is obtained. It predicts an exchange barrier less than 0.1 kcal/mol high and an HIH well more than 3 kcal/mol deep.[80] The geometry of this well is r_{HI} = 1.74 Å for both HI pairs. The photochemical experiments of White, Persky, and coworkers[75] on the system

$$H + DI \longrightarrow HD + I \qquad (16)$$

$$H + ID \longrightarrow HI + D \qquad (17)$$

provide additional restrictions on the H_2I surfaces. To satisfy these constraints a new surface was constructed.[77] The H_2 Sato parameter was simply transferred from the value found previously[77] for the H_2Br system, and the k_{HI} was varied to fit the thermal ratio of abstraction (16) to exchange (17). The resultant surface for reactions 14 and 16 is given in Figure 9. The barrier height and location on this surface differ from those in the Sullivan surface (Figure 8) by only 0.23 kcal/mol and 0.14 Å, respectively, but the new surface gives transition state theory rates for reaction 14 which are within a factor of 2 of the experimental ones.[79] This is shown in Table III. The predicted isotope effects are accurate to 20%. Because of the inaccuracies inherent in transition state theory, especially for this reaction,[63] it is not known how much reliance to place on this result. Figure 15 shows that portion of the multiparameter surface *a propos* reaction 15 or 17. In place of a 3-kcal/mol well (Figure 14) there appears a 2-kcal/mol barrier. On this surface, HIH is bound by less than a 0.25 kcal/mol. This shallow well cannot be seen on the scale of Figure 15. Transition state theory using this surface predicts ascendency of exchange over abstraction at high collision energies as in the bromine case.

Table III: Experimental[79] and Theoretical (Present Calculations Based on Transition State Theory[78] and the Modified LEPS Surface of Parr and Kuppermann) Values for (a) the Rate Constant (10^3 mol cm^{-3} sec^{-1}) for the Reaction I + D_2 and (b) the Ratio of Rate Constants for the I + H_2 and I + D_2 Reactions

T, °C	633	667	710	738	800
Exptl k_{D_2}	0.11	0.58	2.7	6.9	44
Theoret k_{D_2}	0.21	0.86	4.4	11.5	75
Exptl k_{H_2}/k_{D_2}	3.56	2.9	2.7	2.6	2.5
Theoret k_{H_2}/k_{D_2}	2.95	2.7	2.6	2.5	2.4

Recently Raff and coworkers[81] have used a procedure like the Cashion–Herschbach one[40] and the s^3 London equation to obtain a new semiempirical H_2I potential energy surface. However, they adjusted the semiempirical HI "triplet" potential curve so that their method predicts a 42-kcal/mol barrier for the molecular reaction $H_2 + I_2$. They did not examine the linear H–I–H configurations, but found 2-kcal/mol wells for H–H–I and for triangular H_2I. The well for triangular H_2I is surprisingly the deeper one. Based on our experience with spurious wells, we feel no available semiempirical calculations are capable of predicting reliably such small features on potential energy surfaces. The surface of Raff, *et al.*, shows a 0.1-kcal/mol barrier for the abstraction reactions

$$H + HI \longrightarrow H_2 + I \qquad (-14)$$

which is fortuitously close to the 0.1-kcal/mol barrier on the surface of Parr and Kuppermann;[77] however, although both surfaces predict an early barrier, the barrier locations on these surfaces differ by more than 0.75 Å. Raff, *et al.*, did transition state theory and quasiclassical trajectory calculations on their surface which yielded isotope effects on the rate of reaction 14 which were within 20 and 50%, respectively, of Sullivan's experimental data. The trajectory calculations also gave values for k_{14} which are within a factor of 6 of experiment but too low. The surfaces obtained by Raff and coworkers have been very useful for treating the dynamics. However, it is not possible to say which H_2I surface is most accurate or even whether the presently available surfaces are qualitatively correct. Raff and coworkers have applied their methods to a series of reactions with some success,[82] which gives some added confidence in their accuracy.

These studies of the H_2Br and H_2I systems show that changing the parameters in the LEPS surfaces can

(79) J. H. Sullivan, *J. Chem. Phys.*, **30**, 1292 (1959); **36**, 1925 (1962); **39**, 3001 (1963).

(80) A contour plot of the H–I–H potential energy predicted by the LEP method (with Q_{ij}/J_{ij} = 0.163) of Wheeler, *et al.*, ref 60, shows that surface has 5-kcal/mol barriers in the valleys and a 9-kcal/mol well for R_{HI} = 1.6 Å for both HI distances. (R_e for HI is also 1.6 Å.)

(81) L. M. Raff, L. Stivers, R. N. Porter, D. Thompson, and L. B. Sims, *J. Chem. Phys.*, **52**, 3449 (1970).

(82) R. N. Porter, D. L. Thompson, L. B. Sims, and L. M. Raff, *J. Amer. Chem. Soc.*, **92**, 3208 (1970); L. M. Raff, L. M. Sims, D. L. Thompson, and R. N. Porter, *J. Chem. Phys.*, **53**, 1606 (1970); and unpublished work by Raff, Porter, and coworkers.

bring about small changes in the XHH regions important for reactions 10 and 14 while causing large changes in the HXH regions important for the reactions 11 and 15. The Parr–Kuppermann extended LEPS surfaces lead to improved rate calculations in both cases. Although the improvement may be fortuitous, the possibility of obtaining reasonable representation for all configurations of an H_2X system with one LEPS surface remains open.

The transferability of Sato parameters from system to system seems less promising. The constant k_{HH} (0.225) used for the successful H_2Br and H_2I surfaces predicts another spurious well for reaction 1! Further, to avoid HClH wells one must take $k_{HCl} \leqslant 0.08$ and for this range the use of $k_{HH} = 0.225$ leads to barrier heights for reaction 8 that are too large by at least 3 kcal/mol. The H_2Cl potential surface is poorly understood at present. One difficulty inherent in the application of LEPS-type nonionic valence-bond calculations to H_2F and H_2Cl is that the HF and HCl bonds are very ionic.[83] This makes their limited theoretical justification even less valid for these systems and is one reason why a breakdown of the empirical parametrization is not unexpected. It is not known if there is a well in the H–Cl–H surface.

Thus far, the semiempirical schemes we have described for the determination of potential energy surfaces deal only with reaction rates or their ratios. Such quantities are averages over broad thermal distributions of reactant states and collision parameters.[84] Thus they are more sensitive to the height of the reaction barriers and other gross features of the surfaces than to the subtler aspects of their topography. The accumulation of data on dependence of reaction probabilities on initial states and on distributions of product energies and angles of scattering for these reactions will help refine our notions of their potential surfaces. It has been shown[85] that product energies are sensitive to the location of the barrier along the reaction path. Scattering angles are also known to be influenced by the shape of the potential, especially its range. To determine the potential surface by comparison of chemical dynamics calculations with experiment it will be necessary to make the comparison for several properties for the same system. Further theoretical and experimental work on the H_2X systems is necessary before we will be sure of even the qualitative aspects of their potential surfaces and how they influence the chemical reactions.

Because of the possibility of more accurate *a priori* calculations[56] and because of the detailed experimental results[86–88] becoming available, it is probable that the $F + H_2$ potential energy surface will be well understood before the other $X + H_2$ surfaces. This reaction has been studied[89] with a Cashion–Herschbach-like surface and is under further study[90,91] using extended LEPS surfaces.

V. Reactions Involving Halogen Molecules

Recent experiments with multihalogen systems have brought to light some clues regarding the shape of HX_2 and X_3 potential energy surfaces. The semiempirical methods mentioned above have been applied to some of these systems, and they will doubtless be applied to many more. Such application will provide further checks upon the usefulness of these methods for constructing meaningful approximations to the true potential surfaces.

There is some evidence[92–97] that the recombination of halogen atoms takes place through a weakly bound X_3 intermediate. It has been estimated[92,93] that the binding energy of I_3 is about 5 kcal/mol with respect to $I + I_2$. Bunker and Davidson[93] suggested that I_3 is bound by short-range valence forces rather than just the weaker long-range dispersion forces. Porter and Smith[92] suggested I_3 is held together by short-range "electron transfer" forces, that is, by ionic binding. In the latter case, the nonionic (semiempirical) valence bond methods might be expected to be inaccurate (see end of paragraph). Lee, *et al.*,[6d] summarized the evidence on trihalogen stabilities which indicates that such charge-transfer bonding or its lack may be a crucial feature in all cases. Nelson and Pimentel[65] concluded from their infrared observation of Cl_3 in a low-temperature matrix that it is linear and slightly asymmetric. Nelson and Pimentel attribute this slight asymmetry to cage effects and postulate symmetric Cl_3 for the free molecules. The LEPS method predicts stable, symmetric Cl_3 for some k_{ij} but the molecular frequencies for bound Cl_3,

(83) L. Pauling, "The Nature of the Chemical Bond," 3rd ed, Cornell University Press, Ithaca, N. Y., 1960, p 74.

(84) M. A. Eliason and J. O. Hirschfelder, *J. Chem. Phys.*, **30**, 1426 (1959).

(85) P. J. Kuntz, E. M. Nemeth, J. C. Polanyi, S. D. Rosner, and C. E. Young, *ibid.*, **44**, 1168 (1966), and references therein.

(86) J. H. Parker and G. C. Pimentel, *ibid.*, **51**, 91 (1969).

(87) J. C. Polanyi and D. C. Tardy, *ibid.*, **51**, 5717 (1969).

(88) T. P. Schafer, P. E. Siska, J. M. Parsons, F. P. Tully, Y. C. Wong, and Y. T. Lee, *ibid.*, **53**, 3385 (1970).

(89) J. B. Anderson, *ibid.*, **52**, 3849 (1970).

(90) J. Muckerman, private communication.

(91) J. C. Polanyi, K. B. Woodall, and J. L. Schreiber, private communication.

(92) M. I. Christie, R. G. W. Norrish, and G. Porter, *Discuss. Faraday Soc.*, **17**, 107 (1954); M. I. Christie, A. J. Harrison, R. G. W. Norrish, and G. Porter, *Proc. Roy. Soc., Ser. A*, **231**, 446 (1955); G. Porter and J. A. Smith, *Nature*, **184**, 446 (1959); G. Porter, *Discuss. Faraday Soc.*, **33**, 198 (1962).

(93) D. L. Bunker and N. Davidson, *J. Amer. Chem. Soc.*, **80**, 5090 (1958).

(94) R. Engleman and N. R. Davidson, *ibid.*, **82**, 4770 (1960).

(95) E. Hulton and M. Wright, *Trans. Faraday Soc.*, **61**, 78 (1965).

(96) A discussion of some of the earliest evidence for Cl_3 is given in S. W. Benson, "The Foundations of Chemical Kinetics," pp 342, 343.

(97) An early LEP calculation by H. Eyring and G. K. Rollefson, *J. Amer. Chem. Soc.*, **54**, 170 (1932), predicted X_3 might be stable. Since it is known that this method often predicts a well where none really occurs, this calculation does not seem particularly important. Rollefson and Eyring found all four X_3 were bound if $Q_{xx}/J_{xx} = 1/9$ but that all four were unstable if $Q_{xx} = 0$.

obtained from any LEPS potential surface, do not correlate with those observed.

The interhalogen reaction intermediates have been studied in molecular beams. They show little systematic trend in their stabilities. For example, Cl–I–Br,[6b] Cl–I–I,[6b] and Br–I–I[6a,b] appear to be bound; the last has a binding energy of about 10 kcal/mol and is bound by short-range forces.[6a] However, no complexes have been observed for Cl–Br–I[6b] or Cl–Br–Br.[6a,b]

Noble and Pimental[66] have analyzed the infrared spectrum of bound Cl–H–Cl in a rare gas matrix. They find that the symmetric stretching frequency of this linear symmetric compound is about 260 cm^{-1}. No LEPS or extended LEPS potential surface for bound Cl–H–Cl gives a value less than 350 cm^{-1} for this symmetric frequency. For example, the Cl–H–Cl potential surface, arising from the Persky–Klein[68] Sato parameter for HCl and a Sato parameter of 0.1 for Cl_2 (which gives a modest 1.4-kcal/mol well), has a symmetric stretching frequency of 546 cm^{-1}. Thus, if the chemical stability and molecular frequencies of free and matrix-bound molecules are not radically different,[98] the modified LEPS model fails to give an accurate potential surface for Cl_3, Cl–H–Cl, and, possibly, other multihalogen reaction intermediates.

Another aspect of the potential energy surface for HCl_2 has been investigated by Klein and Wolfsberg.[99] They assumed that the reaction

$$H + Cl_2 \longrightarrow HCl + Cl \qquad (18)$$

takes place through an unstable linear H–Cl–Cl transition state. Their transition state theory treatment of their experimental data on reactions −8 and 18 requires a harmonic bending mode frequency of 105 ± 12 cm^{-1} for H–Cl–Cl. A treatment of their data making different assumptions for the other frequencies was carried out by Wilkins.[100] It yields 71 ± 20 cm^{-1} for the harmonic bend in HCl_2. Wilkins also constructed a LEPS surface which yielded 51 cm^{-1}. This may be compared with the value 11 cm^{-1} predicted by the extended LEPS potential energy surface of Polanyi and coworkers,[101,102] who adjusted their surface so that quasiclassical trajectories on it gave distributions over product rotation-vibration energies which agreed with those obtained in their chemiluminescence experiments[101] on reaction 18. The surface[102] for this exothermic reaction has a *very* early barrier (at the 2.51-kcal/mol barrier, R_{HCl} = 3.23 Å and R_{Cl_2} = 2.01 Å; R_e for Cl_2 is 1.99 Å). The same procedure has been used to obtain LEPS potential energy surfaces[14,91,101] for the reactions

$$Cl + HI \longrightarrow HCl + I \qquad (19)$$

$$H + Br_2 \longrightarrow HBr + Br \qquad (20)$$

$$F + H_2 \longrightarrow HF + H \qquad (21)$$

and their deuterium homologs. Polanyi and coworkers concluded[91,100] that the semiempirical method can be used to obtain LEPS surfaces which are accurate enough for this property For reactions 19 and 20 they found the transition state occurred early in the entrance valley. However, while the calculations agree fairly well with experiment, it is possible that a surface having a saddle point further along the entrance valley would give similar results,[103] and no *definite* conclusions about the accuracy of their LEPS surfaces can be drawn *yet*.

These product energy distributions are most sensitive to the location of the energy barrier and the rate of change of energy along the reaction path. The shape of the potential energy surface off the reaction path has less influence upon these and other attributes of thermal reactions. Conversely, such studies do not determine much of the surface topography. However, they do provide more critical insights than either absolute rate or isotope effect data, and they will mate well with crossed molecular beam measurements to offer even more severe challenges to theoretical potential energy surfaces.

VI. Summary

Presently available semiempirical schemes for constructing potential energy surfaces in covalently bonded systems predict a wide range of surface topography for choices of model parameters which are reasonable on the basis of bond strengths and activation energies. This range is more than wide enough to ensure radical differences in chemical dynamics resulting from the various surfaces. Even when detailed information about total reaction rates is utilized to calibrate these methods, the gross features of surface shape are still not uniquely determined. Nevertheless, some cases have been found where the semiempirical calculations presently can explain the experimental observations. Refinement of potential surfaces awaits information about rates for reaction from and into particular quantum states, reactive scattering data from molecular beam experiments, and more accurate theoretical methods.

Acknowledgments. This collaboration was begun while D. G. T. was at the Department of Chemistry of the California Institute of Technology and C. A. P. was at the Department of Chemistry of the University of California at Irvine. We gratefully acknowledge

(98) G. C. Pimental and S. W. Charles, *Pure Appl. Chem.*, **7**, 111 (1963), find deviations in caged molecular species up to but not exceeding 40 cm^{-1}. These deviations may be considered very small for present purposes.

(99) F. S. Klein and M. Wolfsberg, *J. Chem. Phys.*, **34**, 1494 (1961)

(100) R. L. Wilkins, *ibid.*, **42**, 806 (1965).

(101) K. G. Anlauf, P. J. Kuntz, D. H. Maylotte, P. D. Pacey, and J. C. Polanyi, *Discuss. Faraday Soc.*, **44**, 183 (1967); K. G. Anlauf, J. C. Polanyi, W. H. Wong, and K. B. Woodall, *J. Chem. Phys.*, **49**, 5189 (1968).

(102) The unpublished extended LEPS potential surface of J. C. Polanyi and D. C. Tardy has k_{HCl} = 0.0 and k_{Cl_2} = −0.06.

(103) J. C. Polanyi, *Discuss Faraday Soc.*, **44**, 293 (1968).

that some of the computations were supported by research grants administered by Professor A. Kuppermann and Professor J. C. Polanyi, and by the University of Minnesota. We acknowledge helpful discussions with Professors Polanyi and Kuppermann, Professor L. R. Martin, Professor L. M. Raff, Professor E. S. Lewis, and Professor K. B. Wiberg. The 3-D perspective plotting routines were adopted from D. L. Nelson, Technical Report 553, Department of Physics, University of Maryland, 1966. The authors are grateful to Dr. David C. Cartwright for supplying them with his version of these programs.

Spin-Free Quantum Chemistry. IX.[1] The Aggregate Theory of Polyelectronic Systems

by F. A. Matsen* and D. J. Klein

Molecular Physics Group, The University of Texas at Austin, Austin, Texas 78712 *(Received November 30, 1970)*

Publication costs assisted by the Robert A. Welch Foundation and the National Science Foundation

The aggregate theory of polyelectronic systems is applicable to interactions between shells, between atoms, and between molecules. The aggregate theory of an N-electron system consists of the following steps: (1) the construction of a zero-order Hamiltonian by partitioning N electrons among "aggregates"; (2) the construction of a vector space for the full Hamiltonian by induction on the zero-order spaces by S_N, the symmetric group on N objects; (3) the construction of kets which are symmetry adapted to S_N; (4) the application of the Wigner–Eckart theorem for S_N; and (5) a reduction in the number of primary matrix elements by the double coset decomposition of S_N with respect to the group of the zero-order Hamiltonian. The double coset generators are permutations of electrons among aggregates which permit ready identification of exchange types.

1. Introduction

The aggregate theory of polyelectronic systems is applicable to the study of the interaction between shells, between atoms, and between molecules. We present the formal theory in section 3. We partition the electrons of an N-electron system into sets called aggregates. The partitioning is carried out in such a way that the sum of the Hamiltonians for noninteracting aggregates provides a good zero-order Hamiltonian for the total system. We denote the group of the zero-order Hamiltonian by S^0. We take for the vector space of the full Hamiltonian the spaces induced on the zero-order eigenvectors by the symmetric group S_N. The basis vectors in this space are then symmetry adapted to the sequence $S_0 \subseteq S_N$. The Wigner–Eckart theorem reduces the problem to a sum over $N!$ primary matrix elements each of which involves a distinct permutation. In section 4 we make a double coset decomposition of S_N with respect to S^0 and reduce the primary matrix elements to those which involve only a minimal number of interaggregate permutations. In section 5 we discuss approximations to the full aggregate theory and their areas of applicability. In certain cases the zero-order quantum numbers provide good approximate quantum numbers. The aggregate theory is the parent theory to a number of well known theories of polyelectronic systems. These theories and their relation to aggregate theory are discussed in section 6. The aggregate theory is developed in the spin-free formulation of quantum chemistry[2] which is outlined briefly in section 2.

2. The Spin-Free Formulation

The coarse structure of an N-electron system is accurately predicted with a spin-free Hamiltonian

$$\mathbf{H}^{SF} = \sum_{i=1}^{N} \mathbf{H}_i + \sum_{i<j}^{N} e^2/\mathbf{r}_{ij} \qquad (2.1)$$

where $\mathbf{H}_i$ is the one-electron Hamiltonian for the ith electron. Since

(1) Supported by the Robert A. Welch Foundation and the National Science Foundation.

(2) This subject is treated in detail in the other papers in the spin-free series: F. A. Matsen, *Advan. Quantum Chem.*, **1**, 59 (1964); F. A. Matsen, *J. Phys. Chem.*, **68**, 3282 (1964); F. A. Matsen, A. A. Cantu, and R. D. Poshusta, *ibid.*, **70**, 1558 (1966); F. A. Matsen, *ibid.*, **70**, 1568 (1966); A. A. Cantu and F. A. Matsen, *ibid.*, **72**, 21 (1968); F. A. Matsen and D. J. Klein, *ibid.*, **73**, 2477 (1969); A. A. Cantu and F. A. Matsen, *ibid.*, **73**, 2488 (1969); M. L. Ellzey and F. A. Matsen, *ibid.*, **73**, 2495 (1969); F. A. Matsen, D. J. Klein, and D. C. Foyt, *ibid.*, **75**, 1866 (1961).

$$[\mathbf{H}^{SF},\mathbf{P}_t] = 0, \mathbf{P}_t \in S_N \tag{2.2}$$

where S_N is the group of permutations on the spin-free electron coordinates, the spin-free states of the N-electron system are labeled by the partitions $[\lambda]$ of N which identify the irreducible representations of S_N. The physically observed states are the Pauli-allowed states with

$$[\lambda] = [2^p,1^{N-2p}], \quad 0 \leq p \leq N/2 \tag{2.3}$$

$[\lambda]$ is called a permutation quantum number.

To obtain eigenvalues and eigenvectors we diagonalize $\mathbf{H}^{SF}$ in a vector space

$$V = \sum_\nu \oplus V(\nu) \tag{2.4}$$

where

$$V(\nu): \quad \{|\nu;i\rangle, i = 1 \text{ to } f^\nu\} \tag{2.5}$$

is a configuration subspace generated from a single primitive ket $|\nu\rangle$

$$|\nu;i\rangle \equiv \mathbf{P}_i|\nu\rangle, \mathbf{P}_i \in S_N, i = 1 \text{ to } f^\nu \tag{2.6}$$

The permutation quantum number is assigned to the eigenkets by means of the class operators of S_N.

The secular equation is factored and an *a priori* assignment of the permutation quantum number is effected by employing a symmetry-adapted basis for $V(\nu)$. This decomposes $V(\nu)$ into a direct sum of subspaces invariant to S_N. Thus

$$V(\nu) = \sum_{[\lambda]} \oplus V(\nu;[\lambda]) \tag{2.7}$$

where

$$V(\nu;[\lambda]): \quad \{|\nu s;[\lambda]r\rangle, \quad r = 1 \text{ to } f^{[\lambda]}, s = 1 \text{ to } f^{\nu;[\lambda]}\} \tag{2.8}$$

Here r is called the *degeneracy index* and s distinguishes among kets with the same ν, $[\lambda]$, and r. $f^{\nu;[\lambda]}$ is the number of times the irreducible representation $\Gamma^{[\lambda]}$ of S_N occurs in the representation Γ^ν supplied by $V(\nu)$. The dimension statement is

$$f^\nu = \sum_{[\lambda]} f^{[\lambda]} f^{\nu;[\lambda]} \tag{2.9}$$

For a symmetry adapted basis the Wigner–Eckart theorem is applicable. Thus

$$\langle \nu s;[\lambda]r|\mathbf{H}^{SF}|\nu' s';[\lambda']r'\rangle = \delta([\lambda],[\lambda'])\delta(r,r')\langle \nu s;[\lambda]||\mathbf{H}^{SF}||\nu' s';[\lambda]\rangle \tag{2.10}$$

where $\langle \nu s;[\lambda]||\mathbf{H}^{SF}||\nu' s';[\lambda]\rangle$, called a *reduced matrix element*, is independent of r.

The Frobenius (group) algebra $\mathfrak{A}(S_N)$ of the symmetric group is a linear associative algebra with the elements of S_N as a basis. $\mathfrak{A}(S_N)$ also has a matric basis, a basis with elements $\{\mathbf{e}_{rs}^{[\lambda]}\}$ given by

$$\mathbf{e}_{rs}^{[\lambda]} = \frac{f^{[\lambda]}}{N!} \sum_{\mathbf{P}\in S_N} [P^{-1}]_{sr}^{[\lambda]}\mathbf{P} \tag{2.11}$$

Here $[P^{-1}]_{sr}^{[\lambda]}$ is the (s,r)th matrix element of the $f^{[\lambda]} \times f^{[\lambda]}$ matrix which represents $\mathbf{P}^{-1}$ in the irreducible representation $[\lambda]$. The rule of multiplication for matric basis elements is

$$\mathbf{e}_{rs}^{[\lambda]}\mathbf{e}_{tu}^{[\lambda']} = \delta([\lambda],[\lambda'])\delta(s,t)\mathbf{e}_{ru}^{[\lambda]} \tag{2.12}$$

A matrix basis element can be employed to construct a symmetry-adapted basis from a primitive ket $|\nu\rangle$. A symmetry-adapted ket is written

$$|\nu s;[\lambda]r\rangle \equiv \sqrt{\frac{N!}{f^{[\lambda]}}}\,\mathbf{e}_{rs}^{[\lambda]}|\nu\rangle \tag{2.13}$$

By (2.11), (2.12), and (2.13) the reduced matrix element in the Wigner–Eckart theorem is

$$\begin{aligned}\langle \nu s;[\lambda]||\mathbf{H}^{SF}||\nu' s';[\lambda]\rangle &= \frac{1}{f^{[\lambda]}}\sum_v \langle \nu s;[\lambda]v|\mathbf{H}|\nu' s';[\lambda]v\rangle \\ &= \frac{N!}{(f^{[\lambda]})^2}\sum_v \langle \nu|\mathbf{e}_{sv}^{[\lambda]}\mathbf{H}\mathbf{e}_{vs'}^{[\lambda]}|\nu'\rangle \\ &= \frac{N!}{f^{[\lambda]}}\langle \nu|\mathbf{H}\mathbf{e}_{ss'}^{[\lambda]}|\nu'\rangle \\ &= \sum_{\mathbf{P}}[P^{-1}]_{s's}^{[\lambda]}\mathbf{H}_P^{\nu\nu'}\end{aligned} \tag{2.14}$$

where

$$\mathbf{H}_P^{\nu\nu'} \equiv \langle \nu|\mathbf{H}\mathbf{P}|\nu'\rangle \tag{2.15}$$

is called a *primary matrix element.* The eigenkets are denoted

$$|K;[\lambda]r\rangle = \sum_\nu \sum_{s=1}^{f^{\nu;[\lambda]}} |\nu s;[\lambda]r\rangle\langle \nu s;[\lambda]|K\rangle \tag{2.16}$$

If one neglects $\mathbf{H}_P^{\nu\nu'}$ for $\nu \neq \nu'$ one is said to neglect configuration interaction. The eigenkets are then denoted

$$|\nu K;[\lambda]r\rangle = \sum_{s=1}^{f^{\nu;[\lambda]}} |\nu s;[\lambda]r\rangle\langle \nu s;[\lambda]|\nu K\rangle \tag{2.17}$$

3. The Aggregate Theory of Polyelectronic Systems

We partition an N-electron system into aggregates A, B, C, etc. We assign electrons $1 \rightarrow N_A$ to aggregate A, $N_A + 1 \rightarrow N_A + N_B$ to aggregate B, etc., where

$$N = N_A + N_B + N_C + \ldots \tag{3.1}$$

We decompose the spin-free Hamiltonian into a zero-order and a perturbation Hamiltonian as follows

$$\mathbf{H}^{SF} = \mathbf{H}^0 + \mathbf{H}' \tag{3.2}$$

The zero-order Hamiltonian is taken to be

$$\mathbf{H}^0 = \mathbf{H}_A + \mathbf{H}_B + \mathbf{H}_C + \ldots \tag{3.3}$$

where $\mathbf{H}_A$, $\mathbf{H}_B$, $\mathbf{H}_C$, etc. are the Hamiltonians for the noninteracting aggregates A, B, C, etc. The group of $\mathbf{H}^0$ (neglecting point group symmetry) is

$$S^0 \equiv S_A \otimes S_B \otimes S_C \otimes \ldots \tag{3.4}$$

with elements

$$\mathbf{P}^0 = \mathbf{P}_a \otimes \mathbf{P}_b \otimes \mathbf{P}_c \otimes \ldots \tag{3.5}$$

and order

$$N^0 \equiv N_A!N_B!N_C!\ldots \tag{3.6}$$

The eigenkets to $\mathbf{H}^0$ are the products of the eigenkets of the Hamiltonians of the several aggregates and are denoted

$$|\gamma^0 r^0\rangle \equiv |\nu_A K_A;[\lambda_A]r_A\rangle|\nu_B K_B;[\lambda_B]r_B\rangle\ldots \tag{3.7}$$

where

$$\gamma^0 \equiv \{\nu_A K_A;[\lambda_A],\ \nu_B K_B;[\lambda_B],\ \ldots\}$$

and

$$r^0 = r_A \otimes r_B \otimes \ldots$$

Next we construct a vector space for the full Hamiltonian by induction on the zero-order eigenkets. Thus

$$V = \sum_{\gamma^0} \oplus V(\gamma^0\uparrow) \tag{3.8}$$

with

$$V(\gamma^0\uparrow):\ \{|\gamma^0 r^0 i\rangle,\ i = 1 \text{ to } N!/N^0,\ r^0 = 1 \text{ to } f^{[\lambda]^0} \equiv f^{[\lambda_A]}f^{[\lambda_B]}\ldots\} \tag{3.9}$$

with

$$|\gamma^0 r^0 i\rangle = \mathbf{P}_i|\gamma^0 r^0\rangle \tag{3.10}$$

Here $\mathbf{P}_i$ is a left coset multiplier for the ith left coset of S_N with respect to S^0. The dimension of $V(\gamma^0\uparrow)$ is

$$f^{[\lambda]^0\uparrow} = N!f^{[\lambda]^0}/N^0 \tag{3.11}$$

Symmetry adaptation of the basis of $V(\gamma^0\uparrow)$ decomposes it into a direct sum of spaces which are irreducible with respect to S_N. Thus

$$V(\gamma^0\uparrow) = \sum_{[\lambda]} \oplus V(\gamma^0\uparrow;[\lambda]) \tag{3.12}$$

A convenient choice of matric basis elements for the symmetry adaptation is a set which is sequence-adapted[3] to the chain

$$S^0 \subseteq S_N \tag{3.13}$$

A sequence-adapted matric basis element is denoted

$$\mathbf{e}^{[\lambda]}{}_{(\rho[\lambda]^0 r^0)(\rho'[\lambda']^0 r'^0)} = \frac{f^{[\lambda]}}{N!}\sum_{\mathbf{P}}[P^{-1}]^{[\lambda]}{}_{(\rho'[\lambda']^0 r'^0)(\rho[\lambda]^0 r^0)}\mathbf{P} \tag{3.14}$$

where

$$[\lambda]^0 \equiv [\lambda_A] \otimes [\lambda_B] \otimes [\lambda_C] \otimes \ldots$$

and

$$\rho = 1 \text{ to } f^{[\lambda]^0;[\lambda]}$$

Here $f^{[\lambda]^0;[\lambda]}$ is the number of times $\Gamma^{[\lambda]}$ of S_N occurs in $\Gamma^{[\lambda]^0\uparrow}$, the representation of S_N induced from $\Gamma^{[\lambda]^0}$ of S^0. The sequence-adapted matric basis element transforms from the left under elements of S^0 as the (r^0)th column of $\Gamma^{[\lambda]^0}$ of S^0. Thus

$$\mathbf{P}^0\mathbf{e}^{[\lambda]}{}_{(\rho[\lambda]^0 r^0)(\rho'[\lambda']^0 r'^0)} = \sum_{s^0=1}^{f^{[\lambda]^0}}[P^0]^{[\lambda]^0}{}_{s^0 r^0}\mathbf{e}^{[\lambda]}{}_{(\rho[\lambda]^0 s^0)(\rho'[\lambda']^0 r'^0)},\mathbf{P}^0 \in S^0 \tag{3.15}$$

and on the right as the (r'^0)th column of $\Gamma^{[\lambda']^0}$ of S^0

$$\mathbf{e}^{[\lambda]}{}_{(\rho[\lambda]^0 r^0)(\rho'[\lambda']^0 r'^0)}\mathbf{P}^0 = \sum_{s'^0=1}^{f^{[\lambda']^0}}[P^0]^{[\lambda]^0}{}_{r'^0 s'^0}\mathbf{e}^{[\lambda]}{}_{(\rho[\lambda]^0 r^0)(\rho'[\lambda']^0 s'^0)},\ \mathbf{P}^0 \in S^0 \tag{3.16}$$

The sequence-adapted kets are then

$$|\gamma^0(\rho[\lambda]^0);[\lambda](\sigma[\mu]^0 s^0)\rangle = \left[\frac{N!}{f^{[\lambda]}N^0}\right]^{1/2} f^{[\lambda]^0}\mathbf{e}^{[\lambda]}{}_{(\sigma[\mu]^0 s^0)(\rho[\lambda]^0 r^0)}|\gamma^0 r^0\rangle \tag{3.17}$$

Matrix elements over sequence-adapted kets are

$$\langle\gamma^0(\rho[\lambda]^0);[\lambda](\sigma[\mu]^0 s^0)|\mathbf{H}^{SF}|\gamma'^0 \times (\rho'[\lambda']^0);[\lambda'](\sigma'[\mu']^0 s'^0)\rangle = \delta([\lambda],[\lambda'])\delta(\sigma,\sigma')\delta([\mu],[\mu'])\delta(s^0,s'^0) \times \langle\gamma^0(\rho[\lambda]^0);[\gamma]||\mathbf{H}^{SF}||\gamma'^0(\rho'[\lambda']^0);[\lambda]\rangle \tag{3.18}$$

where

$$\langle\gamma^0(\rho[\lambda]^0);[\lambda]||\mathbf{H}^{SF}||\gamma'^0(\rho'[\lambda']^0);[\lambda]\rangle = \frac{f^{[\lambda]^0}f^{[\lambda']^0}}{N^0}\sum_{\mathbf{P}}[P^{-1}]^{[\lambda]}{}_{(\rho'[\lambda']^0 r'^0)(\rho[\lambda]^0 r^0)}\langle\gamma^0 r^0|\mathbf{H}^{SF}\mathbf{P}|\gamma'^0 r'^0\rangle \tag{3.19}$$

where r^0 and r'^0 are determined by the zero-order ket.

4. Double Coset Decomposition

The double coset decomposition of S_N with respect to S^0 is

$$S_N = \sum_q \oplus C_q \tag{4.1}$$

where

$$C_q = S^0\mathbf{G}_q S^0 \tag{4.2}$$

is the qth double coset and $\mathbf{G}_q$ is a generator for that double coset. $\mathbf{G}_q$ is an interaggregate permutation (except for the identity), so permutations over electrons can be replaced by the permutations of aggregate symbols (see Appendix 1).

A sequence-adapted matric basis element can be expressed as a sum of products of double coset generators and the matric basis elements of S^0. Thus

$$\mathbf{e}^{[\lambda]}{}_{(\rho[\lambda]^0 r^0)(\rho'[\lambda']^0 r'^0)} = \frac{f^{[\lambda]}N^0}{N!f^{[\lambda]^0}f^{[\lambda']^0}}\sum_q l_q \times \sum_{t^0=1}^{f^{[\lambda]^0}}\sum_{t'^0=1}^{f^{[\lambda']^0}}[G_q{}^{-1}]^{[\lambda]}{}_{(\rho'[\gamma']^0 t'^0)(\rho[\lambda]^0 t^0)}\mathbf{e}^{[\lambda]^0}{}_{r^0 t^0}\mathbf{G}_q\mathbf{e}^{[\lambda']^0}{}_{t'^0 r'^0} \tag{4.3}$$

(3) D. J. Klein, C. H. Carlisle, and F. A. Matsen, *Advan. Quantum Chem.*, 5, 219 (1970).

where l_q is equal to N^0 divided by d_q, the order of the intersection

$$\mathbf{G}_q S^0 \mathbf{G}_q^{-1} \cap S^0 \tag{4.4}$$

and

$$\mathbf{e}^{[\lambda]^0}{}_{\gamma^0 t^0} \equiv \mathbf{e}^{[\lambda_A]}{}_{\tau_A t_A} \otimes \mathbf{e}^{[\lambda_B]}{}_{\tau_B t_B} \otimes \ldots \tag{4.5}$$

Substituting the decomposition (4.3) into (3.18) yields

$$\langle \gamma^0(\rho[\lambda]^0);[\lambda]||\mathbf{H}^{SF}||\gamma'^0(\rho'[\lambda']^0);[\lambda]\rangle = \sum_q l_q \sum_{t^0,t'^0} [G_q^{-1}]^{[\lambda]}{}_{(\rho'[\lambda']t'^0)(\rho[\lambda]t^0)} \langle \gamma^0 t^0||\mathbf{H}^{SF}\mathbf{G}_q||\gamma'^0 t'^0\rangle \tag{4.6}$$

By the double-coset decomposition of S_N with respect to S^0 the sum over $N!$ permutations in (3.19) has been reduced to a sum over interaggregate permutations. These terms are classified as follows: $\mathbf{G}_q = (AB)$, (AC), ... *single exchange* and $\mathbf{G}_q = (ABC) = (AB)(BC)$, $(AB)^2$, ... *multiple exchange.*

For a system of two aggregates we can choose the double coset decomposition as follows

$$\mathbf{G}_q = (q N_A + q)\mathbf{G}_{q-1},\ q = 1 \text{ to min } \{N_A, N_B\} \tag{4.7}$$

with

$$\mathbf{G}_0 = \mathcal{G} \tag{4.8}$$

and

$$l_q = \binom{N_A}{q}\binom{N_B}{q} \tag{4.9}$$

5. Approximations

Even though aggregate theory simplifies the general polyelectronic theory, it is often necessary to make approximations to render computation more tractable. Two types of approximations are frequently employed.

A. The Neglect of Configuration Interaction. The interaction between different configuration vector spaces $V(\gamma^0 \uparrow)$, $\gamma^0 = \{\nu^0\ K^0;[\lambda]^0\}$ is rigorously zero only in the limit of noninteracting aggregates, for example, a system of widely separated aggregates. Configuration interaction can be neglected to a good approximation in those cases for which the zero-order energies are widely separated. Configuration interaction can also be neglected to a good approximation between states of different $[\lambda]^0$ in those cases for which the aggregates are highly "localized," *i.e.*, there exists essentially zero differential overlap between the aggregates. An example of this case is provided by the derivation of the Heisenberg spin Hamiltonian as described in the following paper.

B. The Neglect of Multiple Interaggregate Exchange Integrals. In this approximation one retains in eq 4.6 only the identity and the transpositions among the double-coset multipliers. The so-called multiple interaggregate exchange integrals are neglected. An example of this case is the computation of the London dispersion energies between aggregates at large interaggregate separation. Some estimates of the contributions made to the several interaggregate exchange integrals can be obtained by considering their exponential behavior in the separated aggregate limit. For suitably accurate wave functions Herring[4] has already considered this problem and found the exponential asymptotic behavior as given in Table I. In this table algebraic and angle dependent factors for the asymptotic behavior of the integrals are neglected; α_{IJ} is an orbital exponent and R_{IJ} is the distance between the aggregates I and J. It is seen that the double coset multiplier terms interchanging the fewest indices among aggregates are most important in terms of their exponential asymptotic behavior.

Table I: Double Coset Multipliers Interchanging Four and Fewer Indices[a]

q	$\mathbf{G}_q$	Number of indices interchanged	Exponential asymptotic behavior
0	$\mathcal{G}$	0	
(IJ)	(ij)	2	$e^{\alpha_{IJ}R_{IJ}+\alpha'_{IJ}R_{IJ}}$
(IJK)	(ijk)	3	$e^{\alpha_{IJ}R_{IJ}+\alpha_{JK}R_{JK}+\alpha_{KI}R_{KI}}$
$(IJ)(IJ)$	$(ij)(i'j')$	4	$e^{\alpha_{IJ}+R_{IJ}+\alpha'_{IJ}R_{IJ}+\alpha''_{IJ}R_{IJ}+\alpha'''_{IJ}R_{IJ}}$
$(IJ)(IK)$	$(ij)(i'k)$	4	$e^{\alpha_{IJ}R_{IJ}+\alpha'_{IJ}R_{IJ}+\alpha_{IK}R_{IK}+\alpha'_{IK}R_{IK}}$
$(IJ)(KL)$	$(ij)(kl)$	4	$e^{\alpha_{IJ}R_{IJ}+\alpha_{JK}R_{JK}+\alpha_{KL}R_{KL}+\alpha_{LI}R_{LI}}$
$(IJKL)$	$(ijkl)$	4	$e^{\alpha_{IJ}R_{IJ}+\alpha_{JK}R_{JK}+\alpha_{KL}R_{KL}+\alpha_{LI}R_{LI}}$
All others of higher order			

[a] Here i and $i' \neq i$ are indices associated with aggregate I; j and $j' \neq j$, with aggregate J; k, with aggregate K; and l, with aggregate L.

The multiple interaggregate exchange integrals are rigorously zero if mutually orthogonal aggregate wave functions are used. The use of strongly mutually orthogonal aggregate wave functions permits the neglect of the multiple exchange terms to a high approximation.[5]

6. The Relationship of the Aggregate Theory to Other Theories

The aggregate theory of polyelectronic systems may be considered as the parent theory for a number of well known theories

(1) Orbital Theory. (a) Orbitals Singly Occupied.

$$|\nu^0 K^0[\lambda]^0\rangle = |a\rangle|b\rangle|c\rangle$$

where

$$K^0 = \{k_a, k_b, \ldots\}$$

and

$$S^0 = S_1 \otimes S_1 \otimes S_1 \otimes \ldots$$

(4) C. Herring, *Magnetism*, **2b**, 1 (1966).

(5) See, for example, R. McWeeny, *Proc. Roy. Soc. Ser. A.*, **253**, 242 (1959); M. Klessinger and R. McWeeny, *J. Chem. Phys.*, **42**, 3343 (1965); J. M. Parks and R. G. Parr, *ibid.*, **28**, 335 (1958).

$$[\lambda]^0 = [1] \otimes [1] \otimes [1] \otimes \ldots$$

The double coset generators are the group elements. One orbital choice is obtained by the optimally projected self-consistent field theory recently described by Gallup,[6a] Poshusta and Kramling,[6b] Matsen and Cantu,[7] Ladner and Goddard,[8] Lowdin and Goscinski,[9] and others. For orthogonal orbitals only the transpositions survive. If orbitals are assigned separate atoms one obtains the Heitler–London theory and its extensions.

(*b*) *Orbitals Doubly Occupied.*

$$|\nu^0 K^0 [\lambda]^0\rangle = |a\rangle|a\rangle|b\rangle|b\rangle \ldots$$

where

$$K^0 = \{k_a^2, k_b^2, \ldots\}$$

and

$$N^0 = S_2 \otimes S_2 \otimes S_2 \otimes \ldots$$

$$[\lambda]^0 = [2] \otimes [2] \otimes \ldots$$

From this primitive ket one can construct only singlet states. If the orbitals are chosen optimally one obtains the Hartree–Fock orbitals. Since the orbitals are orthogonal only transpositions occur.

(*c*) *Geminal Theory.*

$$|\nu^0 K^0 [\lambda]^0\rangle = |aa\rangle|bb\rangle$$

Formally identical with (b).

(*d*) *Mixed Occupancy.*

$$|\nu^0 K^0 [\lambda]^0\rangle = |a\rangle|a\rangle|b\rangle|b\rangle \ldots |e\rangle|f\rangle$$

where

$$K^0 = \{a^2 b^2 \ldots ef\}$$

and

$$N^0 = S_2 \otimes S_2 \otimes \ldots \otimes S_1 \otimes S_1$$

$$[\lambda]^0 = [2] \otimes [2] \otimes \ldots \otimes [1] \otimes [1]$$

7. Summary and Conclusion

We have presented a theory of polyelectronic systems composed of a number of approximately localized aggregates. Symmetry-adapted kets for the total system were constructed by applying sequence-adapted matric basis elements to zero-order kets, products of kets for the individual aggregates. Matrix elements for the total system were broken up into matrix elements over the zero-order product kets through the use of a double coset decomposition. This double coset decomposition for the matrix elements was shown to provide a convenient form to invoke additional approximations, thus making calculations on large systems more tractable. The applicability of the listed approximations was discussed in general. A number of the approximations were found to be asymptotically exact in the limit of complete localization. Although many molecules at their equilibrium nuclear conformation are not composed of such well localized aggregates, there are some chemical systems which may obey such a criterion, as for example, Rydberg states, exchange coupled organic molecules,[10] polynuclear transition metal complexes and molecules near the separated atom limit. In addition, one might further investigate a partial relaxation of the approximations of section 5, which could be applicable to less well localized systems.

Acknowledgments. While this paper was in the final stages of preparation, we learned of the work of Kramer and Seligman, who have applied double coset decomposition to the N-nucleon problem.[11] We acknowledge their courtesy in permitting us to examine their paper in proof.

Appendix 1

We consider the double coset decomposition

$$S_N = \sum_q S^0 \mathbf{G}_q S^0$$

where

$$S^0 = S_A \otimes S_B \otimes \ldots$$

and S_I is the symmetric group of permutations on the indices of set $I = A, B, C, \ldots$.

Theorem. In every double coset, $S^0\mathbf{G}_qS^0$, there is at least one permutation such that when it is expressed in disjoint cycle form no two indices of the same set occur in any one cycle; for if $i,i' \in I$ are in the same disjoint cycle $(i \ldots i' \ldots)$ of a permutation $\mathbf{P} \in S^0\mathbf{G}_qS^0$, then

$$(i \ldots i' \ldots)(ii') = (i \ldots)(i' \ldots)$$

so that the permutation $\mathbf{P}(ii')$, with i and i' in distinct disjoint cycles, is also in $S^0\mathbf{G}_qS^0$. It is also seen that if $i,i' \in I$ and $j,j' \in J \neq I$ are two pairs of indices contained in the same disjoint cycle of a permutation $\mathbf{P} \in S^0\mathbf{G}_qS^0$, then $\mathbf{P}(ii')(jj')$ and $\mathbf{P}(jj')(ii')$ are S^0-*similar*.[12] Also, if $i,i',i'' \in I$ are contained in the same disjoint cycle $(i \ldots i' \ldots i'' \ldots)$ of a permutation $\mathbf{P} \in S^0\mathbf{G}_qS^0$, then the permutations $\mathbf{P}(ii')(ii'')$, $\mathbf{P}(ii'')(i',i'')$, and $\mathbf{P}(i'i'')(ii')$ with i, i', and i'' in different disjoint cycles are all in $S^0\mathbf{G}_qS^0$ and are all S^0-similar. Thus, in reducing a given $\mathbf{P} \in S^0\mathbf{G}_qS^0$ by the application on the right of suitable transpositions contained in S^0, the form in which no two indices from the same set I

(6) (a) G. A. Gallup, *J. Chem. Phys.*, **48**, 1732 (1968); (b) R. D. Poshusta and R. W. Kramling, *Phys. Rev.*, **167**, 139 (1968).

(7) F. A. Matsen and A. A. Cantu, *J. Phys. Chem.*, **73**, 2488 (1969).

(8) R. C. Ladner and W. A. Goddard, *J. Chem. Phys.*, **51**, 1073 (1969).

(9) P. O. Lowdin and O. Goscinski, *Int. J. Quantum Chem. Symp.*, **3S**, 533 (1969).

(10) P. L. Nordio, Z. G. Soos, and H. M. McConnell, *Annu. Rev. Phys. Chem.*, **17**, 237 (1966).

(11) P. Kramer and T. H. Seligman, *Nucl. Phys. A*, **136**, 545 (1969).

(12) Two operators, $\mathcal{O}_1$ and $\mathcal{O}_2$ are S^0-similar if there exists a $\mathbf{P} \in S^0$ such that $\mathbf{P}\mathcal{O}_1\mathbf{P}^{-1} = \mathcal{O}_2$.

appear in the same disjoint cycle is unique up to a S^0-similarity transformation. Thus the set of reduced permutations in $S^0\mathbf{G}_qS^0$, with no two indices from the same I in the same disjoint cycle, uniquely specifies the double coset $S^0\mathbf{G}_qS^0$. Taking any one of these reduced permutations in a $S^0\mathbf{G}_qS^0$ and replacing each index i in each disjoint cycle by the corresponding set label I (such that $i \in I$) yields a label for each double coset.

Appendix 2

In this appendix we give two examples for $N = 4$. $N_A = 3$, $N_B = 1$

$$S^0 = S_3 \otimes S_1 = S_3 \tag{A2.1}$$

and there are two double cosets. The two double coset multipliers may be chosen as

$$\mathbf{G}_1 = g \text{ and } \mathbf{G}_2 = (34) \tag{A2.2}$$

The double coset decomposition of S_4 with respect to S_3 is

$$S_4 = S_3gS_3 \oplus S_3(34)S_3 = S_3 \oplus S_3(34)S_3 \tag{A2.3}$$

For $[\lambda] = [2,1,1]$, $[\lambda]^0 = [\lambda']^0 = [2,1] \otimes [1]$, $r^0 = 1 \otimes 1$ and $r'^0 = 2 \otimes 1$, the decomposition (4.3) becomes

$$\mathbf{e}^{[\lambda]}{}_{([\lambda]^0r^0)([\lambda']^0r'^0)} = \mathbf{e}^{[2,1,1]}{}_{([2,1]1)([2,1]2)} =$$

$$\frac{3\cdot 3!}{(2\cdot 1)^2\cdot 4!}\sum_q l_q \sum_{t^0,t'^0=1}^{2} [G_q{}^{-1}]^{[2,1,1]}{}_{([2,1]t'^0)([2,1]t^0)} \times$$

$$\mathbf{e}_{1t^0}{}^{[2,1]}\mathbf{G}_q\mathbf{e}_{t'^02}{}^{[2,1]} =$$

$$\frac{3}{16}\{(1)\sum_{t^0,t'^0=1}^{2}[g]^{[2,1,1]}{}_{([2,1]t'^0)([2,1]t^0)}\mathbf{e}_{1t^0}{}^{[2,1]}\mathbf{e}_{t'^02}{}^{[2,1]} +$$

$$3\sum_{t^0,t'^0=1}^{2}[(34)]^{[2,1,1]}{}_{([2,1]t'^0)([2,1]t^0)}\mathbf{e}_{1t^0}{}^{[2,1]}(34)\mathbf{e}_{t'^02}{}^{[2,1]} =$$

$$\frac{3}{8}\mathbf{e}_{12}{}^{[2,1]} + \frac{9}{16}\sum_{t^0=1}^{2}[(34)]^{[2,1,1]}{}_{([2,1]t^0)([2,1]t^0)}$$

$$\mathbf{e}_{1t^0}{}^{[2,1]}(34)\mathbf{e}_{t^02}{}^{[2,1]} = \frac{3}{8}\mathbf{e}_{12}{}^{[2,1]} - \frac{9}{16}\mathbf{e}_{11}{}^{[2,1]}(34)\mathbf{e}_{12}{}^{[2,1]} -$$

$$\frac{3}{16}\mathbf{e}_{12}{}^{[2,1]}(34)\mathbf{e}_{22}{}^{[2,1]} \tag{A2.4}$$

and the reduced matrix element (4.6) becomes

$$\langle K^0([2,1]1);[2,1,1]||\mathbf{H}^{SF}||K'^0([2,1]2);[2,1,1]\rangle =$$

$$2\langle K^01;[2,1]1|\mathbf{H}^{SF}|K'^02;[2,1]1\rangle -$$

$$3\langle K^01;[2,1]1|(34)\mathbf{H}|K'^02;[2,1]1\rangle -$$

$$\langle K^01;[2,1]2|(34)\mathbf{H}|K'^02;[2,1]2\rangle \tag{A2.5}$$

$N_A = N_B = 2$

$$S^0 = S_2 \otimes S_{(2)} \tag{A2.6}$$

where $S_2 = \{g,(12)\}$ and $S_{(2)} = \{g,(34)\}$. There are three double cosets, and the three double coset multipliers may be chosen as

$$\mathbf{G}_1 = g;\ \mathbf{G}_2 = (23);\ \mathbf{G}_3 = (14)(23) \tag{A2.7}$$

The double coset decomposition of S_4 with respect to $S^0 = S_2 \otimes S_{(2)}$ is

$$S_4 = S^0 \oplus S^0(23)S^0 \oplus S^0(14)(23)S^0 \tag{A2.8}$$

For $[\lambda] = [2,1,1]$, $[\lambda]^0 = [1^2] \otimes [1^2]$, $[\lambda']^0 = [2] \otimes [1^2]$, $r^0 = r'^0 = 1 \otimes 1$ we have

$$\mathbf{e}^{[\lambda]}{}_{([\lambda]^0r^0)([\lambda']^0r^0)} = \mathbf{e}^{[2,1,1]}{}_{([1^2]\otimes[1^2])([2]\otimes[1^2])} =$$

$$\frac{3\cdot(2\cdot 2)}{1\cdot 1\cdot 4!}\sum_q l_q \sum_{t^0,t'^0=1}^{1}[G_q{}^{-1}]^{[2,1,1]}{}_{([1^2]\otimes[1^2])([2]\otimes[1^2])} \times$$

$$\mathbf{e}_{1t^0}{}^{[1^2]\otimes[1^2]}\mathbf{G}\mathbf{e}_{qt'^01}{}^{[2]\otimes[1^2]} =$$

$$^1/_2\{[g]^{[2,1,1]}{}_{([1^2]\otimes[1^2])([2]\otimes[1^2])}\mathbf{e}_{11}{}^{[1^2]\otimes[1^2]}g\mathbf{e}_{11}{}^{[2]\otimes[1^2]} +$$

$$4[(23)]^{[2,1,1]}{}_{([1^2]\otimes[1^2])([2]\otimes[1^2])}\mathbf{e}_{11}{}^{[1^2]\otimes[1^2]}(23)\mathbf{e}_{11}{}^{[2]\otimes[1^2]} +$$

$$[(14)(23)]^{[2,1,1]}{}_{([1^2]\otimes[1^2])([2]\otimes[1^2])}\mathbf{e}_{11}{}^{[1^2]\otimes[1^2]} \times$$

$$(14)(23)\mathbf{e}_{11}{}^{[2]\otimes[1^2]}\} = \sqrt{2}\mathbf{e}_{11}{}^{[1^2]\otimes[1^2]}(23)\mathbf{e}_{11}{}^{[2]\otimes[1^2]} \tag{A2.9}$$

and

$$\langle K^0([1^2]\otimes[1^2]);[2,1,1]||\mathbf{H}^{SF}||\times$$

$$K'^0([2]\otimes[1^2]);[2,1,1]\rangle =$$

$$2\sqrt{2}\langle K^0;[1^2]\otimes[1^2]|\mathbf{H}(23)|K'^0;[2]\otimes[1^2]\rangle \tag{A2.10}$$

Appendix 3

We present formulas for the irreducible representations appearing in the sequence-adapted matric basis elements. If S^0 is canonical in S_N, the elements of the representation for $[\lambda]^0 = [\lambda']^0$ are

$$[P]^{[\lambda]}{}_{([\lambda]^0t^0)([\lambda]^0t'^0)} =$$

$$\frac{f^{[\lambda]^0}}{N^0}\sum_{P'\in S^0}\chi^{[\lambda]}(P'P)[(P')^{-1}]_{t^0t'^0}{}^{[\lambda]^0} \tag{A3.1}$$

and the remaining elements are given by

$$[\mathbf{P}_1]^{[\lambda]}{}_{([\lambda']^0t'^0)([\lambda]^0t^0)}[P_2]^{[\lambda]}{}_{([\lambda]^0t^0)([\lambda']^0t'^0)} =$$

$$\frac{f^{[\lambda]}}{N!}\sum_{P'\in S_N}[P_1P'P_2]^{[\lambda]}{}_{([\lambda']^0t'^0)([\lambda']^0t'^0)} \times$$

$$[(P')^{-1}]^{[\lambda]}{}_{([\lambda]^0t^0)([\lambda]^0t^0)} \tag{A3.2}$$

Choosing $\mathbf{P}_1 = \mathbf{P}_2{}^{-1}$ yields an expression for the magnitude of $[P_1]^{[\lambda]}{}_{([\lambda']^0t'^0)([\lambda]^0t^0)}$, since the matrix basis for S_N is unitary. The sign of one $[P]^{[\lambda]}{}_{([\lambda']^0t'^0)([\lambda]^0t^0)}$ may be chosen arbitrarily, and consistent phases for the other $[P'']^{[\lambda]}{}_{([\lambda']^0t'^0)([\lambda]^0t^0)}$, $P'' \in S_N$, may be obtained from (A3.2). We illustrate eq A3.1 and A3.2 for $S_4 \supset S_2 \otimes S_{(2)}$

$$[(23)]^{[2,1,1]}{}_{([2]\otimes[1^2])([2]\otimes[1^2])}$$

$$= \frac{1}{4}\sum_{P\in S^0}\chi^{[2,1,1]}(P(23))[P^{-1}]^{[2]\otimes[1^2]}$$

$$= \frac{1}{4}[(-1)(1) + (0)(1) + (0)(-1) + (1)(-1)]$$

$$= -\frac{1}{2} \tag{A3.3}$$

$$[(23)]^{[2,1,1]}_{([1^2]\otimes[1^2])([2]\otimes[1^2])}[(23)]^{[2,1,1]}_{([2]\otimes[1^2])([1^2]\otimes[1^2])}$$
$$= \frac{3}{24}\sum_{P\in S_4}[(23)P(23)]^{[2,1,1]}_{([1^2]\otimes[1^2])([1^2]\otimes[1^2])} \times [P^{-1}]^{[2,1,1]}_{([2]\otimes[1^2])([2]\otimes[1^2])}$$
$$= \frac{1}{8}\left[2(1) + 4\left(\frac{1}{2}\right) + 18(0)\right]$$
$$= \frac{1}{2} \qquad \text{(A3.4)}$$

$$[(23)]^{[2,1,1]}_{([1^2]\otimes[1^2])([2]\otimes[1^2])} = \pm\frac{1}{\sqrt{2}} \qquad \text{(A3.5)}$$

The examples displayed in eq A2.9 and A3.5 are correctly given, in contrast to the similar examples in eq 126 and 127 of ref 3.

Spin-Free Quantum Chemistry. X.[1] The Effective Spin Hamiltonian

by F. A. Matsen,* D. J. Klein, and D. C. Foyt

Molecular Physics Group, The University of Texas at Austin, Austin, Texas 78712 *(Received November 30, 1970)*

Publication costs assisted by the Robert A. Welch Foundation and the National Science Foundation

We construct an effective spin Hamiltonian for coarse structure states which when employed with the appropriate spin space yields a representation identical with that obtained with a spin-free Hamiltonian operating on spin-free space. Application of the aggregate theory of polyelectronic systems (paper IX), together with the Dirac identity, yields a rigorous effective spin Hamiltonian to which the Heisenberg effective spin Hamiltonian is an approximation. These Hamiltonians contain both single and multiple exchange terms.

1. Introduction

The predictions for an N-electron system of the coarse structure chemistry, as distinct from the fine and hyperfine structure, require only a spin-free Hamiltonian. To make these predictions one constructs a representation of the Hamiltonian over a spin-free vector space. There are three formulations for the construction of this representation: the spin-free formulation, the antisymmetrized spin formulation, and the effective spin Hamiltonian formulation.

A. The Spin-Free Formulation. Here one employs a spin-free vector space which is a direct sum of *configuration spaces.*

$$V = \sum_{\nu} \oplus V(\nu) \qquad (1.1)$$

where

$$V(\nu): \quad \{|\nu;i\rangle,\ i = 1 \text{ to } f^\nu\} \qquad (1.2)$$

and

$$|\nu;i\rangle = \mathbf{P}|\nu\rangle \qquad \mathbf{P} \in \mathcal{S}_N \qquad (1.3)$$

(We employ script $\mathcal{S}$ for symmetric groups and S for atomic spins.) The Hamiltonian is diagonalized in this space. Each eigenket is automatically symmetry-adapted to $\mathcal{S}_N$ and carries a group quantum number $[\lambda]$, a partition of N. The representation is factored and $[\lambda]$ assigned *a priori* if one employs a symmetry-adapted basis. The symmetry adaptation decomposes the vector space into irreducible subspaces with respect to $\mathcal{S}_N$. Thus

$$V(\nu) = \sum_{[\lambda]} \oplus V(\nu[\lambda]) \qquad (1.4)$$

Of the several subspaces only those spaces with

$$[\lambda] = [2^p,1^{N-2p}] \qquad (1.5)$$

are associated with physical states.[2]

B. The Antisymmetrized Spin Formulation. Here one employs a vector space which is a product of a spin-free space $V(\nu)$ and a spin space $V(\sigma)$. We symmetry-adapt these spaces to $\mathcal{S}_N{}^\nu$ and $\mathcal{S}_N{}^\sigma$, respectively. The product space is in turn symmetry-adapted to

$$\mathcal{S}_N{}^{\nu\sigma} \Longleftarrow \mathcal{S}_N{}^\nu[\times]\mathcal{S}_N{}^\sigma \qquad (1.6)$$

an inner direct product which is isomorphic to $\mathcal{S}_N$. Thus

$$V(\nu\sigma) = \sum_{[\omega]}\sum_{[\lambda]}\sum_{[\mu]} V(\nu[\lambda],\ \sigma[\mu];\ [\omega]) \qquad (1.7)$$

(1) Supported by the Robert A. Welch Foundation and the National Science Foundation.

(2) (a) This subject is treated in detail in the earlier papers in the spin-free series. These are listed in paper IX, F. A. Matsen and D. J. Klein, *J. Phys. Chem.*, **75**, 1860; (b) for a summary of the spin-free approach, see F. A. Matsen, *J. Amer. Chem. Soc.*, **92**, 3525 (1970).

Because there are two and only two spin orbitals

$$[\mu] = [N - p, p] \tag{1.8}$$

The symmetry-adapted spin kets are eigenkets of $\mathbf{S}^2$ with a spin quantum number

$$S = N/2 - p \tag{1.9}$$

The only subspace of $V(\nu\sigma)$ associated with physical states is the antisymmetric space

$$[\omega] = [1^N] \tag{1.10}$$

in which case

$$[\lambda] = [\tilde{\mu}] = [2^p, 1^{N-2p}] \tag{1.11}$$

A spin-free representation of the Hamiltonian which is equivalent to that obtained in the spin-free formulation is obtained from this space on integrating over the spin coordinates.

C. The Effective Spin Hamiltonian Formulation. Here one employs a spin space and an effective Hamiltonian operating on that space. The effective Hamiltonian is a matrix spin operator which contains spin-free matrix elements as parameters. The construction of a representation on spin space with the effective spin Hamiltonian yields a representation which is equivalent to that obtained in the spin-free formulation.

Effective spin Hamiltonians are widely used in theories of magnetism. The first effective spin Hamiltonian was constructed by Dirac[3a] on the basis of earlier spin-free work by Heisenberg.[3b] This approach was extended by Van Vleck[4] and Serber.[5a] A comprehensive discussion has recently been presented by Herring.[5b] Our treatment differs from previous work in three respects: (a) it applies to multi-electron atoms; (b) it considers configuration interaction; (c) it employs the spin-free formulation in the construction of the spin Hamiltonian, making full use of double coset generators and related group-theoretical techniques. Previous work by Herring[5b] does not have features (b) and (c); previous work by Arai[6a] and Mattheis[6b] does not have feature (a); previous work by Arai[6a] and McWeeny and Yonezawa[6c] does not have feature (b); and previous work by Nesbet[6d] and Van Vleck[6e] does not have feature (c).

In section 2 we develop a general effective spin Hamiltonian, in section 3 we develop an effective spin Hamiltonian appropriate to the aggregate theory of polyelectronic systems,[2a-IX] and in section 4 we discuss approximate effective spin Hamiltonians.

2. A General Effective Spin Hamiltonian

A general effective spin Hamiltonian is a matrix operator on spin space. We construct an effective spin Hamiltonian by the following procedure. Let

$$\mathbf{H} = \sum_{i=1}^{N} \left(-\tfrac{1}{2}\nabla_i^2 - \sum_a \frac{z_a}{\mathbf{r}_{ai}} \right) + \sum_{i<j} \frac{1}{\mathbf{r}_{ij}} \tag{2.1}$$

be the spin-free Hamiltonian and

$$\mathcal{A} = \frac{1}{N!} \sum_{\mathbf{P}} (-1)^{\mathbf{P}} \mathbf{P}^\nu \otimes \mathbf{P}^\sigma \tag{2.2}$$

be the antisymmetrizer. Here $\mathbf{P}^\nu$ and $\mathbf{P}^\sigma$ are permutations on spin-free and spin spaces, respectively.

We denote the effective spin Hamiltonian with respect to the spin-free vector space V by the matrix $[\mathbf{H}_{\text{eff}}]^V$ with elements

$$\mathbf{H}_{\text{eff}}{}^{\nu\nu'} \equiv \langle \nu | \mathbf{H}\mathcal{A} | \nu' \rangle = \frac{1}{N!} \sum_{\mathbf{P}} (-1)^{\mathbf{P}} H_P{}^{\nu\nu'} \mathbf{P}^\sigma \tag{2.3}$$

where

$$H_P{}^{\nu\nu'} \equiv \langle \nu | \mathbf{H}\mathbf{P}^\nu | \nu' \rangle \tag{2.4}$$

Equation 2.3 is called the *effective spin permutation Hamiltonian.*

We choose for the vector space of the effective spin permutation Hamiltonian the following spin space

$$V(\sigma): \quad \{ |m(N)\rangle \ldots \} \tag{2.5}$$

where

$$|m(N)\rangle = |m_1\rangle |m_2\rangle \ldots |m_N\rangle \tag{2.6}$$

with

$$|m_i\rangle = \alpha, \beta \tag{2.7}$$

The dimension of $V(\sigma)$ is

$$f^\sigma = 2^N \tag{2.8}$$

We construct a representation of $\mathbf{H}_{\text{eff}}{}^{\nu\nu'}$ on V^σ as follows

$$\langle m(N) | \mathbf{H}_{\text{eff}}{}^{\nu\nu'} | m'(N) \rangle = \frac{1}{N!} \sum_{\mathbf{P}} (-1)^{\mathbf{P}} [P]^\sigma{}_{m(N)m'(N)} H_P{}^{\nu\nu'} \tag{2.9}$$

where

$$[P]^\sigma{}_{m(N)m'(N)} \equiv \langle m(N) | \mathbf{P}^\sigma | m'(N) \rangle \tag{2.10}$$

The eigenvectors and eigenvalues of $\mathbf{H}_{\text{eff}}{}^{\nu\nu'}$ in $V(\sigma)$ are determined by diagonalizing the representation (2.9). Since

$$[\mathbf{P}^\sigma, \mathbf{S}^2] = [\mathbf{P}^\sigma, \mathbf{S}_z] = 0, \ \mathbf{P}^\sigma \in \mathcal{S}_N{}^\sigma \tag{2.11}$$

the eigenkets to $\mathbf{H}_{\text{eff}}{}^{\nu\nu'}$ are automatically eigenkets to $\mathbf{S}^2$ and $\mathbf{S}_z$ with eigenvalues $S(S+1)$ and M, respec-

(3) (a) P. A. M. Dirac, *Proc. Roy. Soc. Ser. A*, **123**, 714 (1929); "The Principles of Quantum Mechanics," 4th ed, Oxford, 1958; (b) W. Heisenberg, *Z. Phys.*, **49**, 619 (1928).

(4) J. H. Van Vleck, *Phys. Rev.*, **45**, 405 (1934).

(5) (a) R. Serber, *ibid.*, **45**, 461 (1934); *J. Chem. Phys.*, **2**, 697 (1934); (b) C. Herring, *Magnetism*, **2B**, 1 (1963).

(6) (a) T. Arai, *Phys. Rev.*, **126**, 471 (1962); **134**, A824 (1964); (b) L. F. Mattheis, *ibid.*, **123**, 1219 (1961); (c) R. McWeeny and F. Yonezawa, *J. Chem. Phys.*, **43**, S120 (1965); (d) R. K. Nesbet, *Ann. Phys. (Leipzig)*, **4**, 87 (1958); *Phys. Rev.*, **119**, 658 (1960); (e) J. H. Van Vleck, *Mat. Fisica Teo.*, **14**, 189 (1961).

tively. The eigenkets are denoted

$$|SM\tilde{r}\rangle \equiv \sum_{m(N)} |m(N)\rangle\langle m(N)|SM\tilde{r}\rangle \qquad (2.12)$$

Here $\tilde{r}$ distinguishes among eigenkets with the same S and M. The eigenkets are simultaneously symmetry-adapted to $\mathcal{S}_N{}^\sigma$. Consequently we may write

$$|SM\tilde{r}\rangle \equiv |[\tilde{\lambda}]M\tilde{r}\rangle \qquad (2.13)$$

where

$$[\tilde{\lambda}] = [\mu] = [N - p,p] \qquad (2.14)$$

Symmetry-adapted kets transform under elements of $\mathcal{S}_N{}^\sigma$ as follows

$$\mathbf{P}^\sigma|[\tilde{\lambda}]M\tilde{s}\rangle = \sum_{\tilde{s}'}[P]_{\tilde{s}'\tilde{s}}{}^{[\tilde{\lambda}]}|[\tilde{\lambda}]M\tilde{s}'\rangle \qquad (2.15)$$

where $[P]_{\tilde{s}'\tilde{s}}{}^{[\tilde{\lambda}]}$ is the $(\tilde{s}',\tilde{s})$th element in the $f^{[\tilde{\lambda}]} \times f^{[\tilde{\lambda}]}$ matrix representing $\mathbf{P}$ in the $[\tilde{\lambda}]$th irreducible representation $\Gamma^{[\tilde{\lambda}]}$ of $\mathcal{S}_N$. The representation $\Gamma^{[\tilde{\lambda}]}$ conjugate to $\Gamma^{[\lambda]}$ is defined[7] as the Kronecker product of $\Gamma^{[\lambda]}$ and $\Gamma^{[1^N]}$

$$[P]_{\tilde{r}\tilde{s}}{}^{[\tilde{\lambda}]} \equiv (-1)^{\mathbf{P}}[P]_{rs}{}^{[\lambda]} \qquad (2.16)$$

Then the matrix elements of $\mathbf{H}_{\text{eff}}{}^{\nu\nu'}$ on a spin space symmetry-adapted to $\mathcal{S}_N{}^\sigma$ are by (2.16) above and (2.14) of ref 2a-IX

$$\langle[\tilde{\lambda}]M\tilde{s}|\mathbf{H}_{\text{eff}}{}^{\nu\nu'}|[\tilde{\lambda}']M'\tilde{s}'\rangle = \delta([\tilde{\lambda}],[\tilde{\lambda}'])\delta(M,M')\langle\nu s;[\lambda]||\mathbf{H}||\nu's';[\lambda]\rangle \qquad (2.17)$$

where

$$\langle\nu s;[\lambda]||\mathbf{H}||\nu's';[\lambda]\rangle = \sum_{\mathbf{P}}[P^{-1}]_{s's}{}^{[\lambda]}H_P{}^{\nu\nu'} \qquad (2.18)$$

Thus the effective spin permutation Hamiltonian (2.3) operating on a spin space with a basis symmetry-adapted to $\mathcal{S}_N{}^\sigma$ reproduces the spin-free result (eq 2.14 of ref 2a-IX) and is therefore an exact effective Hamiltonian.

An effective spin Hamiltonian is the Hamiltonian which results from replacing the spin permutations by spin operators. This is accomplished by means of the Dirac identity for the transpositions

$$(jk)^\sigma \doteq {}^1/_2\mathcal{I} + 2\vec{\mathbf{s}}_j\cdot\vec{\mathbf{s}}_k \qquad (2.19)$$

Since any permutation can be expressed as a product of transpositions we can replace any permutation by a product of spin operators

$$\begin{aligned}(jkl)^\sigma &= (jk)^\sigma(kl)^\sigma \\ &= {}^1/_4\mathcal{I} + \vec{\mathbf{s}}_j\cdot\vec{\mathbf{s}}_k + \vec{\mathbf{s}}_k\cdot\vec{\mathbf{s}}_l + 4(\vec{\mathbf{s}}_j\cdot\vec{\mathbf{s}}_k)(\vec{\mathbf{s}}_k\cdot\vec{\mathbf{s}}_l) \\ &= {}^1/_4\mathcal{I} + \vec{\mathbf{s}}_j\cdot\vec{\mathbf{s}}_k + \vec{\mathbf{s}}_k\cdot\vec{\mathbf{s}}_l + \vec{\mathbf{s}}_l\cdot\vec{\mathbf{s}}_j + 2i(\vec{\mathbf{s}}_j\cdot\vec{\mathbf{s}}_k \times \vec{\mathbf{s}}_l)\end{aligned} \qquad (2.20)$$

Generally

$$\mathbf{P}^\sigma \doteq \mathbf{P}^\sigma(\vec{\mathbf{s}}_j, \vec{\mathbf{s}}_k, \ldots) \qquad (2.21)$$

so

$$\mathbf{H}_{\text{eff}}{}^{\nu\nu'} = \sum_{\mathbf{P}}(-1)^{\mathbf{P}}H_P{}^{\nu\nu'}\mathbf{P}^\sigma(\vec{\mathbf{s}}_j, \vec{\mathbf{s}}_k, \ldots) \qquad (2.22)$$

Equation 2.22 will also yield the spin-free result (eq 2.14 of ref 2a-IX).

3. An Effective Spin Hamiltonian Appropriate to the Aggregate Theory of Polyelectronic Systems

The aggregate theory of a polyelectronic system[2a-IX] is based on the following decomposition of the spin-free Hamiltonian

$$\mathbf{H} + \mathbf{H}^0 + \mathbf{H}' \qquad (3.1)$$

The zero-order Hamiltonian is

$$\mathbf{H}^0 = \mathbf{H}_A + \mathbf{H}_B + \mathbf{H}_C + \ldots \qquad (3.2)$$

where $\mathbf{H}_A$, $\mathbf{H}_B$, $\mathbf{H}_C$, etc. are the Hamiltonians for a set $\{A, B, C, \ldots\}$ of noninteracting aggregates. We assign electron numbers $1 \rightarrow N_A$ to aggregate A, $N_A + 1 \rightarrow N_A + N_B$ to aggregate B, etc., where

$$N_A + N_B + N_C + \ldots = N \qquad (3.3)$$

The group of $\mathbf{H}^0$ is

$$\mathcal{S}_\nu{}^0 \equiv \mathcal{S}_A{}^\nu \otimes \mathcal{S}_B{}^\nu \otimes \mathcal{S}_C{}^\nu \otimes \ldots \subset \mathcal{S}_N{}^\nu \qquad (3.4)$$

where $\mathcal{S}_A{}^\nu$, $\mathcal{S}_B{}^\nu$, $\mathcal{S}_C{}^\nu$ are symmetric groups on N_A, N_B, N_C, etc. electrons. The order of $\mathcal{S}_\nu{}^0$ is

$$N^0 = N_A!N_B!N_C!\ldots \qquad (3.5)$$

The eigenkets to $\mathbf{H}^0$ are the products of the eigenkets of the several aggregates and are denoted

$$|\gamma^0 r^0\rangle \equiv |\nu_A K_A;[\lambda_A]r_A\rangle|\nu_B K_B;[\lambda_B]r_B\rangle\ldots \qquad (3.6)$$

We construct a vector space for the full Hamiltonian by induction with $\mathcal{S}_N$ on the zero-order kets. Thus

$$V = \sum_{\gamma^0} \oplus V(\gamma^0\uparrow) \qquad (3.7)$$

where

$$V(\gamma^0\uparrow): \quad \{|\gamma^0 r^0 i\rangle,\ i = 1 \text{ to } N!/N^0$$

and

$$r^0 = 1 \text{ to } f^{[\lambda]^0} \equiv f^{[\lambda_A]}f^{[\lambda_B]}\ldots\} \qquad (3.8)$$

with

$$|\gamma^0 r^0 i\rangle = \mathbf{P}_i|\gamma^0 r^0\rangle \qquad (3.9)$$

Here $\mathbf{P}_i$ is the left coset multiplier for the ith left coset of $\mathcal{S}_N$ with respect to $\mathcal{S}^0$. The dimension of $V(\gamma^0\uparrow)$ is

$$f^{[\lambda]^{0\dagger}} = N!f^{[\lambda]^0}/N^0 \qquad (3.10)$$

We next construct (see Appendix I) an antisym-

(7) It is easy to show that: (1) if $\Gamma^{[\lambda]}$ is sequence adapted,[2a-IX] then so is $\Gamma^{[\tilde{\lambda}]}$; (2) if $[P]_{rs}{}^{[\lambda]}$ is in the Young–Yamanouchi representation, then $[P]_{\tilde{r}\tilde{s}}{}^{[\tilde{\lambda}]}$ is related to the conjugate Young–Yamanouchi representation through the unitary transformation $[U]_{\tilde{r}\tilde{s}}{}^{[\tilde{\lambda}]} = \delta_{rs}(-1)^{\tilde{r}}$ where $(-1)^{\tilde{r}}$ is $+1$ or -1 as the permutation σ_{r1} from the standard Young tableau $T_1{}^{[\lambda]}$ to $T_r{}^{[\lambda]}$ is even or odd.

metrizer appropriate to the aggregate theory

$$\mathcal{A} = \frac{N^0}{N!}\sum_q l_q(-1)^{\mathbf{G}_q}\,\mathcal{A}^0(\mathbf{G}_q^{\nu}\otimes\mathbf{G}_q^{\sigma})\mathcal{A}^0 \qquad (3.11)$$

where

$$\mathcal{A}^0 = \sum_{[\lambda]^0}\frac{1}{f^{[\lambda]^0}}\sum_{t^0}\sum_{\tau^0}\mathbf{e}_{t^0\tau^0}^{[\lambda]^0}\otimes\mathbf{e}_{\tilde{t}^0\tilde{\tau}^0}^{[\tilde{\lambda}]^0} \qquad (3.12)$$

(the tilde designates the conjugate matric basis element) and $\mathbf{G}_q^{\nu}\otimes\mathbf{G}_q^{\sigma}$ is a double coset generator for $\mathcal{S}_N^{\nu}\otimes\mathcal{S}_N^{\sigma}$ with respect to the subgroup $\mathcal{S}_{\nu}^0\otimes\mathcal{S}_{\sigma}^0$.

The effective spin permutation Hamiltonian appropriate to aggregate theory is then

$$\mathbf{H}_{\tau^0\tau'^0}^{\gamma^0\gamma'^0} = \langle\gamma^0\tau^0|\mathbf{H}\mathcal{A}|\gamma'^0\tau'^0\rangle$$
$$= \frac{N^0}{N!f^{[\lambda]^0}f^{[\lambda']^0}}\sum_q(-1)^{\mathbf{G}_q}l_q\times \qquad (3.13)$$
$$\sum_{t^0}\sum_{t'^0}\langle\gamma^0t^0|\mathbf{H}\mathbf{G}_q^{\nu}|\gamma'^0t'^0\rangle\mathbf{e}_{\tau^0\tilde{t}^0}^{[\tilde{\lambda}]^0}\mathbf{G}_q^{\sigma}\mathbf{e}_{\tilde{t}'^0\tilde{\tau}'^0}^{[\tilde{\lambda}']^0}$$

A matrix element for $\mathbf{H}_{\tau^0\tau'^0}^{\gamma^0\gamma'^0}$ on a spin basis which is symmetry-adapted to the sequence $\mathcal{S}^0\subset\mathcal{S}_N$ is

$$\langle\gamma^0;[\tilde{\lambda}]M(\rho[\tilde{\lambda}]^0\tilde{r}^0)|\mathbf{H}_{\tau^0\tau'^0}^{\gamma^0\gamma'^0}|\gamma'^0;[\tilde{\lambda}']M'(\rho'[\tilde{\lambda}']^0\tilde{r}'^0)\rangle =$$
$$\delta([\lambda],[\lambda'])\delta(M,M')\langle\gamma^0(\rho[\lambda]^0);$$
$$[\lambda]||\mathbf{H}||\gamma'^0(\rho'[\lambda']^0);[\lambda]\rangle \qquad (3.14)$$

where

$$\langle\gamma^0(\rho[\lambda]^0);[\lambda]||\mathbf{H}||\gamma'^0(\rho'[\lambda']^0);[\lambda]\rangle =$$
$$\sum_q l_q\sum_{t^0,t'^0}[G_q^{-1}]^{[\lambda]}_{(\rho'[\lambda']^0t'^0)(\rho[\lambda]^0t^0)}\langle\gamma^0t^0|\mathbf{H}\mathbf{G}_q|\gamma'^0t'^0\rangle \qquad (3.15)$$

Thus the aggregate effective spin permutation Hamiltonian operating on a spin space with a basis sequence-adapted to $\mathcal{S}^0\subset\mathcal{S}_N$ reproduces the spin-free result (eq 4.6 of ref 2a-IX) and is therefore an exact effective spin permutation Hamiltonian.[8]

Types of exchange are frequently classified in terms of "n-arrow diagrams" which represent various combinations of electron interchanges among aggregates (atoms). In the evaluation of matrix elements the summation over permutations can then be replaced by a summation over "diagrams," due to the antisymmetry of the wave function under coordinate-spin permutations of $\mathcal{S}^0$.[5b] The technique of double coset decomposition provides a rigorous mathematical justification of this procedure in the spin-free formalism, reducing the sum over permutations to a sum over double coset generators. The double coset generators (except for the identity) can be chosen so that they permute electrons only among aggregates.[2a-IX] If we construct an arrow diagram corresponding to the mapping indicated by each double coset symbol, as defined by Matsen and Klein,[2a-IX] we obtain a one-to-one correspondence between double coset generators and arrow diagrams. For example, the double coset generators (ABC), (ACB), and $(AB)(BC)$ correspond, respectively, to the diagrams shown below.

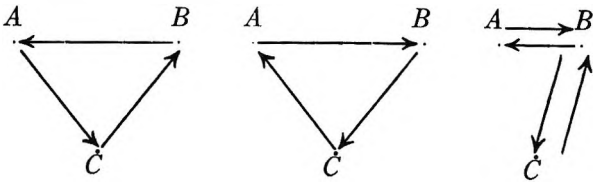

Kramer and Seligman[9] and Matsen and Klein[2a-IX] have given procedures for obtaining double coset generators and the number of members of each double coset for the case of two aggregates. The techniques of Kramer and Seligman also include the case $\mathcal{S}^0\neq\mathcal{S}'^0$ and are easily generalized for any number of aggregates. Thus the formulation in terms of double coset generators facilitates the construction of generalized arrow diagrams that include charge transfer as well as exchange. This may be accomplished as follows. If $d_{AB}{}^q$ is the (AB)th element of the double coset symbol[9] for $\mathbf{G}_q$, draw $d_{AB}{}^q$ arrows from A to B. For example, if $\mathcal{S}^0 = \mathcal{S}_2\otimes\mathcal{S}_2$ and $\mathcal{S}'^0 = \mathcal{S}_1\otimes\mathcal{S}_3$, the double coset symbols are

$$\mathbf{G}_0 = \begin{Bmatrix}1 & 0\\ 1 & 2\end{Bmatrix} \text{ and } \mathbf{G}_1 = \begin{Bmatrix}0 & 1\\ 2 & 1\end{Bmatrix}$$

and the corresponding arrow diagrams are

$$A\cdot\longleftarrow\cdot B \text{ and } A\cdot\rightleftarrows\cdot B$$

We convert (3.13) to an effective spin Hamiltonian by means of the Dirac identity as in section 2

$$\mathbf{G}_q \doteq \mathbf{G}_q(\vec{\mathbf{s}}_a, \vec{\mathbf{s}}_b, \ldots) \qquad (3.16)$$

The Wigner–Eckart theorem enables us to construct an effective spin Hamiltonian which employs only the aggregate operators

$$\vec{\mathbf{S}}_A = \sum_a\vec{\mathbf{s}}_a \qquad (3.17)$$

where $\vec{\mathbf{s}}_a$ is the spin operator for electron a on the Ath aggregate. Following Herring,[5b] we note that $\vec{\mathbf{s}}_a$ and $\vec{\mathbf{S}}_A$ are both tensors of rank one in the spin space of aggregate A, to that for $S_A = S_A'$

$$\langle S_AM_A\tilde{l}_A|\vec{\mathbf{s}}_a|S_AM_A'\tilde{l}_A'\rangle =$$
$$f_A(S_A;\tilde{l}_A\tilde{l}_A')\langle S_AM_A\tilde{r}_A|\vec{\mathbf{S}}_A|S_AM_A'\tilde{r}_A\rangle \qquad (3.18)$$

where

$$f_A(S_A;\tilde{l}_A\tilde{l}_A') = \frac{\langle S_A\tilde{l}_A||\vec{\mathbf{s}}_a||S_A\tilde{l}_A'\rangle}{\langle S_A\tilde{r}_A||\vec{\mathbf{S}}_A||S_A\tilde{r}_A\rangle} \qquad (3.19)$$

is independent of $\tilde{r}_A$. We define $f_A(S_A;\tilde{l}_A,\tilde{l}_A') \equiv 0$ whenever $\langle S_A\tilde{l}_A||\vec{\mathbf{s}}_a||S_A\tilde{l}_A'\rangle$ is zero, so that, for example, $f_A(0;\tilde{l}_A,\tilde{l}_A') \equiv 0$.

For a pair of spin kets with aggregate quantum numbers S_A and S_B, we replace the spin permutation

(8) For a detailed discussion of sequence adaptation, see D. J. Klein, C. H. Carlisle, and F. A. Matsen, *Advan. Quantum Chem.*, **5**, 219 (1970).

(9) P. Kramer and T. H. Seligman, *Nucl. Phys. A*, **136**, 545 (1969).

operators in (3.13) by spin operators as follows

$$(ab)^{\sigma} \doteq {}^1/_2\mathcal{J} + 2\vec{\mathbf{s}}_a \cdot \vec{\mathbf{s}}_b \tag{3.20}$$

and

$$\mathbf{e}_{\tilde{\gamma}^0\tilde{\imath}^0}{}^{[\tilde{\lambda}]^0}(ab)^{\sigma}\mathbf{e}_{\tilde{\imath}^0\tilde{\gamma}'^0}{}^{[\tilde{\lambda}]^0} \doteq$$

$$\{{}^1/_2\mathcal{J} + f_A(S_A;\tilde{\imath}_A\tilde{\imath}_A')f_B(S_B;\tilde{\imath}_B,\tilde{\imath}_B')\vec{\mathbf{S}}_A \cdot \vec{\mathbf{S}}_B\}\mathbf{e}_{\tilde{\gamma}^0\tilde{\gamma}'^0}{}^{[\tilde{\lambda}]^0} \tag{3.21}$$

Now if $\mathbf{G}_q$ has an arrow diagram in which no more than one arrow comes into any given vertex, we make the substitution

$$\mathbf{e}_{\tilde{\gamma}^0\tilde{\imath}^0}{}^{[\tilde{\lambda}]^0}\mathbf{G}_q{}^{\sigma}(\vec{\mathbf{s}}_a, \vec{\mathbf{s}}_b, \ldots)\mathbf{e}_{\tilde{\imath}^0\tilde{\gamma}'^0}{}^{[\tilde{\lambda}]^0} \doteq$$

$$\mathbf{G}_q{}^{\sigma}(f_A(S_A;\tilde{\imath}_A,\tilde{\imath}_A')\vec{\mathbf{S}}_A, f_B(S_B;\tilde{\imath}_B,\tilde{\imath}_B')\vec{\mathbf{S}}_B, \ldots)\mathbf{e}_{\tilde{\gamma}^0\tilde{\gamma}'^0}{}^{[\tilde{\lambda}]^0} \tag{3.22}$$

We note that this use of aggregate spin operators excludes the treatment of configuration interaction among states of different $[\lambda]^0$.

There are a number of terms from different $\mathbf{G}_q{}^{\sigma}$ that will cancel. For instance, if the $\{\mathbf{G}_q{}^{\sigma}\}$ are the canonical double coset generators of Matsen and Klein,[2a-IX] and if $\mathbf{G}_q{}^{\sigma}$ is not Hermitian, then its Hermitian adjoint $\mathbf{G}_{\bar{q}}{}^{\sigma} \equiv (\mathbf{G}_q{}^{\sigma})^{\dagger}$ is also a double coset generator for a different double coset. Then $\mathbf{G}_q{}^{\sigma}$ and $\mathbf{G}_{\bar{q}}{}^{\sigma}$ will have the same coefficient in the effective Hamiltonian. Thus for $\mathbf{G}_q{}^{\sigma} = (abc)^{\sigma}$ and $\mathbf{G}_{\bar{q}}{}^{\sigma} = (acb)^{\sigma}$, for example, the terms $2i\vec{\mathbf{s}}_a \cdot (\vec{\mathbf{s}}_b \times \vec{\mathbf{s}}_c)$ and $2i\vec{\mathbf{s}}_a \cdot (\vec{\mathbf{s}}_c \times \vec{\mathbf{s}}_b)$ from eq 2.20 will cancel. The vanishing of cubic terms has been pointed out by Herring.[5b] In general, one can show that terms of an odd power in spin operators will vanish. This argument is usually made on the basis of time reversal symmetry of the spin-free Hamiltonian.[5b] In Appendix 2 we present a proof that does not depend on time reversal symmetry.

In general for $[\lambda]^0 = [\lambda']^0$ we can replace the individual spin operators in $\mathbf{G}_q{}^{\sigma}$ by spin operators for the aggregates by coupling individual spin operators within the same aggregate to irreducible tensorial form and then using the Wigner–Eckart theorem as above. We expect the resulting effective spin Hamiltonian to be in terms of dot products of aggregate spin operators

$$\mathbf{H}_{\gamma^0\gamma'^0}{}^{\gamma^0\gamma'^0} = \sum_{x,y,z,\ldots} \mathbf{J}_{xyz\ldots}(\vec{\mathbf{S}}_A \cdot \vec{\mathbf{S}}_B)^x(\vec{\mathbf{S}}_A \cdot \vec{\mathbf{S}}_C)^y(\vec{\mathbf{S}}_B \cdot \vec{\mathbf{S}}_C)^z \ldots \tag{3.23}$$

where

$$\mathbf{J}_{xyz\ldots} = \frac{N^0}{N!f^{[\lambda]^0}f^{[\lambda']^0}} \sum_q (-1)^{\mathbf{G}_q} l_q \sum_{t^0,t'^0} \langle \gamma^0 t^0 | \mathbf{H}\mathbf{G}_q{}^{\nu} | \gamma'^0 t'^0 \rangle \times B^q{}_{xyz\ldots}\mathbf{e}_{\tilde{\imath}^0\tilde{\gamma}'^0}{}^{[\tilde{\lambda}]^0} \tag{3.24}$$

Here $B^q{}_{xyz\ldots}$ is a numerical coefficient determined by the appropriate replacements.

Those terms in (3.23) with a single exponent equal to unity and the remainder equal to zero are called *spin single exchange* terms. Otherwise the term is called a *spin multiple exchange* term. The word *spin* distinguishes this classification from that of ref 2a-IX, which is in terms of double coset generators.

In general, the problems for which an effective spin Hamiltonian is used employ a nonorthogonal basis, and the overlap matrix must also be included. In analogy to (3.13), the overlap matrix is to be expanded in terms of double coset generators to give

$$\mathcal{J}_{\gamma^0\gamma'^0}{}^{\gamma^0\gamma'^0} \equiv \langle \gamma^0 t^0 | \mathfrak{A} | \gamma'^0 t'^0 \rangle = \frac{N^0}{N!f^{[\lambda]^0}f^{[\lambda']^0}} \sum_q (-1)^{\mathbf{G}_q} l_q \sum_{t^0,t'^0} \langle \gamma^0 t^0 | \mathbf{G}_q{}^{\nu} | \gamma'^0 t'^0 \rangle \times \mathbf{e}_{\tilde{\imath}^0\tilde{\imath}^0}{}^{[\tilde{\lambda}]^0}\mathbf{G}_q{}^{\sigma}\mathbf{e}_{\tilde{\imath}'^0\tilde{\gamma}'^0}{}^{[\tilde{\lambda}']^0} \tag{3.25}$$

The substitution of aggregate spin operators for the case $[\lambda]^0 = [\lambda']^0$ may then be carried out as described above, and we obtain

$$\mathcal{J}_{\gamma^0\gamma'^0}{}^{\gamma^0\gamma'^0} = \sum_{x,y,z,\ldots} \mathbf{J}'_{xyz\ldots}(\vec{\mathbf{S}}_A \cdot \vec{\mathbf{S}}_B)^x(\vec{\mathbf{S}}_A \cdot \vec{\mathbf{S}}_C)^y(\vec{\mathbf{S}}_B \cdot \vec{\mathbf{S}}_C)^z \ldots \tag{3.26}$$

where

$$\mathbf{J}'_{xyz\ldots} = \frac{N^0}{N!f^{[\lambda]^0}f^{[\lambda']^0}} \sum_q (-1)^{\mathbf{G}_q} l_q \sum_{t^0,t'^0} \langle \gamma^0 t^0 | \mathbf{G}_q{}^{\nu} | \gamma'^0 t'^0 \rangle \times B^q{}_{xyz\ldots}\mathbf{e}_{\tilde{\imath}^0\tilde{\gamma}'^0}{}^{[\tilde{\lambda}]^0} \tag{3.27}$$

4. Approximate Effective Spin Hamiltonians

We have developed a rigorous coarse structure effective spin Hamiltonian, which yields a representation of its parent spin-free Hamiltonian which is completely equilvalent to that obtained in the spin-free formulation. Our Hamiltonian may also be expressed in terms of irreducible tensorial operators with respect to the zero-order group. This is the same procedure that is followed in constructing effective Hamiltonians in a wide variety of fields in which a small perturbation is applied to a zero-order Hamiltonian, including the following: esr, nmr, atomic shell theory, nuclear shell theory, crystal field theory, and elementary particle theory. In all these theories, the coefficients of the irreducible tensorial operators which appear may in principle be evaluated from *ab initio* calculations, though in practice this is often difficult and these coefficients are treated as parameters to be determined empirically.

In our present case, the rigorous coarse structure effective spin Hamiltonian is never used since both the spin formulation and the spin-free formulation are more convenient. However, for systems of more than a few electrons, the number of parameters in all these formulations becomes larger than can reasonably be evaluated, even in an empirical manner. At this point the effective spin Hamiltonian formulation has the advantage that on physical reasoning we can argue: first, that some of its parameters may be the same, because of translational and/or point group symmetry; and second, that some of its parameters will be small, particularly in the case of widely separated aggregates.[5b]

In this connection, several types of approximations are frequently considered: (A) the neglect of configuration interaction (CI) between states with $S^0 \neq S'^0$; (B) the neglect of CI between states with $[\lambda]^0 \neq [\lambda']^0$; (C) the neglect of all CI; (D) the neglect of multiple interaggregate spin exchange terms; (E) the neglect of nonnearest neighbor exchange terms.

Approximations (C) and (D) yield the Heisenberg spin Hamiltonian

$$\mathbf{H}_{\text{Heis}} = -2 \sum_{A<B} J_{AB} \vec{\mathbf{S}}_A \cdot \vec{\mathbf{S}}_B \tag{4.1}$$

Here the scalar (identity) term in (3.23) has been transferred to the left side of the equation. A number of the J_{AB} may be rigorously identical if there is translational and/or point group symmetry present. Assumption (E) is often added

$$\mathbf{H}'_{\text{Heis}} = -2 \sum_{\substack{\text{nearest} \\ \text{neighbors}}} J_{AB} \vec{\mathbf{S}}_A \cdot \vec{\mathbf{S}}_B \tag{4.2}$$

Since $\mathbf{H}_{\text{Heis}}$ and $\mathbf{H}'_{\text{Heis}}$ are contained in the group algebra of $\mathcal{S}_N{}^{\sigma}$, their eigenkets may be symmetry-adapted to the centrum of $\mathcal{S}_N{}^{\sigma}$; and since $\mathbf{S}^2$ is contained in the centrum of $\mathcal{S}_N{}^{\sigma}$, the eigenkets of $\mathbf{H}_{\text{Heis}}$ and $\mathbf{H}'_{\text{Heis}}$ are symmetry-adapted to $\mathbf{S}^2$.

The basis in use is, in general, nonorthogonal, and we must show that (4.1) is still valid to the level of its approximations when the effects of nonorthogonality are included. Under assumptions (C) and (D) above, eq 3.23 and 3.27 become

$$\mathbf{H}_{\tau^0\tau^0}{}^{\gamma^0\gamma^0} \cong \mathcal{J}_g + \sum_{A<B} \mathcal{J}_{AB} \vec{\mathbf{S}}_A \cdot \vec{\mathbf{S}}_B \mathbf{e}_{\bar{\tau}^0\bar{\tau}^0}{}^{[\tilde{\lambda}]^0} \tag{4.3}$$

and

$$\mathcal{J}_{\tau^0\tau^0}{}^{\gamma^0\gamma^0} \cong \mathcal{J}_g' + \sum_{A<B} \mathcal{J}'_{AB} \vec{\mathbf{S}}_A \cdot \vec{\mathbf{S}}_B \mathbf{e}_{\bar{\tau}^0\bar{\tau}^0}{}^{[\tilde{\lambda}]^0} \tag{4.4}$$

The spin eigenvalue problem to be solved is

$$\mathbf{H}_{\tau^0\tau^0}{}^{\gamma^0\gamma^0} |n\rangle = E_n \mathcal{J}_{\tau^0\tau^0}{}^{\gamma^0\gamma^0} |n\rangle \tag{4.5}$$

where $|n\rangle$ is a spin ket. This can be rearranged to the more familiar type of equation

$$\mathbf{H}_{\text{eff}} |n'\rangle = E_n |n'\rangle \tag{4.6}$$

by the method of Löwdin and Carr[10] as follows

$$\frac{\langle n|\mathbf{H}_{\tau^0\tau^0}{}^{\gamma^0\gamma^0}|n\rangle}{\langle n|\mathcal{J}_{\tau^0\tau^0}{}^{\gamma^0\gamma^0}|n\rangle} \cong \frac{\mathcal{J}_g}{\mathcal{J}_g'} + \sum_{A<B} \frac{\mathcal{J}_{AB}}{\mathcal{J}_g'} \vec{\mathbf{S}}_A \cdot \vec{\mathbf{S}}_B - \mathcal{J}_g \sum_{A<B} \mathcal{J}'_{AB} \vec{\mathbf{S}}_A \cdot \vec{\mathbf{S}}_B + \text{higher order terms} \tag{4.7}$$

Here we have used the general type of expansion $1/(1+\delta) = 1 - \delta + \delta^2 - \delta^3 - \ldots$ valid for small δ. Thus through single exchange

$$\mathbf{H}_{\text{eff}} = J_g + \sum_{A<B} J_{AB} \vec{\mathbf{S}}_A \cdot \vec{\mathbf{S}}_B \tag{4.8}$$

with

$$J_g = \frac{\mathcal{J}_g}{\mathcal{J}_g'} \tag{4.9}$$

and

$$J_{AB} = \frac{\mathcal{J}_{AB}}{\mathcal{J}_g'} - \mathcal{J}_g \mathcal{J}'_{AB} \tag{4.10}$$

We have assumed that (4.7) acts only on the spin space of local symmetry $[\tilde{\lambda}]^0 \neq^0$ and that its solutions in spaces of other local permutational symmetries are meaningless.

To illustrate explicitly the relative validity of the Heisenberg spin Hamiltonian in actual *ab initio* calculations and in real physical systems we consider two examples. The first is the case of two metastable triplet helium atoms. The singlet, triplet, and quintet molecular states have been calculated[11] for a simple 1-term wave function without neglecting higher double coset generators. The least-squares fits of these *ab initio* calculations to

$$\mathbf{H}_{\text{eff}} = \mathcal{E}_0 + J \vec{\mathbf{S}}_A \cdot \vec{\mathbf{S}}_B \tag{4.11}$$

are shown in Figure 1. It is seen that the validity of (4.11) increases with internuclear separation, as expected, since the approximation (D) which was made in this fit becomes better the less differential overlap there is between atoms A and B. The second case we consider consists of two ground-state chromium ions, $Cr^{+3}(d^3,{}^4A_2)$, in a ruby crystal: the singlet, triplet, quintet, and septet states for the pair have been determined experimentally[12] by measuring the temperature dependence of the "spin-forbidden" $^4A_2 \rightarrow {}^2E$ transitions for Cr^{3+} ions in the 2nd, 3rd, and 4th nearest neighbor positions. The least-squares fits of these experimental results to the Heisenberg Hamiltonian are illustrated in Figure 2. The validity of (4.9) in this case apparently presumes approximations (A), (B), (C), and (D); yet it is still seen to yield a fair approximation to the states for the pair of ions.

The Heisenberg effective spin Hamiltonian is widely used in theories of magnetism. In these developments several facts are often overlooked. (1) It provides at best a faithful representation of a spin-free Hamiltonian. In particular, the effects of spin-orbit interaction are not included. (2) It frequently provides only a very approximate representation of the spin-free problem, especially in the case of small and moderate internuclear distances. (3) The coupling constants are empirical spin-free parameters which in approximate theory must account for the neglect of

(10) W. J. Carr, *Phys. Rev.*, 92, 28 (1953); *cf.* P. O. Löwdin, *J. Chem. Phys.*, 18, 365 (1950).

(11) D. J. Klein, *ibid.*, 50, 5150 (1969).

(12) P. Kisliuk, N. C. Chang, P. L. Scott, and M. H. L. Pryce, *Phys. Rev.*, 184, 367 (1969).

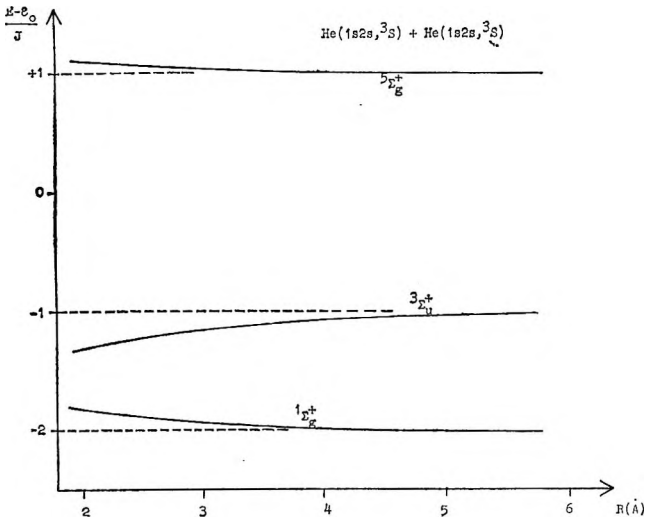

Figure 1. The results of a least-squares fit of the *ab initio* levels to the Heisenberg Hamiltonian for the case of two He(1s2s,^{3}S) atoms.

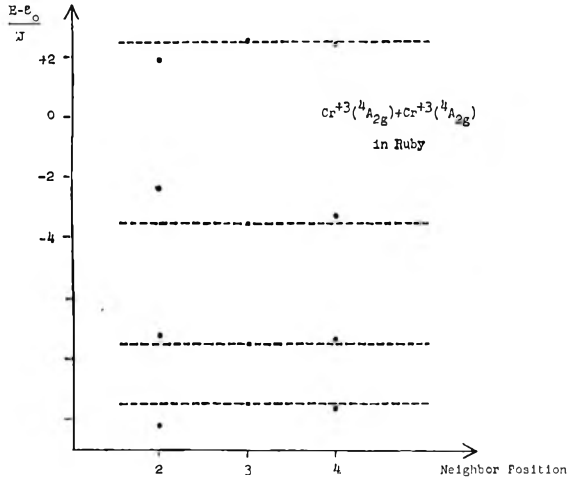

Figure 2. The results of a least-squares fit of the experimental levels to the Heisenberg Hamiltonian for the case of two $Cr^{3+}(d^3,{}^4A_2)$ ions.

configuration interaction, multiple exchange, and nonnearest neighbor exchange. (4) The spin terms $\vec{S}_A \cdot \vec{S}_B$ arise from the antisymmetrizer, which was introduced to satisfy the Pauli principle. Thus they do not represent interaction between magnetic dipoles.

In spite of the limitations of $\mathbf{H}_{\text{Heis}}$, there are many problems for which the use of more rigorous Hamiltonians is not practical. Exact solutions to $\mathbf{H}_{\text{Heis}}$ are relatively easy to obtain for the ferromagnetic end of its spectrum, and exact solutions for some of its low-lying antiferromagnetic states in the one-dimensional case are also available.[13] In the general case, however, exact solutions for a large number of aggregates are much more difficult. Furthermore, one would like to obtain not only the energy level spectrum, but also the partition function, $e^{-\beta \mathbf{H}_{\text{Heis}}}$, so that the associated thermodynamic properties can be calculated. Consequently, a number of methods of obtaining approximate solutions to $\mathbf{H}_{\text{Heis}}$ have been developed, including the following: (1) Weiss molecular field approximation for a single atom;[14] the interaction of atom A with the effective field is given as

$$\mathbf{H}_A = \sum_{B=1}^{z} J_{AB} \vec{\mathbf{S}}_A \cdot \langle \vec{S}_B \rangle_{\text{SCF}} \qquad (4.12)$$

(2) Weiss molecular field approximation for a cluster of atoms;[14] (3) Hartree–Fock[15] and extended Hartree–Fock[16] solutions in terms of Fermion operators for the 1-dimensional case; (4) solutions using Boson operator approximations;[17,18] (5) numerical methods of extrapolation;[19] (6) Green's functions methods;[20] (7) miscellaneous perturbation methods.[21] These different methods of obtaining approximate solutions often have different strengths or weaknesses depending on the characteristics of the case of interest: the value of the local spins S_A, S_B, ...; whether the J_{AB} are such that the lowest-lying solution is ferromagnetic, antiferromagnetic, ferrimagnetic,...; the type of translational and/or point group symmetry present; the dimension of the crystal; etc. We note that making matrix transformations may mix different configurations, allowing ionic states to contribute to the effective J_{AB} integral,[6b,d] and that such contributions are of particular importance in obtaining the correct sign for J_{AB} when orthogonal orbitals are employed.

5. Summary

Employing the spin-free formulation, we have constructed an exact coarse structure effective spin permutation Hamiltonian which reproduces the spin-free result when diagonalized in an appropriate spin space. Substitution by means of the Dirac identity led to an equivalent Hamiltonian in terms of electron spin operators. The technique of double coset decomposition was then introduced, reducing the effective spin permutation Hamiltonian to an expression involving only interaggregate permutations and the identity. This facilitated the identification of unique exchange types, and the double coset generators were found to lie in one-to-one correspondence with n-arrow exchange diagrams. The double coset generators were replaced by

(13) H. Bethe, *Z. Phys.*, **71**, 205 (1931); L. Hulthén, *Ark. Mat. Astron. Fys.*, **26A**, No. 11 (1938); J. des Cloizeaux and J. J. Pearson, *Phys. Rev.*, **128**, 2131 (1962).

(14) J. S. Smart, "Effective Field Theories of Magnetism," W. B. Saunders, Philadelphia, 1966.

(15) S. Rodriguez, *Phys. Rev.*, **116**, 1474 (1969).

(16) T. W. Ruijgrok and S. Rodriguez, *ibid.*, **119**, 596 (1960). Z. G. Soos, *J. Chem. Phys.*, **43**, 1121 (1965).

(17) T. Holstein and H. Primakoff, *Phys. Rev.*, **58**, 1098 (1940).

(18) F. Dyson, *ibid.*, **102**, 1217, 1230 (1956).

(19) J. C. Bonner and M. E. Fischer, *ibid.*, **135**, A640 (1964).

(20) H. B. Callen, *ibid.*, **130**, 890 (1963); T. Morita and T. Tanaka, *ibid.*, **137**, A648 (1965); **138**, A1395 (1965).

(21) H. L. Davis, *ibid.*, **120**, 789 (1960); R. L. Mills, R. P. Kenon, and J. Korringa, *Physica*, **26**, S204 (1960).

electron spin operators, and these in turn were replaced by aggregate spin operators. The resulting exact coarse structure effective Hamiltonian was reduced by successive approximations to yield several approximate Hamiltonians, containing empirical parameters, which are commonly used in theories of magnetism. The assumptions involved in these Hamiltonians were analyzed, and their limitations were discussed.

Acknowledgments. D. J. Klein acknowledges support from an AFOSR-NRC fellowship and helpful discussions with Professor Z. G. Soos.

Appendix 1. Double Coset Decomposition of the Antisymmetrizer

We derive eq 3.11 and 3.12 now. The antisymmetrizer is

$$\mathcal{A} = \frac{1}{N!}\sum_{\mathbf{P}\in\mathcal{S}_N}(-1)^{\mathbf{P}}\mathbf{P}\otimes\mathbf{P} \tag{A1.1}$$

For every $\mathbf{P}\in\mathcal{S}_N$ there are d_q pairs $\mathbf{P}^0, \mathbf{P}'^0 \in \mathcal{S}^0$ such that

$$\mathbf{P} = \mathbf{P}^0\mathbf{G}_q\mathbf{P}'^0 \tag{A1.2}$$

Thus

$$\mathcal{A} = \frac{1}{N!}\sum_{\mathbf{P}^0,\mathbf{P}'^0\in\mathcal{S}^0}\sum_q(-1)^{\mathbf{P}^0\mathbf{G}_q\mathbf{P}'^0}d_q{}^{-1}\mathbf{P}^0\mathbf{G}_q\mathbf{P}'^0\otimes \mathbf{P}^0\mathbf{G}_q\mathbf{P}'^0 \tag{A1.3}$$

and employing the relation

$$\mathcal{A}^0 = \frac{1}{N^0}\sum_{\mathbf{P}^0}(-1)^{\mathbf{P}^0}\mathbf{P}^{0\nu}\otimes\mathbf{P}^{0\sigma} \tag{A1.4}$$

yields the desired eq 3.11.

To derive (3.12), we substitute the relation

$$\mathbf{P}^0 = \sum_{[\lambda]^0,r^0,s^0}[P^0]_{r^0s^0}{}^{[\lambda]^0}\mathbf{e}_{r^0s^0}{}^{[\lambda]^0} \tag{A1.5}$$

into (A1.4) to obtain

$$\mathcal{A}^0 = \frac{1}{N^0}\sum_{\mathbf{P}^0}(-1)^{\mathbf{P}^0}\sum_{[\lambda]^0,r^0,s^0}\sum_{[\tilde{\lambda}']^0,\tilde{r}'^0,\tilde{s}'^0}\times [P^0]_{r^0s^0}{}^{[\lambda]^0}[P^0]_{\tilde{r}'^0\tilde{s}'^0}{}^{[\tilde{\lambda}']^0}\mathbf{e}_{r^0s^0}{}^{[\lambda]^0\nu}\otimes\mathbf{e}_{\tilde{r}'^0\tilde{s}'^0}{}^{[\tilde{\lambda}']^0\sigma} \tag{A1.6}$$

Application of eq 2.16 and the orthogonality relation

$$\sum_{\mathbf{P}^0}[P^0]_{r^0s^0}{}^{[\lambda]^0}[(P^0)^{-1}]_{s'^0r'^0}{}^{[\lambda']^0} = \frac{N^0}{f^{[\lambda]^0}}\delta([\lambda]^0,[\lambda']^0)\delta(r^0,r'^0)\delta(s^0,s'^0) \tag{A1.7}$$

yields eq 3.12.

Appendix 2. Nonoccurrence of "Odd" Powers

We shall show that when $\mathbf{G}_q{}^\sigma$ and $\mathbf{G}_{\tilde{q}}{}^\sigma$ are expressed as a linear combination of products of $\vec{\mathbf{s}}$ operators for individual electrons, then $\mathbf{G}_q{}^\sigma + \mathbf{G}_{\tilde{q}}{}^\sigma$ contains *no* terms of odd powers in the $\vec{\mathbf{s}}$ operators. In general $\mathbf{G}_q{}^\sigma$ will be a product of disjoint cycles. Let us consider one of these cycles, say $(abcd\ldots)^\sigma$. Then we write

$$(abcd\ldots)^\sigma = (ab)^\sigma(bc)^\sigma(cd)^\sigma\ldots \tag{A2.1}$$

$$= (\tfrac{1}{2}\mathcal{I} + 2\vec{\mathbf{s}}_a\cdot\vec{\mathbf{s}}_b)\times(\tfrac{1}{2}\mathcal{I} + 2\vec{\mathbf{s}}_b\cdot\vec{\mathbf{s}}_c)(\tfrac{1}{2}\mathcal{I} + 2\vec{\mathbf{s}}_c\cdot\vec{\mathbf{s}}_d)\ldots \tag{A2.2}$$

Now to "contract" this expression so that any $\vec{\mathbf{s}}$ operator will occur no more than once in a product when the right-hand side of (A2.2) is multiplied out, we use the relations

$$\left.\begin{aligned}
\mathbf{s}_b{}^+\mathbf{s}_b{}^- &= \mathbf{s}_b{}^z + \tfrac{1}{2}\\
\mathbf{s}_b{}^-\mathbf{s}_b{}^+ &= -\mathbf{s}_b{}^z + \tfrac{1}{2}\\
\mathbf{s}_b{}^z\mathbf{s}_b{}^+ &= -\mathbf{s}_b{}^+\mathbf{s}_b{}^z = \tfrac{1}{2}\mathbf{s}_b{}^+\\
\mathbf{s}_b{}^-\mathbf{s}_b{}^z &= -\mathbf{s}_b{}^z\mathbf{s}_b{}^- = \tfrac{1}{2}\mathbf{s}_b{}^-\\
\mathbf{s}_b{}^+\mathbf{s}_b{}^+ &= \mathbf{s}_b{}^-\mathbf{s}_b{}^- = 0\\
\mathbf{s}_b{}^z\mathbf{s}_b{}^z &= \tfrac{1}{4}
\end{aligned}\right\} \tag{A2.3}$$

We, however, introduce the definitious

$$(\mathbf{s}_b{}^\mu\mathbf{s}_b{}^\nu)_{\text{odd}} \equiv \begin{cases}\mathbf{s}_b{}^z, \mu = +, \nu = -\\ -\mathbf{s}_b{}^z, \mu = -, \nu = +\\ 0, \mu = \nu = z\\ \mathbf{s}_b{}^\mu\mathbf{s}_b{}^\nu, \text{otherwise}\end{cases} \tag{A2.4}$$

$$(\mathbf{s}_b{}^\mu\mathbf{s}_b{}^\nu)_{\text{even}} \equiv \begin{cases}\tfrac{1}{2}, \mu = -\nu \neq z\\ \tfrac{1}{4}, \mu = \nu = z\\ 0, \text{otherwise}\end{cases} \tag{A2.5}$$

so that

$$\mathbf{s}_b{}^\mu\mathbf{s}_b{}^\nu = (\mathbf{s}_b{}^\mu\mathbf{s}_b{}^\nu)_{\text{even}} + (\mathbf{s}_b{}^\mu\mathbf{s}_b{}^\nu)_{\text{odd}} \tag{A2.6}$$

We see that $(\mathbf{s}_b{}^\mu\mathbf{s}_b{}^\nu)_{\text{even}}$ when "contracted" involves $\vec{\mathbf{s}}_b$ operators to the zero power and that $(\mathbf{s}_b{}^\mu\mathbf{s}_b{}^\nu)_{\text{odd}}$ when "contracted" involves $\vec{\mathbf{s}}_b$ operators to the first power. Further noting

$$(\mathbf{s}_b{}^\mu\mathbf{s}_b{}^\nu)_{\text{odd}} = -(\mathbf{s}_b{}^\nu\mathbf{s}_b{}^\mu)_{\text{odd}} \tag{A2.7}$$

we see that for a term of $\mathbf{G}_q{}^\sigma$ in contracted form to have an odd number of $\vec{\mathbf{s}}$ operators this term must involve an odd number of odd contractions as in (A2.4) or (A2.7); now it can be seen that $\mathbf{G}_{\tilde{q}}{}^\sigma = (\mathbf{G}_q{}^\sigma)^\dagger$ will have a term which is the same except each odd contraction will be replaced by its negative. Thus in $\mathbf{G}_q{}^\sigma + \mathbf{G}_{\tilde{q}}{}^\sigma$ there will be no terms with an odd number of odd contractions, and there will be no terms of odd powers.

Linear Symmetric HeH_2. A Model Superexchange System[1]

by D. C. Foyt, R. W. Kramling, and F. A. Matsen*

Molecular Physics Group, The University of Texas at Austin, Austin, Texas 78712 *(Received November 30, 1970)*

Publication costs assisted by the Robert A. Welch Foundation and the National Science Foundation

The linear symmetric HeH_2 system provides a convenient model for the study of superexchange. The results of valence-bond calculations for this system are compared with the energy levels of the hydrogen molecule and with the levels obtained with the Heisenberg effective spin Hamiltonian. The characteristics and importance of superexchange and the usefulness of the Heisenberg approximation are assessed in terms of this model system.

1. Introduction

The quantum mechanical treatment of magnetic phenomena is frequently formulated in terms of the Heisenberg effective spin Hamiltonian

$$\mathbf{H}_{\text{Heis}} = -2 \sum_{A<B} J_{AB} \vec{\mathbf{S}}_A \cdot \vec{\mathbf{S}}_B \qquad (1.1)$$

or an approximation to it. This Hamiltonian is, in turn, an approximation to the rigorous effective spin Hamiltonian, whose eigenvalues in an appropriate spin space are identical with those of the spin-free Hamiltonian in the corresponding spin-free space,[2] and to those obtained in the familiar antisymmetrized space-spin formulation.

A problem of importance in magnetism is the case of two magnetic atoms (A and C) which are nearer to a singlet atom or ion (B) than they are to each other. In this case the contribution of this portion of the system to the total Heisenberg energy is reduced to the single-exchange term $-2J_{AC}\vec{\mathbf{S}}_A \cdot \vec{\mathbf{S}}_C$, usually called a superexchange term. The traditional superexchange model begins with isolated atoms for the calculation of J. This appears to be the most useful approach for the case of widely separated atoms,[3a] although other techniques have recently been introduced for the treatment of more strongly interacting systems.[3b] Most applications of the traditional model have been restricted to the case in which the polyelectronic atoms or ions B, A, and C are treated as two- and one-electron aggregates. Although the neglect of nonvalence electrons is a rather drastic approximation,[4] this model nevertheless provides a useful first-order treatment. In this paper we consider the simplest case of such a system, a linear configuration of two hydrogen atoms separated by a singlet helium atom. While this system is of less physical importance than the systems to which the valence shell model has been applied, it has the advantage that it can be treated by an *ab initio* quantum mechanical technique. Comparison of its low-lying energy levels with the corresponding levels of H_2 may thus provide new insight into the nature and importance of superexchange. We also compare these results with those obtained with the Heisenberg Hamiltonian.

2. Energy Levels[5]

The energy levels for the lowest-lying singlet and triplet states of HeH_2 in the linear symmetric configuration were calculated for several different basis sets employing Slater-type orbitals (STO). The three-center integrals over STO's required in the computation were evaluated by means of a single-center expansion.[6] The two levels are closely spaced, and their relative order is sensitive to the choice of basis.

The energies at $R = 3$ au (H–H distance) for several different primitive functions are given in Table I. Functions a–d include only covalent terms, and in each case the triplet state of HeH_2 lies below the singlet, in contrast to H_2. However, when ionic terms are included (function e), the order of levels is that of H_2.

The energies of the two states were calculated as a function of R for a and e. These are shown in Figures 1 and 2, respectively. The corresponding Heitler–London levels for H_2 are given on the same scale for comparison. Since neither a nor e includes united atom configurations, the behavior at small R, and particularly the crossing at $R \cong 1$ au in Figure 2, should not be considered reliable. The order of levels given by e at

(1) Supported by the Robert A. Welch Foundation and the National Science Foundation.

(2) (a) The spin-free formulation is treated in detail in the spin-free series of papers, listed in F. A. Matsen and D. J. Klein, *J. Phys. Chem.*, **75**, 1860 (1971); (b) for a summary of the spin-free approach, see F. A. Matsen, *J. Amer. Chem. Soc.*, **92**, 3525 (1970).

(3) (a) C. Herring, *Magnetism*, **2B**, 1 (1963); (b) P. W. Anderson, *ibid.*, **1**, 25 (1963)

(4) Reference 3b; *cf.* J. Yamashita and J. Kondo, *Phys. Rev.*, **109**, 730 (1958); F. Keffer and T. Oguchi, *ibid.*, **115**, 1428 (1959); D. E. Ellis and A. J. Freeman, *J. Appl. Phys.*, **39**, 424 (1968).

(5) Closed-shell SCF calculations for singlet HeH_2 have recently been reported for a variety of nuclear geometries, including the linear symmetric case [H. Preuss, *Arbeitsbericht Instituts Theoret. Phys. Chem. Universität Stuttgart*, **14**, 94 (1969)]. More detailed calculations of this type are in progress (H. Preuss, private communication). To our knowledge, no other calculations for linear symmetric HeH_2 have been reported.

(6) J. C. Browne, private communication.

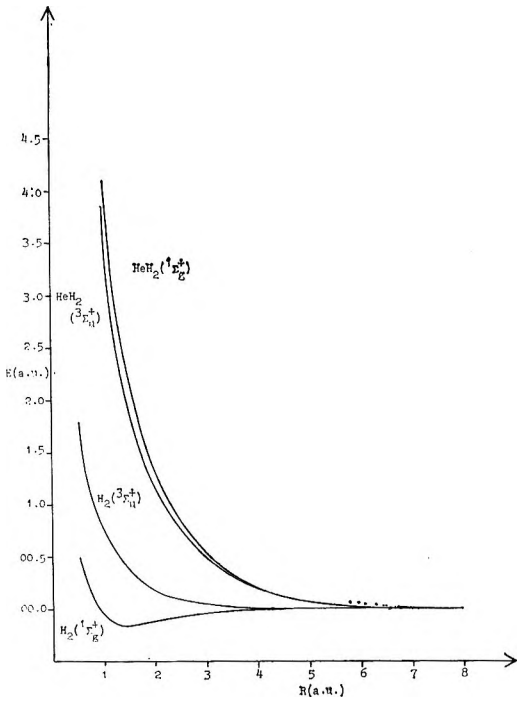

Figure 1. Energy levels of linear symmetric HeH_2 and H_2 relative to separated atom energies for function a of Table I.

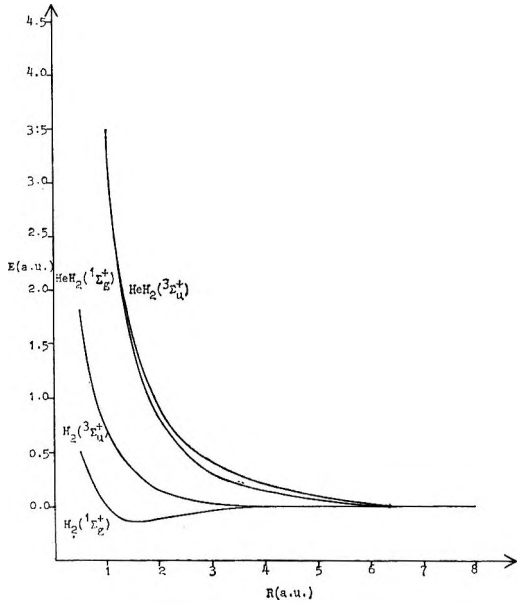

Figure 2. Energy levels of linear symmetric HeH_2 and H_2 relative to separated atom energies, for function e of Table I.

large R is probably the correct one, in spite of the small spacing, since the inclusion of closed-shell configurations would tend to lower the energy of the singlet more than the triplet. (Doubly closed-shell configurations, for example, contribute only to the singlet.)

It is of interest to determine the result of bringing the system out of the linear configuration for function a, since the levels should return to the order characteristic of H_2 as the hydrogen atoms approach each other. That this does occur can be seen from Figure 3. The small minimum in the triplet curve may be an artifact, but at any rate need not correspond to a well in the overall energy surface.

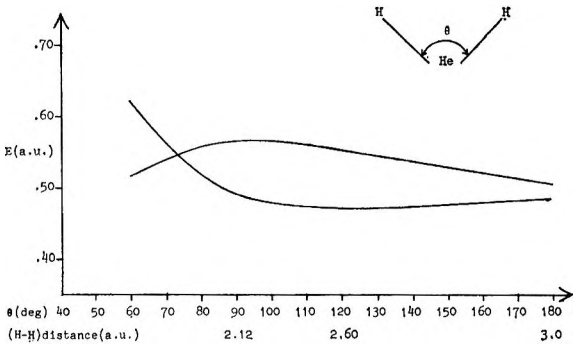

Figure 3. Energy levels of singlet and triplet HeH_2 as a function of angle for configuration a of Table I. The (H–He) distance is constant.

Table I: Energies of Linear Symmetric HeH_2 for Several Basis Sets at R = 3 au

Configuration[a]	$E(^3\Sigma_u^+)$, au	$E(^1\Sigma_g^+)$, au	ΔE
a	−3.389	−3.370	−0.019
b	−3.404	−3.352	−0.052
c	−3.435	−3.387	−0.048
d	−3.392	−3.374	−0.018
e	−3.479	−3.587	+0.108

[a] a, $1s(H_a)1s(He)1s'(He)1s(H_b)$, $\alpha(H)$ = 1.0, $\alpha(He)$ = 1.19, 2.18 (optimum values for separated atoms). b, $1s(H_a)1s^2(He)$-$1s(H_b)$, $\alpha(H)$ = 1.0, $\alpha(He)$ = 1.68 (optimum values for separated atoms). c, Configuration a, optimized: $^3\Sigma_u^+$, $^1\Sigma_g^+$, respectively, $\alpha(H)$, 0.80, 1.05; $\alpha(He)$, 2.10, 1.95; $\alpha'(He)$, 1.27, 1.15. d, configuration interaction with a, not optimized, and $2p_z(H_a)2p_z(H_b)1s(He)1s'(He)$, $\alpha(p_z)$ = 0.5. e, all covalent and singly ionized open-shell configurations supplied by a basis 1s1s' on each center (14 terms for the singlet and 22 for the triplet), employing optimum separated atom exponents [1.039230 and 0.2832215 for H^-, as given by J. N. Silverman, O. Platas, and F. A. Matsen, *J. Chem. Phys.*, **32**, 1402 (1960)]. The value 1.039230 was also employed for the hydrogen atom, instead of 1.0.

3. The Heisenberg Effective Spin Hamiltonian Formulation

In ref 2a-X the theory of effective spin Hamiltonians is developed in the spin-free formalism employed here. The technique of double coset decomposition is described in ref 2a-IX. For HeH_2 we assign electron 1 to H (aggregate A), electrons 2 and 3 to He (aggregate B) and electron 4 to the second hydrogen atom (aggregate C). The zero-order product kets are

$$|\gamma_1^0\rangle = |K_A[\lambda_A]r_A\rangle|K_B[\lambda_B]r_B\rangle|K_C[\lambda_C]r_C\rangle = |[1]\rangle|[2]\rangle|[1]\rangle \quad \text{and} \quad (3.1)$$

$|\gamma_2{}^0\rangle = |K'_A[\lambda'_A]r'_A\rangle|K'_B[\lambda'_B]r'_B\rangle|K'_C[\lambda'_C]r'_C\rangle = |[1]\rangle|[1^2]\rangle|[1]\rangle$

where the indices K_A, K_B, K_C, r_A, r_B, r_C, etc. are all equal to one and are suppressed. We perform a double coset decomposition with respect to the group sequence $\mathcal{S}^0 \subset \mathcal{S}_4$, where

$$\mathcal{S}^0 = \mathcal{S}_A \otimes \mathcal{S}_B \otimes \mathcal{S}_C = \{g,(23)\} \tag{3.2}$$

There are seven double coset generators, which may be chosen as the seven interaggregate permutations given in Table II. The effective spin permutation Hamiltonian (eq 3.13 of 2a-X) is then

$$\mathbf{H}_{\text{eff}}{}^{\gamma^0\gamma'^0} = \frac{N^0}{N!}\sum_q (-1)^{G_q} l_q H_q{}^{\gamma^0\gamma'^0}\mathbf{G}_q{}^\sigma \tag{3.3}$$

Table II: Double-Coset Generators for $\mathcal{S}_4 \supset \mathcal{S}_1 \otimes \mathcal{S}_2 \otimes \mathcal{S}_1$

G_q	Arrow diagram	d_q	l_q
g	A · · · · · · · C	2	1
(12)	A · ⇄ B · C	1	2
(14)	A · ⇄ C, B	2	1
(24)	A · C ⇄ B	1	2
(134)	A → C → B → A	1	2
(143)	A ← C ← B ← A	1	2
(12)(34)	A ⇄ B, C ⇄ B	1	2

where the zero-order matric basis elements $\mathbf{e}_{11}{}^{[\bar{\lambda}]^0}$ and $\mathbf{e}_{11}{}^{[\bar{\lambda}']^0}$ do not alter the zero-order kets and have therefore been omitted. Here

$$H_q{}^{\gamma^0\gamma'^0} = \langle\gamma^0|\mathbf{H}\mathbf{G}_q|\gamma'^0\rangle \tag{3.4}$$

We employ the Dirac identity to replace permutations by spin operators, as described in ref 2a-X. The higher order permutations may be replaced as follows[7]

$$(abc)^\sigma + (acb)^\sigma \doteq {}^1/_2 g + 2\vec{\mathbf{s}}_a\cdot\vec{\mathbf{s}}_b + 2\vec{\mathbf{s}}_b\cdot\vec{\mathbf{s}}_c + 2\vec{\mathbf{s}}_a\cdot\vec{\mathbf{s}}_c \tag{3.5}$$

$$(ab)^\sigma(b'c)^\sigma \doteq {}^1/_4 g + \vec{\mathbf{s}}_a\cdot\vec{\mathbf{s}}_b + \vec{\mathbf{s}}_b{}'\cdot\vec{\mathbf{s}}_c - \vec{\mathbf{s}}_a\cdot\vec{\mathbf{s}}_c - 2i(\vec{\mathbf{s}}_b\cdot\vec{\mathbf{s}}_a \times \vec{\mathbf{s}}_c) \tag{3.6}$$

Equation 3.6 is valid only for $S_B = 0$ and thus may not be used to treat configuration interaction (CI) with states having $S_B \neq 0$. Brackets over operators $\vec{\mathbf{s}}_a\cdot\vec{\mathbf{s}}_b$ and $\vec{\mathbf{s}}_b\cdot\vec{\mathbf{s}}_a \times \vec{\mathbf{s}}_c$ are identically zero for $a,c \in A,C$ and $b \in B$,[7] and the aggregate spin operators for the one-electron aggregates A and C are simply the one-electron spin operators. Substituting spin operators into (3.3) and collecting terms, we obtain the Hamiltonian

$$\mathbf{H}_{\text{eff}} = -2J_g\cdot -2J_{AC}\vec{\mathbf{S}}_A\cdot\vec{\mathbf{S}}_C \tag{3.7}$$

where, writing $H_p{}^{\gamma^0}$ for $H_p{}^{\gamma^0\gamma^0}$

$$-2J_g = H_g{}^{\gamma^0} - H^{\gamma^0}{}_{(13)} - {}^1/_2H^{\gamma^0}{}_{(14)} - H^{\gamma^0}{}_{(34)} + {}^1/_2H^{\gamma^0}{}_{(134)} + {}^1/_2H^{\gamma^0}{}_{(143)} + {}^1/_2H^{\gamma^0}{}_{(12)(34)} \tag{3.8}$$

and

$$-2J_{AC} = -2H^{\gamma^0}{}_{(14)} + 2H^{\gamma^0}{}_{(134)} + 2H^{\gamma^0}{}_{(143)} - 2H^{\gamma^0}{}_{(12)(34)} \tag{3.9}$$

We have omitted the pseudo-normalization factor $N^0/N!$ in eq 3.7 because the Hamiltonian is to be employed with coupled spin kets rather than sequence adapted kets.

All of the multiple exchange double coset generators in (3.3) have been replaced by single exchange spin operators in (3.7). This result is possible only in the case $S_B = 0$, for which eq 3.6 holds. Furthermore, it follows that the only approximation involved in the use of this Heisenberg Hamiltonian for this problem is the neglect of configuration interaction.

Brackets over coupled spin kets corresponding to singlet He yield $-{}^3/_4$ and ${}^1/_4$ for singlet and triplet HeH_2 respectively. Then by (3.7), (3.8), and (3.9), the Heisenberg energies for the two states are

$$\langle\sigma^4;00|\mathbf{H}_{\text{eff}}{}^{\gamma_1{}^0}|\sigma^4;00\rangle = -2J_g + {}^3/_2J_{AC} = H_g{}^{\gamma_1{}^0} - H_{(13)}{}^{\gamma_1{}^0} + H_{(14)}{}^{\gamma_1{}^0} - H_{(34)}{}^{\gamma_1{}^0} - H_{(134)}{}^{\gamma_1{}^0} - H_{(143)}{}^{\gamma_1{}^0} + 2H_{(12)(34)}{}^{\gamma_1{}^0} \tag{3.10}$$

and

$$\langle\sigma^4;11|\mathbf{H}_{\text{eff}}{}^{\gamma_1{}^0}|\sigma^4;11\rangle = -2J_g + {}^1/_2J_{AC} = H_g{}^{\gamma_1{}^0} - H_{(13)}{}^{\gamma_1{}^0} - H_{(14)}{}^{\gamma_1{}^0} - H_{(34)}{}^{\gamma_1{}^0} + H_{(134)}{}^{\gamma_1{}^0} + H_{(143)}{}^{\gamma_1{}^0} \tag{3.11}$$

These brackets and the corresponding overlap matrix elements were computed for $R = 3$ au (H–H separation). In Table III these results are compared with the spin-free result and with the result for the single Heitler–London configuration that correlates with He(^{1}S) in the separated atom limit. The latter is, of course, equivalent to the Heisenberg result for the present problem, since there is no spin multiple exchange.

In the case of the singlet, all three results in Table III are equal because sequence adaptation to the separated atom configuration automatically symmetry-adapted the singlet block of the secular equation to the appropriate point group. This does not occur for the triplet, since the configuration used supplies two triplet states

(7) P. W. Anderson, *Phys. Rev.*, 79, 350 (1950).

Table III: Comparison of Spin-Free, Single Configuration Heitler–London, and Heisenberg Energies for Linear Symmetric HeH_2

	$E(^1\Sigma_g^+)$, au	$E(^3\Sigma_u^+)$, au
Spin-free	−3 370	−3.389
Single configuration Heitler–London	−3 370	−3.384
Heisenberg	−3.370	−3.384

of the same point group symmetry but different separated atom limits.

4. Discussion

At the relatively large separation of 3.0 au, the error due to the approximations of the Heisenberg Hamiltonian for this model system is approximately $^1/_4$ the energy separation between levels, which is itself quite small. Thus it appears that the Heisenberg approximation is a good one for the superexchange problem at large internuclear distance. Several aspects of this model system suggest, however, that the approximations involved may be less significant here than they are in the general superexchange problem.

(1) All multiple exchange double coset generators were rigorously replaced by single exchange spin operators. In the general case this is not always possible, and the neglect of spin multiple exchange will make the Heisenberg energy only an approximation to the single configuration Heitler–London result.

(2) The use of coupled atomic spin kets automatically accomplished factorization of the secular equation. Thus the neglect of configuration interaction among states of different $[\lambda]^0$ (ref 2a-IX) did not introduce any approximation in the singlet energy. For a general basis this is not necessarily the case.

Herring[3a] has examined the approximations of the Heisenberg Hamiltonian and concluded that it is a good model for the superexchange problem in general for systems of widely separated atoms. Our results support this conclusion, but as pointed out above, the Heisenberg approximations are not as significant for our model as they are for the general case.

The close spacing of the calculated energy levels renders the HeH_2 system less useful than one might have hoped as a model for the study of superexchange in antiferromagnetic crystals. However, the sensitivity of the energy level diagram to the choice of basis does serve to emphasize the importance of charge transfer in the construction of models for the prediction of antiferromagnetic phenomena. For other systems, one can anticipate that charge-transfer states will be even more important.

Spin-Free Quantum Chemistry. XI.[1]

Perturbation Theory for Interaction Energies

by F. A. Matsen* and B. R. Junker

Molecular Physics Group, The University of Texas at Austin, Austin, Texas 78712 *(Received November 30, 1970)*

Publication costs assisted by The Robert A. Welch Foundation and the National Science Foundation

Perturbation theory provides a method for a calculation of interaction energies between aggregates (atoms and/or molecules) which, in principle, does not require taking small differences between large quantities. In such a theory consideration must be given to the permutational symmetry. The spin-free formulation of the polyelectronic problem employs directly the permutational symmetry of the problem and is therefore well suited for the treatment of interaction energies. Special restrictions on the perturbation function lead to the Hirschfelder–Van der Avoird, Hirschfelder–Silbey, Murrell–Shaw, and Amos–Musher formalisms. The perturbation energies in these formalisms are a function of those restrictions and only in infinite order is the dependency removed.

1. Introduction

In principle, accurate eigenvalues and eigenfunctions of an N-electron spin-free Hamiltonian can be obtained by diagonalizing the representation of the Hamiltonian in a vector space spanned by a large basis set. In practice this program has been carried out only for systems with small numbers of electrons and nuclei. As the number of electrons and/or nuclei increases the tractability and the accuracy of a calculation decrease rapidly.

Many important properties of polyelectronic systems are determined solely by the interaction energy between aggregates (atoms and/or molecules). From total energy calculations the interaction energies are obtained by subtracting two large numbers. Since interaction energies are small, perturbation theory offers in principle the possibility of computing the interaction energy directly.[2a] That is, the problem may admit formulation in such a way that the zero-order energy is the energy of the noninteracting aggregates and the sum of the higher order perturbation energies is the interaction energy. It is hoped that only a few terms are required in the perturbation expansion.

In this problem proper attention must be given to the permutational symmetry. In section 2 we present in the spin-free formulation[2b] those aspects of permutational symmetry which are important for the perturbation problem. In section 3 we develop a general perturbation theory in the spin-free formulation for systems of aggregates. There occur difficulties in the general perturbation theory which can be alleviated by placing restrictions on the perturbation wave function. This general restricted perturbation theory is discussed in section 4.

2. Spin-Free Quantum Chemistry

The spin-free Hamiltonian, $\mathbf{H}$, for an N electron, M nuclei system commutes with the (symmetric) group S_N of permutations on the electron indices, *i.e.*

$$[\mathbf{H},\mathbf{P}] = 0, \mathbf{P} \in S_N \tag{2.1}$$

As a consequence of (2.1) and the Wigner–Eckart theorem, the eigenfunctions to $\mathbf{H}$ are symmetry adapted to S_N and the Schroedinger equation has the form

$$\mathbf{H}|\mathfrak{K}[\lambda]r\rangle = {}^{[\lambda]}E_{\mathfrak{K}}|\mathfrak{K}[\lambda]r\rangle \tag{2.2}$$

Here, $[\lambda]$, called the *permutation quantum number*, identifies the irreducible representations of S_N, r is the permutation degeneracy index, and $\mathfrak{K}$ represents all other quantum numbers. Since the set $\{|\mathfrak{K}[\gamma]r\rangle, r = 1, \ldots f^{[\lambda]}\}$ is a degenerate set of eigenfunctions of $\mathbf{H}$, we suppress r.

The permutation states which occur in nature are those for which

$$[\lambda] = [2^p,1^{N-2p}] \tag{2.3}$$

and are called *Pauli-allowed permutation states.* The remaining states are called *Pauli-excluded permutation states.* An allowed state in the conventional spin formulation is labeled by the spin quantum number S which is related to a Pauli-allowed permutation quantum number by

$$S = \frac{N}{2} - p \tag{2.4}$$

The multiplicity is then given by

$$\mathfrak{M} = N - 2p + 1 \tag{2.5}$$

(1) Supported by the Robert A. Welch Foundation of Houston, Texas, and the National Science Foundation.

(2) See J. O. Hirschfelder, *Chem. Phys. Lett.*, 1, 325 (1967), for a list of references in the literature concerning this problem; (b) F. A. Matsen, *Advan. Quant. Chem.*, 1, 59 (1964); *J. Amer. Chem. Soc.*, 92, 3525 (1970); D. J. Klein, *Int. J. Quant. Chem. Symp.*, 4, 271 (1971).

Both Pauli-allowed and Pauli-excluded spin-free eigenfunctions of $\mathbf{H}$ exist.

We consider now a system of aggregates (atoms and/or molecules) labeled A, B, ... with N_A, N_B, ... electrons, respectively. At infinite aggregate separation the energy for this system can be computed from a Hamiltonian

$$\mathbf{H}^{(0)} = \mathbf{H}_A(1, 2, \ldots N_A) + \mathbf{H}_B(N_A + 1, \ldots N_A + N_B) + \ldots \quad (2.6)$$

The eigenvectors are products of eigenvectors of $\mathbf{H}_A$, $\mathbf{H}_B$, ...

$$|\gamma^{(0)}\rangle = |\mathcal{K}_A[\lambda_A]r_A\rangle|\mathcal{K}_B[\lambda_B]r_B\rangle\ldots \quad (2.7)$$

and the eigenvalues are sums of the eigenvalues for $\mathbf{H}_A$, $\mathbf{H}_B$, ...

$$\epsilon_{\mathcal{K}}{}^{(0)} = {}^{[\lambda_A]}E_{\mathcal{K}_A} + {}^{[\lambda_B]}E_{\mathcal{K}_B} + \ldots \quad (2.8)$$

In (2.6) we have made a specific assignment of the electrons to the various nuclei. This is, of course, not unique.

For finite interaggregate separations we define the interaction energy of the $(\mathcal{K},[\lambda])$th state as

$$\Delta^{[\lambda]}E_{\mathcal{K}} \equiv {}^{[\lambda]}E_{\mathcal{K}} - \epsilon_{\mathcal{K}}{}^{(0)} \quad (2.9)$$

where $\epsilon_{\mathcal{K}}{}^{(0)}$ is the energy of the separated aggregate state with which the $(\mathcal{K},[\lambda])$th molecular state correlates. We define the interaction operator for $\mathbf{H}$ and $\mathbf{H}^{(0)}$ as

$$\mathbf{H}^{(1)} = \mathbf{H} - \mathbf{H}^{(0)} \quad (2.10)$$

We note that while $\mathbf{H}$ commutes with the elements of S_N, $\mathbf{H}^{(0)}$ commutes only with the elements of $S^{(0)} = S_A \otimes S_B \otimes \ldots$, a subgroup of S_N. Here S_A is the symmetric group for aggregate A, S_B for aggregate B, ... As a consequence

$$[\mathbf{H}^{(0)},\mathbf{P}] = [\mathbf{P},\mathbf{H}^{(1)}] \neq 0 \quad (2.11)$$

for all $\mathbf{P} \notin S^{(0)}$.

An equation equivalent to the Schroedinger eq 2.2 is

$$[(\mathbf{H}^{(0)} - \epsilon_{\mathcal{K}}{}^{(0)} + \mathbf{H}^{(1)} - ({}^{[\lambda]}E_{\mathcal{K}} - \epsilon_{\mathcal{K}}{}^{(0)})]|\mathcal{K}[\lambda]\rangle = 0 \quad (2.12)$$

We formally compute the interaction energy by applying $\langle\gamma^{(0)}|$ to (2.12). Then since

$$\langle\gamma^{(0)}|(\mathbf{H}^{(0)} - \epsilon_{\mathcal{K}}{}^{(0)})|\mathcal{K}[\lambda]\rangle = 0 \quad (2.13)$$

we have by (2.12)

$$\Delta^{[\lambda]}E_{\mathcal{K}} = \frac{\langle\gamma^{(0)}|\mathbf{H}^{(1)}|\mathcal{K}[\lambda]\rangle}{\langle\gamma^{(0)}|\mathcal{K}[\lambda]\rangle} \quad (2.14)$$

3. General Projected Perturbation Theory for Interaction Energies

Equation 2.10 defines a nonunique partitioning of the total Hamiltonian into a term which may be chosen as the zero-order Hamiltonian, $\mathbf{H}^{(0)}$, and a term which may be taken as a perturbation Hamiltonian, $H^{(1)}$. As a consequence of (2.11) any perturbation formalism is nonunique since the left-hand side of (2.11) is zero order and the right hand side is first order. Thus (2.11) could be used to define different perturbation schemes by shifting terms between the various orders.

Equation 2.12 is the Schroedinger equation with the separated aggregate energy explicitly included. In order to express the dependence of $|\mathcal{K}[\lambda]\rangle$ on the separated aggregate state $|\gamma^{(0)}\rangle$ we define a perturbation series for $|\mathcal{K}[\lambda]\rangle$

$$|\mathcal{K}[\lambda]\rangle = \mathbf{e}^{[\lambda]}\sum_{i=0}^{\infty}|\gamma^{(i)}\rangle \equiv \mathbf{e}^{[\lambda]}|\gamma\rangle \quad (3.1)$$

where $|\gamma^{(0)}\rangle$ is the separated aggregate configuration with which the $(\mathcal{K}[\lambda])$th molecular state correlates and $\mathbf{e}^{[\lambda]}$ is the projector for the $[\lambda]$th permutation state. If the energy, ${}^{[\lambda]}E_{\mathcal{K}}$, is also expanded in a perturbation series

$${}^{[\lambda]}E_{\mathcal{K}} = \sum_{i=0}^{\infty}{}^{[\lambda]}\epsilon_{\mathcal{K}}{}^{(i)} \quad (3.2)$$

and if (3.1) and (3.2) substituted are substituted into (2.12) we obtain

$$\mathbf{e}^{[\lambda]}\sum_{i=0}^{\infty}[(\mathbf{H}^{(0)} - \epsilon_{\mathcal{K}}{}^{(0)}) + \mathbf{H}^{(1)} - \sum_{j=0}^{\infty}{}^{[\lambda]}\epsilon_{\mathcal{K}}{}^{(j)} + \epsilon_{\mathcal{K}}{}^{(0)}]|\gamma^{(i)}\rangle = 0 \quad (3.3)$$

Note that since $|\gamma^{(0)}\rangle$ is the wave function of the separated aggregate state with which the $(\mathcal{K}[\lambda])$th molecular state correlates

$${}^{[\lambda]}\epsilon_{\mathcal{K}}{}^{(0)} = \epsilon_{\mathcal{K}}{}^{(0)} \quad (3.4)$$

and

$$\Delta^{[\lambda]}E_{\mathcal{K}} = {}^{[\lambda]}E_{\mathcal{K}} - \epsilon_{\mathcal{K}}{}^{(0)} = \sum_{i=1}^{\infty}{}^{[\lambda]}\epsilon_{\mathcal{K}}{}^{(i)} \quad (3.5)$$

With the requirement above the higher order equations are

$$\mathbf{e}^{[\lambda]}[(\mathbf{H}^{(0)} - \epsilon_{\mathcal{K}}{}^{(0)})|\gamma^{(1)}\rangle + (\mathbf{H}^{(1)} - {}^{[\lambda]}\epsilon_{\mathcal{K}}{}^{(1)})|\gamma^{(0)}\rangle] = 0 \quad (3.6a)$$

$$\mathbf{e}^{[\lambda]}[(\mathbf{H}^{(0)} - \epsilon_{\mathcal{K}}{}^{(0)})|\gamma^{(n)}\rangle + \mathbf{H}^{(1)}|\gamma^{(n-1)}\rangle - \sum_{m=1}^{n}{}^{[\lambda]}\epsilon_{\mathcal{K}}{}^{(m)}|\gamma^{(n-m)}\rangle] = 0 \quad (3.6b)$$

Note that these equations do not differentiate among different states of the same symmetry $[\lambda]$ which arise from the same separate aggregate state $|\gamma^{(0)}\rangle$. Consequently, even if more than one state for a given $[\lambda]$ does correlate with $\gamma^{(0)}$ there can be obtained one and only one energy corresponding to a state with symmetry $[\lambda]$.

A major difficulty with eq 3.6 is that the nth order wave function is required to determine the nth order

energy. This differs from normal Rayleigh–Schroedinger[2a] perturbation theory where the nth-order wave function determines the energy to order $(2n + 1)$. This has occurred since we have introduced the symmetry explicitly by means of $\mathbf{e}^{[\lambda]}$ and thus one cannot form the bracket of (3.6) with $\langle\gamma^{(0)}|$ and eliminate $(\mathbf{H}^{(0)} - \epsilon_{\mathcal{K}}{}^{(0)})|\gamma^{(n)}\rangle$. We call this the symmetry problem.

A possible solution to this difficulty is to substitute from (2.11)

$$\mathbf{e}^{[\lambda]}\mathbf{H}^{(0)} = \mathbf{H}^{(0)}\mathbf{e}^{[\lambda]} + \mathbf{H}^{(1)}\mathbf{e}^{[\lambda]} - \mathbf{e}^{[\lambda]}\mathbf{H}^{(1)} \quad (3.7)$$

into (3.3) for $i \geq 1$. Then the perturbation equations become

$$\mathbf{e}^{[\lambda]}(\mathbf{H}^{(0)} - \epsilon_{\mathcal{K}}{}^{(0)})|\gamma^{(0)}\rangle = 0 \quad (3.8a)$$

$$(\mathbf{H}^{(0)} - \epsilon_{\mathcal{K}}{}^{(0)})\mathbf{e}^{[\lambda]}|\gamma^{(1)}\rangle + \mathbf{e}^{[\lambda]}(\mathbf{H}^{(1)} - {}^{[\lambda]}\epsilon_{\mathcal{K}}{}^{(1)})|\gamma^{(0)}\rangle = 0 \quad (3.8b)$$

$$(\mathbf{H}^{(0)} - \epsilon_{\mathcal{K}}{}^{(0)})\mathbf{e}^{[\lambda]}|\gamma^{(n)}\rangle + \mathbf{H}^{(1)}\mathbf{e}^{[\lambda]}|\gamma^{(n-1)}\rangle - \sum_{m=1}^{n} {}^{[\lambda]}\epsilon_{\mathcal{K}}{}^{(m)}\mathbf{e}^{(\lambda)}|\gamma^{(n-m)}\rangle = 0 \quad (3.8c)$$

A remark similar to that following (3.6) applies here.

We obtain from (3.8b)

$${}^{[\lambda]}\epsilon_{\mathcal{K}}{}^{(1)} = \langle\gamma^{(0)}|\mathbf{e}^{[\lambda]}\mathbf{H}^{(1)}|\gamma\rangle^{(0)}/\langle\gamma^{(0)}|\mathbf{e}^{[\lambda]}|\gamma^{(0)}\rangle \quad (3.9)$$

and from (3.8c)

$${}^{[\lambda]}\epsilon_{\mathcal{K}}{}^{(n)} = (\langle\gamma^{(0)}|\mathbf{H}^{(1)}\mathbf{e}^{[\lambda]}|\gamma^{(n-1)}\rangle - \sum_{m=1}^{n-1} {}^{[\lambda]}\epsilon_{\mathcal{K}}{}^{(m)}\langle\gamma^{(0)}|\mathbf{e}^{[\lambda]}|\gamma^{(n-m)}\rangle)/\langle\gamma^{(0)}|\mathbf{e}^{[\lambda]}|\gamma^{(0)}\rangle, \; n > 1 \quad (3.10)$$

Assuming (3.8b) and (3.8c) have nontrivial solutions, they provide a means for determining $|\gamma^{(1)}\rangle$ and $|\gamma^{(n)}\rangle$, respectively. The equation

$$|\gamma^{(1)}\rangle = -\frac{1}{\mathbf{e}^{[\lambda]}(\mathbf{H}^{(0)} - \epsilon_{\mathcal{K}}{}^{(0)})\mathbf{e}^{[\lambda]}} \times \mathbf{e}^{[\lambda]}(\mathbf{H}^{(1)} - {}^{[\lambda]}\epsilon_{\mathcal{K}}{}^{(1)})|\gamma^{(0)}\rangle \quad (3.11)$$

is the formal first-order solution to eq 3.8.1.

4. General Restricted Perturbation Theory

In this section we show a second method by which the symmetry problem discussed in section 3 can be resolved by placing a very general restriction on the perturbation function. We call this the general restricted perturbation theory. In this development we follow closely a development outlined by Hirschfelder.[2a] The general restriction which we impose on the perturbation function $|\gamma\rangle$ is

$$|\gamma\{\lambda\}\rangle \equiv \sum_{[\mu]\neq[\lambda]} \mathbf{e}^{[\mu]}(\mathbf{H}^{(0)} - \epsilon_{\mathcal{K}}{}^{(0)})|\gamma\rangle \quad (4.1)$$

It is clear that $|\gamma\{\lambda\}\rangle$ does not contain $[\lambda]$ symmetry. If eq 4.1 is added to (3.3) we have

$$[(\mathbf{H}^{(0)} - \epsilon_{\mathcal{K}}{}^{(0)}) + \mathbf{e}^{[\lambda]}\mathbf{H}^{(1)} - \mathbf{e}^{[\lambda]}\Delta^{[\lambda]}E_{\mathcal{K}}]|\gamma\rangle = |\gamma\{\lambda\}\rangle \quad (4.2)$$

The interaction energy is seen to be given by

$$\Delta^{[\lambda]}E_{\mathcal{K}} = \frac{\langle\gamma^{(0)}|\mathbf{e}^{[\lambda]}\mathbf{H}^{(1)}|\gamma\rangle - \langle\gamma^{(0)}|\gamma\{\lambda\}\rangle}{\langle\gamma^{(0)}|\mathbf{e}^{[\lambda]}|\gamma\rangle} \quad (4.3)$$

Substitution of (4.1) into (4.3) yields (2.14).

The strategy now is to expand $\Delta^{[\lambda]}E_{\mathcal{K}}$, $|\gamma\rangle$, and $|\gamma\{\lambda\}\rangle$ in perturbation series like (3.1) and (3.2). This leads to the following perturbation equations.

$$(\mathbf{H}^{(0)} - \epsilon_{\mathcal{K}}{}^{(0)})|\gamma^{(0)}\rangle = |\gamma^{(0)}\{\lambda\}\rangle \quad (4.4a)$$

$$(\mathbf{H}^{(0)} - \epsilon_{\mathcal{K}}{}^{(0)})|\gamma^{(1)}\rangle + \mathbf{e}^{[\lambda]}(\mathbf{H}^{(1)} - {}^{[\lambda]}\epsilon_{\mathcal{K}}{}^{(1)})|\gamma^{(0)}\rangle = |\gamma^{(1)}\{\lambda\}\rangle \quad (4.4b)$$

$$(\mathbf{H}^{(0)} - \epsilon_{\mathcal{K}})|\gamma^{(n)}\rangle + \mathbf{e}^{[\lambda]}\mathbf{H}^{(1)}|\gamma^{(n-1)}\rangle - \sum_{m=1}^{n} {}^{[\lambda]}\epsilon_{\mathcal{K}}{}^{(m)}\mathbf{e}^{[\lambda]}|\gamma^{(n-m)}\rangle = |\gamma^{(n)}\{\lambda\}\rangle \quad (4.4c)$$

Note that again only one state of a given symmetry $[\lambda]$ can be obtained, even if more than one state of $[\lambda]$ symmetry correlates with a given separated atom state $|\gamma^{(0)}\rangle$.

Again if $|\gamma^{(0)}\rangle$ is taken to be the separated aggregate state with which the $(\mathcal{K}[\lambda])$th molecular state correlates and if $|\gamma^{(0)}\{\lambda\}\rangle$ is defined as the zero vector

$${}^{[\lambda]}\epsilon_{\mathcal{K}}{}^{(0)} = \epsilon_{\mathcal{K}}{}^{(0)} \quad (4.5)$$

If the bracket of (4.4c) is formed with $\langle\gamma^{(0)}|$, the following perturbation energies are obtained.

$${}^{[\lambda]}\epsilon_{\mathcal{K}}{}^{(n)} = [\langle\gamma^{(0)}|\mathbf{e}^{[\lambda]}\mathbf{H}^{(1)}|\gamma_{(n-1)}\rangle - \sum_{m=1}^{n-1} {}^{[\lambda]}\epsilon_{\mathcal{K}}{}^{(m)}\langle\gamma^{(0)}|\mathbf{e}^{[\lambda]}|\gamma\rangle^{(n-m)} - \langle\gamma^{(0)}|\gamma^{(n)}\{\lambda\}\rangle/\langle\gamma^{(0)}|\mathbf{e}^{[\lambda]}|\gamma^{(0)}\rangle \quad (4.6)$$

The significance of the last term in (4.6) is that it corrects for the erroneous symmetry which was added in by the left-hand side of (4.1).

There exist an infinite number of restrictions of the type of (4.1) which could be imposed on the perturbation wave function. Lekkerkerker and Laidlaw,[3] Amos,[4] and Klein[2b] discuss the particular restrictions which lead to the Hirschfelder–Silbey[5,6] (HS), Murrell–Shaw,[7] Musher–Amos,[8] and Amos–Musher[9] perturbation formalisms. The "optimum" or "correct" choice of the restriction (4.1) is certainly not obvious, if indeed one does exist. The suggestion which has been made

(3) H. N. W. Lekkerkerker and W. G. Laidlaw, *J. Chem. Phys.*, **52**, 2953 (1970).

(4) A. T. Amos, *Chem. Phys. Lett.*, **5**, 587 (1970).

(5) J. O. Hirschfelder, *ibid.*, **1**, 363 (1967).

(6) J. O. Hirschfelder and R. Silbey, *J. Chem. Phys.*, **45**, 2188 (1966).

(7) J. N. Murrell and G. Shaw, *ibid.*, **46**, 1768 (1967).

(8) J. I. Musher and A. T. Amos, *Phys. Rev.*, **164**, 31 (1967).

(9) A. T. Amos and J. I. Musher, *Chem. Phys. Lett.*, **3**, 721 (1969).

that calculations might resolve this problem is not very practical because of the infinite number of possibilities.

5. Summary

We have presented a spin-free formulation of perturbation theory for interaction energies. We discussed two techniques for treating the symmetry problem raised in section 3. One method utilized explicitly the nonuniqueness resulting from (2.11) while the second method placed certain restrictions on the $|\gamma^{(n)}\rangle$ for $n \geq 1$. The fact that there exist an infinite number of possible perturbation schemes and that there exist no criteria outside of computation for evaluating them, poses a serious problem in perturbation theory for interaction energies.

Acknowledgments. The authors acknowledge helpful discussions and hospitality at the Theoretical Chemistry Institute at the University of Wisconsin.

Diffraction of Light by Nonaqueous Ordered Suspensions

by P. A. Hiltner,* Y. S. Papir, and I. M. Krieger

Department of Chemistry and the Division of Macromolecular Science, Case Western Reserve University, Cleveland, Ohio 44106 *(Received November 12, 1970)*

Publication costs assisted by the Public Health Service

A technique is described for resuspending latex particles in nonaqueous liquids. Suspensions of a monodisperse latex in some polar liquids are iridescent and give Bragg diffraction peaks. The particle separation D in the ordered array, the particle diameter D_0, and the volume fraction ϕ obey the relationship $\phi(D/D_0)^3 = 0.74$, the value 0 74 being the volume fraction occupied by spheres in a close-packed arrangement. The order is attributed to electrostatic repulsion between particles as a result of partial dissociation of ionic surface groups. Intrinsic viscosity measurements indicate that swelling is negligible in most polar liquids. Suspensions in nonpolar liquids are either unstable or highly swollen and do not show Bragg diffraction.

Bragg diffraction by ordered colloidal suspensions was reported in an earlier paper.[1] Measurements on electrolyte-free monodisperse latexes showed that the particles are in a close-packed arrangement which persists throughout the suspension, even when the particles are several diameters apart. The latex particles are charged, owing to bound initiator fragments, and the long-range order is attributed to interaction of the electrical double layers. In the absence of shielding electrolyte, the electrostatic repulsion was found to be effective over distances of several particle diameters. The magnitude and range of the interparticle potential were varied experimentally by addition of electrolyte.[2] The interparticle potential, as well as other properties of the suspension, should depend on the nature of the suspending medium. The present work describes the preparation of stable latex suspensions in nonaqueous liquids and their characterization by optical diffraction.

Experimental Section

Details of the preparation of monodisperse crosslinked latexes have been described previously.[3] Styrene with 0.5–10.0% divinylbenzene was emulsion-polymerized in the presence of both ionic and nonionic surfactants; polymerization was initiated by the thermal decomposition of potassium persulfate. The resulting aqueous suspensions were about 50% polymer by volume and highly iridescent. Particle sizes obtained by electron microscopy ranged from 0.15 to 0.25 μ; the uniformity index (ratio of weight average diameter to number average diameter) was always less than 1.01.

To redisperse the latex particles in nonaqueous media, the aqueous suspension was initially deionized by addition of a monobed ion-exchange resin (Amberlite MB-3, Rohm and Haas Co.) in the ratio of 1 g of resin per 25 g of latex. After 24 hr the resin was removed by filtration. This procedure removes both

(1) P. A. Hiltner and I. M. Krieger, *J. Phys. Chem.*, **73**, 2386 (1969).

(2) P. A. Hiltner and I. M. Krieger, "Order-Disorder Behavior in Monodisperse Colloids," in "Polymer Colloids," R. Fitch, Ed., Plenum Press, New York, N. Y., in press.

(3) Y. S. Papir, M. E. Woods, and I. M. Krieger, *J. Paint Technol.*, **42**, 571 (1970).

free electrolyte and ionic surfactant from the suspension. The only ionic species remaining are the bound surface charges and an equal number of free hydrogen ions. To promote dissociation of the surface charges in low dielectric solvents, the hydrogen ions were replaced by quaternary ammonium ions according to the following procedure. A column of cation-exchange resin (Amberlite IR-120, Rohm and Haas Co.) was converted into the hydrogen ion form and eluted with a 5% aqueous solution of tetraethylammonium hydroxide until the eluent was basic. The resin in the ammonium form was removed from the column, mixed with the deionized latex for at least 6 hr, and removed by filtration.

The latexes were redispersed in organic media, both in the acid form and in the quaternary ammonium form. The aqueous suspension was first dialyzed against methanol using regenerated cellulose tubing $^{27}/_{32}$ in. in diameter. The dialyzate was stirred constantly and replaced daily for at least 1 week. After dialysis, the suspension was diluted if necessary with methanol to yield a solids content of 15–20%, put into fresh dialysis tubing, and immersed in a large excess of the desired solvent. A comparable volume of the medium was often added to the methanol suspension. When the organic medium was miscible with water, identical results were obtained if the methanol dialysis was omitted and the aqueous suspension was dialyzed directly against the organic liquid.

Polymer contents of the suspensions were determined by drying accurately weighed samples to constant weight at 110°. Less volatile liquids were removed in a vacuum oven at 150°. A value of 1.045 g/cc for the density of the polymer was used to convert weight fraction into volume fraction; densities of the solvents were those specified by the manufacturer.

Existence of a stable suspension was verified by intrinsic viscosity measurements and by the appearance of the characteristic iridescent diffraction colors which had been observed in the aqueous suspensions. Intrinsic viscosity measurements were made with internal-dilution viscometers at 30.08°. Flow times were measured by a stop watch, while dilutions were made using weighing burets. The data were plotted as $(\eta_r - 1)/\phi$ *vs.* ϕ, where η_r is the relative viscosity and ϕ the volume fraction; the intrinsic viscosity was obtained from the intercept.

For those redispersed suspensions which exhibited iridescent colors, Bragg diffraction maxima were observed, indicating that the particles maintained an ordered three-dimensional arrangement. In the diffraction experiment, which has been described previously,[1] the intensity of a beam of monochromatic light reflected from a plane surface of the suspension is measured as a function of the incident angle. The angular position of the intensity maximum is determined at several wavelengths; the angle is related to the center-to-center distance between the particles in the array by means of the Bragg equation, modified to include refractive index effects.

Electrophoretic measurements were made on a qualitative basis to detect dissociation of the ionic surface groups. A drop of the resuspended latex and a drop of the pure liquid were deposited on a microscope slide. Two thin wire electrodes were inserted, one in each drop, and a thin bridge of solvent was drawn between the drops. A potential was applied, and the movement of the boundary observed with a microscope at 960×; the polarity was then reversed and the boundary was again observed.

Results

Stable suspensions of latex particles were obtained in a wide variety of nonaqueous media (Table I). There was no indication of settling or coagulation even after standing several months. Many suspensions in polar liquids exhibited the iridescent colors characteristic of aqueous suspensions, indicating an ordered arrangement of the particles. The particle separation D in the array, calculated from diffraction measurements, was always significantly larger than the particle diameter D_0 as determined by electron microscopy. Upon dilution, the diffraction maxima shifted in the direction of larger spacings until a maximum separation was obtained at a volume fraction ϕ_m. When diluted further, the suspension lost the iridescent colors and no diffraction maxima could be detected. Table II gives D values for the same latex in several different media at various volume fractions.

Superposition of the data for different particle sizes was obtained when a reciprocal reduced volume $v_r^{-1} = (D_0/D)^3$ was graphed against the volume fraction ϕ (Figure 1). For a close-packed array of uniform spheres, the theoretical volume fraction is 0.74. The straight line in Figure 1 represents the equation $\phi v_r = 0.74$. The correspondence between the experimental points and the theoretical line implies that a close-packed arrangement of the particles persists throughout the entire volume of the suspension. Upon dilution, the particles move apart while maintaining the close-packed configuration.

This behavior is analogous to that observed in deionized aqueous suspensions.[1] There the close-packed order persists in suspensions as dilute as 1% polymer by volume, where the particle separation is four times the particle diameter. In the aqueous case, the order has been attributed to long-range electrostatic repulsion between the negatively charged particles in the absence of any shielding electrolyte. It must be concluded that the particles in the nonaqueous suspensions are also charged and, therefore, that the surface ionic groups are at least partially dissociated. Additional evidence for the existence of negatively charged particles was given by the moving boundary electrophoresis experi-

Table I: Latex Suspensions in Various Media

Medium	ϵ (25°)	H^+ form	ϕ_m, %	$(Et)_4N^+$ form	ϕ_m, %
n-Hexane	1.89	Unstable		Unstable	
Cyclohexane	2.02	...		Unstable	
1,4-Dioxane	2.21	Stable	17	Stable	18.5
Carbon tetrachloride	2.24	Stable	>50	...	
Benzene	2.28	Stable	>50	Stable	>50
Toluene	2.38	Stable	>50	...	
Anisole	4.76	...		Stable	18.5
Chloroform	4.81	...		Stable	28
Ethyl acetate	6.02	...		Stable	33
Methyl benzoate	6.59	Stable	20	Stable	21
m-Cresol	11.8	Stable	30	...	
Benzyl alcohol	13.1	Stable	31	Stable	31
n-Hexanol	13.3	...		Unstable	
3-Pentanone	17.0	...		Stable	17
Acetophenone	17.4	...		Stable	14
Benzaldehyde	17.8	...		Stable	16
Cyclohexanone	18.3	...		Stable	14
1-Propanol	20.1	...		Unstable	
Benzonitrile	26.5	...		Stable	12.5
Methanol	32.6	Unstable		Unstable[a]	
DMF	36.7	Stable	<10	Stable	>10
Ethylene glycol	37.7	...		Unstable	
DMSO	46.6	Stable	<10	...	
Water	78.5	Stable	<10	Unstable[b]	
Formamide	109	Unstable		Unstable	
N-Methylformamide	182	Unstable		...	

[a] This suspension sometimes exhibited iridescence; however v_r^{-1} fell below the 0.74 line indicating that the suspension was partially coagulated. [b] Although the suspension was fluid, there was some coagulum and no iridescence was observed.

Table II: Particle Separation in the Ordered Suspensions at Various Volume Fractions (D_0 = 155 mμ)

Medium	100φ	D, mμ
Benzyl alcohol	35.7	193.4
	32.7	199.2
	31.2	202.2
Ethyl acetate	30.1	207.1
Methyl benzoate	25.1	219.1
	23.2	223.9
	21.1	233.6
1,4-Dioxane	21.0	235.7
	20.0	240.0
	18.5	245.2
Cyclohexane	20.7	238.2
	18.5	247.6
	16.6	256.9
	14.1	270.0
DMF	11.7	283.9
	9.0	308.9
	8.0	322.7

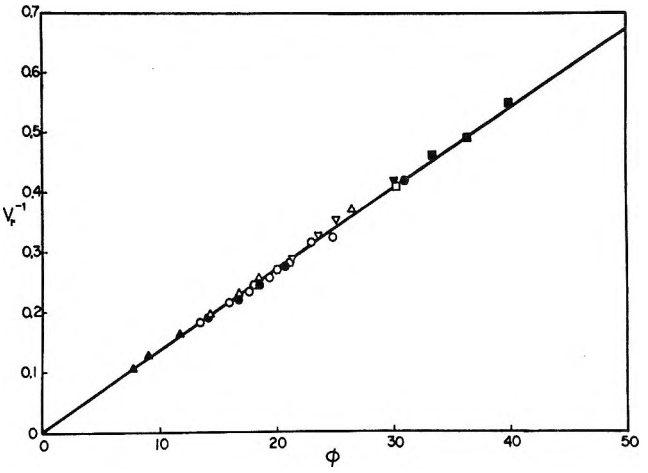

Figure 1. Reciprocal reduced volume as a function of the volume percentage of polymer for nonaqueous suspensions: ▲, DMF; ○, benzonitrile; ●, cyclohexanone; △, acetophenone; ◇, 1,4-dioxane; ▽, methyl benzoate; ▼, ethyl acetate; □, benzyl alcohol, D_0 = 220 mμ; ○, *m*-cresol; ■, benzyl alcohol. D_0 = 155 mμ except where indicated.

ments. In all cases, the boundary between dispersion and pure liquid moved toward the positive electrode.

The degree of dissociation and the magnitude of the interparticle repulsion, as reflected by ϕ_m, depend on the nature of the medium. A high dielectric constant favors dissociation but also acts to attenuate Coulombic forces. In general, the interparticle potential increases with increasing dielectric constant, although there are exceptions such as dioxane where specific properties of the medium are important.

Suspensions in carbon tetrachloride, benzene, and toluene did not give diffraction maxima, indicating

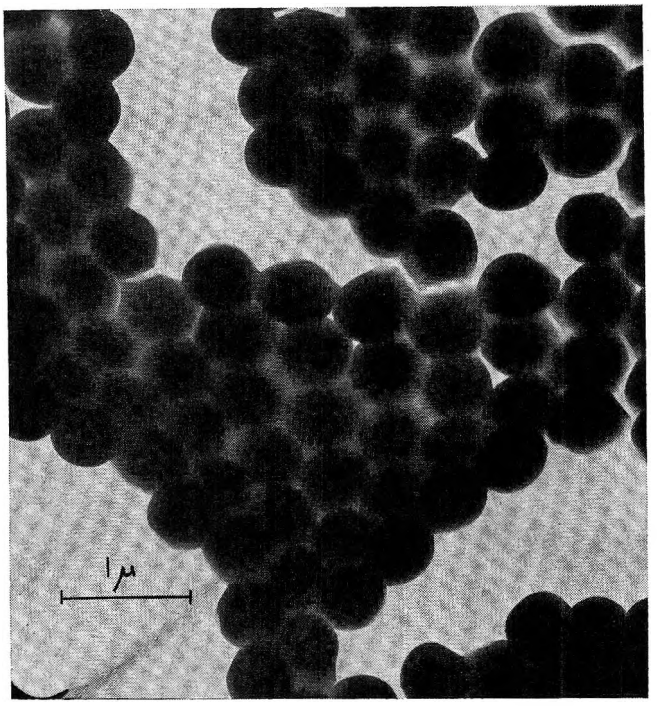

Figure 2. Electron micrograph of a 10% cross-linked latex suspended in toluene.

that the surface charges are not extensively dissociated. However, examination under the optical microscope showed no evidence of coagulation in these suspensions, and electron micrographs (Figure 2) indicate that the particles maintain a high degree of individuality. It is also clear that the particles are no longer rigid but that considerable solvation of the polymer has occurred. The swelling and loss of sphericity are reflected in the intrinsic viscosities (Table III); these values are much

Table III: Intrinsic Viscosities of Suspensions in Different Media

Medium	$[\eta]_\phi$
Benzyl alcohol	2.67
m-Cresol	2.68
Benzene	5.84
Carbon tetrachloride	6.89
Toluene	7.50

greater than those obtained for suspensions in polar media, which are only slightly larger than Einstein's theoretical value of 2.50. Consequently it appears that the important stabilization mechanism in low dielectric media is solvation of the particle by the medium. This may include disentanglement of chain segments to provide steric hindrance to coagulation. Carbon tetrachloride, benzene, and toluene are excellent solvents for polystyrene. Suspensions in saturated hydrocarbons such as *n*-hexane and cyclohexane were not stable.

Other systems which did not form stable suspensions are listed in Table I. Suspensions of the tetraethylammonium form were not stable in hydrogen-bonding liquids (with the exception of the aromatic alcohols); also, diffraction was obtained from the benzyl alcohol suspension only at high volume fractions, indicating an exceptionally low degree of dissociation. It has been proposed[4] that dissolution of quaternary ammonium ions in hydrogen bonding liquids is accompanied by depolymerization of associated solvent molecules, owing to the relatively intense electric field near the unsolvated cation. When solvation of the anion is also hindered, as in the present case, it is reasonable that very little dissociation of the surface groups would occur.

The failure to obtain stable suspensions of the hydrogen ion form in formamide and in *N*-methylformamide is especially interesting, since the solvent properties of these liquids are very similar to those of water. However, it has been observed that carboxylic acids are less dissociated in formamide and *N*-methylformamide than they are in water.[5] This has been attributed to the formation of a cyclic complex between the undissociated acid molecule and the solvent. A similar undissociated complex has been suggested for solutions of benzoic acid in methanol; on the other hand, no evidence for such a complex in water has been found. This suggests a favorable alternative to the dissociation of the surface groups on the latex particle, especially since solvation of the dissociated anion is minimized in this case. A possible structure for the complex is

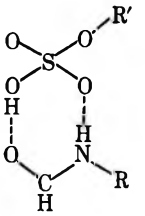

It involves hydrogen bonds through the amide group, which would not be possible if the nitrogen were disubstituted as in dimethylformamide (DMF).

The variation in peak width with concentration of the aqueous suspensions had been attributed to increasing transparency as the density of particles decreased.[1] Using a model of nonabsorbing homogeneous spheres in a perfect crystalline array, the peak width ($\Delta\theta_{1/2}$) at half the maximum intensity was shown to be

$$\Delta\theta_{1/2} = 0.0827(m^2 - 1)\frac{\sin\chi - \chi\cos\chi}{\sin 2\theta} \qquad (1)$$

where $\chi = (3/2)^{1/2}\pi D_0/D$ and $m = 1.60/n_m$ is the ratio of the refractive index of the particles to that of the medium. Equation 1 predicts that an increase in

(4) M. Mandel and P. Decroly, *Nature*, **201**, 290 (1964).

(5) C. M. French and K. H. Glover, *Trans. Faraday Soc.*, **51**, 1418 (1955).

the refractive index of the medium should have the effect of narrowing the peak width, and this trend is observed in water, 3-pentanone, and DMF (Table IV), where the experimental peak widths agree reasonably well with the calculated values. For the most transparent suspensions, however, such as those in benzonitrile and benzyl alcohol, the peaks are consistently too wide. Thus the attenuation effect, which was adequate to explain the peak width of aqueous latexes, can account for only a minor part of the width in more transparent suspensions, such as those in benzyl alcohol; other sources of peak broadening must therefore be taken into account.

Table IV: Experimental and Calculated Values of the Peak Width at Half the Maximum Intensity (D_0 = 155 mμ)

Medium	n_m	λ_0, mμ	100ϕ	Exptl $\Delta\theta_{1/2}$, deg	Calcd $\Delta\theta_{1/2}$, deg
Water[a]	1.333	500	32.0	9.4	8.60
			24.1	8.4	8.27
			11.7	4.6	4.66
			9.0	4.0	3.82
			5.3	3.2	2.80
3-Pentanone	1.394	400	24.8	5.6	4.28
			20.2	4.8	3.92
			16.9	3.8	3.74
DMF	1.427	500	11.7	3.2	2.35
			9.0	2.8	1.97
			8.0	2.2	1.80
Benzonitrile	1.529	450	19.9	4.4	1.21
			18.2	3.6	1.19
			16.4	3.4	1.16
			12.9	3.2	1.11
Benzyl alcohol	1.540	500	35.7	5.6	1.28
			32.7	3.8	1.25
			31.1	3.1	1.22

[a] Reference 1.

Line broadening would be expected if the order were confined to a small number of layers adsorbed on the glass wall. This is not the case, however; the correspondence in Figure 1 shows that the volume fraction of particles in the ordered array is the same as the bulk volume fraction. Like atomic crystals, the ordered suspensions undoubtedly contain defects due, for example, to the presence in the lattice of smaller or larger particles. The micrograph, Figure 3, shows such defects in a dried film. They give rise to separate ordered regions which are not quite parallel to one another and diffract at slightly different angles. The resultant line broadening will be most apparent in the highly transparent suspensions, since more planes contribute to the diffraction, and destructive interference of the reflected beam at angles close to the Bragg angle should be more efficient.

Quantitative expressions for the extinction of the primary beam at the Bragg angle have been derived for

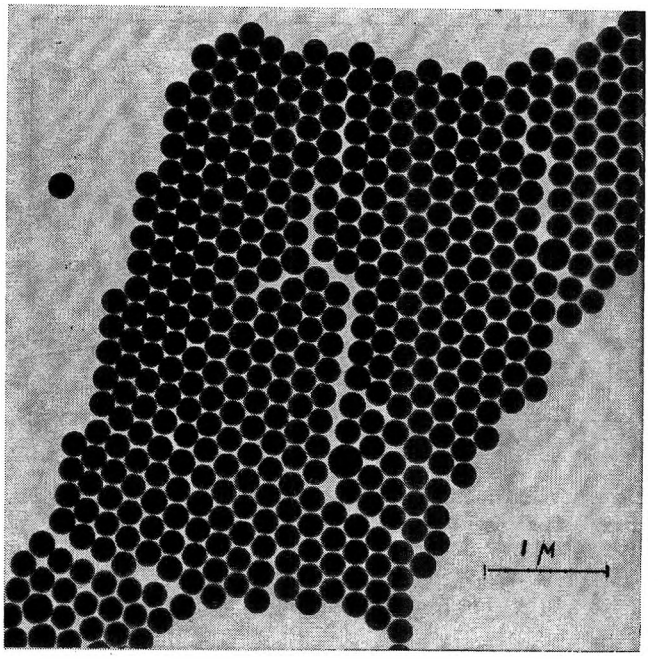

Figure 3. Electron micrograph of a monodisperse latex showing defects caused by nonuniform particles.

X-ray diffraction.[6] For a perfect crystal, the intensity of the primary beam at a distance x into the ordered array is

$$I_x = I_0 \exp(-2x\xi) \quad (2)$$

where $\xi = \pi|q|/4d$ and q is the scattering coefficient for a plane of particles. This equation is valid only when the Bragg condition is fulfilled; the effect should not be confused with ordinary absorption, which is assumed negligible. Equation 2 can be applied to the present case by substitution of the scattering coefficient for a plane of perfectly ordered homogeneous spheres. Using the expression derived previously, the extinction coefficient becomes

$$2\xi = 0.2841 n_s^2 D_0 \lambda_0^{-2} \phi^{-1/3}(m^2 - 1) \times (\sin\chi - \chi\cos\chi) \quad (3)$$

where λ_0 is the wavelength of the incident beam in air and $n_s = n_m(1 - \phi) + 1.60\phi$ is the refractive index of the suspension. Some calculated extinction curves are shown in Figure 4, comparing water (n_m = 1.333), DMF (n_m = 1.427), and benzonitrile (n_m = 1.529). The extinction coefficient is approximately proportional to $(m^2 - 1)$, and the increase in transparency as n_m approaches the refractive index of the polymer can be seen for the 15% suspensions in water, DMF, and benzonitrile, where 3, 10, and 40%, respectively, of the incident beam penetrates to 6000 mμ or about 25 planes. In the 15% benzonitrile suspension, more than 60

(6) Derivations can be found in most monographs on X-ray diffraction; for example, R. W. Jones, "The Optical Principles of the Diffraction of X-Rays," Cornell Press, Ithaca, N. Y., 1947, Chapter II.

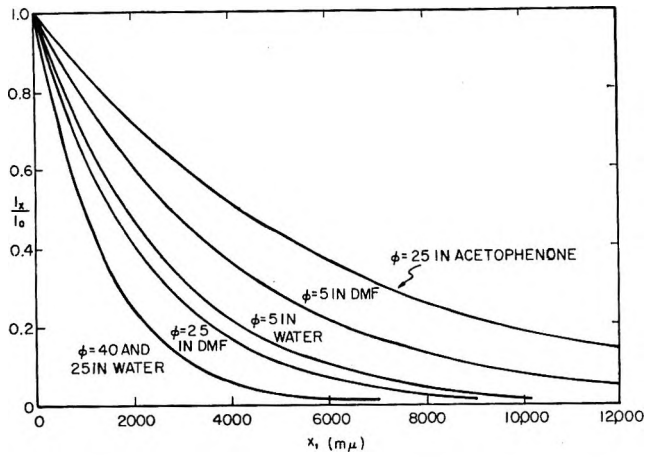

Figure 4. Extinction of the incident beam in the ordered array. For water at $\phi = 40\%$, $2\xi = 6.88 \times 10^{-4}$; at $\phi = 25\%$, $2\xi = 6.87 \times 10^{-4}$; at $\phi = 5\%$, $2\xi = 3.79 \times 10^{-4}$. For DMF at $\phi = 25\%$, $2\xi = 3.98 \times 10^{-4}$; at $\phi = 5\%$, $2\xi = 2.52 \times 10^{-4}$. For benzonitrile at $\phi = 25\%$, $2\xi = 1.53 \times 10^{-4}$.

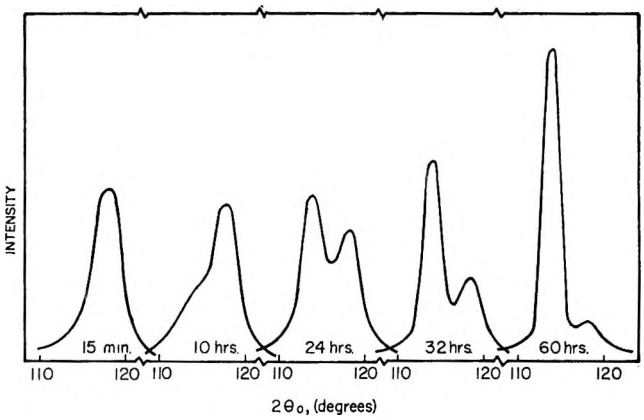

Figure 5. Change in diffraction pattern with time: DMF suspension, $D_0 = 155$ mμ, $\phi = 0.061$. Intensity scale, in arbitrary units, is identical for all scans.

planes, corresponding to a depth of 15 μ, contribute to the diffraction before the primary beam is reduced to 10% of the original intensity. Consequently, it appears that the model of a perfect lattice is valid to depths of at least 5 μ in the aqueous and DMF suspensions; however, for the highly transparent suspensions, imperfections in the order significantly affect the diffraction, and a model which takes lattice imperfections into consideration should be developed to describe quantitatively the shape of the peak.

In addition to lattice distortions and microcrystallinity, stacking faults are a common imperfection in close-packed systems, since face-centered cubic and hexagonal close-packed lattices differ only in the staggered arrangement of successive planes. It is predicted by X-ray diffraction theory that deformation faulting in a face-centered cubic lattice, where the planes stack in the order ABCABABC instead of ABCABC, produces a small shift in the angular position of the diffraction peak and broadens the peak as well. Evidence of deformation faulting in ordered latex suspensions is given by the appearance with time of a second diffraction peak very close to the first (Figure 5), particularly in suspensions approaching the limits of stability of the ordered array. The second peak is sharper than the original peak and is much more intense, indicating that regions of higher order are forming. This evolution of the diffraction pattern resembles that of the X-ray diffraction pattern of a face-centered cubic metal during relaxation of deformation faulting. It is therefore proposed that when the ordered array forms there are stacking faults randomly distributed through the suspension. When interparticle forces are low, these defects can anneal out, leaving perfectly ordered regions. These fault-free regions can be observed visually as the brilliant crystallites on the glass surface.

Acknowledgments. The authors are grateful to Dr. Morton Litt for his valuable suggestions in the preparation of the nonaqueous suspensions. The work reported in this paper was supported by a grant from the Public Health Service.

Adsorption on Flat Surfaces. I. Gas Phase Autophobicity

by T. D. Blake and W. H. Wade*

Department of Chemistry, University of Texas at Austin, Austin, Texas 78712 *(Received December 11, 1970)*

Publication costs assisted by the National Science Foundation

A study of the adsorption of tetramethylsilane, water, and the first five normal aliphatic alcohols on oxidized aluminum foil indicates that the surface of the foil is very similar to that of γ-alumina but may be microporous to water. The results, together with preliminary contact angle measurements, show that the surface is sufficiently well screened by a monolayer of a straight-chain alcohol containing three or more carbon atoms for the alcohol to exhibit both gas and liquid phase autophobicity. Comparison of butyl alcohol adsorption on the foil and on an alumina powder suggests that capillary condensation on powders is not limited to pendular rings and must involve much larger pore spaces.

Introduction

Recent investigations in this laboratory[1,2] have shown that the autophobicity concept of Zisman and coworkers[3,4] may be extended to gas phase adsorption of low-molecular-weight, normal aliphatic alcohols. Adsorption on 104 and 2.72 $m^2 g^{-1}$ alumina powders approached type I, with multilayer character decreasing with increasing adsorbate chain length. Attempts to ascribe uptake in excess of a monolayer to pendular ring condensation were not entirely successful, and one could not preclude the occurrence of some multilayer adsorption at high relative pressures.

To clarify the position still further, adsorption isotherms of tetramethylsilane (TMS), water, and the first five straight-chain alcohols (subsequently designated C_1, C_2, ...C_5) have been measured for an aluminum foil of approximately geometric surface area. Aluminum foil is usually covered by a thin layer of polycrystalline oxide. Immersional heats and catalytic activity[5,6] indicate this to be γ-alumina of sufficient thickness to produce a surface closely resembling that of the alumina powders used previously. In addition to minimizing capillary condensation, this approach has the advantage of employing an adsorbent in a form eminently suitable for contact angle measurements. A parallel study of contact angles was therefore instigated, and some preliminary results will be reported here.

By way of comparison, measurements were also made of the adsorption of C_4 on an oxidized, vapor-deposited aluminum film and on a γ-alumina powder outgassed under the same conditions as the foil.

Experimental Section

Foil and powder isotherms were measured using silica beam microbalances manufactured by Worden Laboratories and adjusted to have a useful sensitivity of up to 5×10^{-8} g/g. Sample tubes were maintained at 20.00 ± 0.02°. Adsorbate vapor was admitted *via* Granville Phillips variable leak valves. Pressures were determined to within ±0.005 Torr with an Apiezon B oil manometer isolated from the grease- and mercury-free adsorption system by a Whittaker Corp. capacitance pressure transducer having a total range of ±0.05 psig. Pressure changes of less than 0.04 μm were readily estimated to the nearest 0.001 Torr from the out-of-balance signal from the transducer.

Foil samples were assembled from rectangular sheets, roughly 4.5 × 6 cm, cut from a continuous ribbon of 99.5% pure, 5-μm aluminum foil supplied by Republic Foil and Metal Mills Inc. Sheets were perforated at each corner and stacked on a light, silica framework as shown in Figure 1, the burred edges of the holes providing good interlaminar separation. Two stacks were prepared having total geometric areas of 2.02 m^2 (package A) and 1.02 m^2 (package B). Each was counterbalanced with an equal mass of aluminum of negligible surface area. Residual buoyancy corrections were determined with nitrogen. Before use, packages were aged for 4 days in an oxygen-rich atmosphere at about 425°. Before each isotherm, the alumina surface was cleaned by overnight treatment with pure oxygen at 400° and outgassed at this temperature to 10^{-6} Torr. After cooling to 20° and constant weight, the surface was pretreated with adsorbate vapor at high relative pressures for at least 8 hr (36 hr with water) to ensure maximum chemisorption (no pretreatment was necessary with TMS). The system was then re-evacuated to 10^{-6} Torr, and isotherm measurement was commenced. Equilibration times of 10–15 min were normal for adsorption on the pretreated surface, although longer

(1) J. Barto, J. L. Durham, V. R. Baston, and W. H. Wade, *J. Colloid Interface Sci.*, **22**, 491 (1966).

(2) B. R. Jones and W. H. Wade, *ibid.*, **28**, 415 (1968).

(3) W. H. Fox, E. F. Hare, and W. A. Zisman, *J. Phys. Chem.*, **59**, 1097 (1955); O. Levine and W. A. Zisman, *ibid.*, **61**, 1068 (1957).

(4) E. F. Hare and W. A. Zisman, *ibid.*, **59**, 335 (1955).

(5) H. Cochrane and R. Rudham, *Trans. Faraday Soc.*, **61**, 2246 (1965).

(6) H. Cochrane, B. Hendricksen, D. Pearce, and R. Rudham, *Soc. Chem. Ind. Mongr.*, **25**, 370 (1967).

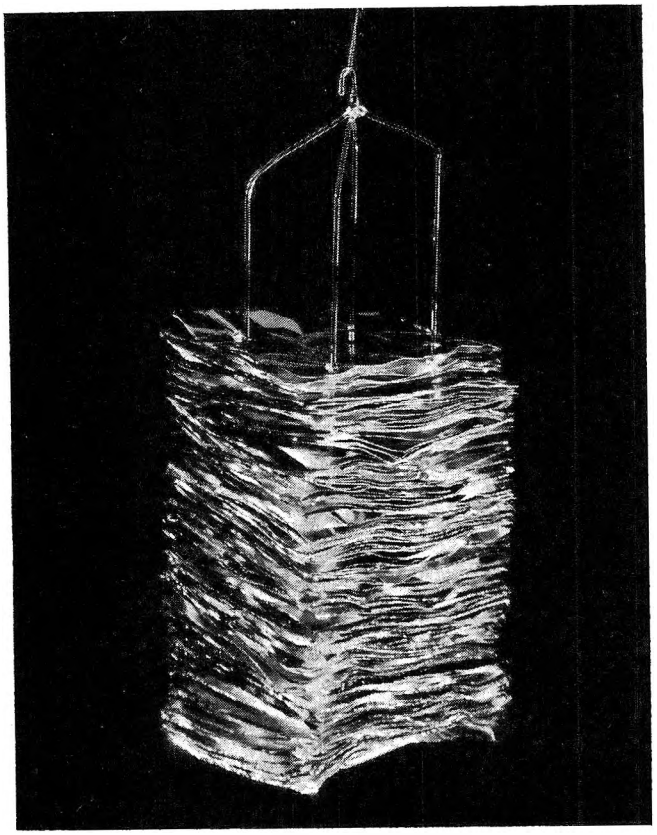

Figure 1. Package B comprising 1.02 m^2 of 5-mm aluminum foil on a silica framework. Each rectangular sheet is roughly 4.5 × 6 cm.

periods were necessary for desorption, especially at very low relative pressures. If saturation was attained or very closely approached, the desorption isotherm was shifted to slightly lower relative pressures, the extent of hysteresis apparently depending on the amount of interlaminar condensate incurred.

The powder sample, Alucer MA, a γ-alumina of surface area $\Sigma = 104\ m^2\ g^{-1}$, supplied by Whittaker, Clark and Daniels, Inc., was oxygen-treated and outgassed in the same way as the foil. The powder was not pretreated with adsorbate, and equilibration times were usually several hours, the complete isotherm taking about a week.

Adsorption on oxidized evaporated films was also measured with a quartz crystal microbalance at 25.2 ± 0.2°. This apparatus and the method of deposition of the aluminum film have been described in detail elsewhere.[7,8] Treatment with oxygen was carried out at successively 10^{-3} and 1 Torr, at room temperature. All pressures were measured with an MKS Baratron.

The alcohols were analyzed reagent grade 99.5% supplied by J. T. Baker Chemical Co. TMS of 99% purity was provided by NMR Specialities. Water was distilled in a two-stage, block tin still. Organic liquids were exhaustively dried over molecular sieve. All liquids were outgassed and distilled under vacuum immediately before use.

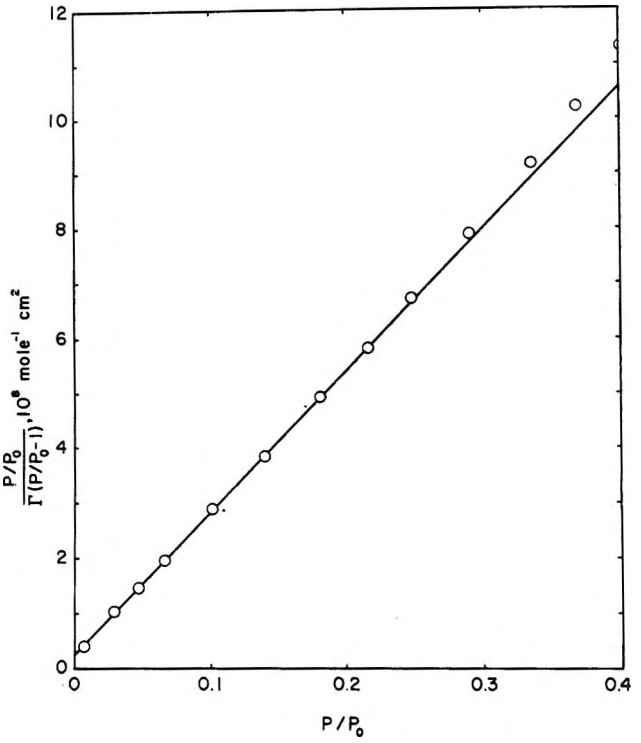

Figure 2. BET plot of the adsorption of tetramethylsilane (TMS) on package A.

Results and Discussion

The suitability of TMS for BET area determinations at normal temperatures has been discussed already,[8] a molecular area of 46.3 Å^2 being found by comparison with nitrogen (16.2 Å^2) on a nonporous, low area alumina. Figure 2 shows the TMS isotherm obtained with foil package A. The molecular area of 43.2 Å^2, calculated from the geometric area of the foil, gives a roughness factor, R, of 1.08. This may be compared with 1.28 obtained by Bowers.[9]

The partial irreversibility of TMS adsorption of alumina[7] caused some doubt as to the effectiveness of subsequent oxidative regeneration of the foil surface, and package B, which was assumed to have the same roughness as package A, was used in all later experiments.

Figures 3–5 show the adsorption isotherms for water, C_1, C_2, C_3, and C_4 on package B, C_5 on package A (prior to TMS), and C_4 on Alucer MA and the oxidized film. The C_1 isotherm is repeated in Figure 5 for comparison with that of water. Desorption isotherms are given for C_2 and C_3 only. Γ is the adsorption per unit area based on the roughness factor of 1.08.

Spectroscopic and thermogravimetric data[10] indicate that an initially hydrated alumina surface, outgassed

(7) R. C. Allen, Ph.D. Dissertation, Austin, 1968.

(8) W. H. Wade and R. C. Allen, *J. Colloid Interface Sci.*, **27**, 722 (1968).

(9) R. Bowers, *Phil. Mag.*, **44**, 467 (1953).

(10) R. B. Perry, Ph.D. Dissertation, Austin, 1966.

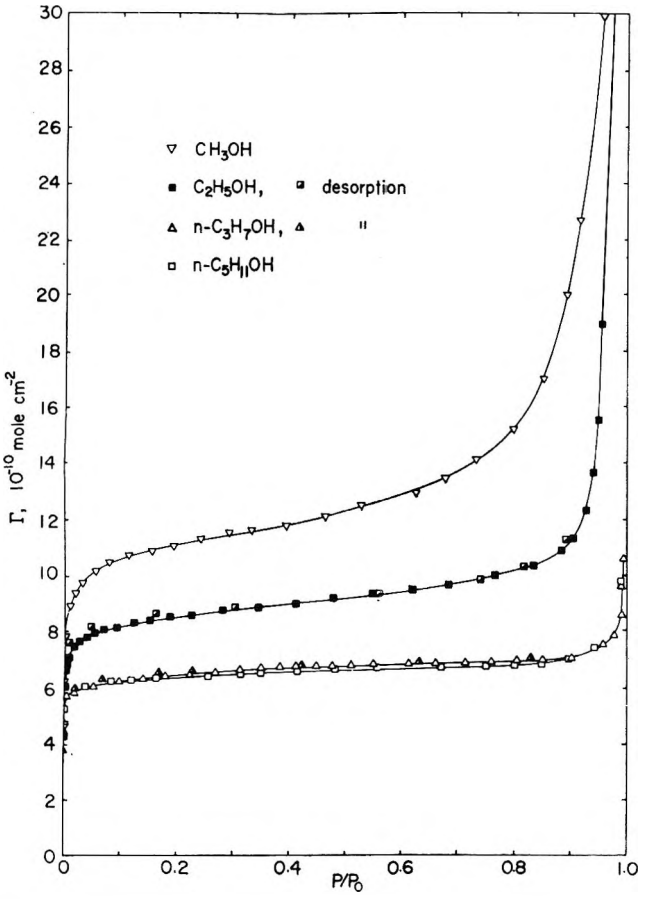

Figure 3. Adsorption of C_1 to C_3 on package B, and C_5 on package A prior to TMS. Desorption isotherms shown for C_2 and C_3 only.

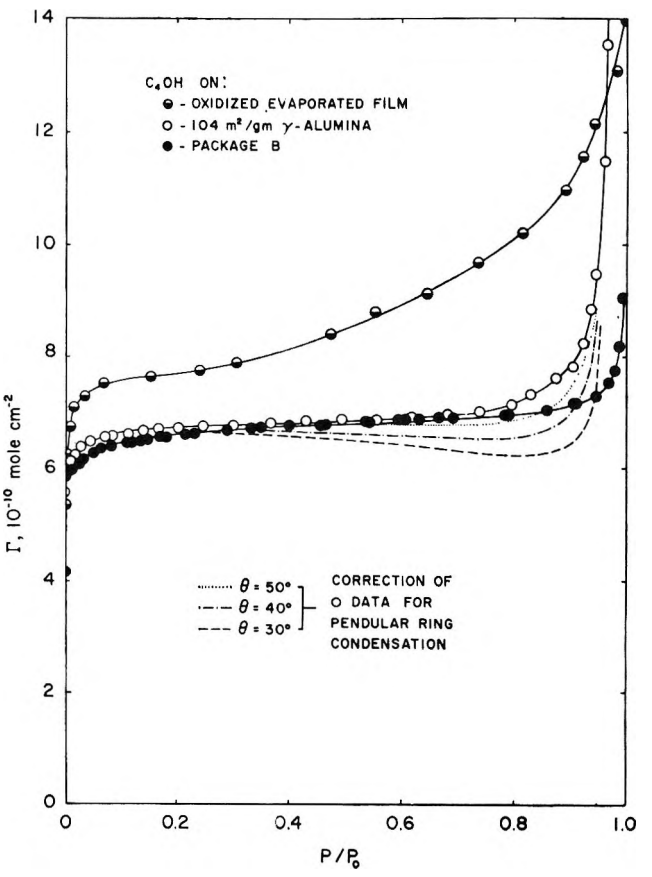

Figure 4. Adsorption of C_4 on oxidized evaporated film, ◒; 104 $m^2\ g^{-1}$ γ-alumina, O; and package B, ●. Residual γ-alumina isotherms are shown by the composite lines. Reading down θ = 50, 40, and 30°, respectively.

at 400°, loses all physically adsorbed water and retains only four hydroxyl groups per 100 Å^2. Dehydroxylation is thought to proceed by elimination of water between adjacent OH's;[5] subsequent exposure to water reverses the process. Analogously, exposure to an alcohol, ROH, is believed to give rise to adjacent surface –OR and –OH groups.[11,12] Neither formation of surface carboxylates nor production of ethers and olefins is likely at normal temperatures. In the present work, alcohol adsorption on the outgassed foil surface, though initially very rapid, took a surprisingly long time to reach equilibrium. At least 5 hr was necessary with C_1 at $p/p_0 \simeq 0.5$, although less time was required by alcohols of higher molecular weight. Equilibrium was approached most readily at high relative pressures. The delays may reflect a slow rearrangement of surface –OR groups to produce greater density and order in an initially random pattern of adsorption. Rearrangement would be favored by similar surface –OR and –OH bond strengths.

Water constituted an extreme case of the above phenomenon. For instance at $p/p_0 = 0.74$, 4.8×10^{-9} mol cm^{-2} were adsorbed on the outgassed surface within 5 min, 5.8×10^{-9} mol cm^{-2} within 7 hr. Apparent equilibrium was attained at 6.5×10^{-9} mol cm^{-2} only after 30 hr. This behavior is similar to that reported by Guderjahn, *et al.*[13] They found that a 7–8 $m^2\ g^{-1}$ alumina outgassed at 300° evolved only two-thirds of its heat of immersion in water immediately, the remainder being produced at a much slower rate. In contrast, detailed studies by Wade and Hackerman[14] have revealed neither slow heat evolution nor the maximum in the heat of immersion taken as a function of outgassing temperature that is characteristic of some silica and titania surfaces. On the other hand, no such maximum has been found for thoria,[15,16] and after outgassing at 500°, this material evidently requires several months to equilibriate with water vapor,[17] the delay here being attributed to the slow buildup of a rigidly structured

(11) R. G. Greenler, *J. Chem. Phys.*, **37**, 2094 (1962).
(12) R. O. Kagel, *J. Phys. Chem.*, **71**, 844 (1967).
(13) C. A. Guderjahn, D. A. Paynter, P. E. Berghausen, and R. J. Good, *J. Chem. Phys.*, **28**, 520 (1958).
(14) W. H. Wade and N. Hackerman, *Advan. Chem. Ser.*, **No. 43**, 222 (1964).
(15) H. F. Holmes and C. H. Secoy, *J. Phys. Chem.*, **69**, 151 (1965).
(16) E. L. Fuller, H. F. Holmes, C. H. Secoy, and J. E. Stuckey, *ibid.*, **72**, 573 (1968).
(17) E. L. Fuller, H. F. Holmes, and C. H. Secoy, *ibid.*, **70**, 1633 (1966).

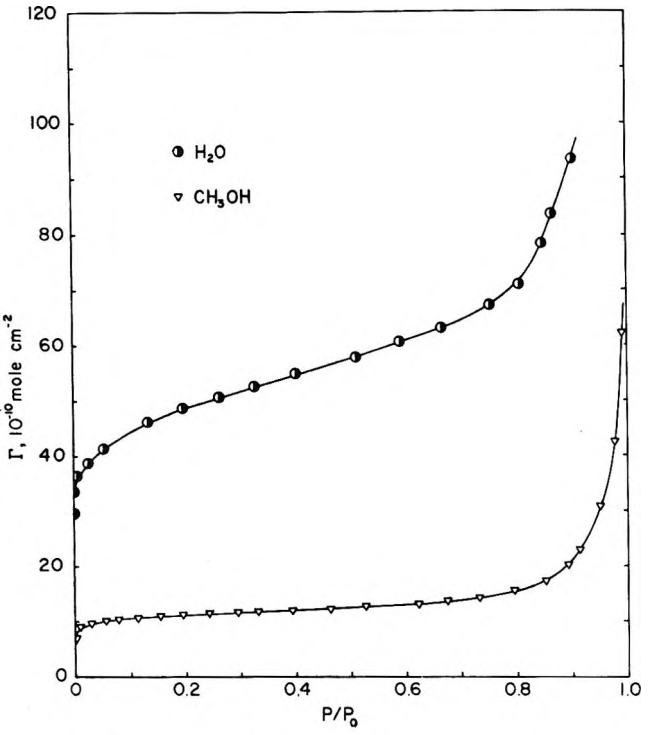

Figure 5. Adsorption of water and C_1 on package B.

hydration layer. A corresponding process may take place at some alumina surfaces.

Estimates of the extent of chemisorption on the foil surface are given in Table I. Here are listed the limiting surface concentrations after pretreatment and evacuation to 10^{-6} Torr at 20°. It should be noted that these values are for *relative pressures* ranging from 10^{-8} for C_1 to 10^{-6} for C_5.

Table I: Limiting Surface Concentrations after Pretreatment with Adsorbate and Evacuation to 10^{-6} Torr at 20°

Adsorbate	H_2O	C_1	C_2	C_3	C_4	C_5
Mol/100 Å²	17.8	2.8	2.5	2.3	2.5	2.8

If steric factors may be ignored and assuming chemisorption is dissociative, the limiting value for C_1 implies that not more than 2.8 (~3) sites are available for chemisorption per 100 Å², and therefore, that the maximum surface OH concentration of γ-alumina is 10 per 100 Å² (four remaining after outgassing plus six). This is roughly half of a previous estimate[18] based on the ionic structure of the bulk solid.

As in the case of thoria,[16,17] the high residual adsorption of water can be ascribed to replacement of surface OH groups followed by formation of a strongly bound hydration layer comprising, in the present case, 17.8 water molecules per 100 Å², or approximately 1.5 monolayers. An alternative possibility is that the oxidized surface of the foil is microporous to water. In addition to increasing the effective surface area, this could explain the lengthy equilibration time for adsorption. Microporosity, if shallow compared with the thickness of the oxide layer, is not incompatible with the known passivity of aluminum. It is, however, unlikely with oxides that have been calcined at temperatures above, say, 1000° during their manufacture, and its absence would explain the relatively low adsorption of water on alumina powders.[19]

Providing pretreatment was carried out reproducibly as specified, adsorption on the foil in excess of the limiting values of Table I was reproducible within ± 10^{-11} mol cm^{-2}, and essentially reversible up to the highest points shown in Figures 3–5. The striking correlation between the powder and foil isotherms for C_4 at low and intermediate relative pressures (Figures 4 and 6) confirms the underlying similarity of the two surfaces if micropore penetration cannot occur. That the isotherms reported previously[1] fall below those given here (this is reflected in Table II, below) indicates that alcohol adsorption is increased by higher outgassing temperatures, presumably because of lower surface hydration. [In the light of subsequent experience, it is thought that the C_4 isotherms reported by Barto, *et al.*,[1] were measured too rapidly, and that they therefore underestimate adsorption, especially at very high and very low relative pressures.] A complete absence of surface OH groups could be the reason for apparently higher C_4 adsorption on the oxidized film (Figure 4). However, the isotherm is plotted assuming $R = 1$, whereas earlier studies[7,8] have revealed values ranging from 1.7 to 4.3. Moreover, vapor-deposited films are likely to be rough or even porous owing to the random nucleation and growth of the individual crystallites of which they are composed.[20] Thus, the true isotherm lies below that shown, and the marked increase in Γ above $p/p_0 = 0.7$ is better ascribed to capillary condensation than to multilayer formation.

Figure 6 contains data from Figures 3–5 presented in Langmuirian form; for clarity, not all points are included. Corresponding BET plots were reasonably linear only up to $p/p_0 = 0.15$ and were therefore discounted. Molecular areas derived from Figure 6 are listed in Table II together with those reported previously[1] and those calculated from molar volumes.

In view of the acknowledged heterogeneity of alumina surfaces and the diverse adsorptive interactions likely with polar adsorbates, the applicability of the Langmuir isotherm to the systems considered here is surprising. The principal features of the Langmuir model are localized adsorption and a free energy of adsorption invariant with coverage. While the former is

(18) W. H. Wade and N. Hackerman, *J. Phys. Chem.*, **64**, 1196 (1960).

(19) R. L. Every, W. H. Wade, and N. Hackerman, *ibid.*, **65**, 937 (1961).

(20) See, for example, S. B. Hyder and M. A. Wilkov, *J. Appl. Phys.*, **38**, 2386 (1967).

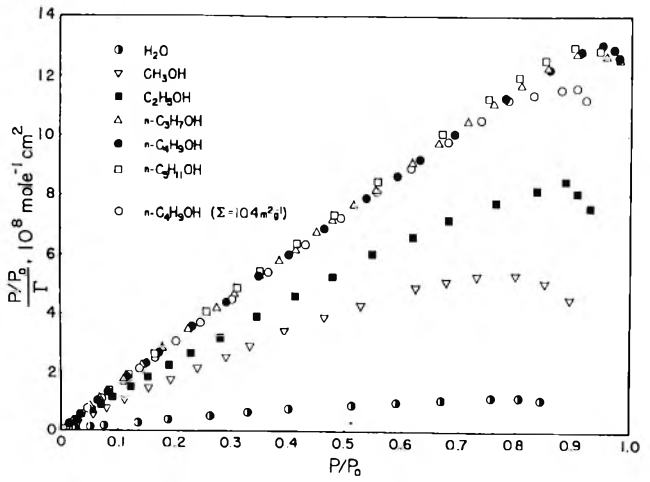

Figure 6. Langmuirian treatment of data from Figures 3–5.

Table II: Experimental and Calculated Molecular Areas for the Five Adsorbates Studied

	Molecular areas, Å²			
Adsorbate	Foil[a]	Alucer MA[a]	Alucer MA[b]	Calcd[c]
C_1	15.9	...	20.4	13.2
C_2	19.9	...	25.7	16.8
C_3	24.6	...	27.9	20.2
C_4	24.4	24.2	28.8	23.4
C_5	24.8	...	...	26.4

[a] Derived from Figure 5. [b] Barto, *et al.*,[1] alumina outgassed at 100°. [c] Calculated using the formula: molecular area = 1.53×10^{-16}(molar volume)$^{2/3}$.

probable, the latter can only result if decreasing adsorbate–adsorbent interactions and configurational entropy contributions are exactly compensated by increasing lateral interactions and thermal entropies of the adsorbed phase. Such compensation has been demonstrated by Barrer and Wasilewski for iodine on a synthetic zeolite.[21]

The new data in Table II show an average increase in molecular area of 4.4 Å² per carbon atom up to C_3. From C_3 to C_5 there is little further change. Hence, on completion of the monolayer, molecules are oriented predominantly normal to the surface, and, as the series C_1 to C_5 is traversed, molecules in second and subsequent layers become increasingly isolated from the influence of the alumina substrate. If adsorbate–adsorbate interactions are due primarily to weak, van der Waals forces, then the result of this isolation will be a decline in multilayer adsorption *plus* an increasing tendency for the bulk liquid to exhibit a nonzero contact angle on its own oriented monolayer. In other words, there should be a direct correlation between gas phase[1,2] and liquid phase[3,4] *autophobicity*.

To check this hypothesis, an ultrahigh vacuum, contact angle apparatus has been constructed, enabling precise duplication of isotherm conditions. A modified sessile drop technique is employed, and angles are measured with a microscope goniometer, some preliminary results are given in Table III. As predicted, the reduction in multilayer adsorption with increasing chain length reported by Barto, *et al.*,[1] and shown here most clearly in Figure 3, is associated with the appearance of an equilibrium contact angle, θ. However, the growth of this angle from C_3 to C_5 is not accompanied by any further reduction in adsorption and is best attributed to increases in the surface tension of the alcohol, γ_{LV}, giving a roughly constant value for $\gamma_{LV} \cos\theta$ that is very close to the critical surface tension of hydrocarbon surfaces composed of terminal $-CH_3$ groups.[22,23] The implication is that an oriented monolayer of C_3 is sufficient to screen the alumina surface entirely. This is perhaps better illustrated by the equilibrium surface pressure at the solid–vapor interface, $\pi_{SV}°$ which falls rapidly from 13.9 dyn cm^{-1} for C_1 to 0.3 dyn cm^{-1} for C_3, but is sensibly independent of carbon chain length thereafter (Table III). Here, the values of $\pi_{SV}°$ were estimated, using the integrated form of the Gibbs equation,[24] by ascribing to the *solid* all material adsorbed up to the completion of the Langmuir monolayer,[25] with $\pi_{SV}°$ arising from adsorption in excess of the Langmuir monolayer component. This approach, while difficult to justify in absolute terms, does provide a convenient way of comparing autophobic systems with other systems having nonzero contact angles. Since *all* adsorption prior to completion of the monolayer is neglected, the values are probably lower than would be found for better-defined surfaces of similar composition. That they are, nevertheless, all positive is especially interesting in the light of the controversy over whether or not $\theta > 0$ implies $\pi_{SV}° = 0$.[26]

In attempting to maximize the Langmuirian component, the foil was outgassed at the high temperatures as noted earlier. This resulted in alcohol adsorption isotherms with approximately two-thirds of the oriented monolayer being produced at immeasurably low pressures. This alleviated any realistic attempt to obtain spreading pressures for the Langmuirian component.

Comparison of the C_4 isotherms for powder and foil samples (Figure 4) shows that they begin to diverge significantly at $p/p_0 = 0.75$; and at $p/p_0 = 0.97$ the

(21) R. M. Barrer and S. Wasilewski, *Trans. Faraday Soc.*, **57**, 1140 (1961).

(22) H. W. Fox and W. A. Zisman, *J. Colloid Sci.*, **7**, 428 (1952).

(23) E. G. Shafrin and W. A. Zisman, *ibid.*, **2**, 166 (1952).

(24) If the vapor behaves ideally up to p_0

$$\pi_{SV}° = RT\int_0^1 \frac{(\Gamma - \Gamma_2)}{p/p_0}\, d(p/p_0)$$

where Γ_2 is the adsorptive contribution of a Langmuirian component to the measured total adsorption, Γ.

(25) H. H. Rowley and W. B. Innes, *J. Phys. Chem.*, **46**, 694 (1942).

(26) (a) W. H. Wade and J. W. Whalen, *ibid.*, **72**, 2898 (1968); (b) R. E. Johnson, Jr., and R. H. Dettre, *J. Colloid Interface Sci.*, **21**, 610 (1960).

Table III: Measured Contact Angles, Calculated Film Pressures, and Derived Quantities

Liquid	Contact angle, deg Advancing	Contact angle, deg Receding	γ_{LV},[a] dyn cm^{-1}	$\gamma_{LV} \cos \theta$,[b] dyn cm^{-1}	$\pi_{SV}°$, dyn cm^{-1}
C_1	0	0	22.6	22.6	13.9
C_2	0	0	22.3	22.3	6.2
C_3	13	<5	23.7	23.1	0.3
C_4	16	5	24.6	23.6	0.4
C_5	31	21	25.0	21.4	0.4

[a] J. Timmermans, "Physico-Chemical Constants of Pure Organic Compounds," Elsevier, Amsterdam, 1950, Supplemented 1965. [b] Advancing angle.

amount of alcohol taken up by the powder has doubled, while adsorption on the foil has increased by only a further 6%. The difference may be attributed to capillary condensation in the interstices of the powder.

In previous attempts to estimate capillary condensation as a function of relative pressure,[1,26a] particles were treated as spheres and all condensate was assumed to be in the form of pendular rings at points of contact between them. By subtraction of the resulting curves from the experimental isotherms, it was hoped to determine the extent of multilayer adsorption. In the absence of experimental data, the contact angle was assigned the minimum value that did not give a minimum in the residual isotherm.

To assess the method as a whole, the calculation has been repeated for C_4 using a coordination number[27] $n = 4$, and $\theta = 30$, 40, and 50°. The mean particle radius was found by electron microscopy to be 59 Å. The condensation corrected isotherms are shown in Figure 4. Those for $\theta = 30$ and 40° have minima; that for 50° diverges sharply from the foil isotherm above $p/p_0 = 0.85$. Evidently the method considerably underestimates condensation at high relative pressures. Some improvement can be gained by allowing θ to vary with coverage.[26a] This increases condensation at low relative pressures and hence permits a lower value of θ at saturation without reaping a minimum in the residual isotherm. However, the effect is marginal, and the experimental angle remain unsuitable. Perhaps the main defect in the method is its neglect of cooperative effects, such as pendular ring overlap, that enable large pore spaces to be filled irreversibly at high relative pressures.

Up to this point in the discussion, it has been tacitly assumed that capillary condensation is entirely absent from the foil isotherms, but owing to the undoubted presence of some areas of foil–foil and foil framework contact within each package, some subsaturation condensation is inevitable; hence, the isotherms may strictly be interpreted only as upper limits of multilayer adsorption. Nevertheless, these limits are much lower than those previously arrived at with comparable systems. They are, for example, lower than those obtained by Derjaguin and Zorin[28] for a flat glass surface. Using an ellipsometric technique, they observed films of C_2 to C_7 ranging from 40 to 75 Å^2 in thickness at $p/p_0 = 0.99$. At or slightly above saturation, even thicker films could apparently exist in equilibrium with a macroscopic droplet phase. In the present study, none of the liquids combines significant multilayer formation below $p/p_0 = 0.993$ (the highest relative pressure experimentally distinguishable from saturation) with $\theta > 0$ for the condensed phase. Where this does occur, the structure of the adsorbed multilayers must be quite different from that of the bulk liquid.[28] If it were not so, then the liquid would be required to establish an equilibrium contact angle on itself.[25] Thus, the ordering influence of glass would seem to be propagated much farther than that of alumina. Clearly, there is an immediate need to apply the ellipsometric method to the alumina surface, since with the present gravimetric apparatus, it is impossible to investigate adsorption at saturation and beyond unless condensation can somehow be suppressed.

Acknowledgments. The authors thank The Robert A. Welch Foundation and the National Science Foundation for their continued interest and financial support, and Mr. J. L. Cayias and Miss J. A. Zerdecki for their help with the contact angle measurements.

(27) W. H. Wade, *J. Phys. Chem.*, **69**, 322 (1965).

(28) B. V. Derjaguin and S. M. Zorin, *Proc. 2nd Int. Congr. Surface Activity*, **II**, 145 (1957).

NOTES

Electron Spin Resonance Spectra of Isocyanatoalkyl Radicals[1]

by Yoon Jin Chung and Ffrancon Williams*

Department of Chemistry, University of Tennessee, Knoxville, Tennessee 37916 *(Received December 7, 1970)*

Publication costs assisted by the U.S. Atomic Energy Commission

This note describes the esr spectra of the α-isocyanatoalkyl radicals generated by γ irradiation of methyl and ethyl isocyanates at 77°K. The original purpose of these studies was to search for evidence of dissociative electron capture[2,3] which would be manifested through the formation of the corresponding alkyl radical and NCO^-. In this approach, we were influenced by previous work[4] on organic cyanides. For example, dimer and monomer radical anions are formed in γ-irradiated acetonitrile crystal I and crystal II, respectively, and these electron-excess centers are easily photobleached to produce methyl radicals.[4] However, since we did not observe methyl radicals in the γ-irradiated isocyanate either before or after exposure of the samples to visible light,[4f] there is apparently no simple parallel between the radiation chemical behavior of methyl cyanide and isocyanate.

Experimental Section

Methyl isocyanate (CH_3NCO) was supplied by Matheson Coleman and Bell, and both ethyl isocyanate (C_2H_5NCO) and *n*-propyl isocyanate ($CH_3CH_2CH_2NCO$) were obtained from Aldrich Chemical Co. All materials were dried over magnesium sulfate and transferred *in vacuo* to esr sample tubes. Our general techniques of sample manipulation have been given in detail.[5]

Crystalline samples of methyl isocyanate were prepared in general by lowering the esr sample tube into a dewar half-filled with liquid nitrogen. Crystallization was easily effected in the cold space above the liquid nitrogen, and the sample was then cooled to 77°K. The same method could not be used to produce crystalline ethyl isocyanate, and a glass was invariably formed when the sample tube was immersed into liquid nitrogen. However, the crystallization of ethyl isocyanate was initiated readily from the glass at 77°K by suddenly warming the tip of the sample tube, and the process was completed by lowering the tube slowly into liquid nitrogen. We found it was impossible to prepare a crystalline sample of *n*-propyl isocyanate by either of the above techniques, and this material was examined only in the glassy state.

Irradiations were carried out at 77°K in a cobalt-60 γ source (Gammacell 200) at a nominal dose rate of 0.17 Mrad hr^{-1}, and the samples were then transferred in the dark to a liquid nitrogen dewar which fitted the cavity of the Varian (V-4502) esr spectrometer. The instrumental arrangement has been described.[5]

Esr spectra were first recorded with the γ-irradiated samples in the dark at 77°K and then again after irradiation *in situ* with visible light from a 1-kW tungsten lamp. A lens was used to focus the light beam on the grid of the V-4531 cavity. Sample temperatures above 77°K were obtained through the use of the Varian (V-4557) variable-temperature accessory.

Results

Figure 1 shows the esr spectrum of γ-irradiated methyl isocyanate obtained at 77°K after exposure of the sample to visible light. In this spectrum, the center region is considerably more symmetrical than in the one recorded with the sample in the dark after γ irradiation, and the main contribution comes from a set of nine lines which is readily grouped into a triplet of triplets as shown in the stick diagram. The larger triplet splitting is characteristic of hyperfine splitting with two equivalent α protons, and this assignment is supported by the fact that the three central components, whose net magnetic quantum number $m_I^H = 0$, are narrower than the $m_I^H = +1$ and -1 outer components, as would be the case for a rotating methylene group.[6] The well-defined 1:1:1 triplet substructure is ascribed to isotropic

(1) This research was supported by the U. S. Atomic Energy Commission under Contract No. AT-40-1-2968 and this is AEC Document No. ORO-2968-58.

(2) D. J. Whelan, *Chem. Rev.*, **69**, 179 (1969).

(3) For a review, see J. E. Willard in "Fundamental Processes in Radiation Chemistry," P. Ausloos, Ed., Interscience Publishers, New York, N. Y., 1968, Chapter 9, p 599.

(4) (a) M. A. Bonin, K. Tsuji, and F. Williams, *Nature*, **218**, 946 (1968); (b) M. A. Bonin, K. Takeda, and F. Williams, *J. Chem. Phys.*, **50**, 5423 (1969); (c) K. Takeda and F. Williams, *Mol. Phys.*, **17**, 677 (1969); (d) K. Takeda and F. Williams, *J. Phys. Chem.*, **74**, 4007 (1970); (e) K. Takeda and F. Williams, Abstracts, Second Symposium on Electron Spin Resonance (Division of Physical Chemistry of the American Chemical Society), Athens, Ga., Dec 1970, No. F4.

(4f) NOTE ADDED IN PROOF. Recent work has shown that ethyl radicals are produced on prolonged photobleaching of γ-irradiated ethyl isocyanate with visible light at 77°K although methyl radicals are not observed from γ-irradiated methyl isocyanate under the same experimental conditions. A full report of these photobleaching studies on γ-irradiated alkyl isocyanates will be submitted for publication in due course.

(5) J. Lin, K. Tsuji, and F. Williams, *J. Amer. Chem. Soc.*, **90**, 2766 (1968).

(6) E. L. Cochran, F. J. Adrian, and V. A. Bowers, *J. Chem. Phys.*, **34**, 1161 (1961).

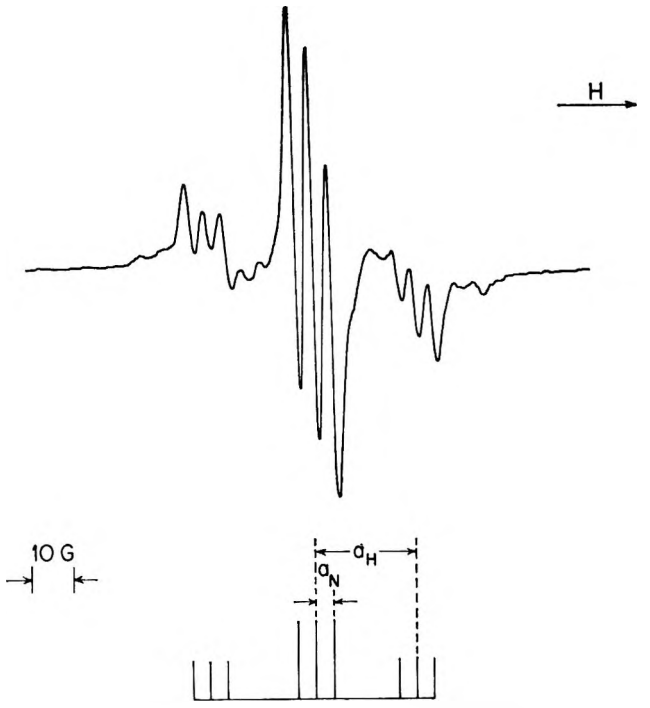

Figure 1. Esr first-derivative spectrum of γ-irradiated crystalline methyl isocyanate at 77°K after exposure to visible light. The irradiation dose was 2 Mrads.

nitrogen coupling and the splitting is 4.5 G. Therefore, we assign the nine-line spectrum to the $\cdot CH_2NCO$ radical. Although the spectrum appears to be very typical of a polycrystalline sample, there was a slight orientation dependence as evidenced by a sharpening of the outer triplets at certain angles.

The crystalline sample of γ-irradiated ethyl isocyanate gave rise to angular-dependent esr spectra which are illustrated in Figure 2. The upper spectrum shows a well-resolved hyperfine structure which can be analyzed into a doublet of quartets of triplets. This spectrum is assigned to the $CH_3\dot{C}HNCO$ radical with the coupling constants $a_\alpha^H = 31.8$ G, $a_\beta^H = 22.3$ G, and $a^N = 4.5$ G. The lower spectrum is not resolved into all the individual line components, but a large effect of magnetic anisotropy is revealed by the decrease in the overall width to 93 G in comparison with 108 G for the upper spectrum. It appears from the triplet structure at the low-field end of the lower spectrum that the nitrogen coupling remains unchanged with orientation and since it is well known that β-proton splittings show very little anisotropy in π radicals, the observed angular dependence can be attributed mainly to the anisotropy of the α-proton splitting. Although such marked orientation effects are not generally observed with crystalline samples grown from the glass, we find that the most successful art of preparing aligned crystals in the esr sample tube depends very much on the material being studied.[4,7] Only poorly resolved powder spectra were obtained from γ-irradiated ethyl and *n*-propyl isocyanate glasses.

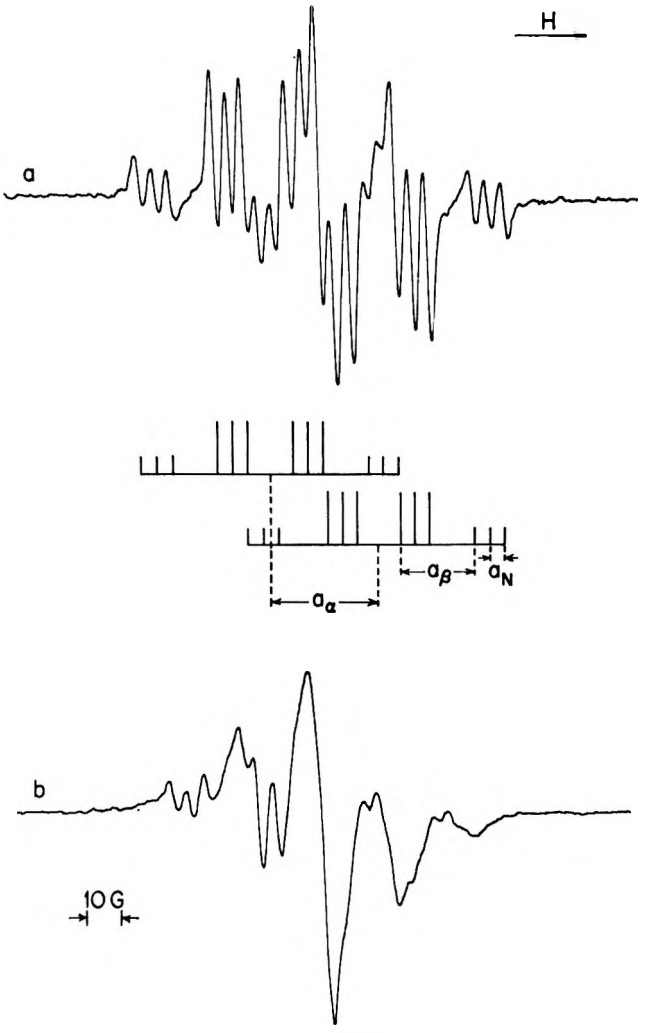

Figure 2. Esr first-derivative spectra of γ-irradiated crystalline ethyl isocyanate at *ca.* 120°K after exposure to visible light. The irradiation dose was 1.7 Mrads. Spectra a and b correspond to a rotation of the sample tube by 90° about the vertical tube axis in the magnetic field.

Discussion

An interesting question concerning the structure of these novel radicals is the extent to which the unpaired electron is delocalized from the p orbital on the α-carbon atom into the π orbitals of the –NCO group.

The spin density on the α-carbon atom of the $CH_3\dot{C}HNCO$ radical can readily be estimated from the magnitude of the isotropic coupling constant (22.3 G) for the β protons. Fessenden and Schuler[8] have proposed a value of 29.3 G for Q_β (CH_3) from which we calculate a spin density of 0.761. This can be set equal to the expression $(1 - 0.081)(1 - \chi)$, where χ represents the reduction in the spin density due to the adjacent –NCO group, so $\chi = 0.17$ in $CH_3\dot{C}HNCO$.

A similar value for χ in $\cdot CH_2NCO$ would lead us to

(7) M. L. Bonin, M. A. Bonin, and F. Williams, *J. Chem. Phys.*, **54**, 2641 (1971).

(8) R. W. Fessenden and R. H. Schuler, *ibid.*, **39**, 2147 (1963).

expect the isotropic coupling constant for the two α protons to be 20 G, assuming Q_α for the $R\dot{C}H_2$ configuration is 24.4 G.[8] Unfortunately, the extraction of the isotropic splitting from the anisotropic (largely polycrystalline) spectrum in Figure 1 is made difficult by the overlapping brought about by the nitrogen triplet substructure. Even though the spectrum indicates that the two protons are equivalent, the line shapes of the individual components in the outer triplets do not resemble those which normally characterize an axially symmetric hyperfine tensor.[6] Also, the structure of the group at low field appears to consist of two inner and two outer features in addition to the more intense triplet. Faced with these facts, we have obtained a tentative value for the isotropic splitting a_H simply from the center of gravity of each flanking group. This procedure results in a value of 26 ± 2 G which is appreciably greater than the 20 G estimated from the Q_α value, but we must concede that the discrepancy could well be due to our oversimplified analysis.

After this note was submitted for publication, we learned that Wood and his coworkers[9] have obtained the isotropic spectra of several isocyanatoalkyl radicals in an adamantane matrix. Their values of a_β^H (21.1 G) and a^N (4.2 G) for the isocyanatoethyl radical agree with our results almost within experimental error, so this supports the inference that the coupling to nitrogen in our spectrum is largely isotropic. The isotropic spectrum of the isocyanatomethyl radical would be of particular interest, but this has not been reported.[9]

Acknowledgment. We thank Professor D. E. Wood for sending us a preprint of his work on the isocyanatoalkyl radicals and for helpful correspondence about the possible interpretations of the powder spectrum of the isocyanatomethyl radical.

(9) D. E. Wood, R. V. Lloyd, and W. A. Lathan, Abstracts, Second Symposium on Electron Spin Resonance (Division of Physical Chemistry of the American Chemical Society), Athens, Ga., Dec 1970, No. D4.

Protolysis Kinetics of Ethyl *N*-Methylcarbamate[1]

by L. C. Martinelli,* C. D. Blanton, and J. F. Whidby

Department of Medicinal Chemistry, School of Pharmacy, University of Georgia, Athens, Georgia 30601
(Received January 15, 1971)

Publication costs borne completely by The Journal of Physical Chemistry

There has been a recent surge of interest in the study of proton exchange kinetics of biologically important classes of organic compounds.[2-6] To date these compounds have been principally amines, carboxylic acids and amides, mercaptans, and peptides. For example, the study of H–D exchange kinetics of polypeptides[7-9] and synthetic polyamides[10] has been useful to biochemists in elucidating chemical behavior of these compounds as a function of their substituents and conformational properties.

We became interested in proton exchange kinetics of biologically active compounds because of the recogniton that physical chemical properties such as oil–water partitioning, dissociation constants, dielectric constants, and electron densities of molecules are important in determining the type and magnitude of their biologic activity.[11] As a prelude to an extensive investigation of the role of proton exchange in biological activity of certain N–H bearing drugs we studied *N*-methylpropionamide and ethyl *N*-methylcarbamate. The title compound is a known general anesthetic[12] and a carcinogen[13] and possesses antileukemic activity.[14] *N*-Methylpropionamide was studied because of (1) its structural and chemical similarity to the title compound, and (2) because of its low degree of biologic activity. The analytical technique used herein was high-resolution nmr spectroscopy.

Experimental Section

All spectra were obtained in the frequency sweep mode on a Hitachi Perkin-Elmer R20A high-resolution nmr spectrometer operating at 60 MHz and equipped with a variable-temperature probe and digital frequency counter. Temperatures reported are within ±1° and were calibrated with ethylene glycol. Spectra were recorded at 30-Hz sweep width at 1000-sec

(1) (a) The authors wish to thank the Office of General Research and the School of Pharmacy, University of Georgia, for partial financial support of this research. (b) Presented at the 161st National Meeting of the American Chemical Society, Los Angeles, Calif., Mar 1971.

(2) W. F. Reynolds and T. Schaefer, *Can. J. Chem.*, **42**, 2641 (1964).

(3) M. Cocivera, *J. Amer. Chem. Soc.*, **88**, 672, 677 (1966).

(4) M. S. Puar and E. Grunwald, *ibid.*, **89**, 4403 (1967).

(5) E. Grunwald and E. K. Ralph, III, *ibid.*, **89**, 4405 (1967).

(6) J. F. Whidby and D. E. Leyden, *J. Phys. Chem.*, **74**, 202 (1970).

(7) H. Lenormant and E. R. Blout, *Nature*, **172**, 770 (1953).

(8) A. Hvidt, G. Johansen, K. Linderstrom-Lang, and F. Vaslow, *Compt. Rend. Trav. Lab. Carlsberg, Ser. Chim.*, **29**, 129 (1954).

(9) K. Linderstrom-Lang, Special Publication No. 2, The Chemical Society, London, 1955, p 1.

(10) I. M. Klotz and B. H. Frank, *J. Amer. Chem. Soc.*, **87**, 2721 (1965).

(11) T. C. Daniels and E. C. Jorgensen, "Textbook of Organic Medicinal and Pharmaceutical Chemistry," 5th ed, C. O. Wilson, O. Gisvold, and R. F. Doerge, Ed., J. P. Lippincott & Co., Philadelphia, Pa., and Toronto, 1966, Chapter 2, p 4.

(12) H. H. King, J. L. Hall, A. C. Andrews, and H. L. Cole, *J. Pharmacol.*, **40**, 275 (1930).

(13) J. C. Arcos and M. Arcos, "Progress in Drug Research," Vol. 4, E. Jucker, Ed., Interscience, New York, N. Y., 1962, p 513.

(14) H. E. Skipper, C. E. Bryan, W. H. Riser, Jr., M. Welty, and A. Stelzenmuller, *J. Nat. Cancer Inst.*, **9**, 77 (1948).

sweep time and were checked to assure saturation did not occur.

pH measurements were determined with a Corning Model 12 pH meter equipped with a Corning Triple Purpose Ag/AgCl electrode and a saturated KCl reference electrode. NBS buffers were used as calibration standards. All pH measurements and nmr spectra were obtained in CO_2 free triply distilled water which was stored under argon. Measurements were determined in a water-jacketed vessel at 34 ± 0.5°. The pH of the solutions were varied using HCl or KOH in CO_2 free water.

Values of τ were computed from individual spectra using an IBM 360/65 computer programmed with the general equations of Arnold,[15] which corrects for T_2 effects; T_2 was obtained from the N–CH_3 line width under slow proton exchange conditions and is limited by the field inhomogeneity.

N-Methylpropionamide. The amide was obtained commercially (Eastman reagent grade) and used without further purification.

Ethyl N-Methylcarbamate. Ethyl chloroformate (0.1 mol) and methylamine hydrochloride (0.1 mol) were added to a mixture of water–ether containing triethylamine (0.2 mol) and stirred for 1 hr. The ether layer was separated, dried over $MgSO_4$, and filtered, and the excess ether was removed to give a yellow oil. Distillation afforded a 65% yield of the carbamate ester, bp 164° at 754 mm [lit.[16] bp 170° (760 mm)].

Results and Discussion

Equations for the probable mechanisms of proton exchange were adapted from the published work on *N*-methylacetamide[17] and are listed below.

$$RH^* + H_3{}^+O \overset{k_{H^+}}{\rightleftharpoons} RH + H_2\overset{+}{O}H^* \text{ (acid catalyzed)} \quad (1)$$

$$RH + \bar{O}H \overset{k_{OH}}{\rightleftharpoons} R^- + HOH \text{ (base catalyzed)} \quad (2)$$

$$RH + HOH + RH^* \overset{k_2}{\rightleftharpoons} RH^* + HOH + RH \text{ (bimolecular)} \quad (3)$$

$$RH^* + HOH \overset{k_3}{\rightleftharpoons} RH + H^*OH \text{ (water catalyzed)} \quad (4)$$

Using these mechanisms, the overall rate expression is

$$\frac{\text{rate}}{RH} = \frac{1}{\tau} = k_{H^+}[H_3O^+] + k_{-OH}[\bar{O}H] + k_2[RH] + k_3[H_2O] \quad (5)$$

The overall rate ($1/\tau$) was determined by following the collapse of the N–CH_3 doublet. The exchange mechanisms were investigated as a function of pH and concentration of exchanging species. Activation energies were determined by measuring the rate of collapse of a doublet by varying the temperature at a fixed pH.

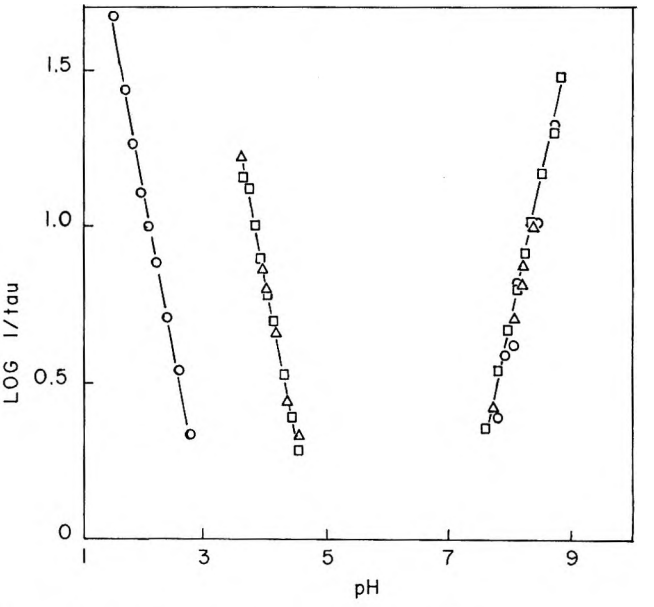

Figure 1. Log rate of proton exchange *vs.* pH:

○, 0.5 *M* $CH_3CH_2\overset{O}{\overset{\|}{C}}—\underset{H}{N}—CH_3$ in H_2O;

□, 0.5 *M* $CH_3CH_2—O—\overset{O}{\overset{\|}{C}}—\underset{H}{N}—CH_3$ in H_2O;

△, 1.0 *M* $CH_3CH_2—O—\overset{O}{\overset{\|}{C}}—\underset{H}{N}—CH_3$ in H_2O.

From a plot of log $1/\tau$ *vs.* pH, Figure 1, it can be seen that carbamate esters are subject to specific acid- and base-catalyzed proton exchange. In this respect they behave similarly to amides.[15] In Figure 1 it can also be seen that again like amides, carbamate ester proton exchange is not a function of concentration, either under acidic or basic conditions. This rules out the possibility of bimolecular mechanisms significantly contributing to any proton exchange rate either under basic or acidic conditions.

It is reported that with amides in water k_3 is small compared to k_{H^+} or k_{-OH}.[18] It was observed by us that k_3 is also small for carbamate esters in water. In a solution where neither $[H_3O^+]$ or $[^-OH]$ is large the

(15) J. T. Arnold, *Phys. Rev.*, **102**, 136 (1956).

(16) "Handbook of Chemistry and Physics," 50th ed, The Chemical Rubber Co., Cleveland, Ohio, 1969–1970, p C-232.

(17) A. Berger, A. Loewenstein, and S. Meiboom, *J. Amer. Chem. Soc.*, **81**, 62 (1959).

(18) T. Schleick, R. Gentzler, and P. H. Von Hippel, *ibid.*, **90**, 5954 (1968).

Table I: Rate Constants for N–H Proton Exchange and Energies of Activation[a]

Compound	k_{-OH}, M^{-1} sec^{-1}	k_{H^+}, M^{-1} sec^{-1}	E_a (acid), kcal/mol	E_a (base), kcal/mol
$CH_3CH_2CONHCH_3$	$3.81 \pm 0.26 \times 10^6$	$1.08 \pm 0.1 \times 10^3$	10.66 ± 0.46	...[b]
$CH_3CH_2OCONHCH_3$	$5.87 \pm 2.07 \times 10^6$	$5.62 \pm 1.23 \times 10^4$	8.56 ± 0.55	11.07 ± 0.50

[a] Rate constants and energies of activation were determined on 0.5 M solutions of amide and carbamate esters. Rate constants were determined at 34°. [b] Hydrolysis occurred at elevated temperatures.

exchange is slow (a sharp well-resolved doublet is observed).

On the basis of these data the overall rate expression is simplified to

$$\frac{\text{rate}}{RH} = \frac{1}{\tau} = k_{H^+}[H_3O^+] + k_{-OH}[\bar{O}H] \qquad (6)$$

Under acidic conditions hydroxide concentration is insignificant, simplifying the expression to

$$\frac{\text{rate}}{RH} = \frac{1}{\tau} = k_{H^+}[H_3O^+] \qquad (7)$$

while under basic conditions, where hydronium ion concentration is considered insignificant, the expression is

$$\frac{\text{rate}}{RH} = \frac{1}{\tau} = k_{-OH}[\bar{O}H] \qquad (8)$$

The acid- and base-catalyzed rate constants and the activation energies of proton exchange of *N*-methylpropionamide (reference compound) and ethyl *N*-methylcarbamate are listed in Table I. Under basic conditions there is no significant difference in the amide and carbamate ester rate constants, while there is a larger difference under acid conditions. Under basic conditions both can donate their proton through similar intermediates (Scheme I). In both cases the carbonyl

Scheme I

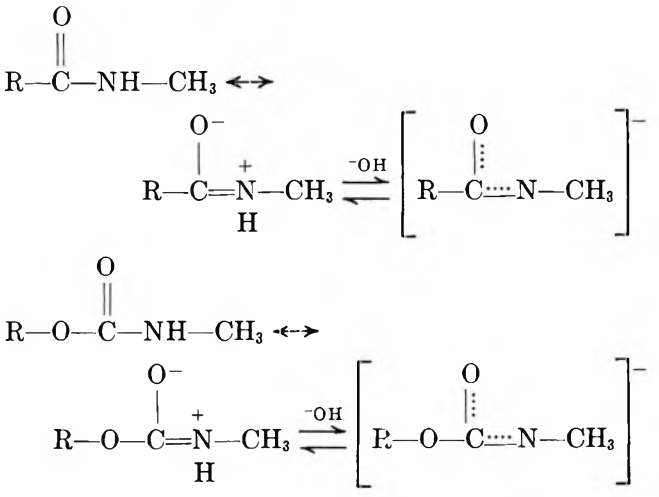

and nitrogen atoms can participate significantly to stabilize the transient negatively charged intermediates. From the data it appears that ester oxygen resonance with the carbamate carbonyl is not a significant factor during base-catalyzed proton exchange. Such reso-

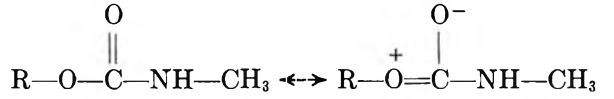

nance would be expected to retard nitrogen carbonyl resonance interaction resulting in a smaller base-catalyzed rate constant (k_{-OH}) than found with the amide.

In the presence of acid (H_3O^+) the carbamate ester has a significantly higher rate constant (k_{H^+}) than the amide (Table I). It has been postulated[17] that under acid conditions amides exchange protons through intermediate C which is in equilibrium with A (Scheme II).

Scheme II

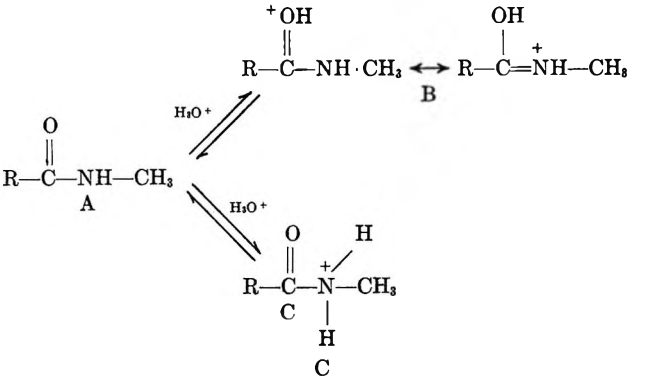

A similar intermediate seems likely to be involved with carbamates. Carbamates can probably be protonated to intermediates E, F, and possibly G (Scheme III). The protonated ester oxygen form G is probably not a significant factor in proton exchange because, in at least strong acid (SbF_5–FSO_3H–SO_2), carbamate esters exhibit only carbonyl protonation.[19] Species E, the carbamate carbonyl protonated form, is significantly different from the similar amide form, B, in that E has an additional stabilizing resonance contributor—the ester oxygen carbonyl resonance. Significant participation of the ester oxygen in resonance with the carbonyl would promote basicity of the nitrogen atom facilitating formation of F and E. The significantly larger protolysis rate constant (k_{H^+}) for the carbamate ester is evidence that carbamate esters possess a significant amount of ester oxygen carbonyl electronic delocalization in an acid medium. In the presence of acid the

(19) G. A. Olah and M. Calin, *J. Amer. Chem. Soc.*, **90**, 401 (1968).

Scheme III

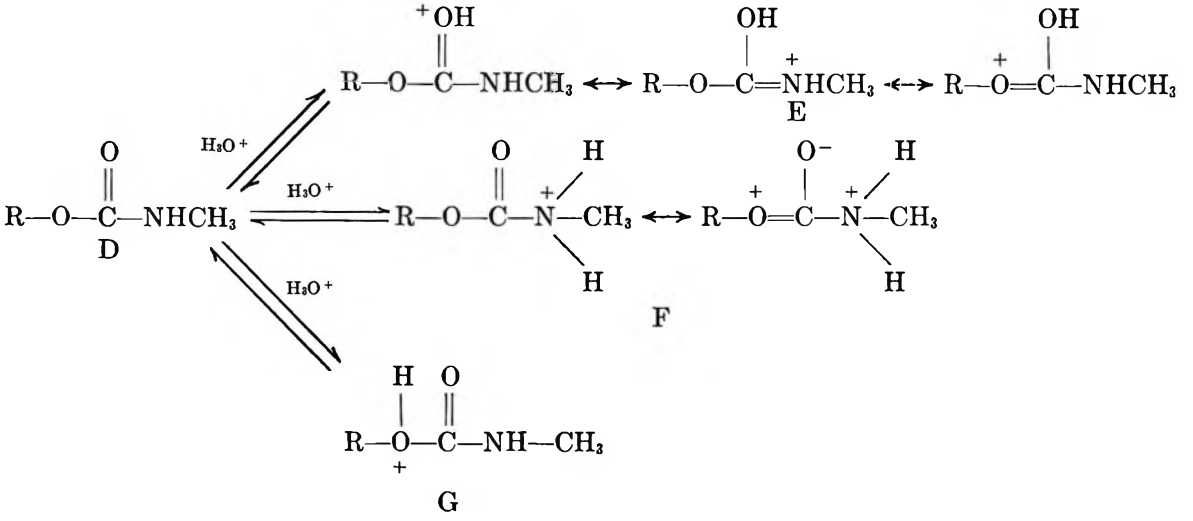

energy of activation of the carbamate ester is lower (8.56 ± 0.55 kcal mol^{-1}) compared to the amide (10.66 ± 0.46 kcal mol^{-1}) offering some further evidence that carbamate esters exchange protons with greater facility than amides.

Summary and Conclusion

From the data, carbamate esters and amides, in the presence of H_3O^+, exchange protons through similar intermediates, but the rates of exchange are significantly different with carbamates exchanging faster than amides. This difference seems best explained as being due to differences in resonance and inductive influences by the two types of neighboring groups on the nitrogen basicities. Under the conditions of this study the carbamate nitrogen thus appears to be more basic than the amide nitrogen. These same influences appear to be of less consequence during base-catalyzed exchange as evidenced by identical rate constants for the amide and carbamate ester.

The Observation of Positive Temperature Coefficients in the Bromine Nuclear Quadrupole Resonance Spectra of the Diethylammonium Salts of Hexabromoantimony(III) and Hexabromobismuth(III)

by T. B. Brill*

Department of Chemistry, University of Delaware, Newark, Delaware 19711

and G. G. Long

Department of Chemistry, North Carolina State University, Raleigh, North Carolina 27607 *(Received January 11, 1971)*

Publication costs assisted by the University of Delaware

The halogen nuclear quadrupole resonance spectra of hexahalometallate ions are of interest because numerous possible variations in the metal halogen bond are detectable simply by changing the metal, while most other factors remain essentially constant.[1,2] The present work was initiated in an attempt to extend the series of MX_6^{n-} ions for which nqr data are known to Sb(III) and Bi(III). It was found that strong ^{79}Br and ^{81}Br resonances could be recorded in $[(C_2H_5)_2NH_2]_3SbBr_6$ and $[(C_2H_5)_2NH_2]_3BiBr_6$. In addition, it was of interest to determine the temperature dependence of the halogen resonance frequencies for the purpose of comparison with other MX_6^{n-} ions.

Experimental Section

Synthesis. The antimony (bismuth) salt was prepared by adding 5 g of $Sb_2O_3(Bi_2O_3)$ to 20 ml of hot concentrated HBr or HCl. After the $Sb_2O_3(Bi_2O_3)$ had dissolved, a stoichiometric amount of diethylamine was added dropwise to the hot solution, and upon cooling, the well-formed colorless crystals of the compound were filtered off and dried over KOH. Other compounds mentioned in this paper were synthesized and analyzed in a similar manner. Carbon and hydrogen analyses were carried out by Galbraith Labs., Knoxville, Tenn. *Anal.* Calcd for $[(C_2H_5)_2NH_2]_3SbBr_6$: C, 17.49; H, 4.42; Sb, 14.78. Found: C, 17.75; H, 4.56; Sb, 14.96; mp 169–170°. Calcd for $[(C_2H_5)_2NH_2]_3BiBr_6$: C, 15.83; H, 3.95. Found: C, 15.84; H, 3.79; mp 194–195°.

Spectral Measurements. The nqr spectra were recorded using a Wilks Scientific NQR-1A spectrometer. Frequency measurements were made by zero-beating an external CW signal generator with the oscillator spectrum on a Tektronix 1L20 spectrum analyzer. The signal generator frequency was then measured precisely with a Monsanto 150A electronic counter. Using superregenerative techniques, two closely spaced reso-

(1) M. Kubo and D. Nakamura, *Advan. Inorg. Radiochem.*, **8**, 257 (1966), and references therein.

(2) T. L. Brown and L. G. Kent, *J. Phys. Chem.*, **74**, 3572 (1970).

nances cannot be separated. Reasonably symmetric resonance multiplets were detected at all temperatures implying that distortions in the anions, although probably present, are minor. Due to the difficulty of determining the center line of the resonance multiplet, the absolute error in the frequencies can be about 0.1 MHz. However, if what appears to be the same line of the multiplet is measured at all temperatures studied, then the relative error in frequency can be much less (1 part in 5000). In Table I the frequencies are reported more accurately than the absolute error justifies because it is the *relative* differences that affect the results presented here.

Table I: Bromine Resonance Frequencies (MHz) in Diethylammonium Salts of Hexabromoantimony(III) and -bismuth(III) at Various Temperatures[a]

Compd	T, °K	$\nu(^{79}Br)$	$S:N$[b]
$[(C_2H_5)_2NH_2]_3SbBr_6$	330	126.10	25:1
	298	126.19[c]	20:1
	275	126.24	20:1
	243	126.06	15:1
	223	125.94	7:1
	193	125.60	3:1
	T, °K	$\nu(^{81}Br)$	$S:N$[b]
$[(C_2H_5)_2NH_2]_3BiBr_6$	330	87.74	18:1
	298	87.93[d]	20:1
	275	88.02	17:1
	243	88.07	14:1
	223	88.01	10:1
	193	87.95	7:1
	77	87.65	10:1

[a] See Experimental Section for error estimates. [b] The filling factor of the radiofrequency coil is significantly less during temperature dependence work so that the signal-to-noise ratios are significantly decreased. At room temperature with the highest filling factor the $S:N$ ratio for $\nu(^{79}Br)$ in $[(C_2H_5)_2NH_2]_3SbBr_6$ is 65:1 and $\nu(^{81}Br)$ for $[(C_2H_5)_2NH_2]_3BiBr_6$ is 60:1. [c] $\nu(^{81}Br)$ is 105.4 MHz. [d] $\nu(^{79}Br)$ is 105.5 MHz.

The line shape of the resonances is, in part, a function of differences in the oscillator operation over the various frequency ranges. The ranges of 120–130 MHz and 80–95 MHz yield better line shapes than the 105-MHz region. For this reason we chose to study $\nu(^{81}Br)$ in the case of bismuth and $\nu(^{79}Br)$ for antimony. Temperature variations were obtained by placing a Dewar cold finger containing the sample and cooling mixture in the radiofrequency coil of the spectrometer. The temperatures in Table I were obtained by the following means: warm H_2O (330°K), ice H_2O (275°K), *o*-xylene (80%)–*m*-xylene(20%)–Dry Ice (243°K), *o*-xyleue (50%)–*m*-xylene (50%)–Dry Ice (223°K),[3] Dry Ice and acetone (193°K), liquid N_2 (77°K). The temperatures are reliable within ±3°K.

Results and Discussion

The number of different cations which form hexahaloantimony(III) and bismuth(III) salts is somewhat more limited than with other metals because of the frequent formation of polynuclear complexes having widely varying stoichiometries. Simple counterions, such as K^+, Rb^+, and NH_4^+, which have been used in nqr studies of other hexahalometallates, frequently do not form C_3MX_6 compounds with Sb(III) and Bi(III) under normal conditions. It is usually necessary to resort to alkyl-substituted ammonium ions for this purpose. Unsuccessful attempts were made here to record room temperature spectra in $[(C_2H_5)_2NH_2]_3BiCl_6$, $[(n\text{-}C_4H_9)_2NH_2]_3BiBr_6$, and $[(CH_3)_2NH_2]_3BiBr_6$. However, $[(C_2H_5)_2NH_2]_3SbBr_6$ and $[(C_2H_5)_2NH_2]_3BiBr_6$ produced strong $^{79,81}Br$ signals and their frequencies are shown in Table I. X-Ray powder diffraction patterns of these two compounds and their ir and Raman spectra show a very good correlation between all the major peaks and it is reasonable to assume that they are isostructural.

Electronic Effects. Sb(III) and Bi(III) in MX_6^{3-} ions have valency shells containing seven electron pairs. If the seventh pair of electrons is stereochemically active, the MX_6^{3-} ion would not have regular octahedral geometry.[4] The fact that only one nqr signal is found in both compounds indicates that ligand–ligand repulsions are more important than electron pair repulsion and the extra electron pair has become inert. X-Ray crystallographic studies are available for $(NH_4)_2SbBr_6$ which contains $SbBr_6^{3-}$ ions[5] and $[(CH_3)_2NH_2]_3BiBr_6$[6] and in both cases the anion is a regular octahedron. It must be kept in mind that the nqr technique "views" the bromine atoms in their averaged environment and that molecular rearrangements are expected to be on about the same time scale as the nqr event.[7]

Comparison of the nuclear quadrupole resonance data for these $SbBr_6^{3-}$ and $BiBr_6^{3-}$ salts is valid since the two compounds are isostructural. Table I shows that there is a very marked difference between the bromine signals in the two, and the increasing metallic character in going from Sb to Bi is readily reflected as an increase in the ionic character of the M–Br bond. Comparisons of the $SbBr_6^{3-}$ and $BiBr_6^{3-}$ data with other hexahalometal salts with different cations are tenuous because the resonance frequencies undoubtedly do not reflect solely the effects of changing the central metal. Variations of the cation would be expected to depress or amplify the extent of the observed effects.

Temperature Dependence Data. Figure 1 shows the effect of temperature variation between 360 and 190°K on the ^{79}Br frequency in $[(C_2H_5)_2NH_2]_3SbBr_6$. The

(3) A. M. Phipps and D. N. Hume, *J. Chem. Educ.*, **45**, 664 (1968).
(4) R. J. Gillespie, *ibid.*, **47**, 18 (1970), and references therein.
(5) S. L. Lawton and R. A. Jacobsen, *Inorg. Chem.*, **5**, 743 (1966).
(6) W. G. McPherson and E. A. Meyers, *J. Phys. Chem.*, **72**, 3117 (1968).
(7) E. L. Muetterties, *Inorg. Chem.*, **4**, 769 (1965).

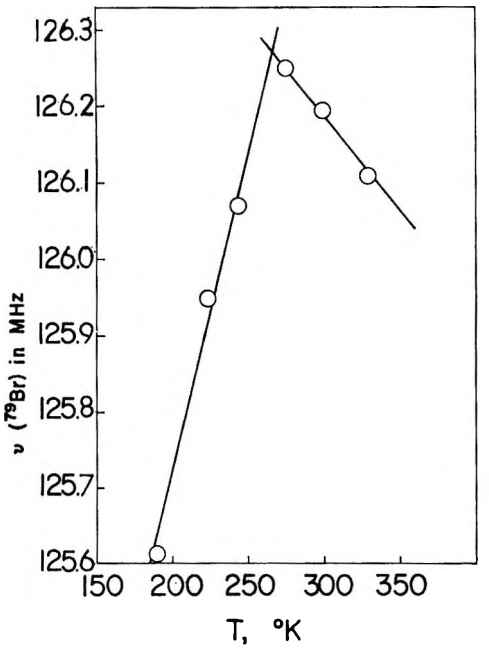

Figure 1. The temperature dependence of the ^{79}Br resonance frequency in $[(C_2H_5)_2NH_2]_3SbBr_6$.

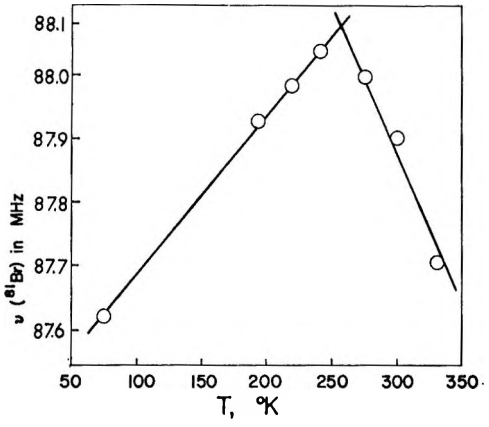

Figure 2. The temperature dependence of the ^{81}Br resonance frequency in $[(C_2H_5)_2NH_2]_3BiBr_6$.

sign of the temperature coefficient, $(\partial\nu/\partial T)_P$, is negative around room temperature but a phase transition takes place at about 265° ± 4°K in this compound below which the sign of $(\partial\nu/\partial T)_P$ becomes positive. The signal gradually becomes weaker as the temperature is decreased and was eventually lost in the noise near the Dry Ice–acetone temperature. No signals were found at 77°K. The same pattern for $(\partial\nu/\partial T)_P$ is found in $[(C_2H_5)_2NH_2]_3BiBr_6$ as is shown in Figure 2. The phase transition in this compound occurs around 255 ± 4°K, and the resonance frequency remains detectable (although somewhat weaker) down to 77°K where measurements were ceased. In both compounds the phase transition is nondestructive.

In recent years much work has appeared related to the interpretation of temperature and pressure coefficients in hexahalometallates. Kubo and Nahamura and their collaborators[1] initiated much of this study. Armstrong and his coworkers[8] have carefully investigated the potassium salts of $PtCl_6^{2-}$, $PdCl_6^{2-}$, $IrCl_6^{2-}$, and $OsCl_6^{2-}$. O'Leary[9] investigated K_2ReCl_6. Brown and Kent[2] reported considerably more data in many C_nMX_6 systems. Among the transition metals with d orbital "holes," positive temperature coefficients in the halogen spectra are best accounted for using a mechanism involving the destruction of metal–halogen π bonding as a function of temperature.[1,2,8,10] Negative temperature coefficients are by far the most common and appear to be related to low-frequency torsional modes of the anion.[8,9,11,12] The cubic antifluorite structure, which exists in most of the compounds in this past work, cannot exist in the $(C_2H_5)_2NH_2^+$ salts. In addition, little Sb–Br and Bi–Br π bonding is likely so that the mechanism causing the reversal in sign of $(\partial\nu/\partial T)_P$ in our compounds is not at all certain. It is evident, however, that phase transitions must be considered as being important in determining the sign of $(\partial\nu/\partial T)_P$.[9]

The resonance frequency can be thought of at constant pressure as being a function of volume and temperature, $\nu = f(V,T)$, so that[12,13]

$$(\partial\nu/\partial T)_P = (\partial\nu/\partial T)_V + (\partial\nu/\partial V)_T(\partial V/\partial T)_P \quad (1)$$

Bayer[11] has shown that $(\partial\nu/\partial T)_V$ is normally negative. $(\partial V/\partial T)_P$ is the important term in thermal expansivity and is positive. If $(\partial\nu/\partial V)_T$ is assumed to be positive,[1] the sign of $(\partial\nu/\partial T)_P$ depends on whether the former or the latter term on the right side of (1) is larger. The volume of the unit cell is crucially dependent on phase transitions so that the latter term could be expected to change markedly in magnitude during the course of a phase transition. The change appears to be significant enough to reverse the sign of $(\partial\nu/\partial T)_P$ in these compounds.

This phase transition explanation is probably not "microscopic" in the sense that low-frequency torsional modes and metal–halogen π bonding are. The onset of a phase transition simply provides a means for the latter two mechanisms to operate under different conditions.

Acknowledgment. The preparative skill of Mr. P. E. Garrou is gratefully acknowledged.

(8) R. L. Armstrong, G. L. Baker, and K. R. Jeffrey, *Phys. Rev.*, *B*, **1**, 2847 (1970); R. L. Armstrong and G. L. Baker, *Can. J. Phys.*, **48**, 2411 (1970); G. L. Baker and R. L. Armstrong, *ibid.*, **48**, 1649 (1970); R. L. Armstrong and D. F. Cooke, *ibid.*, **47**, 2165 (1969); R. L. Armstrong and K. R. Jeffrey, *ibid.*, **47**, 1095 (1969); K. R. Jeffrey and R. L. Armstrong, *Phys. Rev.*, **174**, 359 (1968); K. R. Jeffrey, R. L. Armstrong, and K. E. Kisman, *ibid.*, *B*, **1**, 3770 (1970).

(9) G. P. O'Leary, *Phys. Rev. Lett.*, **23**, 782 (1969).

(10) T. E. Haas and E. P. Marram, *J. Chem. Phys.*, **43**, 3985 (1965).

(11) H. Bayer, *Z. Phys.*, **130**, 227 (1951).

(12) T. Kushida, G. B. Benedek, and N. Bloembergen, *Phys. Rev.*, **104**, 1364 (1956).

(13) H. S. Gutowsky and G. A. Williams, *ibid.*, **105**, 464 (1957).

COMMUNICATIONS TO THE EDITOR

Nuclear Magnetic Resonance Study of Hindered Internal Rotation in Urea in Solution

Publication costs assisted by The Lund Institute of Technology

Sir: Recent studies on rotational barriers around the C–N bonds in alkyl-substituted ureas[1] and thioureas[2,3] indicate that they are considerably lower than in comparable simple amides.[4] No investigation of the C–N barrier in urea in solution has been published, but solid urea has been studied by broad line nmr[5] and by nqr techniques,[6] and both methods have given results interpretable in terms of dynamic reorientation around bonds.

We wish to report a variable temperature pmr study of urea–^{14}N in solution. Initially our aim was to study the di-^{15}N-enriched compound, but no solvent was found in which its spin–spin coupling pattern could be sufficiently well resolved at low temperatures. For this reason ordinary urea, in spite of the quadrupole broadening by the ^{14}N nuclei, showed narrower pmr signals than the ^{15}N-enriched compound. The choice of solvents for a variable temperature study of urea is very limited, and only one usable solvent, dimethylformamide (DMF), has been found. Since the effects of hydrogen bonding can be of great importance for urea, two solvent mixtures, DMF–dimethyl sulfoxide (DMSO) and acetone–tetramethylurea (TMU) were also used to obtain at least some variation in solvent polarity. All spectra were recorded on a Varian Associates A-60A spectrometer equipped with a V-6040 temperature controller. (For Results, see Table I).

The appearance of the proton nmr spectra of urea in the TMU–acetone mixture (see below) at various temperatures is shown in Figure 1. The resulting spectra were analyzed in terms of a two-site exchange process, according to the theory of Gutowsky, *et al.*,[7] and rate constants were evaluated from digitized spectra at temperatures near coalescence by means of an iterative computer program.[8] The variation in effective natural line width was accounted for by interpolation between slow and fast exchange values and the variation in nonexchanging chemical shift difference by extrapolation of slow exchange values. The free energy of activation, $\Delta G^{\ddagger}$, was calculated from the Eyring equation, assuming the transmission coefficient to be unity. The uncertainties in the natural line widths and the extrapolated shift differences for the NH signal(s) are too great to make an evaluation of the activation parameters $\Delta H^{\ddagger}$ and $\Delta S^{\ddagger}$ seem meaningful (*cf.* ref 9).

The $\Delta G^{\ddagger}$ value for hindered rotation around the amide bonds in urea is significantly ($\approx$1.6 kcal/mol) higher than for the dimethylamino group in a trialkyl-substituted urea.[1] Possible rationalizations for this increased barrier height are as follows: (i) stabilization of the ground state by intermolecular hydrogen bonding; (ii) increased electron delocalization across the C–N bond; and/or (iii) removal of steric interaction between *N*-methyl groups and NH protons that are both trans to the carbonyl oxygen. Probably all three factors are of importance. Unfortunately, no large variations in solvent composition or urea concentration

Table I: Results

System (weight fractions)[a]	T, °K[b]	τ, sec[c]	$\Delta G^{\ddagger}$, kcal mol^{-1} [c]
Urea:DMF	218	0.057	11.4
0.030:0.970	220	0.037	11.3
	224	0.016	11.1
	226	0.009	11.0
		Mean value	11.2
Urea:DMSO:DMF	220	0.063	11.5
0.028:0.273:0.699	222	0.047	11.5
	224	0.027	11.4
	229	0.016	11.4
		Mean value	11.5
Urea:acetone:TMU	220	0.048	11.3
0.021:0.355:0.624	224	0.032	11.5
	226	0.023	11.4
	230	0.012	11.3
		Mean value	11.4
		Total mean value	11.33

[a] All systems were more or less supercooled at low temperatures. [b] The estimated accuracy is $\pm 2°$. The reproducibility was better than $\pm 1°$. [c] The error limits are of the order of 10–30% for τ and ± 0.1 kcal mol^{-1} for $\Delta G^{\ddagger}$. This was found by calculating τ and $\Delta G^{\ddagger}$ values using combinations of lineshape parameters and temperatures, taking into account maximum reasonable error limits.

(1) P. Stilbs, *Acta Chem. Scand.*, in press.

(2) G. Isaksson and J. Sandström, *ibid.*, **24**, 2565 (1970).

(3) A. S. Tompa, R. D. Barefoot, and E. Price, *J. Phys. Chem.*, **73**, 435 (1969).

(4) W. E. Stewart and T. H. Siddall, III, *Chem. Rev.*, **70**, 517 (1970).

(5) R. A. Kromhout and W. G. Moulton, *J. Chem. Phys.*, **23**, 1673 (1955).

(6) A. S. Gur'evich and L. I. Strelets, *Zh. Strukt. Khim.*, **10**, 811 (1969).

(7) H. S Gutowsky, D. V. McCall, and C. P. Slichter, *J. Chem. Phys.*, **21**, 279 (1953).

(8) The principles of this program have been described in ref 9. The subroutine STEPIT (obtainable through Quantum Chemistry Program Exchange, Chemistry Dept., Indiana University, Bloomington, Ind. 47401) was used for iteration.

(9) T. Drakenberg, K. I. Dahlqvist, and S. Forsén, *Acta Chem. Scand.*, **24**, 694 (1970).

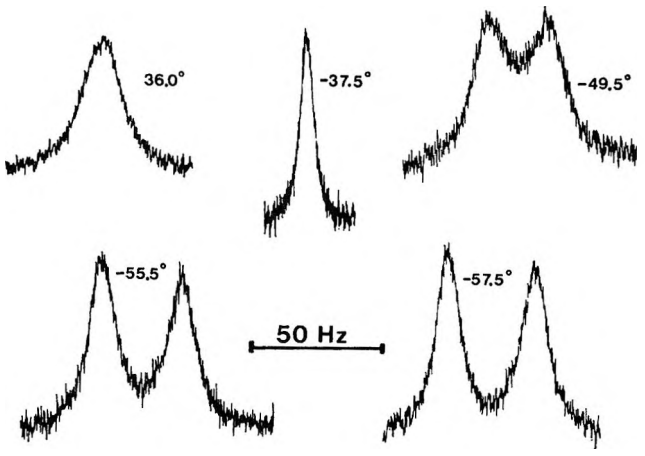

Figure 1. The 60-MHz spectrum of urea in TMU–acetone at various temperatures.

were possible, but it should be noted that the differences in $\Delta G^{\ddagger}$ are very close to being zero within the experimental error for the systems studied.

Extrapolated nqr data[6] indicate that the rate of rotation around the amide bond in solid urea is only a factor of 100 lower than in solution at $-50°$.

Acknowledgments. Helpful discussions with Dr. T. Drakenberg are gratefully acknowledged, and we wish to thank Dr. R. E. Carter for linguistic criticism. P. S. wishes to thank The Bengt Lundqvist Memorial Fund for a grant.

DIVISION OF PHYSICAL CHEMISTRY
THE LUND INSTITUTE OF TECHNOLOGY
CHEMICAL CENTER
S-220 07 LUND 7, SWEDEN

PETER STILBS*
STURE FORSÉN

RECEIVED FEBRUARY 9, 1971